Durham E-Theses

Chemical weathering of sedimentary rocks as a source of carbon dioxide to the atmosphere

OGRIC, MATEJA

How to cite:

OGRIC, MATEJA (2021) *Chemical weathering of sedimentary rocks as a source of carbon dioxide to the atmosphere*, Durham theses, Durham University. Available at Durham E-Theses Online: http://etheses.dur.ac.uk/14179/

Use policy

The full-text may be used and/or reproduced, and given to third parties in any format or medium, without prior permission or charge, for personal research or study, educational, or not-for-profit purposes provided that:

- a full bibliographic reference is made to the original source
- a link is made to the metadata record in Durham E-Theses
- the full-text is not changed in any way

The full-text must not be sold in any format or medium without the formal permission of the copyright holders.

Please consult the full Durham E-Theses policy for further details.

Academic Support Office, Durham University, University Office, Old Elvet, Durham DH1 3HP
e-mail: e-theses.admin@dur.ac.uk Tel: +44 0191 334 6107
http://etheses.dur.ac.uk

Chemical weathering of sedimentary rocks as a source of carbon dioxide to the atmosphere

Mateja Ogrič

A thesis submitted in partial fulfilment for the requirements for the degree of Doctor of Philosophy in Physical Geography

Department of Geography
Durham University
2021

Abstract

The geological carbon cycle maintains sustainable conditions for the Earth's habitability through weathering and erosion. This research focuses on two chemical weathering processes: i) rock organic carbon oxidation and ii) carbonate dissolution by sulfuric acid, both resulting in carbon dioxide (CO_2) release to the atmosphere. The long-term and modern-day fluxes and environmental controls navigating chemical weathering reactions are investigated in small (<1 km^2), densely monitored catchments of two critical zone observatories: i) the Susquehanna Shale Hills (Pennsylvania, USA) and ii) the Draix-Bléone (Provence, France). In the low erosive setting of the Susquehanna Shale Hills observatory, the trace element rhenium (Re) is studied alongside total organic carbon and radiocarbon data to estimate the long-term rock organic carbon oxidation rates. This study confirms that rock organic carbon weathering is a supply-limited process. In addition, substantial anthropogenic perturbation of the surface Re cycle is observed at this site. In the Draix-Bléone observatory an unprecedented high-temporal resolution stream water sampling campaign took place in two nearby catchments. The catchments are contrasting in physical erosion rates and variable extent of vegetation cover, allowing to investigate controls on present-day rock organic carbon oxidation rates and inorganic carbon balance. In the highly erosive and sparsely vegetated catchment the CO_2 release rates are largely dominated by carbonate dissolution by sulfuric acid. Furthermore, strong seasonality in dissolved SO_4^{-2}/HCO_3^- ratios and Re concentrations and in streams is observed, which is interpret as a seasonal signal in sulfuric acid production and rock organic carbon oxidation, respectively. These findings suggest a temperature control on CO_2 release rates through chemical weathering reactions, which is most pronounced in highly erosive and sparse vegetation setting. Overall, this research provides novel insights on environmental controls on chemical weathering rates and proposes a positive climatic feedback on chemical weathering of sedimentary rocks, which carries important implications for future climate studies.

Table of contents

List of tables

List of figures

Chapter 1

Chapter 2

Chapter 3

Chapter 4

Chapter 5

Chapter 6

Statement of copyright

The copyright of this thesis rests with the author. No quotation from it should be published without the author's prior written consent and information derived from it should be acknowledged.

Acknowledgements

I am very pleased for the opportunity to work alongside such an enthusiastic, supportive and kind group of people.

First, I would like to thank my supervisors, Bob Hilton and Mathieu Dellinger. Your never-ending knowledge, creativity and passion for research is incredibly inspiring. I feel privileged to learn from both of you. Thank you for your patience, kindness, knowledge, time and support. My thanks also go to the rest of the ROC-CO2 team, Guillaume Soulet, Katie Grant, Tobias Roylands – it has been a great pleasure to be part of such a supportive team.

This PhD was funded by the ERC-Starting grand to Bob Hilton and I gratefully acknowledge their financial support. The funding allowed me to participate in three international conferences, conduct five fieldtrips and explore a number of analytical methods in the lab. I am also grateful for the additional funding during my maternity leave.

This project provided me with opportunities to collaborate and learn from a large group of great scientists. I would like to thank Susan Brantley and Xin Gu for insightful discussions on the Susquehanna Shale Hills study site. I also thank Sébastien Klotz and Caroline Le Bouteiller from the Draix-Bléone site for providing such a complete sampleset and the inside knowledge. Additionally, I would like to thank Jordon Hemingway, Alexandra Turchyn and Darren Gröcke for introducing me to the world of sulfide mineral oxidation and stable sulfur and oxygen isotopes. I would also like to thank our collaborators from Gisborne City Council in New Zealand, in particular Peter Hancock and Harriet Roil.

My extended thanks go to the laboratory staff at the Department of Geography; Eleanor Ross, Amanda Hayton and Martin West: thank you for sharing your knowledge and expertise in sample preparation and various analytical measurements. My thanks also go to Geoff Nowell from the Department of Earth Sciences for his guidance through the work in the clean lab.

I feel incredibly lucky to make a number of friendships during my time in Durham. Juliet, Rich, Cynthia, Liz, Zoe, Ayushman, Ludovico – thinking back on times when we all lived in Durham and we meet for coffees, dinners, drinks, walks etc. feels so far ago. I am looking forward to see you all again in the future.

Finally, I would like to thank to my partner Christian, for his never-ending support, for being such an incredible co-parent to our daughter and for always believing in me.

Rada bi se zahvalila tudi svoji družini in prijateljem v Sloveniji. Največja zahvala pa gre moji hčerki Freji. Freja, preživljanje časa s teboj je najboljša možna sprostitev in tvoja iskrenost je najboljša pomoč pri premagovanju vsakodnevnih težav – hvala!

CHAPTER 1
Introduction

Drone image of the lower Laval catchment at the Draix-Bléone Critical Zone Observatory, South French Alps;
February 2018; Photo: Thomas Croissant

1.1 Thesis rationale

The primary motivation for this work is to provide an improved understanding of carbon transfer from the carbon storage in sedimentary rocks (organic and inorganic) to the atmosphere. Sedimentary rocks represent the surface lithology of ~65 % of the total continental surface (Amiotte Suchet et al., 2003) and hence represent an important component in the long term carbon cycle. The carbon transfer is governed through reactions of chemical weathering and this thesis focuses on two processes: i) rock organic carbon oxidation and ii) carbonate dissolution by sulfuric acid. The main rationale is to provide better characterization of the rates and controls on the CO_2 release during chemical weathering, which is crucial for understanding the carbon balance between the near surface environments and the atmosphere.

This introduction starts with definitions and background desciptions of the key processes explored in the thesis. At the end of the chapter, thesis aims, main research questions, and thesis synopsis is provided.

1.2 Earths critical zone and critical zone observatories

Earths critical zone is recognized as the region at the Earth's surface expanding from the top of vegetation to the base of groundwater, where complex interactions between rocks, water, atmosphere and living organisms take place (Brantley et al., 2007; Hilton and West, 2020). Chemical weathering is one of the key processes occurring within the Earths critical zone and its reaction rates integrate physical, chemical, geological, biological and hydrological characteristics of the environment (Brantley et al., 2017). To provide a more complete understanding on chemical weathering reactions, an integrated

research involving different scientific disciplines is required across various scales (Brantley et al., 2007). For these purposes, critical zone observatories were established across different environments, with an overall aim to monitor, understand and predict mobility of water, dissolved and solid components in the past, present and future climatic regimes (Brantley et al., 2017; Gaillardet et al., 2018).

In this work, we explore two critical zone observatories: i) the Susquehanna Shale Hills Critical Zone Observatory located in central Pennsylvania and ii) Draix-Bléone Critical Zone Observatory located in South French Alps.

1.3 Geological carbon cycle

The habitability of Earth's climate is governed by the transfer of carbon between biogeochemical reservoirs, which control oxygen (O_2) and carbon dioxide (CO_2) concentrations in the atmosphere over geological timescales (Figure 1.1; Berner and Canfield, 1989; Derry and France-Lanord, 1996; Berner, 2003; Bolton et al., 2006). A traditional view of the geological carbon cycle is that the release of CO_2 to the atmosphere through volcanic degassing (79±9 Mt C yr^{-1}; Plank and Manning, 2019) is compensated by its removal through reactions between carbonic acid and silicate minerals (~90–140 Mt C yr^{-1}; Equation 1.1 and 1.2; Gaillardet et al., 1999; Moon et al., 2014). The latter result in the formation of carbonate minerals in the oceans (Berner & Canfield, 1989). Another major sink of atmospheric CO_2 is occurring through burial of biospheric (modern) organic carbon (Equation 1.3; France-Lanord and Derry, 1997). During the formation of modern organic matter, CO_2 is consumed from the atmosphere (photosynthesis).

Erosion transports modern organic carbon to rivers and oceans where it is buried in sediments (Berner, 1982; Meybeck, 1982).

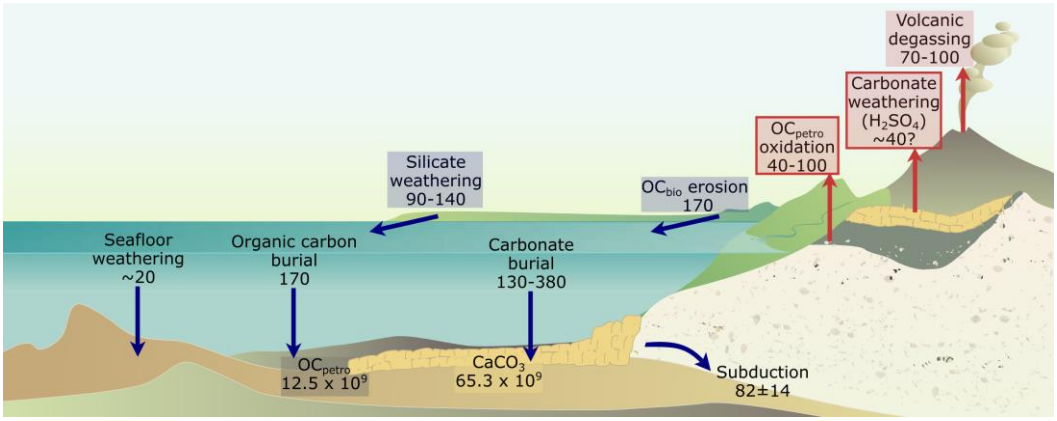

Figure 1.1 Processes involved in the geological carbon cycle. Modified after Gaillardet & Galy (2008). Carbon sequestration in the ocean (blue boxes) is governed by silicate weathering and burial of terrestrial (OC_{bio}) and marine organic carbon into marine sediments. Once these sediments are re-exposed on the Earth's surface, e.g. during mountain building, CO_2 may be released to the atmosphere through oxidation of rock organic carbon (OC_{petro}) and carbonate weathering by sulfuric acid (red boxes). Carbon stocks in sedimentary lithologies are presented in mega tons of carbon (MtC) (Sundquist et al., 2004). Carbon fluxes are in MtC yr-1 (Hilton&West, 2020).

When sedimentary rocks are exhumed and re-exposed at Earth's surface, for instance due to mountain building and tectonic uplift (Dewey and Horsfield, 1970; Willett, 1999), chemical weathering can act as a CO_2 source by two pathways. First, through the oxidation of sulfide minerals (Equation 1.4 and 1.5), and the subsequent dissolution of carbonate minerals by sulfuric acid (Equations 1.6 and 1.7; Calmels et al., 2007; Torres et al., 2014; Kemeny et al., 2021). Second, through the oxidation of rock organic carbon (OC_{petro}), or so-called "geo-respiration" (Equation 1.9; Bolton et al., 2006; Hilton et al., 2014; Petsch, 2014; Hilton and West, 2020). To date these fluxes have remained poorly constrained (Petsch, 2014; Torres et al., 2014; Burke et al., 2018) in comparison to silicate weathering (Hilton and West, 2020), despite first order global

estimates of combined CO_2 release (~40–140 Mt C yr^{-1}), of similar magnitude as the release of CO_2 from volcanic degassing (Figure 1.1).

Box 1: Carbon sources and sinks involved in the geological carbon cycle

CO_2 sink: Silicate weathering by carbonic acid

Dissolution of atmospheric CO_2 in rainwater (H_2O) leads to production of carbonic acid (H_2CO_3), which in reactions with silicate minerals results in production of bicarbonate (HCO_3^-).

$$2CO_2 + 3H_2O + CaAl_2Si_2O_8 \longrightarrow Ca^{2+} + 2HCO_3^- + Al_2Si_2O_5(OH)_4 \quad (1.1)$$

The produced ions can be used to form new carbonate minerals ($CaCO_3$) in the ocean, and result in a net sink of 1 mole of carbon.

$$Ca^{2+} + 2HCO_3^- \longrightarrow CaCO_3 + CO_2 + H_2O \quad (1.2)$$

CO_2 sink: Burial of biospheric organic carbon

Organic matter (CH_2O) is formed through photosynthesis, removing CO_2 from the atmosphere. The newly formed organic matter may be buried in the ocean (Berner and Raiswell, 1984).

$$CO_2 + H_2O \longrightarrow CH_2O + O_2 \quad (1.3)$$

CO_2 source: Carbonate dissolution by sulfuric acid

Oxidation of sulfide minerals occurs via gaseous or dissolved di-oxygen (O_2) or by reduction of the ferric iron (Fe^{3+}). These reactions lead to production of sulfuric acid (H_2SO_4), a strong weathering agent.

$$4FeS_2 + 15O_2 + 14H_2O \longrightarrow 4Fe(OH)_3 + 8H_2SO_4 \quad (1.4)$$

$$FeS_2 + 14Fe^{3+} + 8H_2O \longrightarrow 15Fe^{2+} + 2SO_4^{2-} + 16H^+ \quad (1.5)$$

When H_2SO_4 is in contact with carbonate minerals, CO_2 may be directly released to the atmosphere.

$$CaCO_3 + H_2SO_4 \longrightarrow CO_2 + H_2O + Ca^{2+} + SO_4^{2-} \quad (1.6)$$

Alternatively, the CO_2 release may be delayed by the time of carbonate precipitation in the ocean (10^6 yr) (e.g. Torres et al., 2014).

$$2CaCO_3 + H_2SO_4 \longrightarrow 2Ca^{2+} + SO_4^{2-} + 2HCO_3^- \quad (1.7)$$

$$Ca^{2+} + 2HCO_3^- \longrightarrow CaCO_3 + CO_{2(g)} + H_2O \quad (1.8)$$

CO_2 source: Rock organic carbon oxidation

Organic carbon stored in rocks (OC_{petro}) is oxidized by atmospheric oxygen or oxygen-bearing water (Petsch et al., 2000).

$$CH_2O + O_2 \longrightarrow CO_2 + H_2O \quad (1.9)$$

1.4 Rock organic carbon oxidation

The vast reservoir of rock-derived (or "petrogenic") organic carbon (OC_{petro}) in sedimentary rocks was produced by the burial of the organic matter from the terrestrial and marine biosphere into marine sediments (Equation 1.3; Berner and Raiswell, 1984; Petsch, 2014). Sedimentary rocks may contain up to 5–10% OC_{petro} by weight, for instance in black shales (Jaffe et al., 2002). However, it is more common that OC_{petro} concentrations in sedimentary rocks are ~1 % or less (Wildman, 2004). When sedimentary rocks are re-exposed to surface processes, such as weathering and erosion, OC_{petro} can be oxidized and the C transferred to the atmosphere in gaseous form as CO_2 (Equation 1.9; Bolton et al., 2006).

Previous work has attempted to track OC_{petro} oxidation in weathered rocks that develop over long periods of time, in a weathering profile, with OC_{petro} loss in the surface (weathered) sediments compared to deeper (un-weathered) parts of the profile (Jaffe et al., 2002; Petsch et al., 2000). These study cases have limited constraint on the exact rate of CO_2 release because they lack long-term denudation rates estimates. The main challenges are therefore to determine both the proportion of rock that has been oxidized and the time frame over which the reaction occurred. Additionally, the extent of oxidation from a single weathering profile gives only a local constraint and may not be representative over larger spatial scales.

Recently, a method to make direct measurements of CO_2 release from oxidative weathering of sedimentary rocks was presented by Soulet et al. (2018). In this study, CO_2 flux was measured in chambers drilled into a marl outcrop, with OC_{petro} concentrations ~0.5 % at the Draix-Bléone Critical Zone Observatory (CZO) in South France. The CO_2 fluxes were high, between ~20 and

~3000 mgC m^{-2} day^{-1}, which is within the range of fluxes reported for soil respiration (Soulet et al., 2021). An advantage of this approach is that it directly tracks the CO_2 flux produced within the outcrop. A disadvantage is that partitioning the source of CO_2 between atmospheric, biospheric, and lithological (inorganic and organic) carbon sources can be challenging even by using the stable carbon isotope and radiocarbon signature. Additionally, the measurements are inherently local in scale, and upscaling oxidation rates is not straightforward.

An alternative approach to quantify chemical weathering rates is to measure the products of weathering and erosion carried by rivers, which have the benefit of better integrating processes over large areas (e.g. Gaillardet et al., 1999). However, tracking OC_{petro} oxidation using river loads is not without challenges. Rivers are biogeochemically active and transport large amounts of young, more recently fixed organic carbon, which is commonly lost by active degassing. Quantification of OC_{petro} oxidation is therefore challenging because of the high background of degassing of modern OC (Marx et al., 2017; Richey et al., 2002; Worrall et al., 2013). When tracking the products of erosion in river sediments, there are only a few studies, which attempt to track the loss of OC_{petro} (i.e. OC_{petro} oxidation and CO_2 release) at a catchment scale. For example, Galy et al. (2008) and Bouchez et al. (2010) combined Raman spectroscopy and radiocarbon measurements to determine the proportion of OC_{petro} loss in the Ganges and Amazon river sediments, respectively. However, tracking OC_{petro} oxidation via loss in sediments is challenging when the intensity of weathering is low, which is the case in many locations where erosion and weathering fluxes can be high (Hilton et al., 2011). Most commonly catchment-scale studies on chemical

weathering rates focus on large catchments, however, net carbon fluxes may be variable across the river network as it has been shown on a case study from the Amazon in Clark et al. (2017). Therefore, to provide a detail investigation of the chemical weathering processes and controls navigating the rates, this research turns to small (<1 km^2) headwater catchments, which allow isolation of single mechanisms and factors involved in chemical weathering reactions.

There has been growing recognition that the trace element rhenium (Re) provides a useful proxy to track and quantify OC_{petro} oxidation at both weathering profile (Jaffe et al., 2002) and river catchment scales (Dalai et al., 2002; Hilton et al., 2014). The Re proxy is discussed in more detail herein, but in summary, the proxy relies on the strong association between Re and OC_{petro} in shales and on the mobilization of oxidized Re to the dissolved load in river catchments. The Re proxy is one approach that this thesis will explore to track OC_{petro} oxidation rates from chemical weathering of sedimentary rocks.

1.5 The rhenium proxy

1.5.1 Background

Rhenium (Re) is a trace element in the Earth's crust (average 0.4 ppb; McLennan, 2001; Dubin and Peucker-Ehrenbrink, 2015) but is significantly enriched in reduced sediments, especially in organic carbon-rich black shales (~150 ppb; Colodner et al., 1993; Selby and Creaser, 2003). While oxidative weathering releases CO_2 to the atmosphere (Petsch et al., 2000), oxidized Re is released to streams and rivers in a form of perrhenate ion (ReO_4^-; Figure 1.2A), which is soluble over pH and Eh conditions of most river waters (Brookins, 1986; Colodner et al., 1993). This high mobility upon oxidation makes it a potential

powerful weathering proxy (Colodner et al., 1993), while the coupled loss of Re and OC_{petro} from rocks during oxidative weathering provides further momentum for its application (Figure 1.2B and C; Jaffe et al., 2002; Hilton et al., 2014).

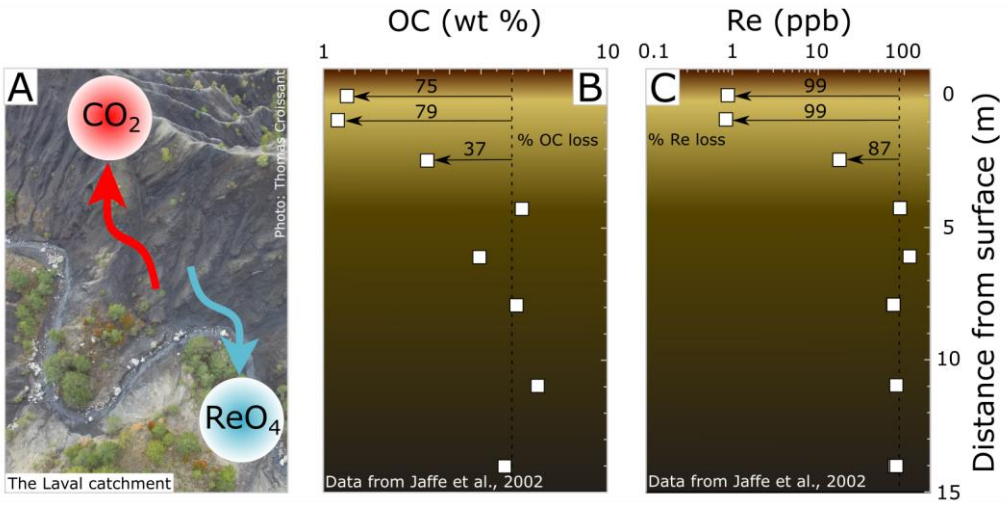

Figure 1.2: Example of the rhenium (Re) proxy for tracking OC_{petro} oxidation. A: Schematic illustration of OC_{petro} oxidation resulting in CO_2 release to the atmosphere, while Re is released to the dissolved load, where it can be measured. Its fluxes may be estimated over catchment scales. **B** and **C:** Coupled loss of organic carbon (OC) and rhenium (Re) from surface layers (>~3m) of the 15 m deep black shale weathering profile sampled in Clay City Kentucky, USA (Jaffe et al., 2002).

The close association of Re with OC_{petro} is an underlying assumption for the application of the Re proxy. Until now, this has been studied in OC- and Re-rich shales (Peucker-Ehrenbrink and Hannigan, 2000; Jaffe et al., 2002; Hilton et al., 2014). These studies identified first-order common Re and OC loss, however, Re was generally more depleted in the surface sediments compared to OC_{petro} (Figure 1.2B and C). A potential explanation for these differences could be that Re is also present in other mineral phases, e.g. sulfide minerals, with faster oxidation kinetics compared to OC_{petro} (Chang and Berner, 1999; Petsch et al., 2000). An alternative explanation would suggest contribution of modern OC in the studied profiles (Jaffe et al., 2002). It is important to also characterize the Re association

with OC in OC-poor environments (<1 %), which are common among sedimentary rocks (Amiotte Suchet et al., 2003). The Re proxy may help the determination of OC_{petro} oxidation rates in this setting, because Re can be measured precisely in sediments with low Re abundances (as low as 10^{-12} g g^{-1}, i.e. ppt; Dellinger et al., 2020), while there are analytical limitations to accurate measurements of low OC concentrations in sedimentary rocks. Here the focus is to study Re and OC_{petro} loss in low OC (<0.05 %) shale weathering profiles at the Susquehanna Shale Hills Critical Zone Observatory (CZO) in central Pennsylvania (Chapter 3).

1.5.2 Rhenium source

1.5.2.1 Mineralogical source

In erosive settings, where mineral supply to the weathering zone is high, weathering of reduced sediments is thought to be the main source of Re to the dissolved river load (Dalai et al., 2002; Horan et al., 2019). A number of studies suggested that Re may be sourced from at least three mineralogical phases: OC_{petro}, sulfide and silicate minerals (Dalai et al., 2002; Horan et al., 2019; Miller et al., 2011). Recently, Horan et al. (2019) quantified the proportion of Re form these sources in sediments and river water using the Re/Na versus Re/SO_4 elemental ratios (Figure 1.3). This was proposed because silicate and sulfide minerals are thought to have low Re abundance (Dalai et al., 2002; Miller et al., 2011), while Re is commonly enriched in the OC_{petro}-rich sedimentary rocks (Colodner et al., 1993; Dai et al., 2015). Nonetheless, until now, the sulfide end-member has remained less well-constrained (Figure 1.3), which is addressed in Chapter 4 of this thesis.

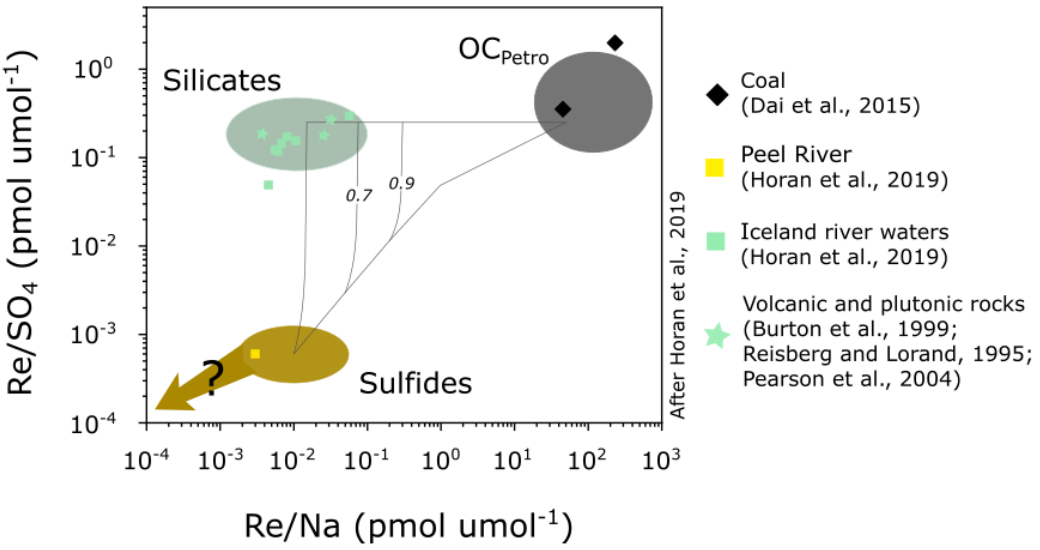

Figure 1.3: Mixing space to determine mineralogical Re source. Samples are plotted in the mixing space to determine the percentage of Re derived from OC_{petro} and other sources. The two vertical lines in the middle of the model display 70% and 90% of Re sourced from OC_{petro}. The sulfate end-member is still not well-constrained.

1.5.2.2 Anthropogenic source

In addition to the mineralogical sources, a large proportion of Re may be derived from anthropogenic inputs (Miller et al., 2011). This is especially important in low erosive environments with low inputs from chemical weathering that are in close proximity to pollution sources. For example, anthropogenic Re inputs have been invoked to explain high dissolved Re concentrations (40–109 pmol l^{-1}) in rivers draining into the Black Sea, despite no indication of black shale lithologies (Colodner et al., 1995). The excess Re was attributed to burning low-grade coal in the vicinity of the river basins. Miller et al. (2011) presented a global compilation of Re concentrations in river water and suggested a number of rivers with elevated Re concentrations, such as Danube (Europe; 74 pmol l^{-1}), Mississippi (N America; 57 pmol l^{-1}), Rhine (Europe, 57 pmol l^{-1}), and Yangtze (Asia, 55 pmol l^{-1}). Based on Re concentrations measured in rain water, they

proposed a global assessment of ~30% of dissolved Re in modern-day large world rivers being anthropogenic origin (Miller et al., 2011). Anthropogenic Re-enrichments have also been recognized in sediment cores from lacustrine basins in uninhabited Eastern Canada (Chappaz et al., 2008) and in black coral records from the Gulf of Mexico, dating the industrial time ~1850s (Prouty et al., 2014).

The transfer of anthropogenic Re between different surface reservoirs (e.g. soil, rivers) and the legacy of the atmospheric deposition of Re at a catchment scale are not known. Since Re is not thought to be cycled through standing biomass and vegetation, and due to its high mobility potential into the hydrological network (Brookins, 1986; Colodner et al., 1993; Miller et al., 2011), the proxy may be used to study the legacy of anthropogenic inputs on a catchment scale, as attempted in Chapter 3.

1.5.3 Calculation of modern-day OC_{petro} oxidation rates

Once Re is measured in the dissolved load and its sources are determined, the dissolved Re flux can be calculated. This provides the basis to quantify the modern-day OC_{petro} oxidation rates (J_{CO2}) as presented in Equation 1.10 (Hilton et al., 2014; Horan et al., 2017, 2019).

$$J_{CO2} = J_{Re-OC_{petro}} \times \left(\frac{OC}{Re}\right)_{petro} \times (1 - f_{graphite}) \qquad (1.10)$$

Here $J_{Re\text{-}OCpetro}$ is the flux of Re derived from OC_{petro} (mol km^{-2} yr^{-1}), $(OC/Re)_{petro}$ is the ratio measured in the catchment rocks, and $f_{graphite}$ is the proportion OC_{petro} which may not be susceptible to oxidation (Galy et al., 2008).

A growing number of studies that have applied the dissolved Re proxy, suggest notable variability in OC_{petro} oxidation rates between 0.63 and 30 tC km^{-2} yr^{-1}. These rates are based on studies set in mountainous catchments, such as Yamuna and Ganga river basins in the Himalaya (Dalai et al., 2002), catchments in Taiwan (Hilton et al., 2014), New Zealand's Southern Alps (Horan et al., 2017), and in the Mackenzie River system (Horan et al., 2019). However, a common limitation of all these previous studies is that the estimates of Re yields are based on a limited number of samples. Studies on major dissolved elements in river waters (e.g. Tipper et al., 2006; Calmels et al., 2011; Li et al., 2015; Winnick et al., 2017) showed that frequent sampling technique may reveal seasonality and flood-event scale variability, which are essential characteristics for precise estimations of the annual elemental fluxes. In addition, small, densely monitored catchments may allow isolation of factors that control the variability in stream water chemistry, e.g. climate, lithology and hydrology (Jiang et al., 2018; West et al., 2002; Yu et al., 2019). A major novelty of this thesis is to use high frequency time-series measurements across various flow regimes and multiple seasons in two small, headwater catchments located in South French Alps, part of the Draix-Bléone CZO, for detail investigation of OC_{petro} rates and controls (Chapter 4).

1.6 Sulfide oxidation and carbonate weathering by sulfuric acid

Sulfide oxidation coupled to carbonate dissolution has been recognized as an important source of CO_2 to the atmosphere over geological time scales (Calmels et al., 2007; Torres et al., 2014). A pyrite-rich shale lithology may lead to the production of sulfuric acid (H_2SO_4) via reactions involving atmospheric O_2 (Box 1,

Equation 1.4) or iron redox cycling (Box 1, Equation 1.5). The resultant acidity can be buffered by dissolution of carbonate, which can directly release CO_2 to the atmosphere (Box 1, Equation 1.6). Alternatively, carbon from carbonate dissolution may enter the bicarbonate pool in river water, then the CO_2 release to the atmosphere is delayed by the timescale of the carbonate precipitation in the ocean (~10^6 yr; Box 1, Equation 1.7; Berner & Berner, 2012; Torres et al., 2014). Weathering of carbonates by sulfuric acid may alter carbonic acid equilibrium, which can have a direct impact on the CO_2 consumption through the silicate weathering (Bufe et al., 2021).

Sulfide oxidation fluxes can be estimated from dissolved SO_4 concentrations across river catchments, providing that the source of SO_4 is known (Calmels et al., 2007; Turchyn et al., 2013). Dominant sources of SO_4 at the catchment scale are atmospheric deposition, oxidation of sulfide minerals, and evaporite dissolution (Karim and Veizer, 2000; Spence and Telmer, 2005; Turchyn et al., 2013). These have been isolated using several approaches, for example: i) the isotopic composition of dissolved inorganic carbon, alongside sulfate concentrations (Galy and France-Lanord, 1999; Li et al., 2008; Spence and Telmer, 2005); ii) the S isotope ratio of dissolved sulfate to other major ions (Torres et al., 2016); and/or iii) the coupled S and O isotope composition ($\delta^{34}S_{SO4}$, $\delta^{18}O_{SO4}$) of dissolved sulfate (Calmels et al., 2007; Karim and Veizer, 2000; Turchyn et al., 2013; Tuttle et al., 2009). The latter method is particularly useful, since the $\delta^{34}S_{SO4}$ in river water can reflect the $\delta^{34}S$ signal of the weathered lithology, while the $\delta^{18}O_{SO4}$ carries information on the oxidizing environment in case of sulfide weathering (Calmels et al., 2007; Turchyn et al., 2013). A complimentary approach to study the role of carbonate weathering by sulfuric

acid is to apportion dissolved cations between the carbonate and silicate weathering source (Gaillardet et al., 1999; Jacobson and Blum, 2003; Winnick et al., 2017), and to determine the prevailing weathering agent, that is carbonic versus sulfuric acid (Blattmann et al., 2019; Li et al., 2008; Spence and Telmer, 2005; Torres et al., 2016; Winnick et al., 2017).

Despite these advances, to date, only a handful of studies have determined the rates of CO_2 release from carbonate weathering on a catchment scale (Calmels et al., 2007; Das et al., 2012; Torres et al., 2014). These studies were mostly focused on large catchments, where isolation of single mechanisms and factors involved in the production of sulfuric acid and carbonate dissolution is challenging (Tipper et al., 2006; Turchyn et al., 2013). This work seeks to determine carbon sequestration and emission rates by studying high temporal resolution stream water chemistry in two headwater catchments, of Draix-Bléone CZO in South French Alps (Chapter 5).

1.7 Controls on oxidative weathering reactions

Controls on chemical weathering can be related to mineral supply, such as lithology, uplift and erosion (Bluth and Kump, 1994; Gaillardet et al., 1999; Millot et al., 2003; Stallard and Edmond, 1983) and climate mechanisms, including temperature (Kump et al., 2000; White and Blum, 1995) and hydrology (Calmels et al., 2011; Gaillardet et al., 1999; Maher, 2011; Maher and Chamberlain, 2014; Tipper et al., 2006; White and Brantley, 2003). The importance of these controls depends on the weathering regime, i.e. whether chemical weathering reactions are limited by the supply of fresh mineral surfaces available for oxidation (supply-limited regime) or by the kinetics of the weathering reactions (kinetic-

limited regime) (Gabet and Mudd, 2009; Hilton and West, 2020; Riebe et al., 2004; West et al., 2005; West, 2012). These weathering regimes have been well-characterized for silicate watering; in a supply-limited regime, silicate weathering fluxes are poorly sensitive to changes in temperature (Riebe et al., 2004; West et al., 2005) and runoff (Maher and Chamberlain, 2014). In contrast, in kinetically-limited regimes (at high erosion rates), silicate weathering fluxes are strongly modulated by temperature and runoff, i.e. there is a strong negative feedback between climate and silicate weathering rates (Hilley et al., 2010; Maher and Chamberlain, 2014; West et al., 2005).

The erosion control on OC_{petro} and sulfide oxidation remains far less studied (Bufe et al., 2021; Calmels et al., 2011; Hilton and West, 2020) compared to the silicate weathering. This thesis studies chemical weathering rates in sedimentary catchments across different erosional regimes, with particular focus on the role of seasonality in air temperatures and precipitation periods (autumn and spring) on weathering reactions. The choice of studied catchments and sampling strategy (the high temporal resolution sampling) adopted here allow us to explore climatic controls in the kinetically- and supply-limited regimes in terms of OC_{petro} and sulfide mineral oxidation.

1.7.1 Erosion control

1.7.1.1 Rock organic carbon oxidation

Oxidation of OC_{petro} occurs at faster rate than chemical weathering of silicate minerals (Chang and Berner, 1999; White, 2003), suggesting that oxidative weathering can keep pace with continuous supply of fresh mineral surfaces in high physical erosion setting (Bolton et al., 2006; Hilton and West, 2020). The

positive link between OC_{petro} oxidation and erosion was recently observed in compiled global datasets on OC_{petro} weathering rates (Figure 1.4A; Hilton and West, 2020).

However, environments with low erosion rates, where the supply of elements to the oxidative weathering surface is limited (i.e. supply-limited regime) have been so far only sparsely investigated. In a low-erosion setting, thick weathering profiles on black shales have been studied in some detail (Petsch et al., 2000; Jaffe et al., 2002; Wildman, 2004), but the corresponding rates of CO_2 release are not well known (Petsch, 2014). Areas with lower erosion rates (<0.5 mm yr^{-1}) comprise a large land mass on the continental surface and may contribute to ~60 % of global chemical denudation (Larsen et al., 2014). Here, this research gap is addressed by studying OC_{petro} oxidation rates in low erosive environment of the Susquehanna Shale Hills CZO (Chapter 3).

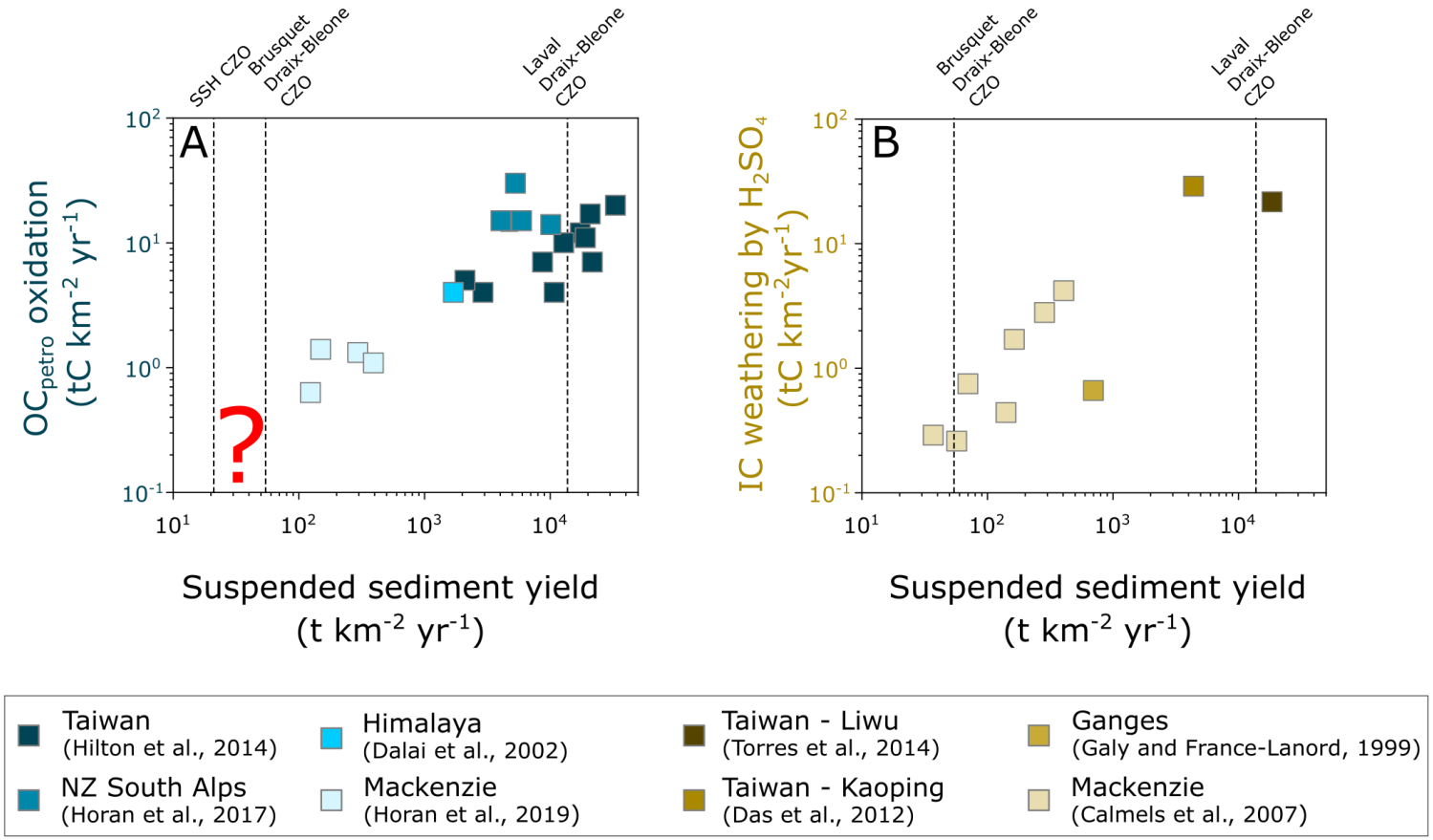

Figure 1.4: Erosion control on modern-day CO_2 release estimates. A: Catchment-scale estimates of rock organic carbon oxidation (OC_{petro}). **B:** Catchment-scale estimates of inorganic carbon weathering by sulfuric acid. SSH CZO stands for the Susquehanna Shale Hills Critical Zone Observatory investigated in Chapter 3. The Laval and Brusquet catchments from the Draix-Bléone CZO are investigated in Chapter 4 and Chapter 5.

1.7.1.2 Sulfide oxidation

Similar to OC_{petro}, sulfide oxidation is characterized by rapid reaction kinetics (Williamson and Rimstidt, 1994), which would suggest an increase in oxidation rates with higher material supply. Indeed, sulfide oxidation shows a broadly positive correlation with an increase in erosion rates across different catchments (Calmels et al., 2011; Hilton and West, 2020), suggesting that oxidation of sulfide minerals is supply-limited even at very high erosion rates (Bufe et al., 2021; Hilton and West, 2020). This is supported by estimates of high sulfide oxidation rates in recently mobilized landslides in South French Alps (Nevers et al., 2020), in anthropogenically modified catchments in the Appalachian Mountains (Ross et al., 2018), and highly erosive catchments in Taiwan (Blattmann et al., 2019; Bufe et al., 2021; Das et al., 2012; Torres et al., 2014).

Here, we provide new estimates on the inorganic carbon weathering by sulfuric acid in a paired catchment study of the Draix-Bléone CZO across large differences in erosion rates (Chapter 5).

1.7.2 Climate controls

1.7.2.1 Rock organic carbon oxidation

In catchments with high to moderate erosion rates, i.e. Taiwan (Hilton et al., 2014) and New Zealand's Southern Alps (Horan et al., 2017), the correlation between erosion and OC_{petro} oxidation is scattered (Figure 1.4A). This scatter may result from the variable OC_{petro} concentrations in catchment rocks. Alternatively, in kinetically-limited regimes, OC_{petro} oxidation may be locally limited by air temperature, oxygen supply or microbial activity (Bolton et al., 2006; Hemingway et al., 2018; Hilton and West, 2020). A recent study by Soulet et al. (2021) found

temperature-driven seasonal changes of CO_2 fluxes derived from chemical weathering of a marl outcrop in the Draix-Bléone CZO. To investigate potential climatic controls (temperature, hydrology) on OC_{petro} weathering rates this study investigates seasonality in chemical weathering products in the dissolved load in two catchments within the Draix-Bléone CZO in Chapter 4. This provides an opportunity to compare two independent methods for determining rates of oxidative weathering (direct CO_2 measurements and dissolved stream load) and potential temperature impact on OC_{petro} mineral oxidation in the same catchment.

1.7.2.2 Sulfide oxidation

Similar to OC_{petro} oxidation, sulfide oxidation is thought to be controlled by temperature through reaction kinetics and microbial activity (Calmels et al., 2007; Hemingway et al., 2018; Percak-Dennett et al., 2017; Petsch et al., 2000). Recent studies used time-series datasets covering several decades of stream water chemistry to search for potential changes in sulfide oxidation with recent climate change. For example, Zhi et al. (2020) observed seasonality in dissolved solutes that are active in soils (DOC, Al, Fe, Pb) in a high elevated catchment in Colorado, while no seasonality was observed in solutes associated to rock weathering (Ca, Mg, Na). In contrast, Crawford et al. (2019) showed increasing trend in dissolved SO_4 flux over the last 30 years in several Alpine catchments around the globe. They revealed a positive correlation between the SO_4 flux and daily temperatures and suggested that production of sulfuric acid and carbonate dissolution may have positive feedback, releasing more CO_2 as the climate warms.

In Chapter 5 we study the temperature dependency on production of sulfuric acid by tracking seasonality in dissolved components in the Draix-Bléone

CZO and we investigate trends alongside direct CO_2 measurements made in the same catchment by (Soulet et al., 2021).

1.8 Thesis aims and research questions

The overall aim of this thesis is to provide new insights on chemical weathering processes resulting in the CO_2 release to the atmosphere. A focus is on investigating mobility of chemical elements in the Earth's critical zone and applying novel proxies to provide estimates of chemical weathering rates. By studying interactions between hydrology, climate, weathering and erosion, this research will shed new light on the controls of CO_2 release from sedimentary rock weathering.

To address these aims the following research questions (RQ) have been outlined:

1. Oxidation of rock-derived organic carbon:
    a. Determine the mobility of OC_{petro} and Re during oxidative weathering.
    b. Quantify the proportion of Re in the bedrock and dissolved load of rivers that it is derived from OC_{petro} versus that from other sources.
    c. Quantify dissolved Re flux and characterize its temporal variability in river catchments.
    d. Estimate the modern-day and/or long-term CO_2 emissions from OC_{petro} oxidation.
    e. Unravel the main controls (e.g. erosion, climate, oxygen supply etc.) on OC_{petro} oxidation in shale-dominated catchments.

2. Carbonate weathering by sulfuric acid:
    a. Investigate the source and oxidation environment of dissolved sulfate in the dissolved load.
    b. Quantify the prevailing weathering lithology (carbonate vs. silicate), determine dissolved fluxes and characterize their temporal variability in river catchments.
    c. Estimate the present-day inorganic carbon budget on small catchment scales.
    d. Unravel the main controls (e.g. erosion, climate, oxygen supply, reaction kinetic) on sulfur oxidation and carbonate weathering in shale-dominated catchments.

1.9 Thesis synopsis

This thesis starts with a brief overview of the geochemical methods and data analysis approaches (**Chapter 2**) used to tackle the thesis aims. The subsequent Chapters 3-5 are presented as research papers that are intended for publication in peer-review journals. The thesis is finalized with a summary section and future directions.

Chapter 3 explores mobilization of Re alongside OC_{petro} weathering in OC-poor (<0.05 %) deep weathering profiles (RQ 1a), sampled in the Susquehanna Shale Hills CZO in central Pennsylvania. This chapter also provides estimates on the long-term OC_{petro} oxidation rates in low erosive setting using the Re proxy and OC_{petro} measurements, which are obtained from radiocarbon analysis (RQ 1d). In addition, this study provides new insight on anthropogenic

sources of Re to the catchment soils and its link to the legacy of industrial activities in the region (RQ 1b).

Chapter 4 studies the production and mobility of Re in a paired catchment approach of two small (<1 km^2) mountainous catchments in South French Alps (Draix-Bléone CZO) which contrast markedly in their physical erosion rates. Here, the stream water dataset sampled across various flow regimes and seasons is used to study different mineral sources of Re to the dissolved load (RQ 1b), with emphasis on constraining the sulfide end-member. Additionally, the high temporal resolution stream dataset allows us to study seasonality in Re production and mobility (RQ 1c), and to discuss the implications for the environmental control on OC_{petro} oxidation (RQ 1e).

Chapter 5 determines the fluxes of silicate and carbonate weathering in paired catchments across large differences in erosion rates in the Draix-Bléone CZO (RQ 2c). An emphasis is on quantifying the role of carbonate dissolution by sulfuric acid (RQ 2a). Elemental ratios of major solutes in stream water are used to determine the silicate and carbonate weathering rates and determine the dominant weathering agent (carbonic acid versus sulfuric acid; RQ 2b). Stable sulfur isotope is measured on dissolved sulfate, suggesting pyrite oxidation as the dominant source of SO_4 (RQ 2a). Stable oxygen isotope on SO_4 gives insights on sulfur oxidation environment. As in Chapter 4, controls on the CO_2 release are investigated (RQ 2d).

Chapter 6 presents a summary of the key results and discusses the potential directions for future work that could arise from this research.

CHAPTER 2
Methods and methodology

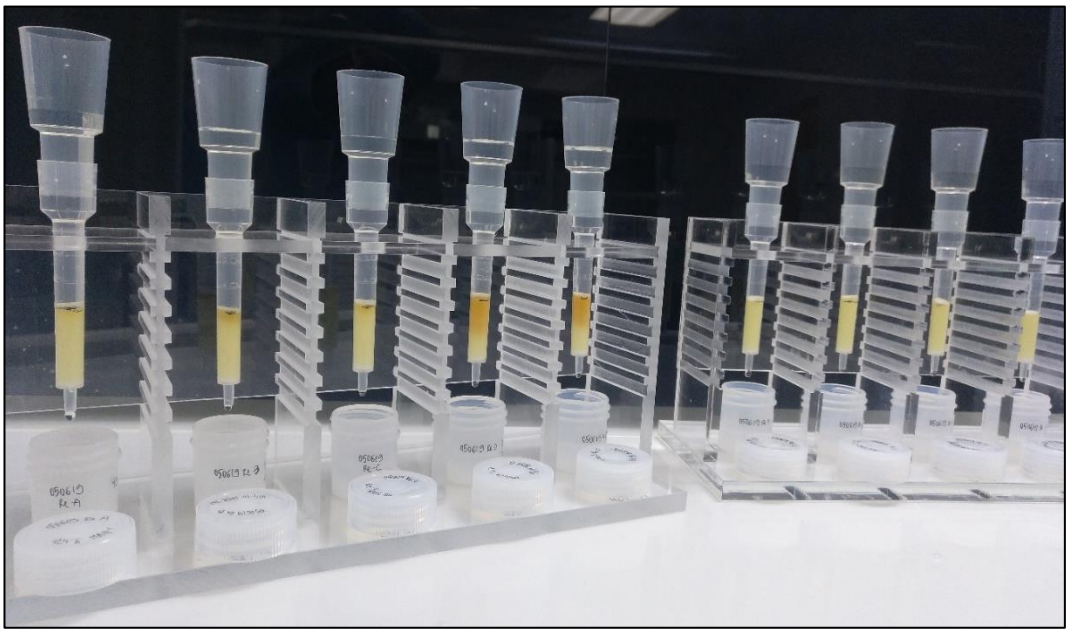

Column chemistry setup for collecting Re solutions after a complete digestion procedure of solid samples; Clean lab facilities at Durham University, Department of Earth Sciences, June 2019

Geochemical analysis of water and solid samples are essential to understand the transfer of elements through the Earth's critical zone by weathering and erosion. In this work, two densely monitored critical zone observation sites have been selected: i) Susquehanna Shale Hills Critical Zone Observatory in central Pennsylvania and ii) Draix-Bléone Critical Zone Observatory in South French Alps. To address the research framework, we put emphasis on using a range of geochemical proxies such as trace element rhenium (Re), total organic carbon (TOC), stable carbon isotope ($\delta^{13}C$), and the major elemental concentrations of solid and water samples. Selected samples were analyzed for radiocarbon ($\Delta^{14}C$), sulfur concentration and stable sulfur and oxygen isotopes. In the following, a short summary and justification for the study site selection is provided and their main characteristics are compared. Then, the analytical methods used in this thesis are described and the precision, accuracy and uncertainties of the measurements are discussed. This is followed by descriptions of computational analysis for estimations of the chemical weathering fluxes. Finally, a flow diagram is presented in Figure 2.8. to illustrate the link between the generated data, the research questions and the scientific chapters 3, 4, and 5.

2.1 The study sites

With an aim to investigate chemical weathering rates across different sedimentary environments, we here investigate three small headwater catchments: i) the Shale Hills catchment at the Susquehanna Shale Hills CZO in central Pennsylvania, and two neary catchments: ii) the Laval catchment and iii) the Brusquet, located at the Draix-Bléone CZO in South French Alps.

Work within critical zone observatories allows us to investigate complementary datasets of air temperature and precipitation measurments, discharge rates, suspended sediment and bed load yields. Investigating small catchment areas (all <1 km^2) provides constrains on the local controls on the chemical weathering processes and rates, such as small-scale lithological variability, vegetation cover, and hydrology while other parameters, for example, the climate is consistent. All three catchments are set in temperate climate and draining sedimentary, shale lithology, making the results conducted from this study representable for the large proportion of the Earth's surface (Amiotte Suchet et al., 2003; Copard et al., 2007). However, the study catchments differ in the OC_{petro} concentrations of the sedimentary rock, which are the lowest at the Shale Hills site (<0.05 % TOC; Jin et al., 2014) and higher at the Laval (~0.5 %TOC; Graz et al., 2012) and at the Brusquet (~1 % TOC; Graz et al., 2012). The catchments lithology further differs in the percentage of the carbonate and sulfur fractions (Table 2.1), allowing us to explore how these lithological differences navigate the catchments' scale carbon budgets. Another large differences between the catchments arises from the export of the suspended sediment yield and denudation rate, which is the lowest at the Shale Hills and the Brusquet, but strikingly high at the Laval (Table 2.1). Differences in suspended

sediment yield export is partly reflected in the extent of the vegetation cover, which is the lowest at the Laval (32%), but more similar at the Brusquet and the Shale Hills sites (~90%).

Beside the geological characteristics of the Shale Hills site, the main advantage of studying this catchment is the opportunity to investigate deep weathering profiles (up to ~30 m), which provide new insights on the source and mobility of Re and OC_{petro} during shale weathering. So far, this has not been constrained in the OC-poor shale. In addition, an extensive archive of surface soil samples give us opportunity to shed new light on the potential anthropogenic perturbation of the surface Re cycle, as it has been previously researched for other metals at this site (Herndon et al., 2015b, 2011, Herndon and Brantley, 2011, Kraepiel et al., 2015, Ma et al., 2014).

Catchments within the Draix-Bléone observatory are being monitored since the early 1980s for the continuous measurement of water discharge, suspended sediment and bed load concentrations and fluxes (Mathys et al., 2003). This provides detailed datasets for accurate quantification of dissolved and particulate geochemical fluxes and gives contextual information on decadal erosion rates. Additionally, previous research on long-term erosion rates (Mathys et al., 2003), quantification of the solid export of un-weathered OC_{petro} (Graz et al., 2012) and catchment hydrology (Cras et al., 2007; Marc et al., 2017) can help to broader our understanding on the controls on chemical weathering rates. Finally, the sites are part of a broader weathering experiment, which include direct in-situ measurements of CO_2 production during weathering (through ROC-CO2 project collaborators Dr. Guillaume Soulet and Tobias Roylands).

Table 2.1. Main characteristics of the investigated catchments. Physical characteristic of the study sites (area, vegetation cover, slope, denudation rate) for the Draix-Bléone study sites are from Mathys et al., 2003 and for the Shale Hills site from West et al., 2013. *A range of slopes instead of the average catchment slope is given for the Shale Hills catchment. Denudation rate (mm yr^{-1}) for Draix-Bléone study sites is calculated based on the long term suspended sediment yield export (Carriere et al., 2020) and for rock density of ~2 t m^{-3}. Chemical characteristics of the bedrock, i.e. Total organic carbon (TOC), sulfur (S) and inorganic carbon (IC) concentrations for the Draix-Bléone study sites are from Graz et al., 2012 and Soulet et al, 2021. Chemical characteristics of the bedrock for the Shale Hills are from Jin et al., 2014; and Gu et al., 2020.

Study site	Catchment	Area	Vegetation cover	Average catchment slope	Denudation rate	Dominant lithology	TOC	S	IC
		km^2	%	°	mm yr^{-1}	-	%	%	%
Draix-Bléone CZO	Laval	0.86	32	58	~ 7	Black Marls (Late Jura)	~0.5	~0.6	~45
	Brusquet	1.07	87	53	~0.04	Black/grey shales and carbonates (Early Jura)	~1	~0.4	~45
Susquehanna Shale Hills CZO	Shale Hills	0.08	-	8-30*	0.01 – 0.025	Grey shales (Silurian)	<0.05	~0.1	~0.02

2.2 Analytical methods

2.2.1 Total organic carbon and its isotopic composition

Total organic carbon (TOC) and stable carbon isotope ($\delta^{13}C$) of solid samples were determined to track TOC loss during chemical weathering or addition through biological input. Analysis of TOC require the removal of detrital carbonates from sample powders. This was done by weighing out ~40 mg of a dry sample into a pre-combusted silver capsule (450 °C for four hours) and by adding 1N HCl, followed by drying the sample in an oven at 60 °C. To ensure the complete removal of carbonates, each sample was rinsed with 1N HCl three times. The TOC and $\delta^{13}C$ measurements were carried out with a mass spectrometer connected to an elemental analyzer at Elemtex, Stable Isotope Analytical Laboratory, Cornwall, UK. Corrections for procedural and instruments blanks were applied and the $\delta^{13}C$ was normalized to the composition of international standards, reported relative to the Vienna Pee Dee Belemnite (VPDB) with a precision of 0.2 ‰.

The method was validated by measuring the soil standard material NCS-DC73319 and two international certified synthetic standards, IAEA 600 (caffeine) and IAEA CH3 (cellulose), for $\delta^{13}C$ values. The standard materials were processed in the same way as the samples. The accuracy on TOC concentrations was better than 1% (n=6), and the accuracy of $\delta^{13}C$ values was 0.01–0.04 ‰ (n=6) compared to the standard materials. Sample replicates run at the beginning and the end of an analytical sequence show high precision of the analysis, even at low TOC concentrations measured in this study. The TOC concentrations show a positive correlation between the sample replicates with $r^2 \sim 1$ and slope of 1.03 (Figure 2.1A). The high precision was further validated by analyzing a subset of samples

at two different laboratories, Elemtex, Stable Isotope Analytical Laboratory (Cornwall, UK) and National Ocean Sciences Acceleration Mass Spectrometry Facility (NOSMAS) at Woods Hole Oceanographic Institution (WHOI). The TOC concentration measurements obtained at these two laboratories are in close agreement, with a correlation coefficient r^2 of 0.99 (Figure 2.1B).

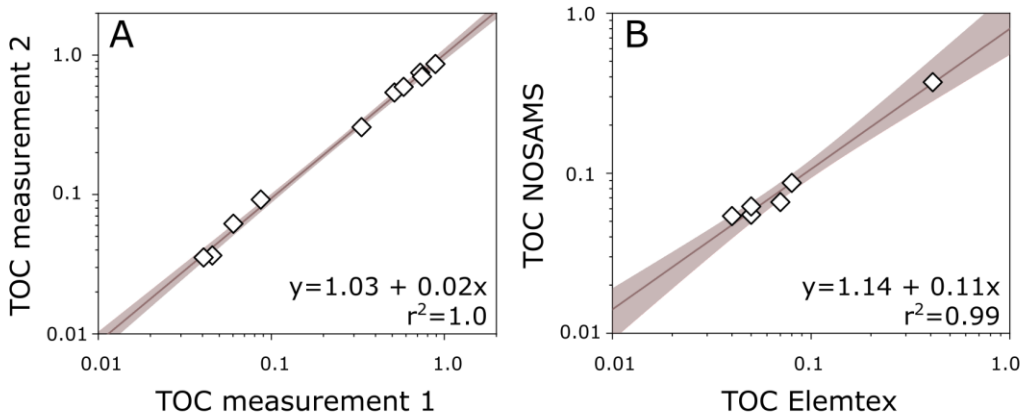

Figure 2.1: Precision of total organic carbon (TOC) concentration measurements. A: Replicate measurements of TOC concentration for samples run at the beginning and the end of the analytical sequence. The linear regression line results in an excellent fit between the sample replicates. **B:** Comparison of TOC measurements of the same samples measured in Elemtex, Stable Isotope Analytical Laboratory, Cornwall, UK (X-axis) and National Ocean Sciences Acceleration Mass Spectrometry Facility (NOSMAS) at Woods Hole Oceanographic Institution (Y-axis). The TOC concentration measurements show a close fit between the two different laboratories. The envelope around the regression line represents the 95% confidence interval.

A subset of solid samples from deep weathering profiles from the Susquehanna Shale Hills Critical Zone Observatory were analyzed for radiocarbon. The detrital carbonates were removed by acid leach (1N HCl) in clean, pre-combusted glass wear (at 450 °C). The samples were centrifuged and the supernatant was discarded. The sample residue was rinsed with deionized water and oven dried at 60 °C at Durham University, Department of Geography. The radiocarbon measurements were made at National Ocean Sciences Acceleration Mass Spectrometry Facility (NOSMAS) at Woods Hole

Oceanographic Institution (WHOI) following the standard procedures for Atomic Mass Spectroscopy (AMS; McNichol et al., 1994).

2.2.2 Rhenium concentrations

Rhenium is one of the rarest elements present in the Earth's environment with concentrations in solid materials ranging between 10^{-12} g g^{-1} and 10^{-9} g g^{-1} (Dellinger et al., 2020). Consequently, Re concentrations in natural river waters are commonly low, that is between 8.7×10^{-13} to 4.7×10^{-12} g g^{-1} (Colodner et al., 1993; Dalai et al., 2002; Miller et al., 2011; Hilton et al., 2014; Horan et al., 2017, 2019).

2.2.2.1 Direct calibration technique for Re concentrations in waters

In previous studies, various methods have been applied to determine dissolved Re concentrations in river waters. For example, the standard addition method (Miller et al., 2011, Hilton et al., 2014), or the combination of isotope dilution and ion exchange column chemistry technique, both resulting in sufficiently low detection limit for Re determination (Colodner et al., 1993; Hilton et al., 2014; Horan et al., 2017, 2019). Both methods require time-consuming sample preparation before measurements. More recently, Horan (2018) directly measured Re in dissolved load without any sample preparation by using multi-elemental calibration standards on a quadrupole inductively-coupled-plasma mass spectrometer. The main advantage of this method is minimal sample preparation, which limits potential sources of sample contamination, and provides similar results to isotope dilution technique. Additionally, this technique requires a small sample volume (2.75 ml) and has a short processing time (Horan, 2018).

In this thesis, we measured Re concentrations in water samples without sample preparation using Agilent 7800 quadrupole inductively coupled plasma mass spectrometer (Q-ICP-MS) at Durham University, Department of Geography. A range of multi-elemental standard solution was prepared to cover the expected range of trace element concentrations in river waters (a 7-point calibration line with Re concentrations from 0.3 to 70 ng l^{-1}). To correct for any potential matrix effect, an internal standard containing a mixture of Sc, Tb, Rh, In, Bi, and Ge was added to each acidified river water sample (final concentration of 0.025 mg l^{-1}). In each measurement session, the detection limit was calculated as three standard deviations of all the measured blank solutions and returned an average value of 0.01 ppt Re.

The accuracy of the measurements was checked by measuring Ottawa River water reference material SLRS-5 (Canadian National Research Council). This water reference is not certified for Re, however, Re was repeatedly measured in this sample in two French laboratories, where they reported a mean value of Re at 66±12 pmol l^{-1} (n=35; Yeghicheyan et al., 2013). Horan (2018) reported similar mean value for the SLRS-5, that is 59.8±1.7 pmol l^{-1} (n=12), which is based on Re preparation by isotopic dilution. Here the SLRS-5 standard material was measured at the beginning and the end of each sample batch. The reference material was prepared in the same way as the samples, by adding internal standards.

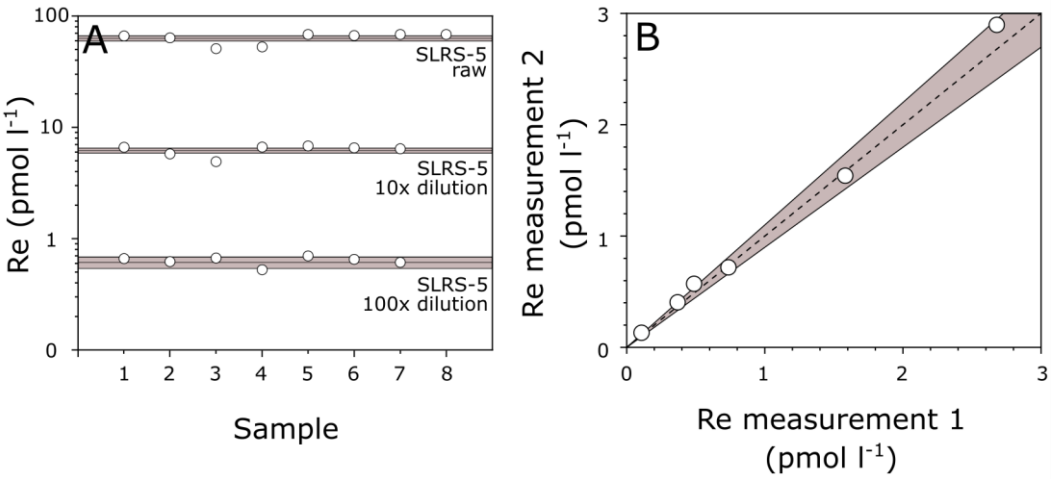

Figure 2.2: Accuracy and precision of dissolved Re concentration measurements. A: Re concentration measurements on a standard reference river water material (SLRS-5) and its 10- and 100-times dilutions. The mean line represents the long-term mean and the envelope around shows ±1SD around the mean. **B:** Sample reproducibility run within the same analytical session. The stippled line is 1:1 and the envelope around is ±10% deviation from the 1:1 line.

The mean Re concentration measured in SLRS-5 in this study is 62.6±7.6 pmol l^{-1} (n=7, ±1SD), which is in agreement with previously published values in Yeghicheyan et al. (2013) and Horan (2018). Additionally, a 100- and 10-times dilution of the reference material was prepared and analyzed to determine the detection limit of the element and to monitor the Re concentrations in more dilute river samples. The long-term in-house concentration measurements on the diluted reference material are 6.19±0.32 pmol l^{-1} (n=21; ±1SD) and 0.61±0.07 pmol l^{-1} (n=35; ±1SD), for 10- and 100-times dilutions, respectively. The samples run during our analysis closely fit to the long-term in-house measures (Figure 2.2A). Precision of the analysis was taken from sample reproducibility, which shows a close agreement with samples run within the same session (Figure 2.2B). All replicate samples plot closely to the 1:1 line and within ±10% deviation line.

2.2.2.2 Complete digestion protocol for Re concentrations in solids

Rhenium concentrations in solid samples were determined following a complete digestion protocol after Dellinger et al. (2020). Dry and homogenized solid samples were digested with a mixture of nitric acid (HNO_3) and hydrofluoric acid (HF) (1:1), to dissolve the carbonate (Equation 2.1) and silicate (Equation 2.2) matrix.

$$CaCO_3 + 2HNO_3 \longrightarrow Ca(NO_3)_2 + H_2O + CO_2 \quad (2.1)$$

$$CaSiO_3 + 8HF \longrightarrow H_2SiF_6 + CaF_2 + H_2O \quad (2.2)$$

The reaction of HF with silicate compounds results in production of hexafluorosilicic acid (H_2SiF_6), which is a volatile species, meaning all silica bound to it will be evaporated from the sample during sample evaporation. However, the co-precipitated calcium fluoride (CaF_2) may be difficult to dissolve. The use of HNO_3 limits precipitation of CaF_2, since the CaF_2 is soluble in HNO_3 (Wilding and Rhodes, 1970). Next, the organic matrix is dissolved with aqua-regia (Equation 2.3), which is a mixture of strong hydrochloric acid (HCl) and nitric acid (HNO_3).

$$3HCl + HNO_3 \longrightarrow 2H_2O + NOCl + Cl_2 \quad (2.3)$$

A product of aqua-regia is nitrosyl chloride (NOCl), a strong oxidizing agent that has been long recognized as a very efficient substance for oxidizing organic matter, sulfides, and carbonates in a sample matrix (Xu et al., 2012). The number of aqua-regia steps varied based on sample characteristics, in particular the concentration of TOC. Generally, the aqua-regia was repeated until all sample residue was in 1N HCl solution (~40–50 ml).

After the strong acid digestion, the Re was purified from the sample matrix using column chemistry. Here a polypropylene column and 1 ml of AG1-X8 resin (200–800 mesh) was used. The resin was cleaned with approx. 16 ml of 8M HNO_3 and 10 ml of ultrapure water (Milli-Q). The resin was then conditioned with 5 ml of 1N HCl before the sample was introduced. The sample matrix was eluted with 10 ml of 1M HCl, 15 ml of 0.5M HNO_3, and 1.5 ml of 4M HNO_3. Next, the Re was eluted with 12.5 ml of 4M HNO_3. The Re solution was evaporated and re-fluxed in 1.5 ml of 16M HNO_3 at 120 °C for 24h. Finally, 0.5M HNO_3 Re solution was prepared for measurements of Re concentration on a multicollector inductively coupled plasma spectrometer (MC-ICP-MS) at Durham University, Department of Earth Sciences.

A range of different standard reference geological materials were digested in each batch to validate the method: a marine sediment (MAG-1: Re=3.6±0.6 ppb, ±2SD, n=3), basalts (BHVO-2: Re=0.62±0.07 ppb, ±2SD, n=6 and BCR-2: Re=11.59±0.72 ppb, ±2SD, n=3), and serpentinite (UB-N: Re=0.21±0.02 ppb, ±2SD, n=3). These values are in agreement with previous published concentrations on the same material (Figure 2.3A) (MAG-1: Re=3.9 ppb; Meisel and Moser, 2004), basalts (BHVO-2: Re=0.54±5.3, ±2SD, n=6; and BCR-2: Re=12.6±15.9, ±2SD, n=4; Jochum et al., 2016), and serpentinite (UB-N: Re=0.21±4.8, ±2SD, n=14; Meisel and Moser, 2004). Previous studies have determined Re concentrations in reference materials by isotopic dilution, which further validates the method presented here and in Dellinger et al. (2020). The obtained data on reference materials were also validated to long-term in-house repeated measurements of Re concentrations, where all samples agree within 10% (Figure 2.3B).

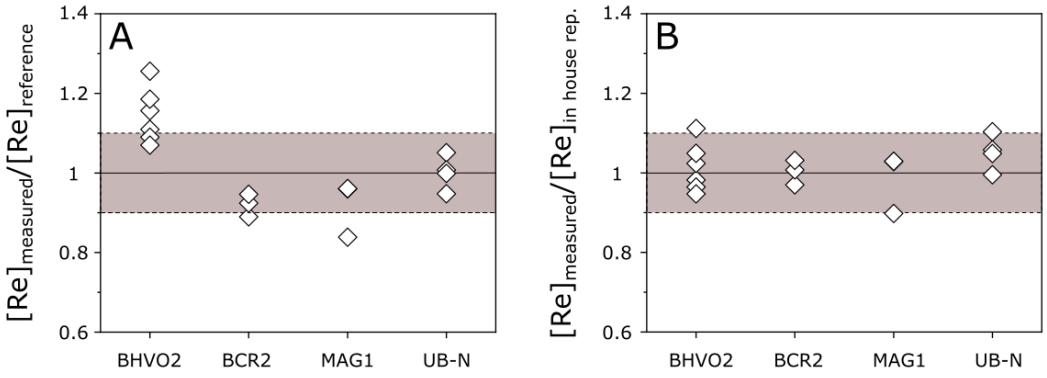

Figure 2.3: Accuracy and precision of Re concentration measurements in solids. A: Measured Re concentration in reference materials normalized over the mean reference value obtained from the literature (Meisel and Moser, 2004; Jochum et al., 2016). **B:** Measured Re concentrations in reference materials normalized over the mean long-term in-house value (Dellinger et al., 2020). The full line represents complete agreement with reference values, the stippled line represents ±10 % deviation from the full line.

2.2.3 Stable sulfur and oxygen isotope on dissolved sulfate

A subset of water samples from the Draix-Bléone CZO was prepared and analyzed for stable sulfur ($\delta^{34}S_{SO4}$) and oxygen ($\delta^{18}O_{SO4}$) isotope of dissolved sulfate in order to investigate source of high SO_4 concentrations in these catchments and give insight on its oxidation environment (Calmels et al., 2007; Turchyn et al., 2013). Extremely high SO_4 concentrations (>>1,000 µmol l^{-1}) allowed for direct precipitation of barite ($BaSO_4$) from river water samples following the methodology of Turchyn et al. (2013). In summary, approx. 3 ml of 0.3 M BaCl solution was added to 5 ml of non-acidified stream water sample to precipitate $BaSO_4$. The precipitate ($BaSO_4$ powder) was separated from the supernatant and 1 ml of 6 M HCl was added to the $BaSO_4$ powder in order to dissolve potential co-precipitated carbonates ($BaCO_3$). The $BaSO_4$ powder was then rinsed with deionized water and dried in an oven on 70 °C.

The powders were analyzed for $\delta^{34}S$ by flash Elemental Analyzer (EA) coupled by continuous flow to a Delta V mass spectrometer at the Godwin Laboratory for Paleoclimate research at the University of Cambridge. The samples were run with standard reference material: NBS-127 bracketing sets of samples. The $\delta^{18}O$ on the barite was measured in triplicates on a High Temperature Conversion Elemental Analyzer (TC/EA) at Department of Earth & Planetary Sciences, Harvard University. The measurements were corrected to the Vienna Standard Mean Ocean Water (VSMOW) using a 2-point calibration curve (OAEA SO-6 and NIST NBS-127), and applying the $\delta^{18}O$ values from Brand et al. (2009). Isotopic accuracy was monitored through repeated analysis of international standards IAEA SO-6 = -11.3±0.3 ‰ VSMOW (n=8; accepted value=-11.35±0.31 ‰ VSMOW) and NIST NBS-127: 8.6±0.3 ‰ VSMOW (n=8; accepted value=8.59±0.26 ‰ VSMOW). Average triplicate sample uncertainty was 0.2 ‰ (n=20).

2.2.4 Major elements in water and solid samples

2.2.4.1 Ion chromatography technique for major ions in waters

Major ions in water samples were measured by ion chromatography on a Thermo Scientific Dionex ICS 6000 ion chromatograph at Durham University, Department of Geography. Calibration standards were used to construct a six-point calibration curve, covering a range of typical river water compositions. The analytical accuracy of the results was determined by repeated measurements of a certified river water reference standard material (Sangamon-03), which is collected in Sangamon River in Mahomet, Illinois. The reference material was treated in the same way as samples and was analyzed at the beginning and end

of each analytical run. The analytical precision through all runs was better than 5% for SO_4^{2-}, Na^+, K^+, Ca^{2+}, and Mg^{2+}, and better than 10% for Cl^- (Figure 2.4). Additionally, sample replicates were run during and between each batch, resulting in precision better than 1% for Ca^{2+} and Mg^{2+}, better than 2% for SO_4^{2-}, Na^+ and K^+, and better than 3% for Cl^- and Sr^{2+}.

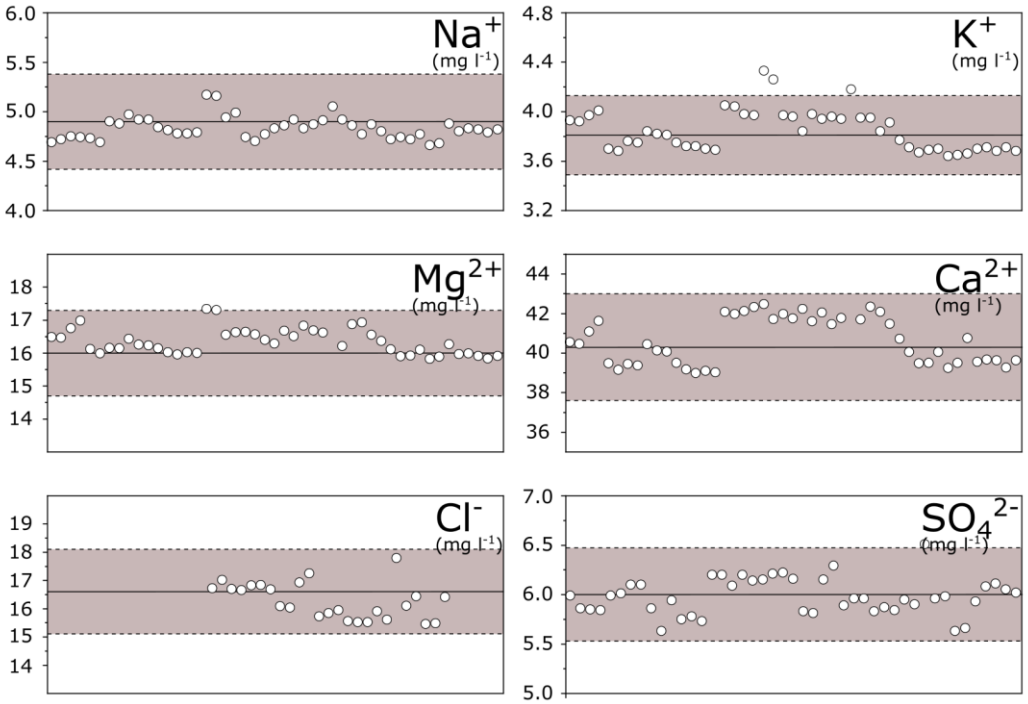

Figure 2.4: Accuracy of major elements in waters. Measurements of major elements in Sangamon-03 river water reference material. The full line represents the certified value in mg l^{-1}, the envelope around represents the reported uncertainty on the certified value, which is ±2SD.

Bicarbonate concentration in water samples collected during field visit of the sites was determined by the Gran titration method (Edmond, 1970). In time series water samples, the bicarbonate concentrations were calculated by charge balance, assuming that all unmet positive charge is equal to concentration of the HCO_3^- in milliequivalents (Equation 2.4).

$$HCO_3^- = \sum Cations - \sum Anions \qquad (2.4)$$

This calculation is valid, when the relative abundance of bicarbonate is the dominant species of alkalinity in stream water, which results at pH~8 (Neal et al., 1998). Nonetheless, calculating concentration of bicarbonate from the charge balance approach was challenging in the Draix-Bléone CZO catchments, where high dissolved load concentration was continuously measured, with prevailing SO_4^{2-} concentrations (>10,000 µmol l^{-1}), resulting in complete SO_4 dominance on the anion site and giving negative concentrations of HCO_3^- by charge balance. Given an uncertainty of ~5%, this high absolute value makes residual using the charge balance more uncertain (±500 µmol l^{-1}) of zero. For these samples (19% of the dataset), the concentration of bicarbonate ions was not determined.

2.2.4.2 Major elemental concentrations in solids

Solid samples collected in the Draix-Bléone CZO catchments were analyzed for major and trace elements using flow injection and low pressure on-line liquid chromatography coupled to inductively coupled plasma mass spectrometer (ICP-MS) at the French National Centre for Scientific Research (CNRS) Service d'Analyse des Roches et des Minéraux (SARM) following a protocol described in Carignan et al. (2001).

A subset of solid samples from the Draix-Bléone CZO catchments were analyzed for sulfur concentration and stable sulfur isotope ($\delta^{34}S$) on a Costech Elemental Analyzer coupled to a Thermo Fisher Delta V Plus in the Stable Isotope Biogeochemistry Laboratory at Durham University, Department of Archeology. Isotopic accuracy was monitored through repeated runs of standard material (sulphanilamide) and international standards (IAEA-SO-5, IAEA-SO-6, NBS-127), providing isotopic range of $\delta^{34}S$ from -31 ‰ to 20.3 ‰. The percentages of sulfur

were calculated as part of the isotopic analysis using sulphanilamide (S=18.62 %).

Additionally, this work takes advantage of previously published major elemental concentrations and sulfur concentrations for solid samples obtained from the Susquehanna Shale Hills CZO. Details on sample collection and analytical methods for these samples can be find in Brantley et al. (2013), Sullivan et al. (2016) and Gu et al. (2020).

2.3 Computational data analysis for solute fluxes

Rivers are natural integrators of weathering processes and transport dissolved components from headwaters to catchment outlets (Gaillardet et al., 1999). Chemical weathering fluxes represent a mass flux of solutes, transported at a point in a stream over a set time period, and are calculated as a product of concentration and discharge measurements (mol km^{-2} yr^{-1}; Aulenbach and Hooper, 2006). Numerous methods have been applied for calculation of the chemical weathering fluxes, such as averaging methods, regression or curve rating models, interpolation models, or a mix of different techniques (Appling et al., 2015; Aulenbach and Hooper, 2006; Worrall et al., 2013). Each method has positives and negatives due to various factors that can impact flux estimates, such as catchment hydrology, sources and mobility of the solute of interest, correlation with discharge, and scale of the system (Appling et al., 2015). Additionally, the flux calculations are sensitive on data resolution and sampling design (Cooper and Watts, 2002; Skarbøvik et al., 2012). In this section, four different methods for estimating annual chemical weathering yields are presented, with an

emphasis to determine solute fluxes applied for the studied catchments of the Draix-Bléone CZO in Chapter 4 and Chapter 5 of this thesis.

2.3.1 Average and discharge weighted average

The most straightforward way to estimate chemical weathering yields (mol km^{-2} yr^{-1}) is the product of mean concentration of dissolved elements ($[\bar{X}]_{Year}$; mol l^{-1}) and the mean annual flow ($[\bar{Q}]_{Year}$; l s^{-1}) divided by catchment area (A), and using K as a conversion factor to take account for the time period (Equation 2.5).

$$[\bar{X}]_{Flux} = K \frac{[\bar{X}]_{Year} \, x \, [\bar{Q}]_{Year}}{A} \qquad (2.5)$$

The uncertainty of this estimate can be determined from the standard error of the average concentration (Aulenbach and Hooper, 2006). The method is suitable in catchments with limited dataset, where a constant concentration is observed with changing water discharge, and seasonal variability of elements is of secondary importance. This average method has been the most commonly used for defining estimates of Re fluxes (Dalai et al., 2002; Rahaman et al., 2012; Hilton et al., 2014; Horan et al., 2017). The method application was justified by negligible dilution trend of dissolved Re with increased discharge (e.g. Hilton et al., 2014). Nonetheless, low frequency sampling may not capture the overall variability in chemical weathering rates, resulting in biased annual estimates (Appling et al., 2015; Godsey et al., 2009).

If the samples are collected randomly through time, then the flux load estimates should be flow-weighted (Equation 2.6).

$$[\bar{X}]_{Flux} = K \left[\frac{\frac{[\overline{X\ x\ Q}]_i}{\bar{Q}_i}\ x\ [\bar{Q}]_{Year}}{A} \right] \quad (2.6)$$

Here, K, A, and X are the same parameters as described for Equation 2.5(2.5) (above), Q_i is instantaneous discharge and Q_{Year} is average yearly discharge. The uncertainty on this calculation arises from the analytical uncertainty of the investigated solute and the variability around the mean on the concentration and discharge, expressed as standard error. The method is commonly used for calculation of silicate and carbonate weathering fluxes in datasets, where a certain relationship between solutes and discharge is observed, but the river water sampling times are limited (Moon et al., 2014; West et al., 2002). Miller et al. (2011) applied this method for calculating dissolved Re fluxes on large world's rivers. Similar as the sharp average, this approach fails to capture any seasonal variability in flux estimates.

2.3.2 Regression model

A regression model exploits a relationship between elemental concentration in stream water and continuous variable, such as stream water discharge, season, or time (Aulenbach, 2013; Stenback et al., 2011). Solute concentrations for un-sampled periods are then estimated from fitting a function through, for example, concentration-discharge (C-Q) dataset (e.g. Figure 2.5). This method can provide an accurate and precise flux estimate when the concentration-discharge relationship is well-fitted by a function, or functions (for example using seasonal or rising and falling-limb based C-Q relationships). A commonly used function to fit C-Q data is a power law (Equation 2.7).

$$C = a \times Q_i^b \quad (2.7)$$

Here C is the concentration of a solute, Q_i is instantaneous water discharge, and a and b are the modeled parameters. This flux calculation is sensitive to the accuracy of the proposed model (Aulenbach and Hooper, 2006), therefore, the uncertainty may be estimated from a 95% confidence interval of the fitted parameters (Torres et al., 2015). The models can produce poor flux estimates when the few available predictors fail to capture variability in flux (Appling et al., 2015; Guo et al., 2002; Stenback et al., 2011). Previous studies have shown that error estimates may be reduced by increasing sampling frequency (Verma et al., 2012) and by including event sampling, to ensure adequately defined concentration-discharge relationship (Cooper and Watts, 2002; Skarbøvik et al., 2012).

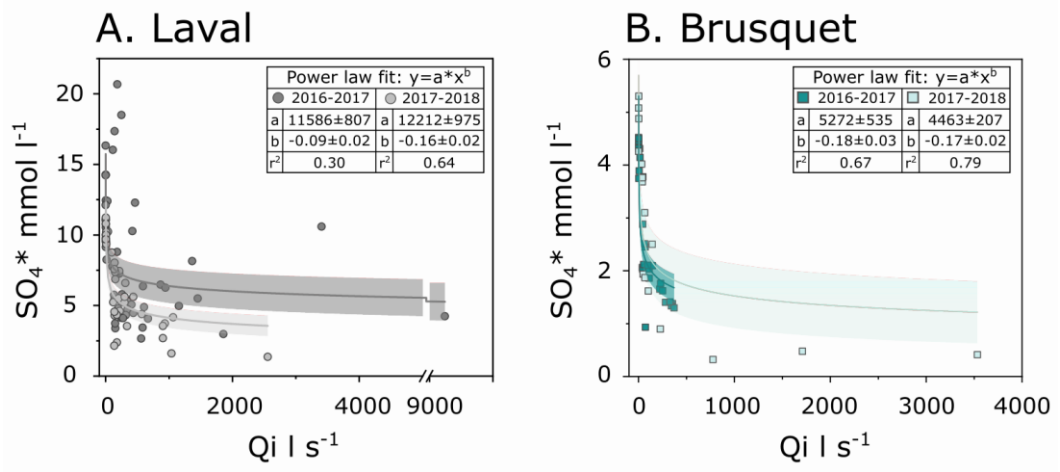

Figure 2.5: Power law model fit to a discharge-concentration relationship. This is an example of a power law fit model using water samples collected in the Laval and Brusquet catchments at the Draix-Bléone CZO and measured as part of this study (Chapter 4 and Chapter 5). The darker points in each plot are data from the first observation year (09/2016-09/2017) and the lighter points are data from the second observation year (09/2017-09/2018). The power law function was fitted with a Power Law fitting curve using OriginLab. The shaded area around the power law model represents the 95% confidence interval.

2.3.3 Interpolation model

Measured concentrations in streams are thought to represent a period around which the sample was collected. For that purpose, a linear interpolation method may be used to estimate concentrations at un-sampled times by connecting concentration measures with a single line through time (Larson et al., 1995; Vanni et al., 2001). Then the product of concentration and discharge is summed to determine the annual load (Aulenbach and Hooper, 2006). An interpolation model is particular useful when the rating-curve approach does not fully capture the relationship between the available data, and when observations are frequent enough to represent the non-sampled time intervals (Appling et al., 2015). The high sampling frequency is one of the main limitations for the interpolation models, since this method may produce large bias in flux estimates when the sampling does not sufficiently capture the concentration variation during the storm events. When sampling frequency is sufficient, then the resulting concentration estimates provide higher temporal resolution data and more accurate estimates and uncertainty bounds on the annual fluxes (Appling et al., 2015) compared to the averaging methods or regression modelling.

2.3.4 Combined model

Aulenbach and Hooper (2006) presented a composite method for estimation of solute fluxes, which combines a regression-model (accounting for seasonal variability in solute chemistry) with a linear interpolation model (to account for short-term variability). This method was developed for small watershed studies with solute concentration dataset sampled at varied time-intervals (e.g. monthly sampling combined with high frequency sampling of storm events). In the

following we present the computational method developed for calculating solute fluxes in the Laval and Brusquet catchments of the Draix-Bléone CZO, using an example of discharge and SO_4 concentrations measured in both catchments.

2.3.4.1 Sampling design and defining the low flow domain

The studied catchments (the Laval and Brusquet) within the Draix-Bléone CZO are small (<1 km^2), and characterized by intermitted steam discharge, with naturally extended periods of zero flow, interrupted by flush storm events (Figure 2.6; Mathys and Klotz, 2008). In order to track seasonal variability in stream water chemistry, as well as short-term storm event variability, hand sampling of the low flow regime and automatic sampling (ISCO auto sampler) of high flow regime took place between September/October 2016 and September/October 2018 in the Laval/Brusquet. The sampling strategy resulted in integrated time series data of low flow regime and high temporal sampling of high-flow events obtained for both catchments (Figure 2.6). Detailed descriptions of the catchments and sampling methods are provided in Chapter 4, Section 4.3.1.2., p107).

There are several methods to separate the main hydrological flow regimes (low flow and storm events) and the samples collected during these time periods, e.g. flow duration curves, continuous low flow intervals, and others (see review Smakhtin, 2001 and references herein). Here, we define the low flow domain by expressing a percentile of mean annual flow (Smakhtin, 2001). That is the maximum discharge of the lower quartile (Q1; <25%) of all discharge measurements across the observation period. This corresponds to flows <28.5 l s^{-1} for the Laval and <7.2 l s^{-1} for the Brusquet.

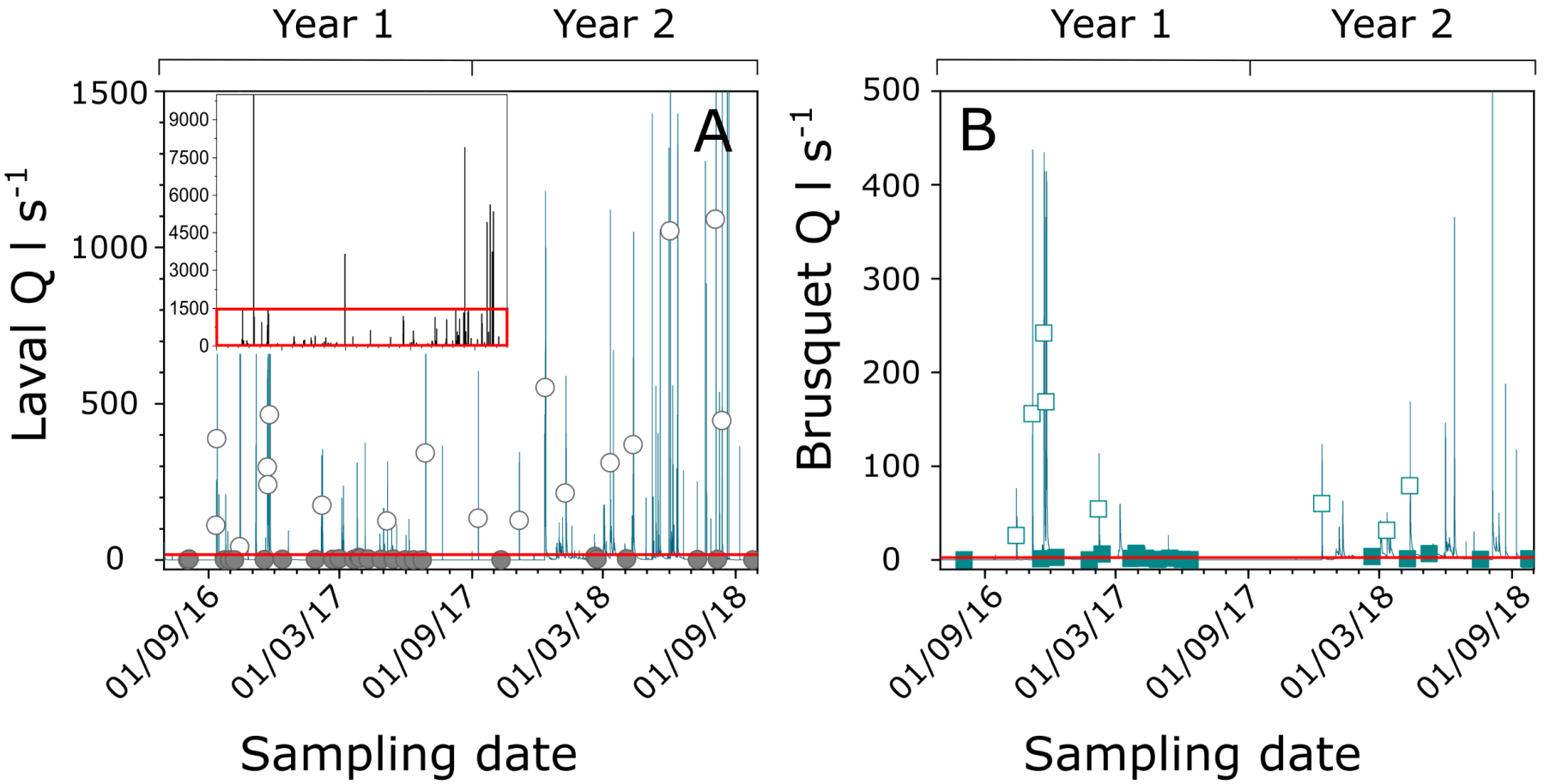

Figure 2.6: Sampling strategy for the Laval and Brusquet catchments. A: In the Laval, storm events can reach up to 10,000 l s^{-1} stream discharge (inlet). **B:** In the Brusquet the majority of storm events reach discharge values of up to 500 l s^{-1}. The red line represents the defined low flow domain (28.5 l s^{-1} for the Laval and 7.5 l s^{-1} for the Brusquet). Open symbols mark sampled storm events (auto-sampler) full symbols mark low flow regime sampling (hand sampling).

Previous studies have shown that seasonal datasets with incorporated high resolution sampling at high flow regimes better define concentration patters through time and may reduce flux estimation errors (Cooper and Watts, 2002; Skarbøvik et al., 2012; Verma et al., 2012). This scheme produces discharge measurements at irregular time intervals, with densely monitored high flow events and less frequent sampling of low flow regimes. For the observation period, 11,119 and 3,975 discharge measurements were taken in Laval and Brusquet, respectively, of which ~ 75% are covering the high flow regime in both catchments. In terms of time, the high flow regime represents 4% and 2% of the observation period in the Laval and Brusquet, respectively. However, ~70% of the water flow during the year occurred in these events (Table 2.2). The sampling trend is followed in the concentration data, where among the 91 water samples collected from the Laval, 74% were sampled during high flow events. In the Brusquet, 69% of the 50 water samples were collected, during the high flow (Table 2.2). Using the averaging methods for flux estimates (Section 2.3.1) with this sampling strategy would likely to result in bias estimates towards the solute concentrations of the high flow regime.

Table 2.2. Stream water sampling and water fluxes in the Laval and Brusquet catchments.

Study Site	Observation Period	Flow category	Number water samples	Water flux raw dataset	Water flux modelled dataset	Percentage of the total water flux
				x10^8 l yr^{-1}		%
Laval	11/09/2016 - 10/09/2017	*Total*	59	2.60	2.53	-
		High flow	41	-	-	67
		Low flow	18	-	-	33
	11/09/2017 - 10/09/2018	*Total*	32	4.23	4.17	-
		High flow	27	-	-	68
		Low flow	5	-	-	32
Brusquet	10/10/2016 - 09/10/2017	*Total*	32	1.35	1.32	-
		High flow	22	-	-	73
		Low flow	10	-	-	27
	10/10/2017 - 09/10/2018	*Total*	18	1.59	1.55	-
		High flow	14	-	-	65
		Low flow	4	-	-	35

2.3.4.2 Model construction

With an aim to simplify the computational process, the measured discharge values, collected based on a flow-rate dependent scheme (Mathys and Klotz, 2008) are resampled to a uniform time interval of 5 min. This short time interval was chosen in order to fully represent the high flow events, which are especially characteristic for the Laval catchment (Cras et al., 2007; Mathys and Klotz, 2008). To ensure that no major data manipulation problem occurred during this resampling step, we compared the annual water flux for the raw discharge data with the resampled dataset and found a good agreement between the two values within 3% (Table 2.2)

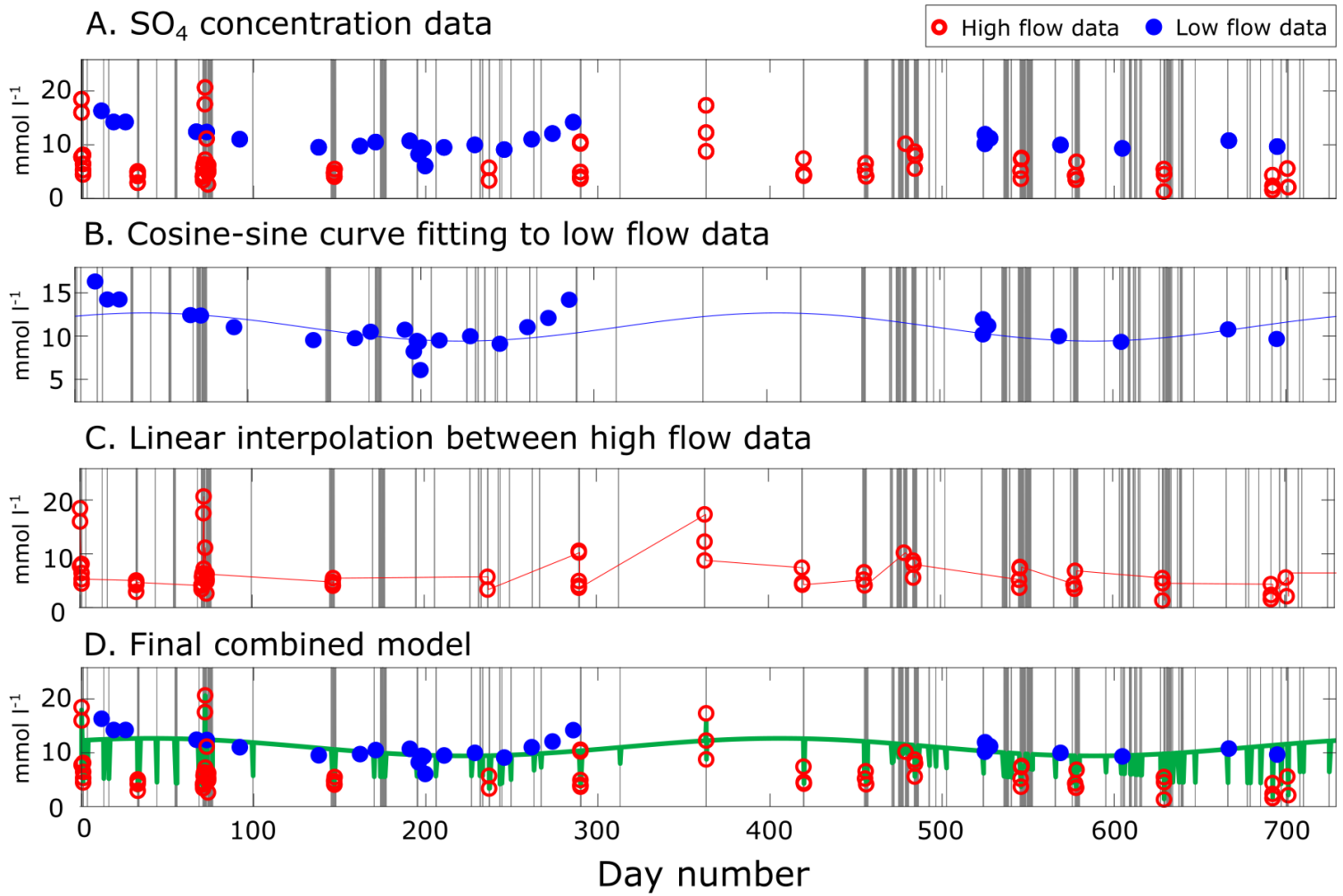

Figure 2.7: Combined model for predicting SO_4 concentrations. Example from the Laval catchment. The concentrations are predicted over short, 5-minutes time intervals based on seasonal and short-term variability observed in the data. The grey vertical bars represent time periods when discharge is >28.5 l s^{-1} (the low flow threshold for Laval; Section 2.2.4.2). **A:** SO_4 measurements used to build the model into a low flow (blue) and high flow (red) divide. **B:** Seasonal variability in the low flow regime with a fitted cosine-sine function. **C:** Linear interpolation between the high flow regime samples. **D:** Final combined model (green line).

Then, we take a advantage of the integrated time series sampling by combining a regression (Section 2.3.2) and interpolation model (Section 2.3.3) with solute concentrations data, using the following three-steps, presented here using an example of SO_4 (Figure 2.7). Firstly, we note that the low flow samples reveal a seasonal pattern in concentration, which can be described by a cosine curve fit (Figure 2.7B). We choose to represent the low-flow regime in this way, because the samples are more robustly represented with this method than with a linear interpolation, which is more sensitive to outliers. Secondly, we use a linear interpolation between high flow samples (Figure 2.7C). This allows us to account for the short-term variability within each flood event, where the gaps between samples are of the order of minutes to hours. It also allows us to capture seasonal variability that appears to be present in the storm event samples. The linear interpolation is used to model the solute concentration of floods which were not sampled. Thirdly, we combine the models of concentration variability at high and low flow regimes (Figure 2.7D). By following this methodology, we are able to capture the seasonal variability of the low flow concentrations, in addition to robustly describing individual storms, and seasonal patterns in storm events. For further details and results, see Chapter 4 and Chapter 5.

2.3.4.3 Solute flux calculation and uncertainty

The flux (J_x in mol km^{-2} yr^{-1}) is calculated with the following equation:

$$J_X = K \frac{\overline{X_{5min} \times Q_{5min}}}{A} \quad (2.8)$$

Where K is a conversion factor to take account for the time period (seconds to year), X_{5min} is the elemental concentration modelled for the 5 min time interval (mol l^{-1}), Q_{5min} is discharge modelled for the 5 min time interval (l s^{-1}), and A is

the study catchment (km^2). The uncertainty on the flux estimates is assessed by propagation of the analytical errors, data variability, and assessing how the sampling frequency influences the annual yields. To do this, solute fluxes are calculated using between 20% and 100% of the dataset over 10,000 different iterations. The population forms a close-to-gaussian (normal) distribution; hence, the final reported flux value can be defined as the population mean, and the uncertainty as the standard deviation of these 10,000 yields.

The main advantages of this method are: i) accounting for seasonality in solute concentrations, ii) direct incorporation of all high resolution (high flow event) data, iii) providing estimates for the non-sampled time periods and iv) allowing calculation of fluxes over different time scales (daily – annual).

The annual fluxes for dissolved sulfate were compared to estimates from the straight average approach and the rating-curve approach, fitting a power law function (Table 2.3). The mean annual fluxes for all three methods are close within the uncertainties, meaning that the estimates from the mixed approached presented here are reliable. In both catchments, the power low fitting gives the highest flux estimate, which may result from the over-prediction of SO_4 concentrations for the low flow regime (when the SO_4 concentrations are the highest; Figure 2.5). In contrast, the estimates for the straight average flux may be biased towards the high flow (diluted) samples, which are more frequently sampled compared to the low flow regime. The uncertainty estimate is the highest on the straight average approach, while the uncertainty bounds are much better constrained for the mixed method and curve rating method. The advantages for the mixed method presented above and the similarity in flux estimates to other standard methods, supports the application of this

computational technique to estimate annual Re, carbonate and silicate weathering fluxes in the Chapter 4 and Chapter 5.

Table 2.3. Comparison of different computational methods for flux estimates.

Catchment	Observation Period	Straight Average		Curve Rating		Mixed Method	
		Mean Annual Flux	±	Mean Annual Flux	±	Mean Annual Flux	±
		$x10^5$ mol km^{-2} yr^{-1}		$x10^5$ mol km^{-2} yr^{-1}		$x10^5$ mol km^{-2} yr^{-1}	
Laval	11/09/2016 - 10/09/2017	25.8	13.4	29.2	2.0	22.1	1.0
	11/09/2017 - 10/09/2018	30.3	14.7	36.6	3.9	33.2	5.9
Brusquet	10/10/2016 - 09/10/2017	3.4	1.6	4.8	0.8	3.2	0.1
	10/10/2017 - 09/10/2018	4.2	2.5	5.1	0.4	4.5	0.4

2.4 Linking the generated data with the research questions

To address the research questions presented in Section 1.8 (p21) a large number of geochemical and hydrological data was generated. A flow diagram in Figure 2.8 provides a link between the collected sample sets, newly generated geochemical data, hydrological and environmental measures, the research questions and the scientific chapters presented in this thesis.

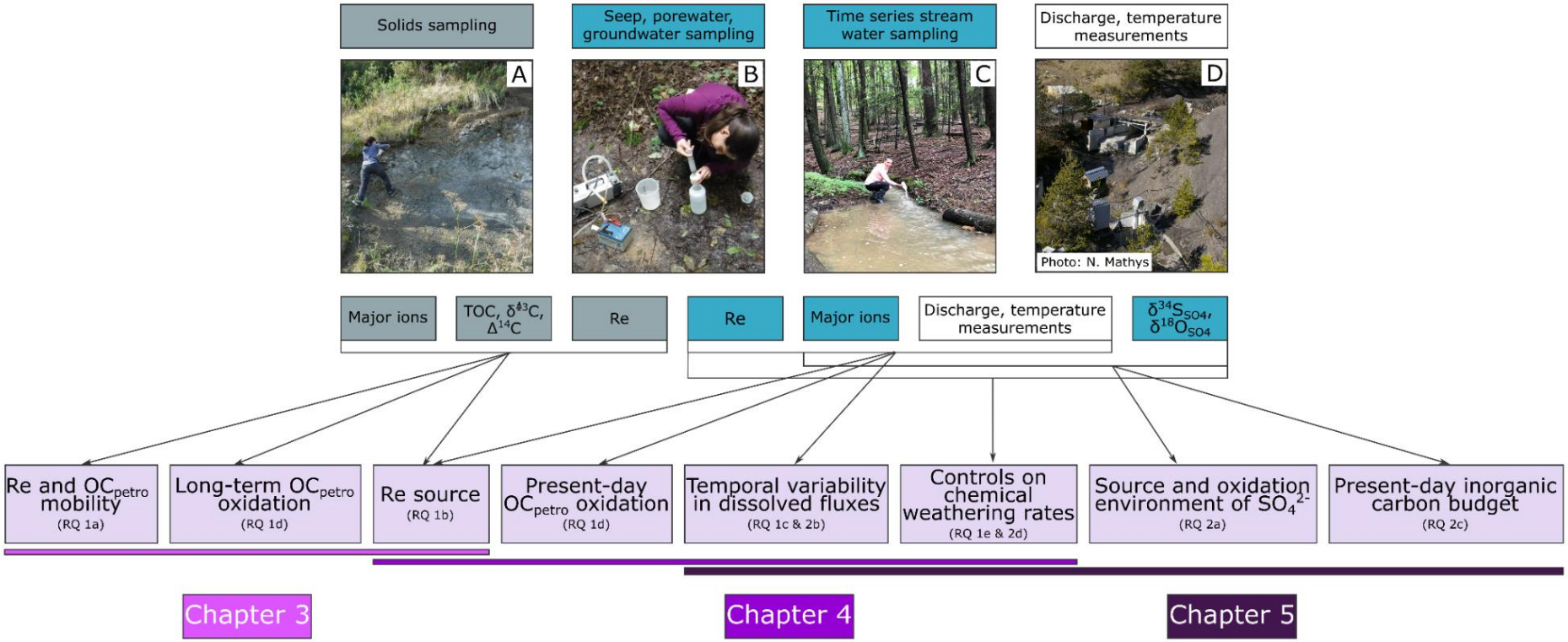

Figure 2.8: Flow diagram linking the generated data with the research questions and the scientific chapters. A: Sampling a weathering profile developed on shales in the Brusquet catchment (Draix-Bléone CZO). **B:** Filtering groundwater immediately after collection at the Shale Hills catchment (Susquehanna Shale Hills CZO). **C:** Jennifer Williams (collaborator from the Susquehanna Shale Hills CZO) hand sampling stream water for the time-series dataset. **D:** The gauging station equipped for monitoring discharge, precipitation and auto-collection of time series samples at the Laval catchment (Draix-Bléone CZO). The author of the photo "D" is N. Mathys, available at: https://oredraixbleone.inrae.fr/en/photos/. Abbreviations: TOC – total organic carbon, $\delta^{13}C$ – stable carbon isotope, $\Delta^{14}C$ – radiocarbon, Re – rhenium, $\delta^{34}S$ – stable sulfur isotope, $\delta^{18}O$ – stable oxygen isotope, OC_{petro} – rock organic carbon, RQ - research questions.

CHAPTER 3
Rock organic carbon oxidation and surface rhenium cycling

The Shale Hills catchment at the Susquehanna Shale Hills Critical Zone Observatory, Pennsylvania, US; August 2018.

A version of this chapter will be submitted to a peer-reviewed journal.

The authors on this paper will be:
Mateja Ogrič[1], Mathieu Dellinger[1], Katherine E. Grant[1], Valier Galy[2], Xin Gu[3], Susan L. Brantley[3] & Robert G. Hilton[1]

Affiliations:
[1]*Department of Geography, Science Laboratories, South Road, DH1 3LE Durham, UK.*
[2]*Woods Hole Oceanographic Institution, Department of Marine Chemistry and Geochemistry, Woods Hole, MA 02543, USA.*
[3]*Department of Geosciences, Penn State, University Park, PA 16802, USA.*

Authors contributions:
The research design and project goals were devised by myself with guidance from Robert G. Hilton and Mathieu Dellinger. The archived samples were provided by the SSHCZO (P.I. Susan L. Brantley). The stream water and groundwater samples were collected by myself, Xin Gu and Jennifer Williams. The analytical work on Re, TOC, and major elements analysis was carried out under supervision of Mathieu Dellinger and Robert G. Hilton. The analytical work on ^{14}C analysis was carried out by Katherine E. Grant and Valier Galy. Data processing and critical scientific evaluation was carried out with Robert G. Hilton, Mathieu Dellinger, Xin Gu, and Susan L. Brantley. The chapter was written and edited by myself, Robert G. Hilton and Mathieu Dellinger.

Abstract

The oxidation of rock organic carbon (OC_{petro}) is an important natural source of carbon dioxide (CO_2) to the atmosphere over geological timescales. The rates and patterns of OC_{petro} oxidation in locations that experience low rates of denudation remain poorly constrained, although these places account for a large part of Earth's land surface. Here, we track OC_{petro} oxidation using radiocarbon and the rhenium (Re) proxy in deep weathering profiles, soils and stream waters at the Susquehanna Shale Hills Critical Zone Observatory. In a ridge-top borehole, radiocarbon measurements reveal the presence of a broad OC_{petro} weathering front, with ~40% loss of OC_{petro} occurring over ~6 m (from 21.5 m to 15.4 m). However, the low OC_{petro} concentration (<0.05 %) and inputs of carbon from the biosphere in the upper profile make the OC_{petro} loss difficult to quantify. The OC_{petro} weathering front coincides with a zone of Re depletion (92% loss), and we estimate that ~83% of Re in the rock is associated with OC_{petro}, based on Re/Na and Re/S ratios. In contrast, the pyrite weathering front is narrower, occurring over ~0.4 m at ~15.4 m depth with 99% loss. Using estimates of long-term denudation, the observed OC_{petro} loss and the Re proxy return a very low OC_{petro} oxidation yield of $<2.0\times10^{-2}$ tC km^{-2} yr^{-1}. Such a low OC_{petro} oxidation rate is consistent with both the low OC_{petro} concentrations in the studied shale and low erosion rates. In addition, we find that the surface cycle of Re is decoupled from the deep weathering at this site, with an enrichment of Re in surface soils of the catchment (upper 0.3 m) and elevated Re concentrations in stream water, precipitation and shallow groundwater samples. Using a simple Re mass balance, we propose that this can be explained by a considerable anthropogenic contribution of Re to the stream water. This anthropogenic Re may be derived

from past and present local industrial sources (iron smelting, coal burning). We estimate that the topsoil Re pool could take centuries to deplete and call for a renewed focus on anthropogenic perturbation of the surface Re cycle in low denudation rate settings.

3.1 Introduction

The transfer of carbon between biogeochemical reservoirs is one of the main drivers of climate change over geological timescales (Berner and Canfield, 1989; Derry and France-Lanord, 1996; Berner, 2003). Over long time periods, carbon dioxide (CO_2) emissions through volcanism, carbonate weathering by sulfuric acid, and oxidation of rock-derived organic carbon (petrogenic, OC_{petro}) are counterbalanced by CO_2 sequestration through silicate weathering, carbonate formation, and burial of biospheric organic carbon (OC_{bio}). The CO_2 emissions from OC_{petro} oxidation and carbonate weathering by sulfuric acid (Burke et al., 2018; Petsch, 2014; Torres et al., 2017) may be of similar magnitude to the release of CO_2 from volcanic degassing (79±9 MtC yr^{-1}, Plank and Manning, 2019). Yet, the global rates and patterns of OC_{petro} oxidation remain poorly constrained (Hilton and West, 2020; Petsch, 2014).

The oxidative weathering of OC_{petro} has been assessed in river catchments using the trace element rhenium (Re) as a proxy (Dalai et al., 2002; Hilton et al., 2014; Horan et al., 2019, 2017). Rhenium is of low abundance in the Earth's crust (average 0.4 ppb; McLennan, 2001), but is enriched in sediments deposited in reducing conditions, especially in organic carbon-rich black shales (average 150 ppb; Colodner et al., 1993) and sedimentary rocks (10-30 ppb; Morford et al., 2012). Coupled loss of Re and OC_{petro} has been observed during oxidative

weathering (Hilton et al., 2014; Jaffe et al., 2002), with the mobilization of Re in the dissolved load under pH and Eh typical of most river waters (Colodner et al., 1993). As such, dissolved Re flux has been used as a proxy to estimate catchment-wide OC_{petro} oxidation rates in highly erosive catchments of the Himalaya (Dalai et al., 2002), Taiwan (Hilton et al., 2014) and New Zealand (Horan et al., 2017) and in moderate erosive setting of the Mackenzie River basin (Horan et al. 2019).

A focus on applying the Re proxy to settings with moderate to high erosion rates has been important for establishing the role of OC_{petro} supply in driving weathering fluxes (Hilton et al., 2014; Horan et al., 2017). However, there are key reasons why lower erosion rate settings are worthy of focus. First, low denudation rates (<0.5 mm yr^{-1}) are common over the majority of Earth's continents, and these settings comprise ~60% of global chemical denudation (Larsen et al., 2014). Second, low erosion rates can lead to the development of thick weathering profiles, helping to reveal reaction fronts of OC_{petro} and sulfide oxidation (Petsch et al., 2000; Wildman, 2004; Brantley et al., 2013) and track the relative mobility of Re during weathering (Jaffe et al., 2002). Finally, settings with lower chemical denudation could be more sensitive to Re inputs from anthropogenic sources (Miller et al., 2011; Rahaman et al., 2012) and help us better understand the modern-day perturbation of the Re cycle (Sen and Peucker-Ehrenbrink, 2012). This is because Re is enriched in fossil fuels (Bertine and Goldberg, 1971; Selby et al., 2007), volatile at temperatures >270 °C (Colodner et al., 1995), and can be deposited from ash fallout after coal combustion. Anthropogenic Re inputs have been invoked to explain high dissolved Re concentrations in large European rivers (Danube, Rhine), the

Yangtze and the Mississippi rivers (Miller et al., 2011) alongside lake and marine records from North America (Chappaz et al., 2008; Prouty et al., 2014).

Here, we explore Re mobility and source in the Shale Hills catchment of the Susquehanna Shale Hills Critical Zone Observatory. The Shale Hills site is a low denudation rate setting of 0.01 – 0.025 mm yr^{-1} (West et al., 2013) and provides an opportunity to explore deep weathering profiles (Jin et al., 2010; Brantley et al., 2013; Sullivan et al., 2016; Gu et al., 2020). We quantify oxidative rate of OC_{petro} using a combination of radiocarbon and Re measurements, and previously published S and major element concentration data (Brantley et al., 2013; Sullivan et al., 2016). In parallel, we explore the potential anthropogenic input of Re using samples from surface soils, rainwater and stream water.

3.2 Study site

Shale Hills is a small (0.08 km^2) sub-catchment within the Susquehanna Shale Hills Critical Zone Observatory (SSHCZO) (Figure 3.1). The first-order stream catchment is almost exclusively underlain by Rose Hill Formation of Silurian age, characterized by low total organic carbon (TOC) concentrations <0.05 % (Jin et al., 2014). Shale beds layered with limestone and sandstone units have been observed towards the catchment outlet (Jin et al., 2010; Sullivan et al., 2016). The Rose Hill formation has experienced minor metamorphism during burial and exhumation (Gu et al., 2020). Located in the Appalachia, the site has gentle slopes, forest cover and very low long-term denudation rates of 0.01 – 0.025 mm yr^{-1} based on measurements on meteoric beryllium-10 (^{10}Be; West et al., 2013) and uranium isotope disequilibrium (Ma et al., 2010). The rates of soil production

vary between 0.015–0.065 mm yr^{-1} (Ma et al., 2013, 2010), based on measurements of uranium isotope series in weathering profiles at SSHCZO.

The climate is humid-continental, with a mean annual temperature of 10 °C and mean annual precipitation of 1070 mm (Jin et al., 2010; NADP, 2020). Stream seasonal discharge variations are dominated by snowmelt in spring, and storms in summer and autumn. For the period of this study (June 2018–June 2019), daily discharge varied between 0 and 1329 $m^3\ day^{-1}$, with high-discharge events occurring in autumn and spring.

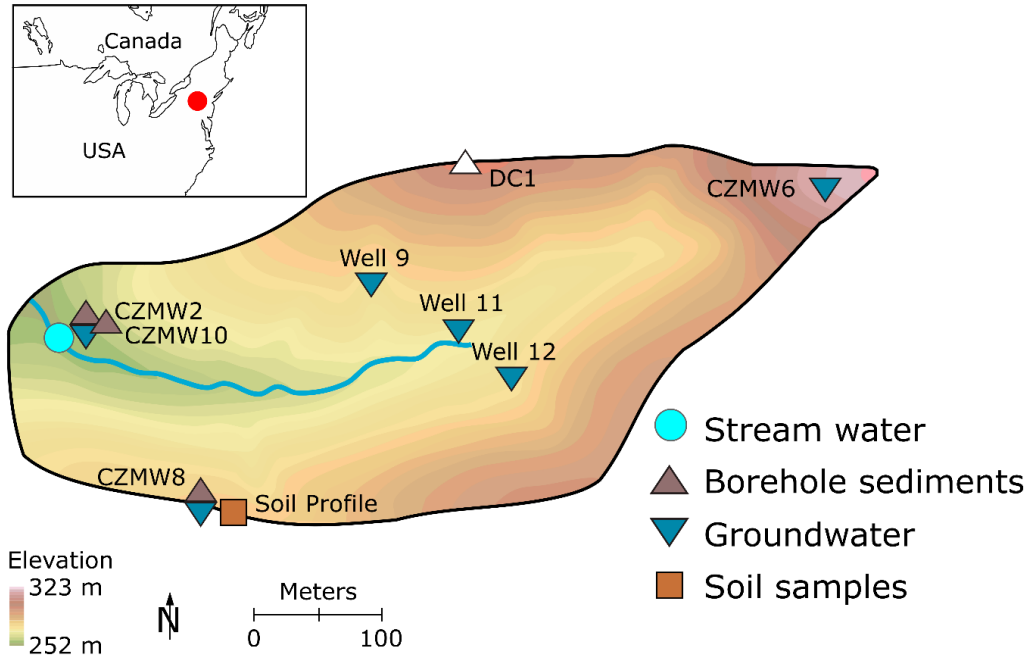

Figure 3.1: The Shale Hills catchment of the SSHCZO in central Pennsylvania. Samples analyzed in this study are shown: borehole sediments (CZMW2, CZMW10, CZMW8; brown triangles), a soil profile (brown square), groundwater samples (blue triangles), and time series stream water samples (June 2017 - June 2018; blue circles).

From the early 1800s, the beginning of industrialization, the Shale Hills catchment and wider region was logged for charcoal production to support the local steel industry (Herndon et al., 2011; Kraepiel et al., 2015). Today, the majority of steel production in the vicinity of the Shale Hills has stopped.

However, recent studies report Mn and Pb enrichments in Shale Hills soils derived from coal burning and iron smelting inputs (Herndon et al., 2011; Herndon and Brantley, 2011; Ma et al., 2014). This anthropogenic activity has resulted in acidic (pH ~5.4) and SO_4 enriched local precipitation (Jin et al., 2011). Nonetheless, a steadily increasing trend in the rain water pH is observed since the early 2000s (NADP, 2020).

As a CZO, extensive prior research at Shale Hills helps support our work. Of most relevance here are insights on carbonate and silicate weathering (Jin et al., 2014, 2011, 2010), oxidative weathering of pyrite (Brantley et al., 2013), water-rock interactions (Herndon et al., 2015a; Sullivan et al., 2016), porosity generation and chemical weathering (Gu et al., 2020), and accumulation of metals in top soils from past coal-burning activities (Herndon et al., 2015b, 2011; Herndon and Brantley, 2011; Kraepiel et al., 2015; Ma et al., 2014). In terms of physical rock degradation, four weathering stages of the Rose Hill shale have been identified: i) soil (hand-augerable material), ii) highly fractured saprock, iii) less fractured saprock and iv) the largely unaltered protolith (Brantley et al., 2013; Jin et al., 2014; Sullivan et al., 2016; Gu et al., 2020). The term saprock describes fractured bedrock that can reach close to the catchment surface. Fracturing has been attributed to frost shattering processes during the last glaciation (Kuntz et al., 2011). Additionally, previous work has attempted a first order estimate of OC_{petro} oxidation, assuming a complete depletion from depth to the surface, returning an estimate of 1.3 mol m^{-2} kyr^{-1}, or 1.5×10^{-2} t C km^{-2} yr^{-1} (Jin et al., 2014). However, the authors noted the considerable uncertainty due to the low OC concentrations in the deep profile and inputs of carbon from the biosphere in the upper profile.

3.3 Materials and Methods

Samples processed and analyzed in this study include archived borehole and soil samples that were previously collected and have been analyzed for a range of elements (Herndon et al., 2011; Brantley et al., 2013; Sullivan et al., 2016). We have undertaken new measurements of Re concentration, total organic carbon concentration, stable carbon isotope composition and radiocarbon activity. In addition, we collected new stream water and groundwater samples (Figure 3.1) and analyzed archived precipitation samples. For these water samples, we present new data on major ion and dissolved Re concentrations.

3.3.1 Materials

3.3.1.1 Borehole sediments and soil samples

Samples were selected from boreholes to capture deeply weathered materials nearer the surface and less weathered samples at depth, using published sulfur concentrations (Brantley et al., 2013; Sullivan et al., 2016) to help guide where we expect oxidative weathering fronts to be located (Figure 3.2). We focused on two boreholes located in the valley ('CZMW2' and 'CZMW10'; Figure 3.1). Borehole CMZW2 (n=11) covers depths between 0.46 m and 16.00 m and captures prominent weathering fronts (Brantley et al., 2013). Deeper samples (7.62 m to 34.90 m) from borehole CZMW10 (n=5) were selected, because they capture a wider zone of alteration below the valley bottom (Figure 3.2A). The boreholes CZMW2 and CZMW10 were drilled less than 5 m distance from another, and are interpreted as a continuous profile. A third borehole CZMW8, located on the South ridge of the catchment (Figure 3.1), has a deeper weathering front, and 8 samples were selected from 0.24 m to 30.63 m in depth (Figure 3.2B).

To examine Re in soils, 4 samples from the upper 50 cm deep soil profile previously collected on the south ridge of the catchment (Figure 3.1) described in Herndon et al. (2011) were selected.

Details of soil and borehole collection methods are provided in previous work (Herndon et al., 2011; Brantley et al., 2013; Sullivan et al., 2016). In summary, the solid samples were air dried and crushed to a fraction size of <150 μm and analyzed for major elements by inductively coupled plasma atomic emission spectroscopy (ICP-AES) at Pennsylvania State University. Total Sulfur (S) concentrations were measured using a LECO Sulfur Coulometer at Pennsylvania State University. Concentration data have been previously published for boreholes CZMW2 and CZMW8 in Brantley et al. (2013) and Sullivan et al. (2016), respectively. We combine these published measurements with sulfur concentrations from CZMW10 measured at Pennsylvania State University and published here (Table 3.1).

3.3.1.2 Water samples

In this study, 11 stream water samples from the catchment outlet gauging station were collected between June 2018 and June 2019. In August 2018, groundwater samples were sampled from wells CZMW2, CMZW8, CZMW6, and wells nr. 9, 11 and 12 (Figure 3.1). Surface water and groundwater samples were collected in clean Nalgene bottles, pre-rinsed with the sample water and immediately filtered through 0.22 μm Millipore filters and transferred into acid-cleaned Nalgene bottles, as per methods previously applied for dissolved Re measurements (Hilton et al., 2014; Horan et al., 2017). All samples used for trace elements and major cations analyses were acidified to pH~2 with HNO_3. An un-acidified aliquot was collected in bottles pre-cleaned with demineralized water and filtered

stream water for anion analysis. Upon return to the laboratory, samples were stored at 4 °C in the dark. In addition, four archived precipitation samples that were collected at SSHCZO in 2013 (July and October) and 2014 (February and October) were analyzed here. The precipitation samples were collected and stored by similar methods.

3.3.2 Geochemical analysis

3.3.2.1 Total organic carbon and its isotopic composition

Solid samples from the boreholes (CZMW2, CZMW8) were analyzed for total organic carbon (TOC) and their stable C isotope ratio (reported as $\delta^{13}C$ relative to VPDB). To remove detrital carbonates from the sample, ~40 mg of a dry sample was weighted into a pre-combusted silver capsule (450 °C for 4 hours) and acidified with 1M HCl, followed by drying of the sample in an oven at 60 °C. To ensure the complete removal of carbonates, each sample was rinsed with 1M HCl three times. The samples were measured on a Sercon ANCA-EA system linked to a Sercon 2022 isotope ratio mass spectrometer (Elemtex, Stable Isotope Analytical Laboratory, Cornwall, UK). Corrections for the procedure and instrumental blanks were applied. The method was validated by measuring the soil standard material NCS-DC73319 for TOC concentration and two international certified synthetic standards, IAEA 600 (caffeine) and IAEA CH3 (cellulose), for $\delta^{13}C$ values. The standard materials were treated in the same way as the samples. The precision of TOC concentrations for the soil standard was 0.19 % (n=6) and the precision for $\delta^{13}C$ values was 0.20 ‰ and 0.15 ‰ for IAEA 600 (n=6) and IAEA CH3 (n=6), respectively (Chapter 2, Section 2.2.1, p29). Replicability on TOC concentrations varied between 3% and 20% of the carbon

mass, reflecting the low TOC concentrations (0.04–0.06 %) and potential for some heterogeneity of the samples.

Radiocarbon measurements were made on nine rock samples from the CZMW8 ridgetop borehole. Crushed samples were acid leached (1M HCl) in pre-combusted glass wear (at 450 °C) in order to remove any carbonate minerals. Samples were centrifuged, rinsed with deionized water, and dried in a 60 °C oven at Durham University, Department of Geography. De-carbonated samples were sent to the National Ocean Sciences Acceleration Mass Spectrometry Facility (NOSAMS) at Woods Hole Oceanographic Institution (WHOI) for ^{14}C analysis. A sample aliquot was combusted at 550 °C in a closed tube to remove contaminate gasses and to graphitize the sample before measuring for radiocarbon and $\delta^{13}C$ following standard procedures via Atomic Mass Spectroscopy (AMS; McNichol et al., 1994). All measurements were corrected for a total procedural blank (combusted quartz sand put through the whole process) according to conventional radiocarbon reporting standards and reported as Fraction modern ($F^{14}C$) as per Stuiver and Polach (1977).

3.3.2.2 Rhenium concentrations in solids

Rhenium concentrations in the borehole solids were measured following acid digestion and anion exchange column chemistry. A detailed description of the methodology can be found in Dellinger et al. (2020) and in Chapter 2, Section 2.2.2.2, p34. The Re solutions were measured on a Thermo Scientific Neptune Plus at Durham University, Department of Earth Sciences. A range of standard reference materials were digested in each batch to validate the method, a marine sediment (MAG-1), basalt (BHVO-2, BCR-2), and serpentinite (UB-N), which returned values for this study in close agreement (<15%) with previously

published data (Jochum et al., 2016; Meisel and Moser, 2004) and with long-term in-house reproducibility better than 10% (Dellinger et al., 2020).

3.3.2.3 Major and trace elements in waters

Major ions (Cl^-, SO_4^{2-}, Na^+, K^+, Ca^{2+}, Mg^{2+}) in water samples were determined by ion chromatography using a Thermo Scientific Dionex ICS 6000 at Durham University, Department of Geography. The data were validated by analyzing a certified river water reference standard material (Sangamon–03). The difference between our measurements and certified reference material values for all major elements was <5% (n=3). The analytical precision determined by running replicates on selected samples was <3% (n=5) for all reported major ions (Chapter 2, Section 2.2.4.1, p37)

Concentrations of dissolved Re and other trace metals were determined using Agilent Technologies 7900 inductively coupled plasma mass spectrometer (ICP-MS) at Durham University, Department of Geography. A multi-element standard solution was prepared to cover the expected range of trace elements in river waters (0.3–70 ng l^{-1} for Re), creating a 7-point calibration line. To correct for any potential matrix effect, an internal standard containing a mixture of Sc, Tb, Rh, In, Bi, and Ge was added to each acidified river water sample. The detection limit defined as 3 standard deviations of the replicate measurements of a blank solution was 0.01 ppt for Re. Repeated measurements of the river water standard sample SLRS-5 for Re are 64.6±6.1 ppt (±1SD, n=6) and 10- and 100-times dilutions are 6.2±0.7 ppt (±1SD, n=6) and 0.63±0.1 ppt (±1SD, n=6), respectively. Our measurements are in agreements with the long-term in-house reproducibility, that is SLRS-5 = 63.0±3.5 ppt (±1SD, n=24), SLRS-5×10 = 6.2±0.3 ppt (±1SD, n=21), and SLRS-5×100 = 0.61±0.1 ppt (±1SD,

n=35), and with Re concentrations for SLRS-5 reported in literature: 66±12 ppt (Yeghicheyan et al., 2013).

3.3.3 Calculation of a mass transfer coefficient (τ)

In the borehole sediments and top soils, a mass transfer coefficient (Tau - τ) was calculated to characterize the mobility of S, TOC, and Re during weathering. The coefficient tau (τ) describes a gain or loss of an element relative to the parent material by applying Equation 3.1 (Brimhall and Dietrich, 1987; Brantley et al., 2013).

$$\tau_{i,s} = \frac{C_{j,s}\, C_{i,p}}{C_{j,p}\, C_{i,s}} - 1 \qquad (3.1)$$

Here C is the concentration of the mobile element (j) or immobile element (i) in the protolith (p) or soil/saprock (s) material. The approach assumes that composition of the protolith is homogeneous and that the species (i) is immobile through the weathering profile. A negative τ value describes a relative depletion of an element compared to the parent material. We use Ti as the immobile element because previous work suggest little variability within the catchment (Gu et al., 2020; Herndon et al., 2015b).

3.4 Results

3.4.1 Solid samples

3.4.1.1 Sulfur concentration from published research

The depletion of S in the borehole samples provides insight on oxidative weathering at Shale Hills (Brantley et al., 2013; Sullivan et al., 2016). Here we summarize previous work for context. In the valley (CZMW2, CZMW10), the S concentrations are low from the surface through the weathered saprock to depths of ~6 m, with a mean S of 0.005±0.002 % (n=17, ±1SD; Brantley et al., 2013). An increase in S concentration at ~6 m is observed and S tends to increase with depth, to reach a mean S concentration of 0.11±0.05 % in the protolith (n=43, ± 1SD; Figure 3.2A). On the ridge, the weathered saprock extends deeper, to ~16 m and has a mean S of 0.02±0.03 % (n=10, ±1SD; Sullivan et al., 2016). Beneath the S-depleted layers, a sharp increase in S concentrations from 0.001 % to 0.14 % is observed between 16.0 m and 16.4 m depth. The increase in S concentration is consistent with decrease of saprock fracturation (Figure 3.2). Thin section observations have shown that the main S-bearing mineral is pyrite, meaning that S-depletion front coexists with pyrite depletion front in this setting (Brantley et al., 2013; Sullivan et al., 2016).

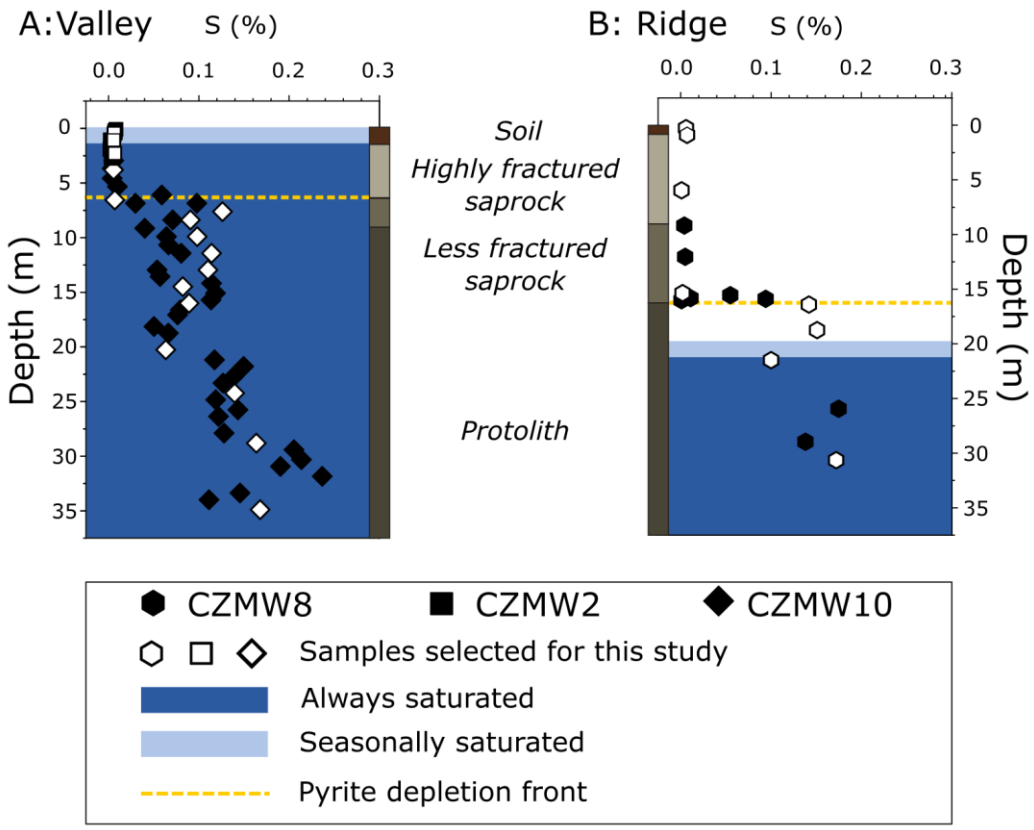

Figure 3.2: Previously published sulfur (pyrite) depletion profiles from the SSHCZO. A: Boreholes CZMW2 (Brantley et al., 2013) and CZMW10 (S data published here) located in the valley **B:** Borehole CZMW8 located on the ridge (Sullivan et al., 2016). Depths of changes in the weathered material structure, pyrite depletion front, and approx. groundwater depths are taken from Gu et al. (2020). Black symbols represent samples which have been previously analysed for major elements and sulfur at Penn State University. White symbols are samples selected in this study to track changes in TOC and Re concentration.

3.4.1.2 Total organic carbon and its isotopic composition

The TOC concentrations are highest in the surface soil, with 0.14 % and 0.32 % measured in the valley (0–1.07 m; CZMW2) and 0.41 % measured on the ridge (0–0.27m; CZMW8). Lower TOC concentrations are found in the weathered saprock, with values of 0.06 % and 0.07 % (2.29–6.55 m) in the valley and between 0.03 % and 0.09 % on the ridge (0.88–15.36 m) (Figure 3.3, Table 3.1). The TOC concentrations of the deeper protolith samples are similar to those of the saprock samples. On the ridge (CZMW8), TOC in the protolith varies between

0.04 % and 0.07 %. In the valley, TOC concentrations in the protolith are similar, between 0.03 % and 0.05 %. The TOC values are close to those reported by Jin et al. (2010, 2014) for surface soils (1.8 %) and the protolith (0.03–0.05 %) sampled in borehole DC1, which is located on the North ridge of the Shale Hills catchment, opposite from the CZMW8 (Figure 3.1).

The stable carbon isotopic composition of the organic carbon ($\delta^{13}C$) varies by up to ~2 ‰, but does not show any systematic variation between the soil, saprock and protolith samples, in both boreholes CZMW2 (-26.3 ‰ to -24.4 ‰, with a mean $\delta^{13}C$=-25.7 ± 0.6 ‰) and CZMW8 (-27.0 ‰ to -26.2 ‰, mean $\delta^{13}C$=-26.6 ± 0.3 ‰) (Figure 3.3, Table 3.1). These values are similar to $\delta^{13}C$ values of soils (-25.8 ‰ to -25.3 ‰) and protolith samples (-27.1 ‰ to -25.9 ‰) previously published for Shale Hills in Jin et al. (2014). However, the $\delta^{13}C$ values of the organic carbon in the borehole samples cannot be distinguished from the isotopic signature of the modern forest cover (~26 ‰) (Jin et al., 2014).

The radiocarbon activity, reported as Fraction modern ($F^{14}C$), was measured on nine samples from CZMW8 ridgetop borehole. The $F^{14}C$ measurements vary between 0.91±0.005 in the surface soil, to 0.24±0.003 in the saprock, at 15.36 m depth (Figure 3.3, Table 3.1). The high $F^{14}C$ measured in the top soil is consistent with expectations, that the radiocarbon signature can be dominated by modern (biospheric) inputs, resulting in a $F^{14}C$ value close to 1 (Trumbore, 2009). Within the saprock, lower $F^{14}C$ values are consistent with some input of OC_{petro} from the Silurian Rose Hill formation that was deposited ~443–416 million years ago ($F^{14}C$ value=0 within precision). However, the presence of ^{14}C, with $F^{14}C$ between 0.26±0.003 and 0.32±0.003 in the deep

profile, suggests potential aging of modern OC and/or percolating of modern C into the deepest samples (see Section 3.5.1 for discussion).

3.4.1.3 Rhenium concentrations

The protolith samples (below ~6 m) under the valley (CZMW2 and CZMW10) have the highest Re concentrations, with a range of values between 0.10 ppb and 0.42 ppb and a mean value of 0.19±0.11 ppb (n=11, ±1SD; Figure 3.3). These are similar to Re concentrations for the protolith under the ridge (below ~16 m in CZMW8) varying between 0.11 ppb to 0.23 ppb, with a mean value of 0.16±0.06 ppb (n=4, ± 1SD) (Figure 3.3, Table 3.1). The Re concentrations in the Shale Hills protolith are more than 100-times lower than those measured in black shale weathering profiles from the US (Jaffe et al. 2002) and Nepal (Pierson-Wickmann et al., 2002), but similar to those from river bed material in the western Southern Alps of New Zealand (0.12±0.02 ppb), which is derived from an OC-poor (TOC ~0.13±0.01 %) metamorphized greywacke (Horan et al., 2017).

In the valley, Re is depleted in the weathered saprock (2.29–6.54 m) to between 0.02 ppb and 0.03 ppb (Figure 3.3). Similar Re concentrations are measured in saprock under the ridge (0.88–16.0 m). The pattern of Re depletion is broadly spatially consistent with the S depletion profiles at Shale Hills (Figure 3.2; Brantley et al., 2013; Sullivan et al., 2016; Gu et al., 2020) and is consistent with weathering profiles developed on black shales (Jaffe et al., 2002; Pierson-Wickmann et al., 2002), despite the large differences in Re concentration between these sites. A slight increase in Re concentration towards the surface soil is measured in both boreholes (0.06 ppb and 0.05 ppb, under the valley and ridge, respectively) and in the 50 cm deep ridgetop soil profile (Figure 3.3-inlet Soil

profile). The highest Re concentration of 0.12 ppb is measured in the top soil sample (0–5 cm), which decreases to 0.01 ppb at 42.5 cm depth.

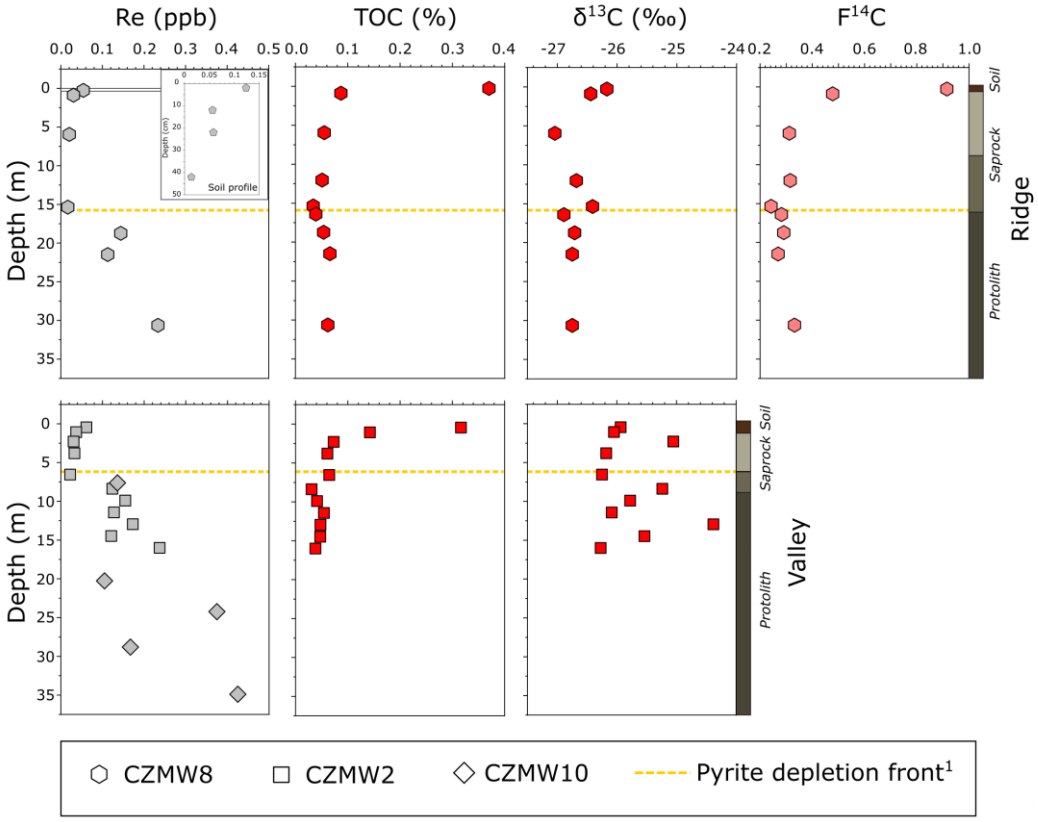

Figure 3.3: Rhenium (Re), total organic carbon (TOC), stable carbon isotope ($\delta^{13}C$) and fraction modern ($F^{14}C$) variation with depth. Borehole sediments sampled from the catchment ridge (CZMW8) and valley (CZMW2 and CZMW10) and soil profile sampled next to the CZMW8 (Figure 3.1). The yellow line on all plots shows the pyrite depletion front (Brantley et al., 2013; Sullivan et al, 2016). The bars to the right of the plot show approx. depths of structural changes due to chemical and physical degradation of the protolith.

3.4.1.4 Mass transfer coefficient

To assess the loss or gain of elements during weathering, the composition of the parent material (i.e. protolith, or least weathered material) has to be characterized. At Shale Hills, this is not straightforward due to potential heterogeneity of the parent material over the deep weathering zone (Brantley et al., 2013; Gu et al., 2020) and due to the role of deep fractures that have additional weathering depletion (Gu et al., 2020). Here the deepest sample

is used to characterize the parent material. For S, this concentration is within ±1SD of the parent material previously presented by Brantley et al. (2013) and Sullivan et al. (2016).

The calculated tau values reveal similar patterns in both boreholes (Figure 3.4), with nearly complete loss of S from the top ~6.5 m under the valley (τ_S=-0.95±0.08; mean±1SD) and from the top ~16 m under the ridge (τ_S=-0.89±0.19; mean±1SD), agreeing with results reported by previous work (Brantley et al., 2013; Sullivan et al., 2016; Gu et al., 2020). The tau values for Re loss are less negative than S, but still show substantial depletion in the valley (τ_{Re}=-0.84 to -0.93) and under the ridge (τ_{Re} =-0.77 to -0.92). The depletion profiles reveal a reaction front, which is close to the S depletion front (Figure 3.4). The tau values of Re increase in the upper-most samples from both boreholes, which is explored in more detail by the surface soil samples (Figure 3.4–inlet Soil profile). Tau values in the soil profile are negative in the top 45 cm, due to lower Re concentration in soils compared to the protolith samples (0.23 ppb at 30.6 m). However, tau values increase towards the surface from - 0.97 (42.5 cm) to -0.72 (top 5 cm), suggesting an addition profile. There is TOC accumulation in the top meter of the profile under the valley (τ_{TOC}=+8.3 and +3.0) and in the top 0.27 m under the ridge (τ_{TOC}=+5.11). For the ridge profile, TOC shows a net decrease in tau between 21.49 m 15.36 m and, with a minimum value of τ_{TOC}=-0.48 (Figure 3.4). This loss tracks the depths of the Re loss profile. A less pronounced decrease is observed in borehole under the valley, with the most depleted sample having τ_{TOC} of -0.14 at 8.38 m depth.

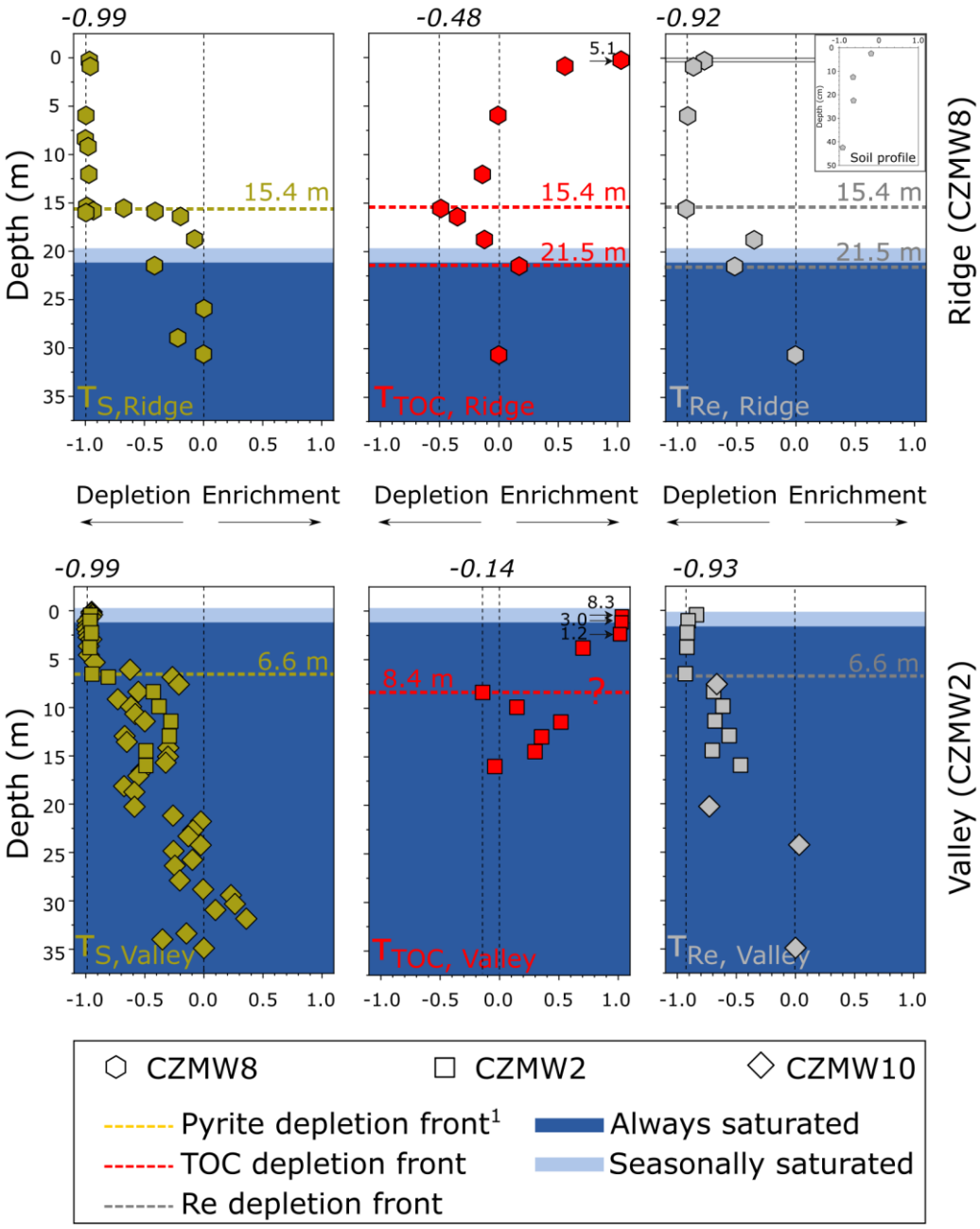

Figure 3.4: Mass transfer coeficient tau (τ) versus depth for boreholes CZMW2 (valley) and CZMW8 (ridge). The parent composition was determined from the concentration measured on the deepest protolith sample in the CZMW8 and CZMW2+CZMW10, respectively. [1]Data and interpretation of the S depletion front is from Brantley et al, 2013 (CZMW2) and Sullivan et al., 2016 (CZMW8). The vertical stippled line at negative τ represents the most depleted sample and the vertical stippled line at τ=0 represents the parent material.

Table 3.1. Geochemistry of the borehole samples at Shale Hills. Published and unpublished sulfur concentrations alongside new measurements made in this study of total organic carbon (TOC), stable carbon isotope ($\delta^{13}C$), radiocarbon activity ($F^{14}C$), and rhenium (Re) in the studied borehole profiles. Determination of OC_{petro} concentration and uncertainty bounds are discussed in Section 3.5.1

Borehole	Sample Depth (m)	Material type	$\delta^{13}C$ ‰	TOC (%)	$F^{14}C$	OC_{petro} (%)	OC_{petro} +1σ	OC_{petro} -1σ	Re (ppb)	S (%)	Reference for S (%)
CZMW8	-0.27	*Soil*	-26.2	0.37	0.91 ± 0.005	0.03	0.05	0.01	0.05	0.006	Sullivan et al., 2016
	-0.88	*Saprock*	-26.4	0.09	0.47 ± 0.003	0.03	0.04	0.02	0.03	0.007	Sullivan et al., 2016
	-5.94	*Saprock*	-27.0	0.06	0.30 ± 0.003	0.03	0.03	0.02	0.02	0.001	Sullivan et al., 2016
	-12.04	*Saprock*	-26.7	0.05	0.31 ± 0.003	0.03	0.03	0.02	-	0.005	Sullivan et al., 2016
	-15.36	*Saprock*	-26.4	0.03	0.24 ± 0.003	0.02	0.02	0.02	0.02	0.002	Sullivan et al., 2016
	-16.40	*Protolith*	-26.9	0.04	0.27 ± 0.003	0.02	0.02	0.02	-	0.142	Sullivan et al., 2016
	-18.75	*Protolith*	-26.7	0.05	0.28 ± 0.003	0.03	0.03	0.02	0.14	0.122	Sullivan et al., 2016
	-21.49	*Protolith*	-26.8	0.07	0.26 ± 0.003	0.04	0.04	0.03	0.11	0.100	Sullivan et al., 2016
Parent	-30.36	*Protolith*	-26.8	0.06	0.32 ± 0.003	0.03	0.04	0.02	0.23	0.172	Sullivan et al., 2016
CZMW2	-0.46	*Soil*	-25.9	0.32	-	-	-	-	0.06	0.006	Brantley et al., 2013
	-1.07	*Soil*	-26.0	0.14	-	-	-	-	0.04	0.006	Brantley et al., 2013
	-2.29	*Saprock*	-25.1	0.07	-	-	-	-	0.03	0.007	Brantley et al., 2013
	-3.81	*Saprock*	-26.2	0.06	-	-	-	-	0.03	0.006	Brantley et al., 2013
	-6.55	*Saprock*	-26.2	0.06	-	-	-	-	0.02	0.007	Brantley et al., 2013
	-8.38	*Saprock*	-25.2	0.03	-	-	-	-	0.12	0.091	Brantley et al., 2013
	-9.91	*Protolith*	-25.8	0.04	-	-	-	-	0.15	0.098	Brantley et al., 2013
	-11.43	*Protolith*	-26.1	0.05	-	-	-	-	0.13	0.114	Brantley et al., 2013
	-12.96	*Protolith*	-24.4	0.05	-	-	-	-	0.17	0.110	Brantley et al., 2013
	-14.48	*Protolith*	-25.5	0.05	-	-	-	-	0.12	0.082	Brantley et al., 2013
	-16.01	*Protolith*	-26.3	0.04	-	-	-	-	0.24	0.089	Brantley et al., 2013
CZMW10	-7.62	*Saprock*	-	-	-	-	-	-	0.14	0.126	this study
	-20.27	*Protolith*	-	-	-	-	-	-	0.10	0.063	this study
	-24.23	*Protolith*	-	-	-	-	-	-	0.37	0.140	this study
	-28.80	*Protolith*	-	-	-	-	-	-	0.17	0.164	this study
Parent	-34.90	*Protolith*	-	-	-	-	-	-	0.42	0.168	this study

3.4.2 Water samples

3.4.2.1 Stream water chemistry

Major ions in the Shale Hills stream are relatively dilute, compared to large world rivers (Gaillardet et al., 1999). The dissolved load is dominated by Ca^{2+}, with a mean value of 205±83 μmol l^{-1} (all stream waters: n=11, ± 1SD, unless otherwise stated). Mg^{2+}, Na^{+}, and SO_4^{2-} concentrations are lower, with a mean value of 88±21 μmol l^{-1}, 28±5.6 μmol l^{-1} and 80±6.6 μmol l^{-1}, respectively. The stream water chemistry is consistent with data collected at Shale Hills between 2006 and 2011, discussed in Herndon et al. (2015a). The major ions show a broad dilution trend with increased discharge, albeit one with less constraint at high flow (Figure 3.5A – example for SO_4^{2-}). Dissolved Re concentrations show less variation than the major ions (Figure 3.5B), with values between 3.8 pmol l^{-1} and 5.5 pmol l^{-1}, and a mean of 4.3±0.6 pmol l^{-1}. These values are towards the lower end of published values for dissolved Re concentrations in river water (Hilton et al., 2014; Horan et al., 2019, 2017; Miller et al., 2011). No clear trend is observed between Re concentration measured in stream water and discharge (Figure 3.5B), while the highest Re concentration (5.5 pmol l^{-1}) is measured at the highest discharge (20 l s^{-1}).

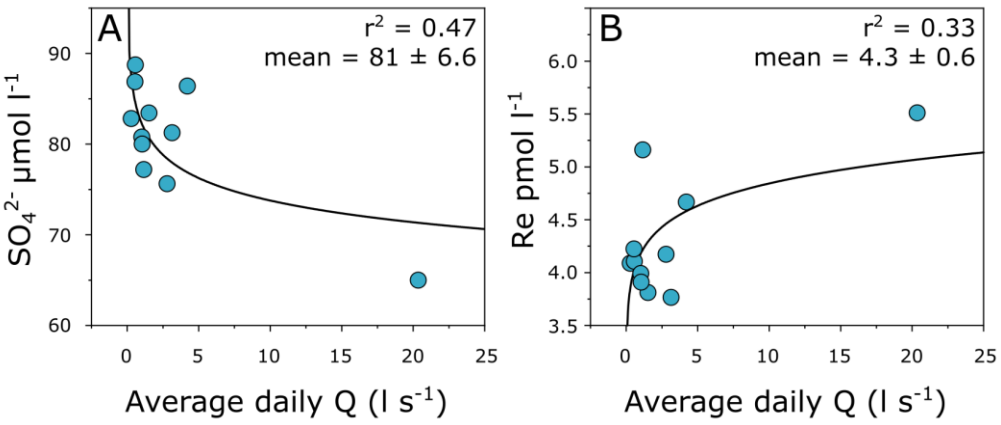

Figure 3.5: Discharge-concentration (Q-C) relationship for SO_4^{2-} and Re. The black line is a power law regression fit to all samples (n=11). The fit for each element is described by correlation coefficient (r^2).

3.4.2.2 Groundwater and precipitation chemistry

In agreement with previous work on major ions (Jin et al., 2014), groundwater is more concentrated in Na^+, Ca^{2+}, and Mg^{2+} ions compared to stream water (Table 3.2). In contrast, the mean SO_4^{2-}concentration in groundwater (76±30 µmol l^{-1}) is similar to values measured in the stream. Rhenium concentrations in groundwater samples show a larger range (1.3–10.0 pmol l^{-1}). The highest Re concentrations were measured in two wells located in the valley, of 6.3 pmol l^{-1} and 10.0 pmol l^{-1} for CZMW2 and Well 11 (Figure 3.1), where the level of the water table was aligned with the stream water level, indicating a groundwater contact with Re-rich surface soils. The Re concentration in the four precipitation samples analyzed in this study ranged between 0.4 pmol l^{-1} and 3.0 pmol l^{-1}, with a mean value of 1.3±1.1 pmol l^{-1} (n=4; ±1SD). The highest Re concentration in precipitation samples is similar to those measured in stream water. These values are in agreement with the values reported for rainwater Re from Falmouth, Massachusetts, on the East coast of the US, which range between 0.03 pmol l^{-1} and 5.9 pmol l^{-1} (Miller et al., 2011).

Table 3.2. Dissolved load chemistry at Shale Hills. Major ions and Re on stream water, groundwater and precipitation samples. Major ions on the precipitation samples are from NADP database (NADP, 2020) obtained in the same week as the samples analyzed for Re.

Sample Name	Sampling Date	Sample type	Location	Average discharge $m^3\ day^{-1}$	Cl^- µmol	SO_4^{2-} µmol	Na^+ µmol	K^+ µmol	Mg^{2+} µmol	Ca^{2+} µmol	Re pmol
SH18-04	19/08/2018	*Stream water*	Gauging station	100	21	77	30	28	101	242	5.2
SH 20-06-18	20/06/2018	*Stream water*	Gauging station	24	23	83	40	29	131	332	4.1
SH 03-08-18	03/08/2018	*Stream water*	Gauging station	1760	16	65	20	26	53	57	5.5
S19-1	06/02/2019	*Stream water*	Gauging station	241	20	76	25	25	69	101	4.2
S19-2	27/02/2019	*Stream water*	Gauging station	132	17	83	25	22	79	146	3.8
S19-3	13/03/2019	*Stream water*	Gauging station	363	18	86	23	20	74	292	4.7
S19-4	31/03/2019	*Stream water*	Gauging station	49	18	89	29	22	97	243	4.1
S19-5	17/04/2019	*Stream water*	Gauging station	271	16	81	23	23	73	149	3.8
S19-6	01/05/2019	*Stream water*	Gauging station	47	19	87	33	25	104	256	4.2
S19-7	23/05/2019	*Stream water*	Gauging station	89	18	81	28	25	94	218	4.0
S19-8	03/06/2019	*Stream water*	Gauging station	91	18	80	28	25	91	212	3.9
SH18-02	19/08/2018	*Groundwater*	Well nr. 11	-	28	80	40	29	86	69	10.0
SH18-05	19/08/2018	*Groundwater*	CZMW2	-	29	132	296	17	214	1028	6.3
SH18-10	20/08/2018	*Groundwater*	Well nr. 09	-	25	78	43	35	99	97	4.9
SH18-12	20/08/2018	*Groundwater*	Well nr. 12	-	37	47	162	37	504	330	1.3
SH18-11	20/08/2018	*Groundwater*	CZMW8	-	20	64	31	25	49	39	3.6
SH18-13	20/08/2018	*Groundwater*	CZMW6	-	23	54	29	36	270	257	4.5
Rain 10/07/13	07/10/2013	*Rain*	-	-	1.3	4.5	0.9	2.6	0.7	1.1	0.4
Rain 2014/10/23	23/10/2014	*Rain*	-	-	1.0	19.2	0.2	0.2	0.5	1.9	3.0
Rain 7/1/13	01/07/2013	*Rain*	-	-	1.0	7.8	0.3	0.3	0.4	1.6	1.0
Snow 02/07/14	07/02/2014	*Snow*	-	-	2.1	3.9	0.7	0.2	0.2	0.7	0.7

3.5 Discussion

The borehole sediments from Shale Hills display notable Re loss profiles (Figure 3.4), with a reaction front which broadly coincides with that of pyrite (S) loss. Directly assessing the location of the OC_{petro} reaction front is more challenging, with clear evidence for OC inputs in the near surface and saprock (Figure 3.4). Here we use radiocarbon to characterize OC_{petro} distribution in more detail, and examine its behavior alongside the sulfide oxidation front (Brantley et al., 2013; Sullivan et al., 2016). We also assess the mobility of Re in the deep weathering zone, and seek to quantify the long-term Re and OC_{petro} oxidation rates. Finally, we discuss the enrichment of Re in the near surface soils, stream water and precipitation, in the context of anthropogenic inputs of Re in a low erosion rate setting.

3.5.1 Evidence for OC_{petro} loss during weathering

The borehole profiles of TOC and τ_{TOC} contain information on OC_{petro} loss, and show a depletion of TOC coincident with the Re and S reaction fronts (Figure 3.3 and Figure 3.4). Because the TOC concentration in the Rose Hill shale is low (Table 3.1, Jin et al., 2014), the contribution of OC_{bio} needs to be assessed carefully. Unfortunately, the stable isotopic composition of the TOC is not helpful in this regard, showing no systematic variation between the soil, saprock, and protolith (Figure 3.3) and so not providing an indication of the source of OC.

Instead, we can use the radiocarbon activity ($F^{14}C$) of the bulk organic matter in the ridgetop borehole (CZMW8) sediments (Figure 3.3). However, we find no fully ^{14}C-depeleted sample (Figure 3.3), and thus require a source of OC that contains radiocarbon. The most ^{14}C-enriched source in the catchment is

recent organic matter formed by photosynthesis ($F^{14}C \sim 1$). The surface sample composition ($F^{14}C = 0.91$) can be explained by input from modern OC_{bio}. In a deep weathering profile such as the one studied here, there may be additional ^{14}C-depeleted inputs, and these need to be considered to assess OC_{petro} contributions.

The aging of plant-derived organic matter lowers $F^{14}C$ (e.g. a $F^{14}C$ value of 0.7 corresponds to 2,865 radiocarbon years). This could partly explain the ^{14}C-depletion of the sample at 0.88 m depth ($F^{14}C = 0.47$). The transport of this modern or aged OC into the saprock could occur as dissolved OC (DOC), percolating downwards from the surface via flow pathways through the saprock (Marin-Spiotta et al., 2011), or it could be associated with colloidal transport (Yan et al., 2018). An additional source of ^{14}C could be from the dissolved inorganic carbon (DIC) pool, which can derive from a mixture of atmospheric CO_2 and carbonate mineral weathering (Jin et al., 2014), producing a $F^{14}C$ between 0.5 and 1.0. This would have to be used by microbes at depth, perhaps under saturated conditions during SO_4^{2-} reduction (Schwab et al., 2019). Considering the uncertainties that come from these multiple pathways for ^{14}C addition, we assume that the bulk OC pool is a mixture between OC_{petro} ($F^{14}=0$) and an ^{14}C-enriched pool (Blair et al., 2003; Galy et al., 2008; Hemingway et al., 2018). The $F^{14}C$ values of the enriched pool can be between 1.1 (potential bomb ^{14}C inputs) to 0.5 (potential aged DOC and DIC inputs). This range is used for each sample with a Monte Carlo simulation (1,000-times per sample) to return OC_{petro} concentration values, reported as the 50% (median), +1σ (84.1%) and -1σ (15.9%) percentile of these predicted OC_{petro} values (Figure 3.6, Table 3.1).

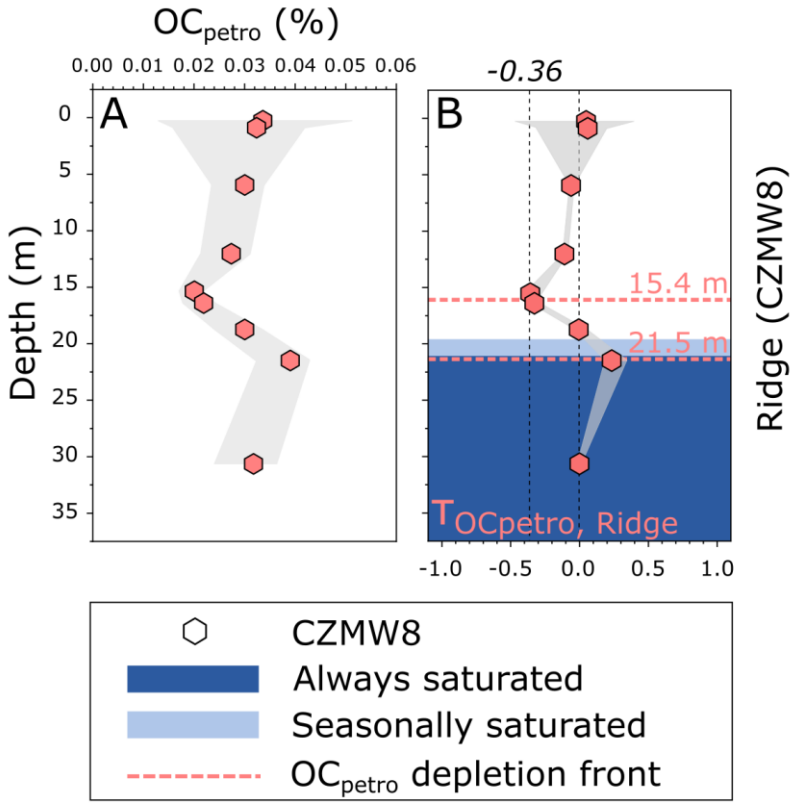

Figure 3.6: OC_{petro} concentrations and a depletion profile for the ridgetop borehole. A: The median OC_{petro} concentrations based $F^{14}C$ activity and binary mixing model, versus depth. The symbols represent the median value and the grey shading ±1 sigma (σ). B: Mass transfer coefficient tau calculated for OC_{petro} concentrations ($\tau_{OCpetro}$) versus depth for borehole CZMW8 (ridge).

The least well constrained OC_{petro} content values are from the top most samples of the profile, with values between 0.012 % and 0.051 %. These correspond to a $\tau_{OCpetro}$ value varying between +0.40 and -0.47. This uncertainty comes from the modest ^{14}C-depeletion, which could be explained by very little OC_{petro} addition (i.e. biospheric OC aging), and because the OC_{petro} contents are low compared to the %TOC values (Figure 3.3). It is likely that the approach here over-estimates OC_{petro} in the upper most sample. With increasing depth OC_{petro} concentration is better constrained. Between 21.5 m and 15.4 m there is a distinct decrease in OC_{petro}, from 0.039 % to 0.024 % (Figure 3.6A). The corresponding

$\tau_{OC_{petro}}$ decreases from +0.19 to -0.36 (Figure 3.6B), signaling OC_{petro} weathering front.

Despite the very low OC_{petro} contents of the protolith at Shale Hills, and the challenges of applying ^{14}C as a proxy for its input, there is evidence for an OC_{petro} reaction front. Future work could unpack OC inputs and C cycle processes using the ramped pyrolysis oxidation (RPO) coupled to radiocarbon technique, to isolate OC with different thermal reactivity (Grant et al., 2019; Hemingway et al., 2017). Here, we turn to the loss of Re to better constrain oxidative weathering processes and fluxes at Shale Hills.

3.5.2 Rhenium source and mobility during oxidative weathering

3.5.2.1 Re/TOC and Re/OC_{petro} ratios in the protolith

The Re/TOC and Re/OC_{petro} ratios of the deep, least weathered (i.e. protolith) samples can provide information on the association of Re and its host at the Shale Hills site. We focus on samples collected below ~16 m in the ridgetop borehole (where we have ^{14}C and OC_{petro} estimates) and below ~6.5 m under the valley (where we only have %TOC). The Re/TOC ratios range between 1.6×10^{-7} g g^{-1} and 62×10^{-7} g g^{-1}. The Re/OC_{petro} ratio varies between 2.9×10^{-7} g g^{-1} and 74×10^{-7} g g^{-1}.

The Re/TOC and Re/OC_{petro} ratios determined at Shale Hills is within range of the numerous previous studies, which include black shales, and metamorphosed sediments (Figure 3.7). In terms of TOC concentrations, the Shale Hills lithology is more than two orders of magnitude lower than some previous studies on black shales (Jaffe et al., 2002; Peucker-Ehrenbrink and Hannigan, 2000; Ross and Bustin, 2009). The TOC concentrations at Shale Hills are most similar to bed load samples collected from catchments in New Zealand's

Southern Alps (Horan et al., 2017), which also show comparable Re/TOC ratios. These observations could suggest OC_{petro} is a common host-phase for most of the Re in these samples.

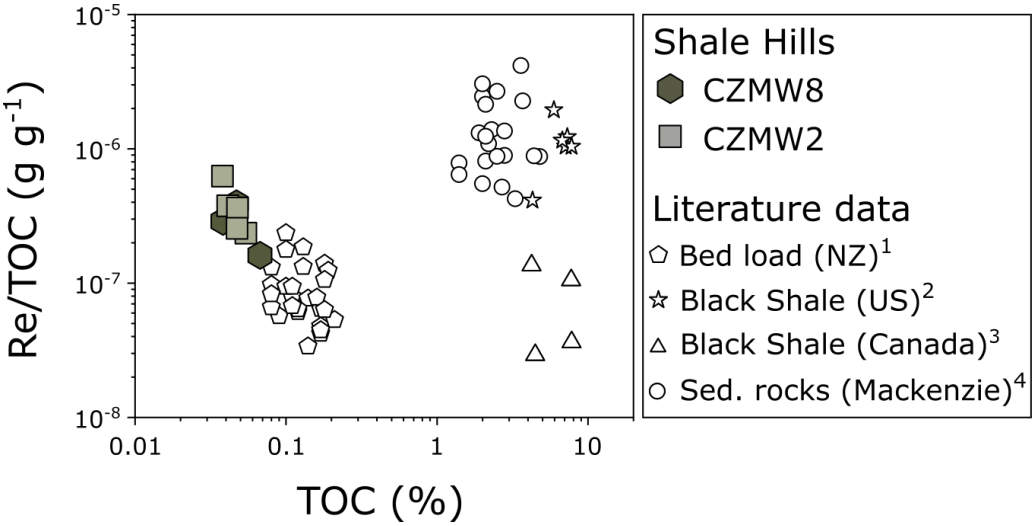

Figure 3.7: Assessment of the Shale Hills Re/TOC rations across different sedimentary environments. The Re/TOC ratios in protolith samples from Shale Hills (CZMW2, CZMW8) are compared to ratios obtained on bed load sediments in New Zealand's Southern Alps [1]Horan et al. (2017), Devonian black shales from Clay City, US [2]Jaffe et al. (2002), Silurian black shales from Quebec [3]Peucker-Ehrenbrink and Hannigan (2000), and a series of sedimentary rocks from the Mackenzie River basin [4]Ross and Bustin (2009).

To explore this further, we turn to the ratio of Re to Na and S, which has been previously applied to quantify the role of sulfide and silicate-derived Re (Horan et al., 2019). Generally, it is expected that Re concentrations in silicate and sulfide minerals will be low, resulting in low Re/Na ratios for silicates, and low Re/S ratios for sulfides (Peucker-Ehrenbrink and Hannigan, 2000; Miller et al., 2011). In contrast, Re enrichment associated with OC can increase Re/Na and Re/S ratios (Das et al., 2012). Here we use end-member compositions for the sulfides (Re/S~0.0006 pmol/μmol; Horan et al., 2019) and silicates (Re/Na = 2.4×10^{-4} to 2.2×10^{-3}; Dellinger et al., in prep.; Dalai et al., 2002) to assess Re sourced from OC_{petro}. There is a large uncertainty on these compositions, in

particular for the sulfide end-member. The mixing model and end-member composition will be re-assessed in Chapter 4 of this thesis. The three-component mixing model (Figure 3.8) suggests that in the protolith samples at Shale Hills, Re is largely associated with OC_{petro}, having a range of values between 81% and 93% and a mean value of 83±5.5% (± 1SD n=13).

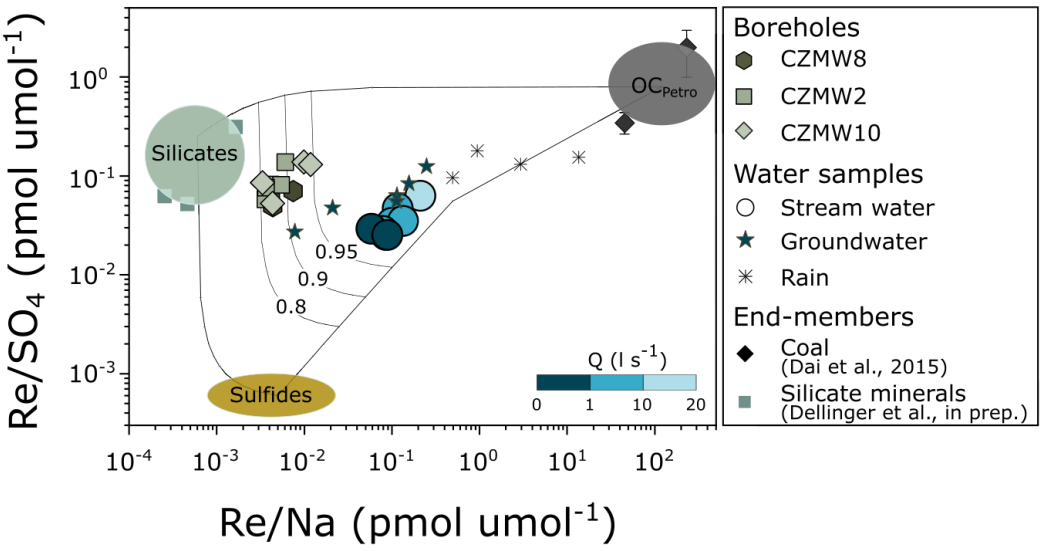

Figure 3.8: Assessing the source of Re in solids and water samples from the Shale Hills catchment. A mixing space defined by rhenium to sodium versus rhenium to sulfur ratios is used to determine the end-member composition in OC_{petro}, coal (Dai et al., 2015), silicate minerals (Dellinger et al., in prep.) and sulfides (Horan et al., 2019).

3.5.2.2 Loss of Re, S, and OC_{petro} through weathering

The ridgetop borehole (CZMW8) shows broadly coincidental loss of S, OC_{petro} and Re at 15.36 m (Figure 3.4 and Figure 3.6). However, the pyrite oxidation (S loss) front is much sharper, with an abrupt change in τ_S from -0.99 to -0.19 over a short vertical distance of 0.4 m. The depletion profiles of OC_{petro} across the weathering front appears more steadily (Figure 3.6), with $\tau_{OCpetro}$ values from -0.36 to +0.19 occurring over a longer vertical distance of ~6 m. The number of samples for Re at this depth make the comparison harder, but the Re loss profile looks similar

(i.e. broad reaction front) to the OC_{petro} profile (Figure 3.4). This is consistent with our assessment that ~83 % of the Re is associated with OC_{petro}. The decoupling of S from OC_{petro} and Re is also clear in the tau values of saprock samples. In the ridgetop borehole, there is a nearly complete depletion of S (τ_S ~-0.99), but τ_{Re} varies between -0.77 and -0.93. If ~80 % of the Re is hosted OC_{petro}, this would suggest a $\tau_{OCpetro}$ of between -0.6 and -0.7. At the reaction front, $\tau_{OCpetro}$ is -0.36. The higher tau value for OC_{petro} could partly reflect the uncertainty in its quantification, for which we may be overestimating OC_{petro} concentration using the ^{14}C-mixing model approach (Section 3.5.1).

The patterns in the data could also come about by incomplete OC_{petro} oxidation. Metamorphic alteration of the studied shale (Gu et al., 2020) could thermally mature the organic matter in the rock, potentially making the OC in the rock more resistant to weathering (Petsch, 2014). Un-weathered, graphitized organic matter has been found in river sediments of the Amazon and Ganges rivers, leading the authors to suggest that high-temperature alternation of organic matter in bedrock makes it resistant to weathering and oxidation (Bouchez et al., 2010; Galy et al., 2008). Alternatively, association of OC_{petro} or its weathered products with clay minerals may protect them from further oxidation (Hemingway et al., 2019). For Re, an additional factor could be the presence of Re in silicate phases. Incomplete and more gradual weathering fronts have been described for Na, Mg, and K, which represent chlorite and plagioclase silicate minerals in the studied boreholes CZMW2 and CZMW8 (Gu et al., 2020).

The decoupling of S loss from OC_{petro} and Re loss has been previously observed in black (Ohio) shale weathering profile (Jaffe et al., 2002). There, the S oxidation front was at least 3 m deeper than the coupled Re and OC oxidation.

The shift in S and OC_{petro} oxidation fronts can reflect the more rapid reaction kinetics of pyrite (Georgiev et al., 2012; Petsch et al., 2000). Indeed, at Shale Hills the oxidation of pyrite minerals plays a crucial role in subsequent oxidative weathering and acid hydrolysis reactions (Brantley et al., 2013). This is because pyrite oxidation produces sulfuric acid, that can dissolve both carbonates and clay minerals, resulting in increased pore space in the weathered matrix (Gu et al., 2020). After pyrite is completely exhausted from the saprock, oxygen can more effectively enter through the new porosity, reacting with the remaining rock matrix (Jin et al., 2010; Brantley et al., 2013; Gu et al., 2020) and resulting in OC_{petro} and Re oxidation.

3.5.3 Long-term OC_{petro} oxidation rates

The depletion of OC_{petro} and Re in the borehole samples can be used to quantify the long-term OC_{petro} oxidation rates, and by inference, calculate the release of CO_2 from the lithosphere due to weathering at this site. As the radiocarbon activity of the samples show evidence for OC_{petro} loss at a deep weathering front, we can use this to estimate corresponding CO_2 release over the timescales of weathering front formation (Equation 3.2).

$$J_{OCpetro} = \omega \times \frac{([OCpetro]_p - [OCpetro]_s)}{100} \times \rho_P \qquad (3.2)$$

Here ω is denudation rate representative for ridge area at the Shale Hills catchment (45 m Myr^{-1}; Ma et al., 2010), $[OC_{petro}]_p$ is the concentration below the reaction front (0.04 %) and $[OC_{petro}]_s$ is the concentration at the top of the weathering front (0.02 %). Density of the protolith samples (ρ_P) is 2.42 g cm^{-3} (Herndon and Brantley, 2011). The long-term OC_{petro} weathering at Shale Hills is estimated to 1.6×10^{-2} tC km^{-2} yr^{-1}.

In addition, the trace element Re has been more precisely determined in these OC-poor samples. To apply the Re proxy to track OC_{petro} oxidation rates ($J_{OCpetro\text{-}Re}$), the following Equation 3.3 is used.

$$J_{OCpetro-Re} = \omega \times \frac{\left([Re]_p - [Re]_s\right)}{\left[\frac{Re}{OC}\right]_{petro}} \times F_{Re-OC} \times \rho_P \qquad (3.3)$$

Here, the ω and ρ_P are the same as defined above and $F_{Re\text{-}OC}$ stands for fraction of Re, derived from OC_{petro}, as presented in Figure 3.8 ($F_{Re\text{-}OC}$ = 0.83±0.05 %). The $[Re/OC]_{petro}$ is the ratio below the weathering front (4.3×10^{-7} g g^{-1}), $[Re]_p$ is the Re concentration directly below the front (0.11 ppb), and $[Re]_s$ is the Re concentration above the front (0.02 ppb). The long-term OC_{petro} emissions at Shale Hills determined by the Re proxy are thus estimated to be $2.0\pm0.2\times10^{-2}$ tC km^{-2} yr^{-1}.

A previous estimate of CO_2 release from OC_{petro} oxidation at Shale Hills was made by Jin et al. (2014). There, the CO_2 release from OC oxidative weathering was determined by calculating the amount of OC present in the volume of bedrock (using bulk OC concentrations measured in the protolith and rock density) multiplied by rate of soil production (20 mM yr^{-1}, Ma et al., 2010). The CO_2 release rate presented in Jin et al. (2014) was 1.5×10^{-2} t C km^{-2} yr^{-1}, which is broadly similar, given uncertainties, to our estimates presented above, using OC_{petro} loss at the reaction front (1.6×10^{-2} t C km^{-2} yr^{-1}) and the Re proxy ($2.0\pm0.2\times10^{-2}$ tC km^{-2} yr^{-1}).

The OC_{petro} oxidation rate at Shale Hills is expected to be low for two reasons: i) the OC_{petro}-depleted shale; and ii) extremely low denudation rates. Numerical models of OC_{petro} oxidation, constrained by the reactivity of coal from abiotic laboratory incubations (Chang and Berner, 1999), suggest that OC_{petro} oxidation is limited by supply of fresh, un-oxidized material (Bolton et al., 2006). Dissolved Re fluxes from catchments in Taiwan and New Zealand confirm this, and suggest that increases in erosion are linked to increases in OC_{petro} weathering (Hilton et al., 2014; Horan et al., 2017). Our estimate of OC_{petro} oxidation at Shale Hills is 2–3 orders of magnitude lower than OC_{petro} oxidation rates that use the dissolved Re proxy in high erosive catchments of the Himalaya (Dalai et al., 2002), Taiwan (Hilton et al., 2014), New Zealand (Horan et al., 2017), and the Mackenzie river system (Horan et al., 2019) (Figure 3.9). This reaffirms that erosion is the driving force of OC_{petro} oxidation on a global scale.

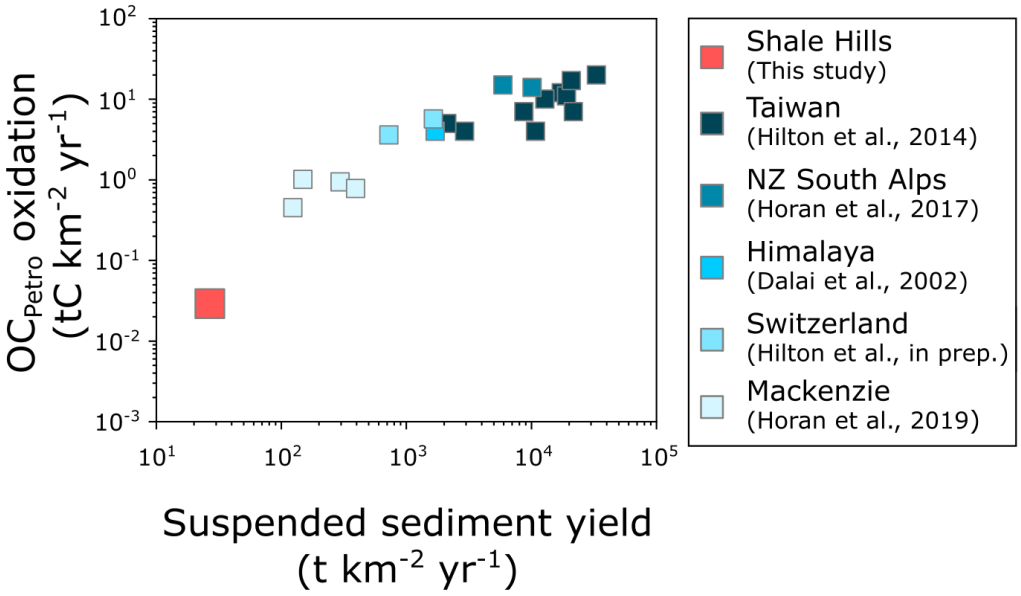

Figure 3.9: Global compilation of the erosion control on the OC_{petro} oxidation rates (tC km^{-2} yr^{-1}). The suspended sediment yield is a proxy for erosion rate and OC_{petro} oxidation rates are determined with the Re proxy.

3.5.4 Decoupling of stream water Re from deep weathering

At Shale Hills, we find stream water Re concentrations that are high (Figure 3.5), despite the very deep Re weathering front and relatively low Re concentrations of the protolith (Figure 3.3). We also observe enrichment of Re in surface soils (Figure 3.3 – inlet Soil profile). Previous work has suggested that dissolved Re could be influenced by anthropogenic perturbation of the Re cycle (Miller et al., 2011; Rahaman et al., 2012). Here we explore its potential role at Shale Hills, providing a case study of a low denudation landscape that contrasts with most recent work on dissolved Re (Hilton et al., 2014; Horan et al., 2019, 2017).

3.5.4.1 Rhenium supply from weathering

The present-day Re flux in stream water leaving the catchment (Re_{stream}, pmol m^{-2} yr^{-1}) based on the Re measurements collected in this study, can be calculated using the discharge-weighted average as in Equation 3.4.

$$Re_{stream} = \frac{\overline{Re \times Q_i}}{\overline{Q_i}} \times \overline{Q_a} \quad (3.4)$$

Here Re (pmol l^{-1}) is Re concentration measured in stream water over the sampling period, Q_i (l s^{-1}) is the instantaneous discharge measure at the time of sample collection, and Q_a (l s^{-1}) is the mean annual stream discharge for the sampling period. The present-day Re flux from the Shale Hills catchment is 4.7×10^3 pmol m^{-2} yr^{-1}.

A mass balance approach can estimate the release of Re to the stream water associated with weathering of the protolith (Re_{CW}; pmol m^{-2} yr^{-1}), using Equation 3.5.

$$Re_{CW} = \left(\overline{[Re]_p} - \overline{[Re]_S}\right) \times \rho_P \times \omega \quad (3.5)$$

The terms used here are defined in Equation 3.3. The expected release of Re to the stream due to weathering of the protolith (Re_{CW}) is calculated to 8.0×10^{1} pmol m^{-2} yr^{-1}. This is much lower than the dissolved Re flux from the Shale Hills stream. Indeed, only ~2% of the dissolved Re in stream water at Shale Hills appears to originate from chemical weathering. To explore why there is such a stark decoupling of weathering inputs and dissolved exports, we turn to the precipitation and surface soil samples.

3.5.4.2 Evidence for atmospheric deposition of Re

Previous studies have suggested that atmospheric deposition may supply an important amount of Re to the surface of some catchments (Colodner et al., 1993; Miller et al., 2011; Rahaman et al., 2012). The area surrounding the Shale Hills catchment is known for coal burning activities, with a number of historical iron furnaces, fueled by local Pennsylvania coal (Herndon et al., 2011; Kraepiel et al., 2015). Furthermore, the Shale Hills catchment is located downwind of contemporary coal power plants located in Western Pennsylvania (Lima et al., 2005; Ma et al., 2014). During coal combustion (500–700 °C), Re may be volatized and released to the atmosphere as Re_2O_7 (Colodner et al., 1995). It is then deposited on the surrounding soils and streams through either wet or dry deposition (Novo et al., 2015). The abundance of Re in coal fly ash, a by-product of coal burning, may be significant, as suggested by high Re concentration (5.2 ppb) measured in a Coal Fly Ash standard reference material 1633a (product of Pennsylvania and West Virginia coals) for this study, and a coal fly ash sample from Inner Mongolia with Re concentration of 7.3 ppb (He et al. 2018). Significant

atmospheric deposition of Re is consistent with the elevated Re/Na and Re/SO_4 ratios in precipitation samples from Shale Hills, which plot close to the OC_{petro} (coal) end-member (Figure 3.8).

The present-day atmospheric Re flux (Re_{Atm}) may be estimated by multiplying the average Re concentration of precipitation samples (1.28±0.99 pmol l^{-1}) with the mean annual precipitation for Shale Hills, of 1070 mm yr^{-1}, (Jin et al., 2014). A modern-day atmospheric deposition of Re at Shale Hills is 1.4±1.1×10^3 pmol m^{-2} yr^{-1} (Figure 3.10). By itself, the modern Re input from rainwater is almost 20-times the chemical weathering supply of Re, and can account for ~30% of the dissolved Re flux in this small catchment.

Groundwater samples collected at Shale Hills provide further insight. In the valley, samples collected during conditions with a high-water table have elevated Re concentrations (Table 3.2) and Re/Na and Re/SO_4 ratios (Figure 3.8). The high Re concentrations in the stream and shallow groundwater suggest additional inputs to explain their concentrations. These can come from surface soils, where rainfall events may leach previously deposited Re through an overland, surface flow. At the Shale Hills catchment, the surface soils appear to act as a temporary Re reservoir enriched in anthropogenic Re, suggesting that present-day Re cycle in the dissolved load has been perturbed by recent human activities.

3.5.4.3 Rhenium cycling in surface soils

Rhenium deposited in the catchment through wet or dry atmospheric deposition, reacts with soil and surface waters and is converted to the perrhenate ion: ReO_4. In this form, Re is thought to be stable through the entire river water pH (Colodner et al., 1993) and highly mobile. Therefore, long-term accumulation of

Re in circumneutral top soil is not expected. However, forest soil at the Shale Hills catchment has been long exposed to acidic precipitation (pH 4.2–4.4) from 1980 until the early 2000s (NADP, 2020). Present day soil pH vary between 4.0±0.1 on the ridge and 4.7±0.2 in the valley (Herndon et al., 2015b; Jin et al., 2011). A laboratory based study by Kim et al. (2004) showed that more than 40% of ReO_4^- could be reabsorbed onto organic molecules at pH ~4. With the increasing pH of precipitation over recent years, the reabsorbed Re could be leached into the surface waters, explaining the high Re concentrations in stream waters and the chemostatic Re behavior in the dissolved load (Figure 3.5B). Indeed, at Shale Hills we observe an enrichment in Re concentration towards the top-most soil layer in a 50 cm deep soil profile collected on the ridge top, close to borehole CZMW8 (Figure 3.3-inlet Soil profile). Accumulation of several other metals in the top soil layer is also seen at the Shale Hills, e.g. Mo and Mn (Herndon et al., 2011; Kraepiel et al., 2015) and Pb (Ma et al., 2014), which might accumulated from past industrial activity, modern day steel plants and coal burning, or gasoline combustion activities (Herndon et al., 2011).

To better understand the potential stocks of Re in the near surface soils, we estimate the Re mass in the soil by calculating the depth-weighted mean as follows in Equation 3.6:

$$Re_{soil} = \frac{\overline{[Re]_{soil} \times \rho_{soil} \times d}}{d} \quad (3.6)$$

here $[Re]_{soil}$ is the mean Re concentration in soil (0.06 ppb, n=4) and ρ_{soil} is the soil density (ρ_{Soil} = 1.4 g/cm^3; Lin et al., 2006) at a certain depth (d). The Re reservoir in the soil profile is 4.5×10^5 pmol m^{-2} (d = 50 cm); however, the highest

Re reservoir is apparent in the top 5 cm of the organic soil (6.2×10^5 pmol m^{-2}), which gradually decreases with depth to 1.1×10^5 pmol m^{-2} (40-50 cm deep).

Rhenium leaching from surface soils could represent an important pathway. To explain the measured dissolved Re flux, soil leaching ($Re_{leach,soil}=Re_{stream} - Re_{atm} - Re_{cw}$) would have to contribute 3.2×10^3 pmol m^{-2} yr^{-1} (Figure 3.10). With this constraint, we can estimate the time needed to deplete the accumulated Re in the surface soil (turnover time), assuming this leaching of Re is constant over time and acts to deplete the surface soil reservoir (Equation 3.7).

$$T_{Re} = \frac{m_{Re,soil}}{Re_{leach,soil}} \tag{3.7}$$

Here $m_{Re,soil}$ is mass of Re in the top 5 cm of the soil profile (6.2×10^5 pmol m^{-2}) and $Re_{leach,soil}$ is the inferred rate of Re loss from leaching the soil (3.2×10^3 pmol m^{-2} yr^{-1}). This returns an estimate of T_{Re} of 193 years. This is a considerable timeframe over which dissolved Re concentrations could be elevated.

The Shale Hills study shows that low denudation rates coupled with anthropogenic pollution via atmospheric metal deposition, can significantly perturb surface Re cycling and dissolved Re concentrations in stream water. While our study covers only a very small surface, these findings echo global assessments suggesting that the current cycling and usage of Re associated with human activities is equivalent to a Re flux of 0.15±0.01 Gg yr^{-1}, which is three times larger than the natural Re flux 0.05±0.03 Gg yr^{-1}, globally. Our study calls for future work to better constrain modern and historic Re inputs to the surface

of catchments, and highlights that the dissolved Re proxy for OC_{petro} oxidation (Dalai et al., 2002; Hilton et al., 2014) may result in overestimation in low denudation settings.

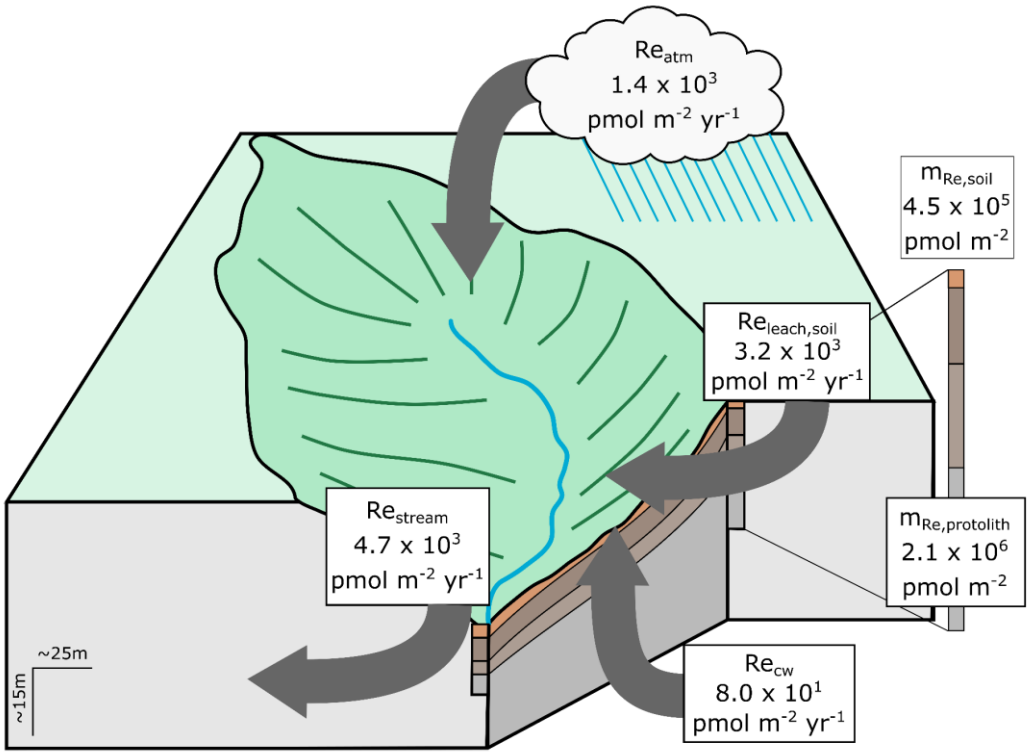

Figure 3.10: Rhenium (Re) reservoirs (pmol m^{-2}) and fluxes (pmol m^{-2} yr^{-1}) at the Shale Hills catchment. Abbreviations: Re_{atm} = Re derived from present day atmospheric deposition; Re_{cw} = Re derived from chemical weathering of the protolith; $Re_{leach,soil}$ = Re leaching through surface soils; Re_{stream} = Re export from the catchment via stream discharge; $m_{Re,soil}$ = Re stock in the top 0.5 m of the surface soils; $m_{Re,protolith}$ = Re stock over 11m of the protolith.

3.6 Conclusions

This study combines measurements of radiocarbon in organic matter and the trace element Re to examine the processes of oxidative weathering of OC_{petro} in a setting experiencing low denudation. In deep weathering profiles developed at the Shale Hills Critical Zone Observatory, we find evidence for OC_{petro} depletion across a broad, ~6 m wide weathering front in a borehole from the ridge (CZMW8), with a tau ($\tau_{OCpetro}$) value of up to -0.36. However, the measurements of radiocarbon require a deep percolation of ^{14}C-enriched OC, which makes the determination of OC_{petro} loss challenging in the weathered saprock. We turn to the trace element Re, and find the Re/OC_{petro} ratio in the deep, least weathered samples similar to other sedimentary lithologies, suggesting organic matter is an important host of Re in the rocks. We use Re/Na and Re/S ratios to estimate that ~83% of Re is sourced in OC_{petro} in this setting. The depletion profile of Re occurs over a broad reaction front (similar to OC_{petro} front), with τ_{Re} between -0.77 and -0.93. In contrast, the pyrite weathering front (S loss) in the ridgetop borehole is much narrower (~0.4 m) at a similar depth of 15.4 m and the S is almost fully depleted (τ_S = -0.99). We use the OC_{petro} depletion and the Re loss profiles to quantify long-term OC_{petro} oxidation rates, which are low ($<2.0\times10^{-2}$ t C km^{-2} yr^{-1}), but consistent with low denudation rates (0.01-0.025 mm yr^{-1}), confirming the important role of mineral supply and erosion rate on OC_{petro} oxidation.

At Shale Hills we find a pronounced difference between the deep weathering cycle of Re and Re cycling at the surface of the catchment. We calculate that the low oxidative weathering rates can supply only small amounts of Re to the stream (~8.0×10^{1} pmol m^{-2} yr^{-1}), and note that the upper ~15.4 m of the saprock is Re

depleted. In contrast, the dissolved Re export from the catchment is calculated as 4.7×10^{3} pmol m^{-2} yr^{-1}, with precipitation, shallow groundwater, and upper 10 cm of surface soils all having elevated Re concentrations. To explain these patterns, we suggest that there is an anthropogenic Re input into the catchment due to historical steel production and coal burning activities. Atmospherically derived Re may have accumulated in the surface soil under acidic conditions and is now being slowly leached to the stream waters. The current reservoir of Re in the surface soil could take centuries to deplete. This study highlights that anthropogenic inputs of Re from the atmosphere can be a large component of the Re budget in settings with low denudation rates. It calls for renewed focus on the recent perturbation of the Re cycle and how this element could help understand the legacy of pollution impacts in catchment soils.

CHAPTER 4
Climate and erosion control on rhenium production and mobility

The Brusquet catchment at the Draix-Bléone Critical Zone Observatory, South French Alps; Photo taken from the north ridge towards the south; October 2017; Photo: Robert G. Hilton

A version of this paper will be submitted to a peer-reviewed journal.

The authors on the paper will be:
Mateja Ogrič[1], Mathieu Dellinger[1], Guillaume Soulet[2], Sebastien Klotz[3], Caroline Le Bouteiller[3], Christian Schiffer[4] & Robert G. Hilton[1]

Affiliations:
[1]*Department of Geography, Science Laboratories, South Road, DH1 3LE Durham, UK.*
[2]*Institut Français de Recherche pour l'Exploitation de la Mer (IFREMER), Unité de Recherche 12 Géosciences Marines, F-29280 Plouzané, France.*
[3]*Univ. Grenoble Alpes, INRAE, UR ETNA, 2 rue de la papeterie, BP 76, 38402 Saint-Martin-d'Hères, Cedex, 10 France*
[4]*Department of Earth Sciences, Uppsala University, Villavägen 16, 75236 Uppsala, Sweden*

Authors contributions:
The research design and project goals were devised by myself with guidance from Robert G. Hilton and Mathieu Dellinger. The samples were collected by myself, Robert G. Hilton, Mathieu Dellinger, Guillaume Soulet and Sebastien Klotz (time series sampling). The analytical work was carried out under supervision of Mathieu Dellinger. The hydrological data were provided by Sebastien Klotz and Caroline Le Bouteiller. The chemical weathering fluxes were modelled with assistance of Christian Schiffer. Data processing and critical scientific evaluation was carried with Robert G. Hilton and Mathieu Dellinger. The chapter was written and edited by myself, Robert G. Hilton and Mathieu Dellinger.

Abstract

The oxidation of organic carbon in sedimentary rocks (OC_{petro}) plays an important role in setting the concentrations of oxygen and carbon dioxide in the atmosphere over geological time. Despite this recognition, the fluxes and climate controls on the release of CO_2 and consumption of O_2 during this process are poorly constrained. Here, we use the dissolved rhenium (Re) proxy in the Laval and Brusquet catchments of the Draix-Bléone Critical Zone Observatory, France to explore potential climatic and erosional feedbacks on OC_{petro} oxidation. The mean proportion of the dissolved Re flux sourced from OC_{petro} is 54±3% and 77±5 % for the Laval and Brusquet, respectively. We observe a large variability in the proportion of the Re sourced from the OC_{petro}, which may be explained by the seasonality in climate factors that control the production and mobilization of weathering products. In summer and autumn months, Re concentrations are up to ~10 times higher than during the winter and spring months in the Laval catchment (0.86 km^2). There, high erosion rates appear to promote weathering, which is kinetically limited. In contrast, less pronounced seasonal patterns in Re concentrations are observed in the less erosive Brusquet (1.07 km^2). We estimate a corresponding CO_2 release from OC_{petro} oxidation using the Re proxy of ~0.4±0.1 tC km^{-2} yr^{-1} and ~0.3±0.1 tC km^{-2} yr^{-1} for the Laval and Brusquet, respectively. These values, especially for the Laval, are significantly lower relative to other erosive catchments around the world. We suggest that the low runoff (~300 mm yr^{-1}) and high solid load in the Laval may result in some of the oxidized Re being exported in the solid load, with the Re yield of suspended sediment being >100-times higher than the dissolved Re yield. In small, erosive catchments with low runoff, the dissolved Re proxy for OC_{petro} oxidation may not be

conservative. Despite these challenges, the dissolved Re suggests a strong temperature control on OC_{petro} oxidation rates in a kinetically-limited regime, while a supply-limited weathering regime could lead to a less pronounced temperature feedback on OC_{petro} oxidation.

4.1 Introduction

Over geological timescales, erosion and weathering can transfer carbon to and from the lithosphere, thereby influencing the concentrations of oxygen and carbon dioxide in the atmosphere and setting Earth's climate and habitability (Berner and Canfield, 1989; Bolton et al., 2006). The solid Earth releases CO_2 during volcanism and metamorphism (Plank and Manning, 2019), and this atmospheric CO_2 is in part removed by silicate weathering by carbonic acid, resulting in the formation of new carbonate minerals (Gaillardet et al., 1999; Moon et al., 2014). At the same time, burial of new terrestrial and marine organic carbon in sediments also acts as a CO_2 sink (Gaillardet and Galy, 2008). However, when rocks containing carbonate and organic matter are re-exposed on Earth's continental surface, erosion and weathering can act as a CO_2 source via carbonate dissolution by sulfuric acid (Calmels et al., 2007; Torres et al., 2014) and rock organic carbon (OC_{petro}) oxidation (Hilton et al., 2014; Petsch et al., 2000). Oxidative weathering of OC_{petro} remains difficult to track and therefore, the rates and environmental controls on OC_{petro} oxidation are poorly constrained (Hilton and West, 2020).

Recent work has explored the patterns and rates of OC_{petro} oxidation using the trace element rhenium (Re) in rivers (Dalai et al., 2002; Hilton et al., 2014; Horan et al., 2019, 2017). The application of the dissolved Re proxy is based on

its association with OC_{petro} in sedimentary rocks (Jaffe et al., 2002; Peucker-Ehrenbrink and Hannigan, 2000) and fast mobilization upon oxidation. As such, the Re proxy may provide a catchment-integrated estimate of OC_{petro} oxidation rates, offering a powerful tool to evaluate wider-scale rates of CO_2 release from weathering of sedimentary rocks. The Re proxy approach has been applied to several catchments around the globe, with varying drainage area, erosion rate and sedimentary lithology (Dalai et al., 2002; Hilton et al., 2014; Horan et al., 2019, 2017). The estimates, so far, cover OC_{petro} oxidation yields between 0.63 tC km^{-2} yr^{-1} and 30 tC km^{-2} yr^{-1} and these are broadly positively correlated with physical erosion (Hilton and West, 2020). This suggests that the kinetics of OC_{petro} oxidation can keep pace with the increased supply of fresh mineral surfaces in high erosive catchments (Bolton et al., 2006). However, annual Re yields have generally been calculated from a relatively limited number of samples (Dalai et al., 2002; Hilton et al., 2014; Horan et al., 2017; Miller et al., 2011) which do not fully capture seasonal variability and/or hydrological controls on Re mobility. Studies of major dissolved elements in river waters, have revealed notable seasonality and flood-event scale variability in concentrations (Hindshaw et al., 2011; Rode et al., 2016; Tipper et al., 2006; Winnick et al., 2017) and this can impact the accuracy of weathering flux estimates (Schleppi et al., 2006; Skarbøvik et al., 2012; Verma et al., 2012). Systematic sampling of the dissolved load across flood-events can also help reveal shifts in the production and mobilization of weathering products, and shed light on the role of climate and hydrology for weathering fluxes (e.g. Winnick et al., 2017).

This paper seeks to improve our understanding of the Re proxy for determination of OC_{petro} weathering rates in sedimentary catchments, by

exploring high temporal resolution sampling in headwater streams, the Laval and Brusquet, in the southern French Alps. These catchments provide a case study of high sulfide oxidation rates (Chapter 5), which allow us to explore the role of sulfides in the supply of Re to the dissolved load. Additionally, the climatic controls on dissolved Re production and mobilization are discussed in relation to direct measurements of CO_2 release in the weathering zone from the Laval study site (Soulet et al., 2018). Finally, the annual dissolved Re yields are quantified and challenges for estimation of the OC_{petro} oxidation rates at the study sites are outlined. Dissolved Re displays a strong seasonal signal in its production in the weathering zone and export by flood events, suggesting an important role of temperature in OC_{petro} oxidation at the catchment-scale.

4.2 Study site

The Draix-Bléone Critical Zone Observatory (CZO) is located in south France, near the village Draix (Figure 4.1A) and it operates under the French network of observatories for the study of the critical zone, OZCAR (Gaillardet et al., 2018). The observatory was established in 1983 to monitor erosion, sediment flux and hydrology in a steep mountain terrain dominated by extremely erosive black marls (Mathys et al., 2003; Mathys and Klotz, 2008).

The Laval (0.86 km^2) and Brusquet (1.07 km^2) catchments share similar climatic conditions, topographic slopes and rock types with rock organic carbon (OC_{petro}; ~0.5 %), carbonate (~45 %) and sulfide (~0.6 %) concentrations (Graz et al., 2012), commonly found in sedimentary rocks (Amiotte Suchet et al., 2003; Copard et al., 2007). The two catchments differ in the age of exposed rocks (Figure 4.1B) with late Jurassic (Bajocian, Lower Bathonian-Callovo-Oxfordian)

black marls ("Terres Noires") prevailing in the Laval as opposed to alternating early Jurassic (Toarcian) black/grey shale and carbonates (Aalenian-Bajocian) in the Brusquet (Graz et al., 2011; Figure 4.1B). The black shales in the Brusquet were deposited during the Toarcian Oceanic Anoxic Event (T-OAE), which was characterized by notable shifts in the ocean chemistry, reflected in the isotope systematics of sedimentary rocks (Gill et al., 2011; Rodríguez-Tovar, 2021). A slightly higher total organic carbon (TOC) was measured in Toarcian black shales (0.7 %), compared to grey shale (0.5 %), marl (0.3 %), and limestone (0.1 %) in the Brusquet (Graz et al., 2011). Clayey mineralogy makes the rocks in both catchments very sensitive to chemical and physical weathering and prone to develop a typical "badland" morphology, with pervasive V-shaped gullies (Mathys et al., 2003).

The two catchments have a notable contrast in the extent of vegetation cover, which impacts catchment hydrology and the export of sediment (Carriere et al., 2020; Mathys et al., 2003). The Brusquet catchment was afforested in the early 1900s in order to decrease erosion rates and sediment export from the catchment (Cosandey et al., 2005; Mathys and Klotz, 2008). Today the vegetation covers 87 % of the total surface area, with the highest proportion near the catchment outlet, while some steep slopes of the headwaters are bare rock outcrops (Cras et al., 2007; Mathys et al., 2003). In contrast, the Laval catchment is more sparsely vegetated (32%), partly due to historic deforestation and overgrazing in the 19th century (Graz et al., 2012).

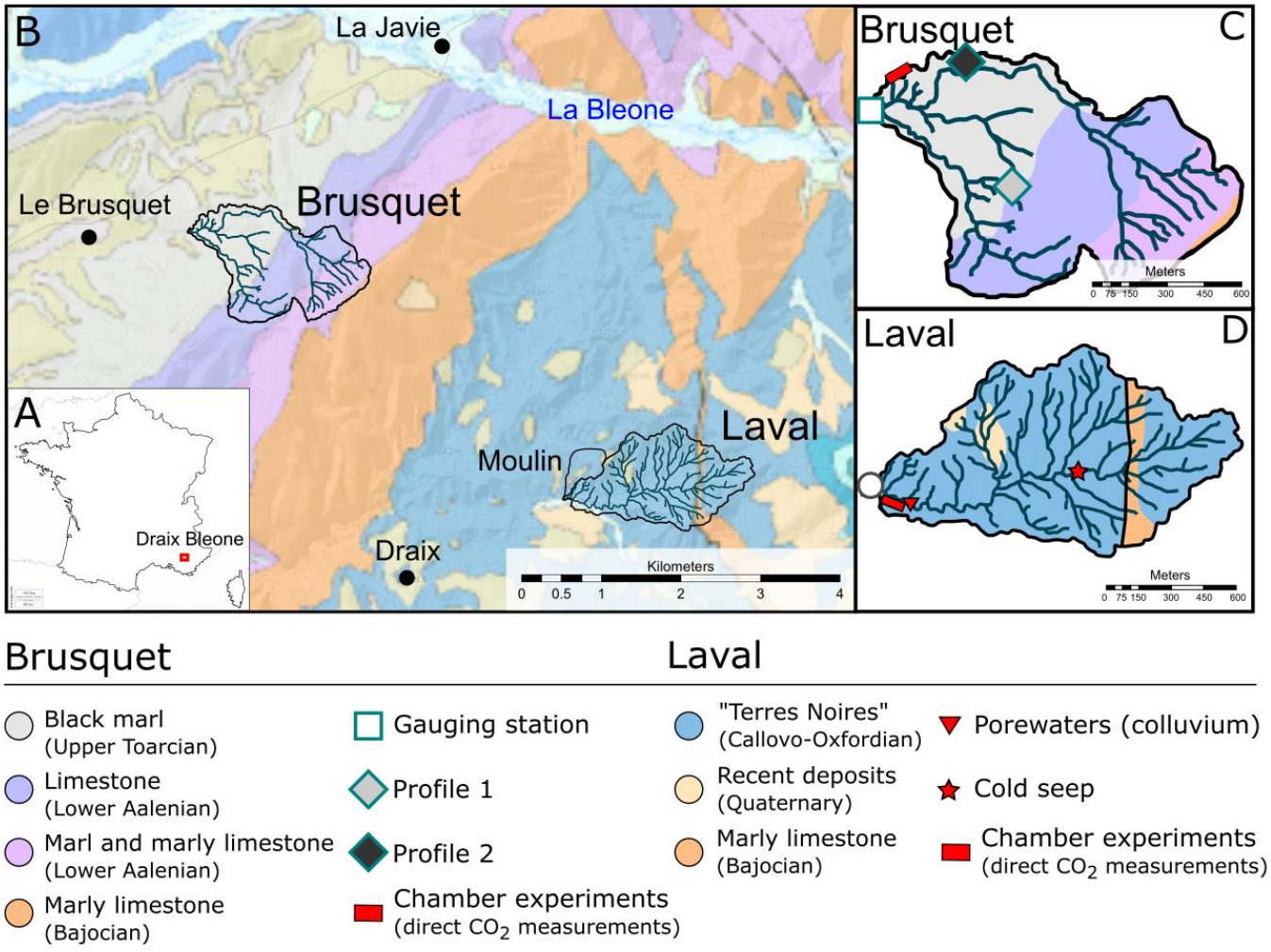

Figure 4.1: Geographical location and geology of the Draix-Bléone CZO. A: Draix-Bléone CZO in the South French Alps. **B:** Geological map of the observatory. **C:** Sampling locations of time-series samples (gauging station) and weathering profiles in the Brusquet. **D:** Sampling locations of time-series samples (gauging station), seep, pore water samples, and surface rocks in the Laval catchment.

The climate at the study site is Mediterranean-Alpine, with large temperature differences between the Alpine winter and the Mediterranean summer seasons. For the observation period from September/October 2016 to September/October 2018, the daily average air temperature varied from ~ -6 °C to ~+27 °C. The mean annual precipitation is slightly lower in the Brusquet (850 mm yr^{-1}), compared to the Laval (950 mm yr^{-1}), with most of the annual precipitation occurring in the autumn and spring seasons, while intense storm events may interrupt hot and dry summers.

The seasonality in climate is reflected in an annual cycle of sediment export from the catchments, which is especially pronounced in the Laval. Freeze-thaw cycles and extreme day-night time temperature differences in winter causes cracks and physical breakdown of bedrock, resulting in a mantle of weathered material on catchment slopes, which is moved into the streambed during storm events in spring (Mathys et al., 2003). In the Laval, these conditions result in one of the highest total sediment yields (suspended load and bed load) in the world, with a long-term average over 30 years of 14,300 t km^{-2} yr^{-1} (Carriere et al., 2020). While the Brusquet does have some areas of steep, exposed bedrock, the catchment-averaged erosion rates are lower. Following afforestation, the 30-year average sediment yield from Brusquet is 70 t km^{-2} yr^{-1} (Carriere et al., 2020). The denser vegetation and surface soil cover can potentially buffer some of the intense rainfall and temperature variations, and inhibit transport of bedrock-derived material to the streambed (Carriere et al., 2020).

4.3 Materials and methods

4.3.1 Materials

The Draix-Bléone CZO sites offer a unique opportunity to study Re mobility during marl and shale weathering at the source lithology and in dissolved and solid load. Both experimental catchments are equipped with Parshall flumes, discharge recorders and automatic sample collectors providing continuous measurements of water discharge (Mathys and Klotz, 2008). Optical fiber sensors measure sediment concentration and, combined with discharge measurements, are used to calculate the suspended sediment yield (Mathys et al., 2003). Upstream from the gauging station, a sediment trap retains the coarse material in order to estimate the total amount of bed load transported in the stream. Time series data on discharge and sediment export from both study sites are available from the Draix-Bléone website: Cambon et al. (2015).

4.3.1.1 Solid samples

The solid sample dataset includes surface rock clasts, weathering profiles, river bed load and suspended load samples. Additionally, a pyrite vein and secondary evaporites were sampled in the Laval and Brusquet, respectively. Solid samples were collected during field visits in August 2016, November 2016, March 2017, and September 2018.

Surface rock clasts were sampled at the locations of experimental chambers for direct measurements of CO_2 release (Roylands et al., In prep.; Soulet et al., 2018) in the Laval and Brusquet (Figure 4.1C and D). Two regolith profiles were sampled from exposed marl outcrops in the Brusquet (Figure 4.1C). Profile 1 was sampled close to the geological boundary between Toarcian black marls and

Aalenian limestone. Profile 2 was sampled on Toarcian black marls. In both profiles, a color change was evident from dark grey at the lowest point (bottom samples), through to lighter grey and orange, potentially indicating oxidative weathering. The surface samples had evidence for roots and modern plant litter mixed with rock clasts.

Previous work has established that river suspended load is dominated by erosion of rock outcrops (Graz et al., 2012) and for that purpose, river suspended load samples were recovered from a single storm event in the Laval (24/11/2016) and the Brusquet (05/11/2016). Suspended sediment was recovered from an ISCO auto-sampler after settling, decomposing of clear water and oven drying (60 °C). This method leads to minor bias in the grain size or amount of suspended sediment mass in the Draix catchments due to the very high suspended sediment concentrations in stream water (Mathys et al., 2003; Mathys and Klotz, 2008). River bed load samples were collected at the catchment outlet (Figure 4.1C and D).

4.3.1.2 Water samples

The prevailing Mediterranean climate and small catchment areas result in annual hydrographs which have long periods of low flow punctuated by high flow storm events (Figure 4.2). The stream water sampling strategy was designed to capture storm events using automatic sampling (ISCO auto sampler), while sampling of the low flow regimes took place approximately monthly by hand (Figure 4.2A and C). The sampling program captured 16 and 9 storm events for the Laval and Brusquet, respectively, corresponding to 68 and 34 individual samples collected on the rising, peak and falling limb of the storm events (~2-6 samples per storm, depending on the storm duration, Figure 4.2B and D). Sampling of the low flow

regime resulted in 23 and 14 samples collected from the Laval and Brusquet, respectively.

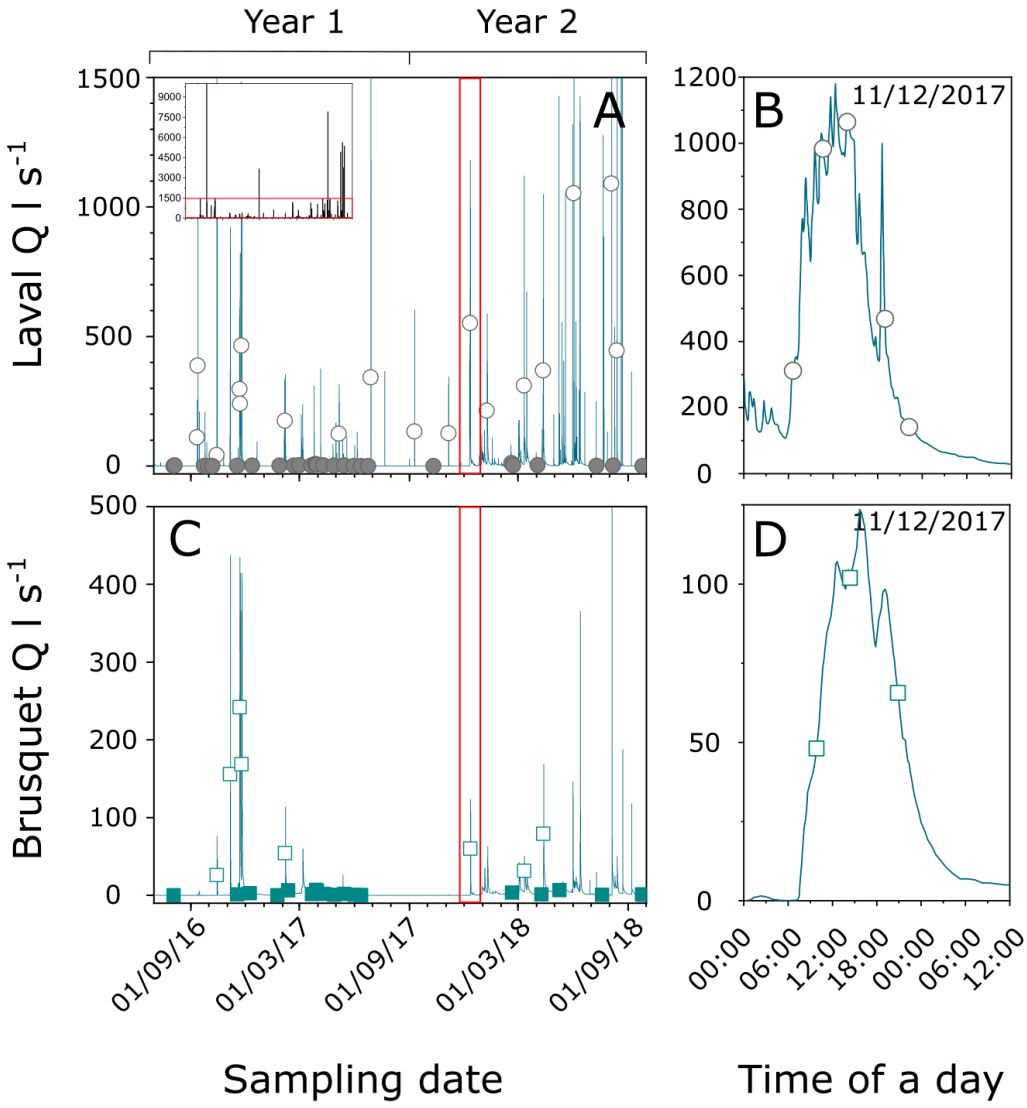

Figure 4.2: Hydrographs and stream water sampling strategy. A: Hydrographs over the observation period for the Laval catchment, with samples collected during low flow regime (full symbols, hand sampling) and high flow regime (open symbols, automatic sampling). **B:** An example of a storm event sampling in the Laval; open circles are water samples collected for concentration analysis. **C:** Hydrograph for the Brusquet catchment (note difference in discharge scale compared to the Laval), with samples collected during low flow regime (full symbols) and high flow regime (open symbols). **D:** An example of storm event sampling for the Brusquet, open squares are water samples collected for concentration analysis.

An additional set of water samples was collected from porewaters in colluvium and cold seeps from the Laval catchment using Rhizon pore water samplers. A potential contribution from atmospheric Re is explored with 12 precipitation samples collected at the Laval gauging station, during storm events within the studied period (09/2016–09/2018).

4.3.2 Analytical methods

4.3.2.1 Solid samples

All solid samples were freeze-dried on return to Durham, hand or ball milled in an agate mill to provide a homogeneous sample, and stored in a clean glass container.

For organic carbon (OC) and stable carbon isotope ($\delta^{13}C$) measurements, solid samples were decarbonated by three repeated additions of 1M HCl, followed by evaporation of the supernatant at 65 °C (see Chapter 2, Section 2.2.1, p29). The OC concentrations (%) and $\delta^{13}C$ (‰) measurements were carried out with a mass spectrometer connected to an elemental analyzer at Elemtex, Stable Isotope Analytical Laboratory, Cornwall, UK. The precision on $\delta^{13}C$ measurements was determined by repeated measurements of international certified synthetic standards IAEA 600 (caffeine) and IAEA CH3 (cellulose). Additionally, international certified soil standard NCS-DC73319 was repeatedly measured to verify carbonate removal and OC concentration. The OC concentrations were in agreement with the certified value (<4%, n=6), as well as the $\delta^{13}C$ values (0.01-0.04 ‰; n=6). The analytical precision for the $\delta^{13}C$ was 0.2 ‰.

Rhenium (Re) concentrations in solid samples were determined following a complete digestion and anion column chemistry protocol after Dellinger et al.

(2020). The Re solutions were measured on a multicollector inductively coupled plasma spectrometer (MC-ICP-MS) at Durham University, Department of Earth Sciences. A range of different standard reference geological materials were digested to validate the method (Chapter 2, Figure 2.3, p36). Agreement between our concentration measurements and published data is within 15%, and agreement with long-term in-house reproducibility is within 10% (Dellinger et al., 2020).

The solid samples were measured for Ti using flow injection and low pressure on-line liquid chromatography coupled to inductively coupled plasma mass spectrometer (ICP-MS) at the French National Center for Scientific Research (CNRS) Service d'Analyse des Roches et des Minéraux (SARM) following a protocol described in Carignan et al. (2001). Eight samples were analyzed for total sulfur (S) concentration and $\delta^{34}S$ on a costech elemental analyzer coupled to a Thermo Fisher Delta V Plus in the Stable Isotope Biogeochemistry Laboratory at Durham University, Department of Archeology. Details on this method are presented in Chapter 2, Section 2.2.4.2, p39.

4.3.2.2 Water samples

Shortly after sample collection, all water samples were filtered using single use, sterile 0.22 µm pore size syringe filters (Polyethersulfone, Merck Millipore) into a pre-cleaned LDPE bottle that was rinsed with filtered river water. One aliquot of 60 ml of filtered water was acidified to ~pH 2 with trace element grade HNO_3 (1M) for cation and trace element analysis, while a 30 ml sample was left un-acidified for measuring anions. All filtered waters were refrigerated at 4 °C in the dark prior to shipping to Durham.

Major anion (Cl^-, SO_4^{2-}, NO_3^-, NO_2^-, Br^-, PO_4^{3-}, F^-) and cation (Li^+, Ca^{2+}, Mg^{2+}, NH_4^+, Na^+, K^+, Sr^{2+}) concentrations were measured on an ion chromatograph (Thermo Scientific Dionex ICS 6000) at Durham University, Department of Geography. The analytical precision was determined by repeated measurements of a certified river water reference standard material (Sangamon – 03). All major elements resulted in precision better than 5% (Chapter 2, Figure 2.4, p38). Additionally, sample replicates were run during and between each batch, resulting in precision better than 1% for Ca^{2+} and Mg^{2+}, better than 2% for SO_4^{2-} and Na^+, and better than 3 % for Cl^-.

A suit of trace elements, including Re, were measured by a direct calibration method using an Agilent Technologies 7900 inductively coupled plasma mass spectrometer (ICP-MS) at Durham University, Department of Geography. Repeated measurements of Ottawa River water reference material (SLRS-5) for this study returned an average Re concentration of 64.6±6.1 pmol l^{-1} (n=6, ± 1SD), which is in agreement with long-term in-house measurements (63.0±3.5 pmol l^{-1}; n=24, ± 1SD) and values reported in the literature, that is 66±12 pmol l^{-1} (n=35) (Yeghicheyan et al., 2013). Additionally, 10- and 100-times dilutions of the SLRS-5 reference material were analyzed, which are closer in Re concentrations to the Laval and Brusquet stream water. Measurements on the diluted reference materials; 10-times dilution: 6.2±0.7 pmol l^{-1} (n=6, ±1SD) and 100-times dilution: 0.63±0.06 pmol l^{-1} (n=6, ± 1SD) returned a mean value which is in agreement with the long-term in-house measurements. Here we also report concentrations of Zn, Al and Mn, which are relevant for the precipitation samples.

4.3.3 Computational method for dissolved Re yields

Until now, dissolved Re yields have been calculated from a relatively limited number of samples, applying a straight average (Dalai et al., 2002; Hilton et al., 2014; Horan et al., 2017; Rahaman et al., 2012), or discharge-weighted average approach (Miller et al., 2011). The high temporal sampling resolution of low and high flow samples in this study results in a dataset with denser sampling of short-lived storm events, which is a common feature of many hydrological studies (Smakhtin, 2001). The sampling strategy adopted here is well-suited for a mixed method of quantifying dissolved ion fluxes, as for example presented in studies by Aulenbach and Hooper (2006) and Appling et al. (2015).

The computational analysis for predicting solute concentrations at non-sampled periods and flux calculations is provided in Chapter 2, Section 2.3.4, p44. Here we give a brief summary for context. First, the main hydrological flow regimes (low flow vs. storm events) are defined by the discharge of the lower quartile (Q1; <25%) (Smakhtin, 2001), which is <28.5 l s^{-1} for the Laval and <7.2 l s^{-1} for the Brusquet, and the samples collected during these periods are separated accordingly. The water discharge is measured based on a flow-rate dependent scheme at the sites (Mathys and Klotz, 2008). To aid data processing, these are resampled to a uniform time interval of 5 min. The dissolved Re concentrations are modelled for the short 5-min long intervals, accounting for the seasonal pattern in concentration of the low flow samples by fitting a cosine and sine curve, and seasonal pattern and short-term variability in the storm events by fitting a linear interpolation between the samples (Figure S4.1, Supplementary materials).

The total annual Re yield is calculated as follows in Equation 4.1:

$$J_{Re} = K \frac{\overline{Re_{5min} \times 10^{-12} \times Q_{5min}}}{A} \quad (4.1)$$

here K is a conversion factor to take account for the time period (seconds to years), Re_{5min} are the Re concentrations modelled for 5 min intervals in pmol l^{-1}, a factor 10^{-12} is used for unit conversion to mol l^{-1}, Q_{5min} are the discharge measurements resampled to 5 min time intervals in l s^{-1}, and A is the study area (km^2). The uncertainty was assessed by propagation of the analytical error and by assessing the influence of the sampling frequency on the annual yields by randomly selecting 20-100% of the dataset for 10,000 models.

4.4 Results

4.4.1 Hydrological and sediment yield measures

All hydrological and sediment yield measures were obtained from the Draix-Bléone observatory database (Cambon et al., 2015) for the two observation years (09/2016–09/2017 and 09/2017–09/2018). In both catchments, yields are lower in the first observation year relative to the second observation year (Table 4.1). Mean annual precipitation in the Laval is 865 mm yr^{-1} and 1,157 mm yr^{-1} (09/2016–09/2017 and 09/2017–09/2018, respectively) and in the Brusquet is 757 mm yr^{-1} and 957 mm yr^{-1} (10/2016–10/2017 and 10/2017–10/2018, respectively). The first observation period was drier and the second observation period was wetter compared to the long-term average (850 mm yr^{-1} in the Brusquet and 950 mm yr^{-1} in the Laval) in both catchments. This annual contrast in precipitation translates into differences in annual discharge and runoff (normalized to the catchment area) between the two observation years. The annual runoff for the 09/2016–09/2017 observation year in the Laval is lower

(249 mm yr^{-1}), compared to 09/2017–09/2018 period (485 mm yr^{-1}). Less pronounced differences are observed in the Brusquet, with annual runoff of 123 mm yr^{-1} and 144 mm yr^{-1} (10/2016–10/2017 and 10/2017–10/2018, respectively).

The total sediment yield (TSY) for the 09/2016–09/2017 period in the Laval is 13,166 t km^{-2} yr^{-1}, which is similar to the long term average 14,300 t km^{-2} yr^{-1} (1988-2016; Carriere et al., 2020). In the 09/2017–09/2018 period, the TSY in the Laval is 23,456 t km^{-2} yr^{-1}, which is ~1.6-times higher than the long-term average. Of the total yield, ~70 % corresponds to the suspended load (8,693 t km^{-2} yr^{-1} and 15,829 t km^{-2} yr^{-1}, 09/2016–09/2017 and 09/2017–09/2018, respectively) and ~30% to the bed load (4,473 t km^{-2} yr^{-1} and 7,627 t km^{-2} yr^{-1}, 09/2016–09/2017 and 09/2017-09/2018, respectively). In the Brusquet, the long-term TSY is 70 t km^{-2} yr^{-1} (Carriere et al., 2020), which is more than two-order of magnitude lower compared to the Laval. For the observation period, TSY in Brusquet is 51 t km^{-2} yr^{-1} and 516 t km^{-2} yr^{-1} (10/2016–10/2017 and 10/2017–10/2018, respectively, respectively). Of the TSY ~90% corresponds to the suspended load (45 t km^{-2} yr^{-1} and 492 t km^{-2} yr^{-1}) and ~10 % to the bed load (6 t km^{-2} yr^{-1} and 24 t km^{-2} yr^{-1}). The TSY in the 10/2017–10/2018 period in the Brusquet is ~7-times larger than the long-term average TSY.

Table 4.1. Hydrological measures from the Laval and Brusquet. Annual precipitation (P), discharge (Q), runoff (R), suspended sediment yield (SSY) and bed load yield (BLY) at the Laval and Brusquet catchments for the observation period.

Observation Period	Catchment	P	Q	R	SSY	BLY
		mm yr^{-1}	$\times 10^8$ l yr^{-1}	mm yr^{-1}	t km^{-2} yr^{-1}	t km^{-2} yr^{-1}
09/2016-09/2017	Laval	865	2.53	294	8,693	4,473
09/2017-09/2018		1,157	4.17	485	15,829	7,627
10/2016-10/2017	Brusquet	757	1.32	123	45	6
10/2017-10/2018		957	1.55	144	492	24

4.4.2 Chemical composition of the solid samples

Geochemical data on all solid samples analyzed in this study can be find in Appendix 2. A summary of the total organic carbon, stable carbon isotope and Re concentrations is provided in a Table 4.2 below.

4.4.2.1 Organic carbon and its isotopic composition

In the Laval catchment, the OC concentrations are between 0.36 % and 0.87 % with a mean value of 0.54±0.09 % (±1SD, n=29). We observe no notable differences between sample types (surface rock, soil, bed load, suspended load; Table 4.2). These concentrations are similar to previously published values of between 0.50–0.70 % (Copard et al., 2006; Graz et al., 2012, 2011). The stable carbon isotope ($\delta^{13}C$) composition of OC in solid samples from the Laval varies between -26.8 ‰ to -25.0 ‰, with a mean value of -25.9±0.5 ‰ (±1SD, n=29), similar to the range of values (-27.3 ‰ to -25.8 ‰) reported in Graz et al. (2011).

In the Brusquet, we observe higher OC concentrations, ranging between 0.46 % and 1.59 % and a mean value of 0.91±0.33 % (±1SD, n=14) across all analyzed solid samples, except surface soils (Table 4.2). This average is similar to OC concentrations (0.57–0.89 %) from Graz et al. (2011). The highest OC

concentrations are observed in suspended load between 1.07 % and 1.59 %, which is in the range of OC in surface soil litters (1.05–1.61 %). The mean $\delta^{13}C$ value across all samples (except soils) in the Brusquet is -26.4±0.7 ‰ (±1SD, n=14), while $\delta^{13}C$ in soils is lower (-25.7 ‰). The $\delta^{13}C$ values are in agreement with mineral soils (-26.2 ‰ to -25.2 ‰) and bedrock samples (-26.7 ‰ to -25.7 ‰) from the previous study set in the Brusquet (Graz et al., 2011).

4.4.2.2 Rhenium concentrations and Re/OC ratios

In the Laval, Re concentrations in solid samples range between 0.7 ppb and 5.8 ppb, with a mean value of 2.6±1.0 ppb (±1SD; n=21). The largest variability is observed in the surface rocks samples, of between 0.7 ppb and 5.8 ppb, with a mean value of 2.9±1.5 ppb (±1SD; n=9). The Re concentrations of the suspended load and bed load samples are more similar, ranging between 2.0 ppb and 2.7 ppb, and a mean value of 2.4±0.1 ppb (±1SD; n=12). A pyrite vein sample collected in the Laval catchment has a Re concentration of 3.2 ppb, similar to the upper range of Re concentrations measured on surface rock samples (Table 4.2).

In the Brusquet, Re concentrations in solid samples are lower than those in the Laval, with a range of values between 0.4 ppb and 3.4 ppb and a mean value of 1.4±0.6 ppb (±1SD; n=21). Again, the largest variability in Re concentration is observed in surface rock samples, with a range of values between 0.4 ppb and 1.7 ppb and a mean value of 1.1±0.5 ppb (±1SD; n=6). Re concentrations in bed load are ranging between 1.1 ppb and 3.4 ppb and have a mean value of 1.7±0.8 ppb (±1SD; n=8). Suspended load samples are within the range of the bed load (1.3 ppb to 1.8 ppb; n=3).

In the context of published measurements of Re concentrations in sedimentary rocks, the values in Draix are higher than Re concentrations

measured in Silurian Rose Hill Shale (0.2±0.1 ppb, n=9, ±1SD) from the SSHCZO (Chapter 3), and similar to bed load sediments from Taiwan (0.6–1.0 ppb, Hilton et al., 2014), and from the Mackenzie river system (0.7–4.4 ppb, Horan et al., 2019).

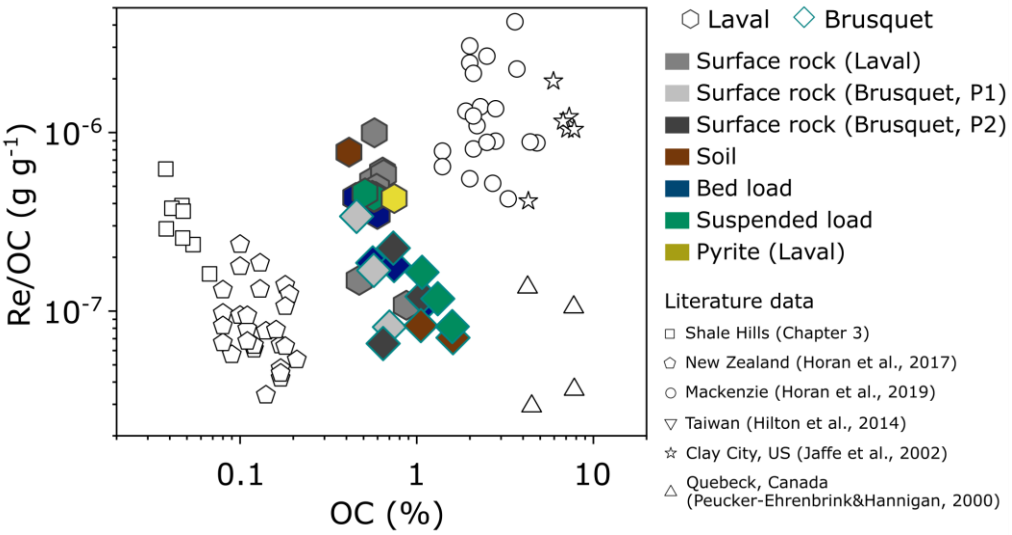

Figure 4.3: Variability in Re/OC ratios across different sedimentary environments in Draix-Bléone CZO. Solid samples collected in the Laval (hexagons, grey edge) and Brusquet catchments (diamonds, green edge). P1 is profile 1 and P2 is profile 2 in Figure 4.1.

The solid samples (excluding soils) collected in the Laval catchment have Re/OC ratios between 1.1×10^{-7} g g^{-1} and 10×10^{-7} g g^{-1} and a mean value of $4.6\pm2.0\times10^{-7}$ g g^{-1} (±1SD, n=16; Figure 4.3). The mean Re/OC is similar to bed load sediments in mountainous catchments of Taiwan ($2.6–4.6\times10^{-7}$ g g^{-1}; Hilton et al., 2014) and the bed load samples and rocks from the Mackenzie river basin ($3.3 – 6.3\times10^{-7}$ g g^{-1}; Horan et al., 2019). The solid samples from the Brusquet (excluding soils) have notably lower Re/OC ratios compared to the Laval, with a Re/OC ratio of between 0.66×10^{-7} g g^{-1} and 3.4×10^{-7} g g^{-1}, with a mean of $1.5\pm0.8\times10^{-7}$ g g^{-1} (± 1SD, n=12). These Re/OC ratios are similar to OC-rich Toarcian shales sampled in coastal outcrops in the UK, with a mean value of $1.8\pm0.9\times10^{-7}$ g g^{-1} (Cohen et al., 1999).

4.4.2.3 Weathering profiles

The two regolith profiles sampled in the Brusquet display an increase in OC concentration towards the surface, from 0.47 % to 1.05 % in the profile 1 and from 0.65 % to 1.61 % in the profile 2 (Appendix 2). The $\delta^{13}C$ values of samples range between -25.4 ‰ and -26.8 ‰ and between -24.8 ‰ and -26.6 ‰ in profile 1 and 2, respectively.

The OC and Re concentrations were normalized to titanium (Ti), to examine elemental loss or gain during chemical weathering (Chapter 3). The increase in OC/Ti, and decrease in $\delta^{13}C$ values near the top of the profile 1 suggest inputs of modern OC from plant litter and roots (Figure 4.4), In contrast, Re/Ti ratio show a decrease towards the surface, which may be attributed to a Re loss during chemical weathering.

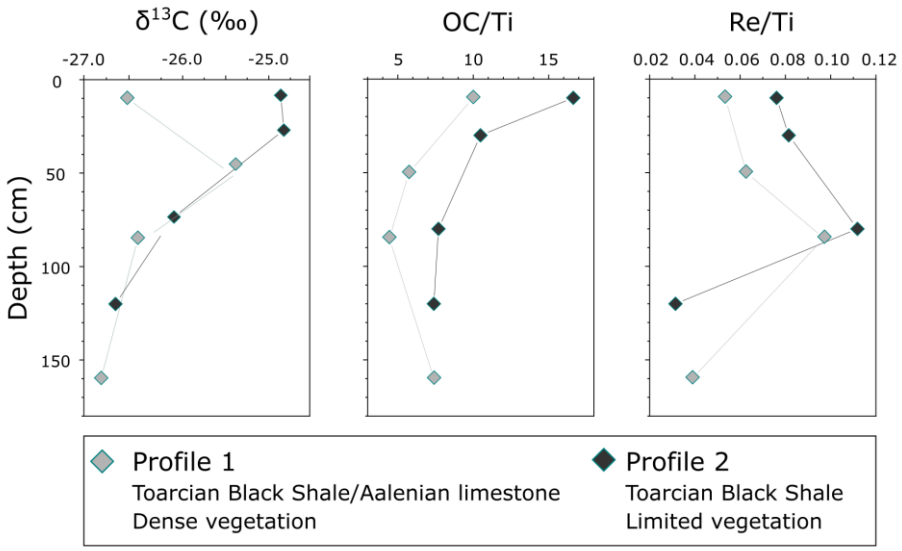

Figure 4.4. Weathering profiles sampled in the Brusquet catchment. Increase in OC/Ti ratio and decrease in $\delta^{13}C$ may indicate a contribution of modern OC in the surface layers. Small variability in Re/Ti ratio in the surface samples is observed.

Table 4.2: Elemental concentrations on solid samples from Draix-Bléone CZO. Averages of organic carbon (OC, %), stable carbon isotope ratio ($\delta^{13}C$, ‰) and rhenium concentration (Re, ppb). The concentrations were measured on the solid samples collected from the Laval and Brusquet catchments. For concentration data on each sample see Appendix 2. * Soil samples are not included in the average.

Sample Type	Catchment	OC (%)					$\delta^{13}C$ (‰)					Re (ppb)				
		n	Min	Max	Mean	1SD	n	Min	Max	Mean	1SD	n	Min	Max	Mean	1SD
Surface rocks	Laval	18	0.47	0.87	0.57	0.09	18	-26.5	-25.0	-25.7	0.5	9	0.7	5.8	2.9	1.5
Bed load		4	0.36	0.60	0.48	0.10	4	-26.7	-25.4	-26.2	0.6	4	2.0	2.5	2.2	0.2
Suspended load		7	0.28	0.59	0.51	0.11	7	-26.8	-25.7	-26.1	0.5	8	2.2	2.7	2.5	0.2
Soil		1	-	-	0.41	-	1	-	-	-25.7	-	1	-	-	3.2	-
Pyrite vein		-	-	-	-	-	-	-	-	-	-	1	-	-	3.2	-
Average*		***29***	-	-	***0.54***	***0.1***	***29***	-	-	***-25.9***	***0.5***	***21***	-	-	***2.6***	***1.0***
Profile 1	Brusquet	3	0.46	0.70	0.58	0.12	3	-26.8	-25.4	-26.2	0.7	3	0.6	1.6	1.0	0.5
Profile 2		3	0.65	1.07	0.82	0.22	3	-26.7	-24.8	-25.9	0.9	3	0.4	1.7	1.1	0.6
Bed load		4	0.56	1.14	0.83	0.24	4	-27.0	-25.9	-26.5	0.5	8	1.1	3.4	1.7	0.8
Suspended load		4	1.07	1.59	1.29	0.22	4	-27.2	-26.8	-26.9	0.2	7	1.3	1.8	1.4	0.2
Soil (Profile 1 and 2)		2	1.05	1.61	1.33	0.39	2	-26.5	-24.9	-25.7	1.2	2	0.9	1.1	1.0	0.2
Secondary evaporite		1	-	-	0.27	-	1	-	-	-25.4	-	1	-	-	0.3	-
Average*		***14***	-	-	***0.91***	***0.33***	***14***	-	-	***-26.4***	***0.7***	***21***	-	-	***1.4***	***0.6***

4.4.3 Dissolved load chemistry

Geochemical data on all water samples analyzed in this study can be find in Appendix 3.

4.4.3.1 Stream water chemistry

Both catchments are highly concentrated in stream solutes (Figure 4.5). In the Laval, the anions are dominated by SO_4^{2-}, with a mean value of 7.6±4.2 mmol l^{-1} (all Laval stream waters: ±1SD; n=91; unless otherwise stated). For the cations, concentrations of Mg^{2+} (3.5±1.7 mmol l^{-1}) and Ca^{2+} (3.4±1.6 mmol l^{-1}) are similar, while Na^{+} concentrations are lower (2.6±3.5 mmol l^{-1}). In comparison, in the Brusquet all major ion concentrations are lower in than in the Laval (Figure 4.5). Stream water samples from the Brusquet display mean SO_4^{2-} of 2.9±1.5 mmol l^{-1} (all Brusquet stream waters: ±1SD; n=50; unless otherwise stated), Mg^{2+} of 2.2±1.0 mmol l^{-1}, and Ca^{2+} of 2.4±1.0 mmol l^{-1}, while the Na^{+} concentrations are much lower, at 0.3±0.4 mmol l^{-1}. The new measurements from the Laval show values in general agreement with previous studies (Cras et al., 2007; Marc et al., 2017); however, our study has an extended coverage of low flow samples and captures a notable seasonal variability of major dissolved ion concentrations (Figure 4.5). In both catchments, samples collected during the low flow regime (Figure 4.5, full symbols) display higher concentrations in all major elements, compared to more diluted storm waters (Figure 4.5, open symbols).

A large range of dissolved Re concentration is observed for the sampling period in the Laval, between 0.97 pmol l^{-1} to 41.2 pmol l^{-1}, and a mean value of 7.3±8.0 pmol l^{-1} (±1SD; n=87). In contrast to major ions, Re concentrations are the highest during high flow regimes, with a mean value of 8.8±8.9 pmol l^{-1}

(±1SD; n=64), and lowest during low flow conditions, with a mean value of 3.2±1.9 pmol l^{-1} (±1SD; n=23). Additionally, Re displays a seasonal variability within the high flow storm-event data. The highest Re concentrations were measured in the summer months (June, July, August), between 5.4 pmol l^{-1} and 22.2 pmol l^{-1}, and a mean value of 14.7±5.8 pmol l^{-1} (n=10; ±1SD). Opposite, storm events sampled in the winter months (December, January, February) range from 1.6 pmol l^{-1} and 5.3 pmol l^{-1} with a mean value of 3.1±1.2 pmol l^{-1} (n=11; ±1SD). In the Brusquet, dissolved Re concentrations are lower and there is less variability compared to the Laval. The mean Re concentration over the sampling period is 2.5±3.4 pmol l^{-1} (±1SD; n=50). Again, the highest Re concentrations are measured during high flow regimes, with a mean value of 3.2±3.9 pmol l^{-1} (±1SD; n=34) and the lowest during the low flow conditions, with a mean value of 0.8±0.4 pmol l^{-1} (±1SD; n=15). An interesting outlier was measured during a large storm event occurring in August 2018 (Figure 4.5), during which the Re concentration in stream water reached 22.5 pmol l^{-1}, which is ~10-times higher compared to the Brusquet-mean and in range of Re concentrations in the Laval. The Re concentrations measured in these two small catchments fall within the range reported for global rivers of 4.7±0.2 pmol l^{-1} to 25.4±1.2 pmol l^{-1} (Colodner et al., 1993; Dalai et al., 2002; Hilton et al., 2014; Miller et al., 2011).

4.4.3.2 Porewater and seep chemistry

The chemistry of porewater and samples is reported in Table S4.1 (Supplementary materials). The most pronounced difference between the two water types is in Cl^- and Na^+ concentrations, which are lower in porewaters (Cl=0.025±0.003 mmol l^{-1} and Na=0.073±0.03 mmol l^{-1}), compared to the seeps (Cl=1.7±1.3 mmol l^{-1} and Na=4.9±4.9 mmol l^{-1}. Rhenium concentrations in these

samples are within the lower range of stream water samples (1.2 – 7.9 ppb).

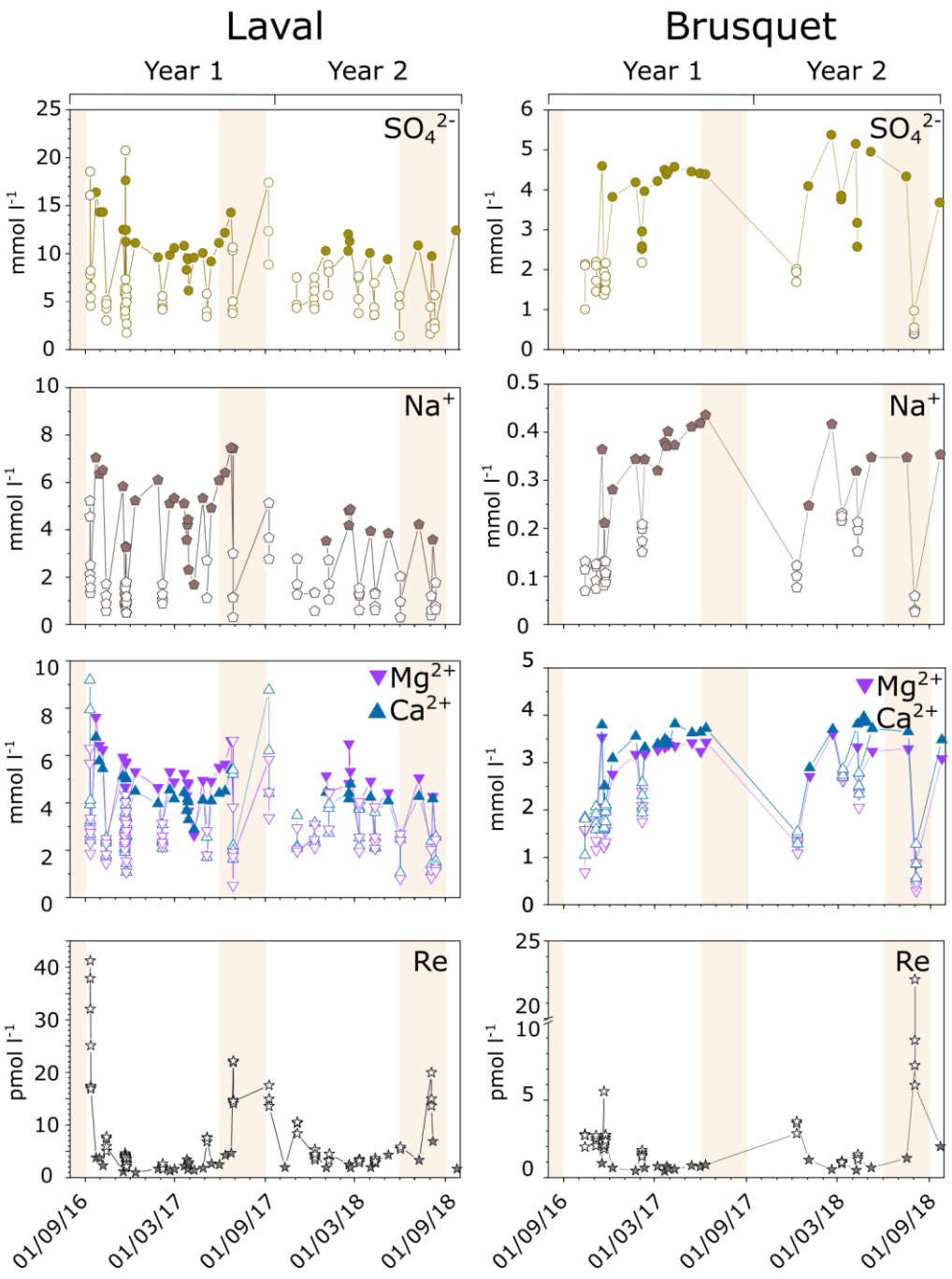

Figure 4.5. Stream water chemistry. Major ions and Re concentrations on samples collected between September 2016 and September 2018 in the Laval (left) and between October 2016 and October 2018 in the Brusquet (right). Full symbols represent samples collected during low flow regime. Empty symbols represent samples collected during high flow regime. Orange shading marks meteorological summer (01/June–31/August).

Table 4.3. Dissolved load chemistry for the Laval and Brusquet. Summary of raw stream water chemistry measurements over the observation period and across different hydrological regimes (low flow, high flow). Mean concentration values of precipitation, seep and porewater chemistry. For concentration data on each sample see Appendix 3.

Catchment	Observation Period	Dataset	n	Cl^- (mmol)		SO_4^{2-} (mmol)		Na^+ (mmol)		Mg^{2+} (mmol)		Ca^{2+} (mmol)		n	Re (pmol)	
				Mean	SD	Mean	SD	Mean	SD	Mean	SD	Mean	SD		Mean	SD
Laval	All samples		91	0.29	0.37	7.6	4.2	2.6	2.1	3.5	1.7	3.4	1.6	87	7.3	8.0
	2016-2017	Complete	59	0.37	0.42	8.4	4.6	3.0	2.4	3.8	1.8	3.7	1.8	59	8.1	9.1
		Low flow	18	0.81	0.44	12.1	2.7	5.8	1.5	5.6	1.2	4.8	1.0	18	3.0	1.9
		High flow	41	0.18	0.24	6.8	4.4	1.8	1.5	3.0	1.3	3.3	1.9	41	10.3	10.2
	2017-2018	Complete	32	0.14	0.15	5.9	2.7	1.7	1.2	2.9	1.3	2.8	1.0	28	5.7	4.4
		Low flow	5	0.37	0.16	10.1	0.6	4.0	0.3	4.7	0.3	4.2	0.1	5	3.8	2.0
		High flow	27	0.10	0.10	5.1	2.2	1.3	0.8	2.6	1.1	2.6	0.9	23	6.1	4.7
Brusquet	All samples		50	0.05	0.05	2.9	1.5	0.3	0.4	2.2	1.0	2.4	1.0	50	2.5	3.4
	2016-2017	Complete	32	0.05	0.06	3.0	1.4	0.3	0.5	2.2	1.0	2.5	0.9	32	1.9	1.3
		Low flow	10	0.08	0.10	4.5	0.7	0.6	0.8	3.1	0.9	3.4	0.7	10	1.3	1.7
		High flow	22	0.03	0.01	2.2	0.9	0.2	0.1	1.8	0.7	1.9	0.6	22	2.1	1.0
	2017-2018	Complete	18	0.05	0.02	2.9	1.7	0.2	0.1	2.1	1.1	2.3	1.1	18	3.7	5.3
		Low flow	4	0.05	0.00	5.0	0.5	0.4	0.04	3.4	0.2	3.7	0.1	4	0.7	0.4
		High flow	14	0.04	0.03	2.4	1.4	0.2	0.1	1.7	1.0	2.0	0.9	14	4.5	5.8
Precipitation			12	0.013	0.006	0.021	0.016	0.030	0.029	0.014	0.007	0.063	0.043	12	0.4	0.3
Seep			3	1.7	1.4	10.3	1.8	4.9	4.9	3.4	1	3.3	1.1	2	4.8	4.2
Porewater			3	0.024	0.003	7.5	3.5	0.07	0.03	4.4	1.5	3.8	1.8	3	2.1	0.8

4.4.3.3 Precipitation chemistry

Precipitation samples have lower major ion concentrations than stream waters in both catchments (Table 4.3, Table S4.2, Supplementary material). Rhenium concentrations in the precipitation samples show a variation between <0.03 pmol l^{-1} and 1.12 pmol l^{-1}, with a mean value of 0.36±0.32 pmol l^{-1} (n=12, ±1SD). The lowest concentrations (below the detection limit of 0.03 pmol l^{-1}) are similar to low concentrations found in rain from the Western Southern Alps, New Zealand (Re<0.02 pmol l^{-1}; Horan et al., 2017). However, the higher Re concentrations presented here are similar to the concentrations measured in the Shale Hills catchment (Pennsylvania, US; Chapter 3) and samples from the US American east coast (Miller et al., 2011), where high Re concentrations were attributed to anthropogenic inputs. The Draix-Bléone CZO is located in the rural French Alps, where contemporary anthropogenic inputs are thought to be minimal. Larger industrial areas are situated ~200 km north in the valley of Grenoble (Guédron et al., 2016) and ~200 km south, where large cities as Marseille and Nice are situated.

To provide additional constraint, we use the chemistry of precipitation water and atmospheric dust from the observation station "Le Casset", which is located in the vicinity of Grenoble. Long term (2002-2018) precipitation chemistry is available at this station (EBAS, 2017). Trace element ratios of atmospheric dust collected between 2011 and 2013 are available from the same site (Fu et al., 2017). There are notable differences between Na/Cl ratios of rainwater from the Laval (0.52–5.8, n=12) compared to the "Le Casset" station (0.15–0.50, n=195). For reference, evaporation of seawater is expected to produce rainwater with a Na/Cl ratio of ~0.85 (West et al., 2002). Thus, some

precipitation samples from Laval display an enrichment in Na^+ (Figure 4.6A), indicating a potentially non-cyclic origin of rainwaters in the Laval.

Trace metals measured in atmospheric dust at "Le Casset" show elevated Zn/Al and Mn/Al ratios compared to rain water samples collected in the Shale Hills (Chapter 3) or New Zealand (Horan et al., 2017) (Figure 4.6B). The precipitation samples from the Laval have a slightly higher Zn/Al ratio compared to the atmospheric dust samples from the "Le Casset", implying contamination of the rainwater samples by atmospheric dust.

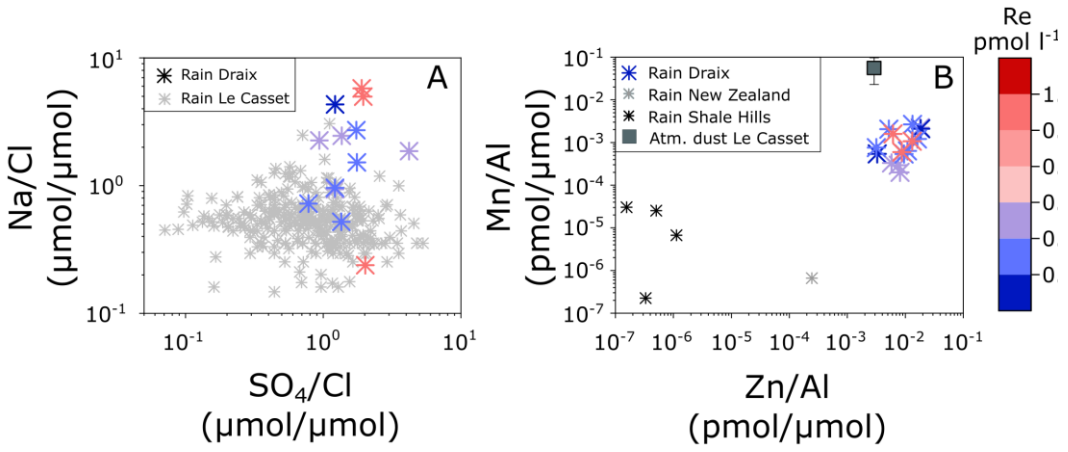

Figure 4.6: Precipitation chemistry. A: The SO_4/Cl versus Na/Cl ratios in precipitation samples from the Le Casset station (grey) and the Laval (color-coded by Re concentration: red – high, blue - low). **B:** Trace elements measured in precipitation samples in the Laval (colored samples), New Zealand (grey), Shale Hills (black) and atmospheric dust particles at Le Casset (square, Fu et al., 2017).

Here, we suggest that some precipitation samples might have been contaminated by atmospheric dust and therefore, the following assumption is made: precipitation samples with Na/Cl ratio <1 (broadly reflecting the Na/Cl ratio of seawater) and Re concentration <0.4 pmol l^{-1} (Figure 4.6A) are the least compromised samples by local dust contamination. These samples are used for estimation of Re inputs through the atmosphere and to correct major elements for the atmospheric deposition as presented in Chapter 5, Section 5.4.3, p174.

4.4.4 Annual Re yields

The annual dissolved Re yields in the Laval are 11.0±0.6×10^{-4} mol km^{-2} yr^{-1} and 21.0±5.7×10^{-4} mol km^{-2} yr^{-1} for the 09/2016–09/2017 and the 09/2017–09/2018 observation period, respectively. In the Brusquet, annual dissolved Re yields are 2.2±0.2×10^{-4} mol km^{-2} yr^{-1} and 4.5±2.0×10^{-4} mol km^{-2} yr^{-1} for the 10/2016–10/2017 and the 10/2017–10/2018 observation period, respectively (Table 4.4).

Rhenium inputs through the atmosphere are estimated from the mean Re concentration of precipitation samples with Na/Cl ratio <1 (0.23±0.11 pmol l^{-1}; n=3 ±1SD) multiplied by precipitation measurements (Table 4.1). In the Laval, atmospheric Re input is 2.0±1.0×10^{-4} mol km^{-2} yr^{-1} (09/2016–09/2017) and 2.7±1.3×10^{-4} mol km^{-2} yr^{-1} (09/2017–09/2018). In the Brusquet, the atmospheric Re flux is 1.7±0.8×10^{-4} mol km^{-2} yr^{-1} (10/2016–10/2017) and 2.2±1.1×10^{-4} mol km^{-2} yr^{-1} (10/2017–10/2018) (Table 4.4).

Solid Re export is estimated using the annual suspended and bed load yields (Table 4.1) and Re concentrations measured in suspended and bed load (Table 4.2). In the Laval, the Re export through the suspended sediment load is 1,150×10^{-4} mol km^{-2} yr^{-1} and 2,093×10^{-4} mol km^{-2} yr^{-1}, for the 09/2016–09/2017 and the 09/2017–09/2018 observation period, respectively, which is approx. two orders of magnitude larger compared to the Re yield thorough the dissolved load (Table 4.4). In the Brusquet, the Re export in suspended sediment is 3.5×10^{-4} mol km^{-2} yr^{-1} and 37.9×10^{-4} mol km^{-2} yr^{-1} for the 10/2016–10/2017 and the 10/2017–10/2018 observation period, respectively. Rhenium export through suspended sediment equals that of the dissolved load for the first

observation year. However, in the second year, the Re export through suspended sediment is ~10-times higher compared to the dissolved load (Table 4.4).

Table 4.4. Annual rhenium yields for the Laval and Brusquet. Abbreviations: SL=suspended load, BL=bed load.

Catchment	Observation period	Dataset	Rhenium yield			
			Dissolved	Atmosphere	SL	BL
			× 10^{-4} mol km^{-2} yr^{-1}			
Laval	11/09/2016-10/09/2017	*Complete*	11.0 ± 0.6	2.0 ± 1.1	1,150	523
		High flow	8.9 ± 0.6	-	-	-
		Low flow	2.2 ± 0.2	-	-	-
	11/09/2017-10/09/2018	*Complete*	21.0 ± 5.7	2.7 ± 1.3	2,093	892
		High flow	16.3 ± 1.3	-	-	-
		Low flow	4.7 ± 0.9	-	-	-
Brusquet	14/10/2016-13/10/2017	*Complete*	2.2 ± 0.2	1.7 ± 0.8	3.5	0.5
		High flow	2.0 ± 0.2	-	-	-
		Low flow	0.2 ± 0.1	-	-	-
	14/10/2017-13/10/2018	*Complete*	4.5 ± 2.0	2.2 ± 1.1	37.9	2.2
		High flow	4.0 ± 1.2	-	-	-
		Low flow	0.5 ± 0.1	-	-	-

4.5 Discussion

The production and mobilization of Re during weathering, and its delivery to the dissolved load of rivers (Colodner et al., 1993; Miller et al., 2011) has provided a proxy for oxidative weathering (Dalai et al., 2002; Hilton et al., 2014; Horan et al., 2017). Of particular interest is the link between the mobilization of Re and the oxidation of OC_{petro} (Jaffe et al., 2002; Chapter 3), and the inference that dissolved Re can thus be used to explore the patterns and rates of OC_{petro} oxidation (Hilton et al., 2014; Horan et al., 2017). Here we explore the production, source and flux of dissolved Re in two paired catchments, which drain similar marl and shale bedrocks, but contrast largely in their relative erosion rates. Firstly, we explore the association of Re and OC_{petro} in solid samples, the evidence for their mobility during weathering, and we quantify the source of Re to the dissolved load. We

then seek to explain the distinct seasonal variability of dissolved Re concentrations (Figure 4.5) to provide improved understanding on the production and mobilization of Re during weathering. In combination with the dissolved Re yield, and estimated CO_2 release from OC_{petro} oxidation, the paired catchment study provides new insight on the roles of supply-limitation versus kinetic limitation for oxidative weathering across river catchments.

4.5.1 Limited weathering signal in solid samples

The high physical erosion rates in the Laval catchment result in a pervasive gully morphology with steep slopes that are often bare of vegetation and soil (Mathys and Klotz, 2008). While the Brusquet catchment has a lower catchment-average sediment yield (Table 4.1), ~13 % of the catchment represent exposed bedrocks and erosion rates can be high on these steep slopes. The rapid erosion limits the time that material resides in the near-surface weathering zone. The total sediment yield of 18,306 t km^{-2} yr^{-1} (averaged between the two years) in the Laval (Table 4.1) equates to an erosion rate of ~9 mm yr^{-1} (for a ρ = 2 t m^{-3}). Given the regolith thickness of ~10 cm (Maquaire et al., 2003; Mathys and Klotz, 2008), this material thus resides in the catchment for only a decade. The chemical weathering signal of the regolith is thus expected to be uncommon, compared to sites with low denudation (e.g. Chapter 3 and Petsch et al., 2000). Indeed, this is supported by the observation that the river suspended sediments, bed loads and surface rock samples are indistinguishable in terms of their relative abundance of Re (Figure 4.3), and supports previous work where very high mechanical erosion exports large amounts of sediment with minor evidence for weathering (Graz et al., 2012).

On steep sections of exposed shale in the Brusquet catchment, we also find no clear evidence for significant weathered material in the landscape. In two regolith profiles sampled at a track cut (Figure 4.1) we observe a decrease in Re/Ti ratios in the upper three samples (Figure 4.4), which could indicate oxidation of Re-bearing phases, implying loss of Re to stream water. In addition, there is evidence for negligible Re enrichment in the near surface, suggesting minor net contributions from atmospheric deposition. However, the Re/Ti ratios in the bottom-most sample of both profiles is lowest. This could result from lithological heterogeneity within the marl, which has cm-scale bedding of OC-rich mud-sediments and Ca/Mg-carbonates (Antoine et al., 1995), making it difficult to definitively track loss of Re in these profiles. Alternatively, it could reflect partial leaching of Re produced during oxidative weathering, and accumulation in parts of the weathering profile, where it may be flushed by water, and/or mobilized as part of the suspended load (see also Section 4.5.4).

The solid samples, while showing only minimal evidence for weathering loss due to the high erosion rates, do provide insight on the source and host phase of Re. The mean Re/OC ratio in bed load samples from the Laval at $4.1\pm0.3\times10^{-7}$ g g^{-1} is higher than the Brusquet at $1.6\pm0.2\times10^{-7}$ g g^{-1}. The contrast is likely to reflect the depositional environment at time of burial (Colodner et al., 1993; Sheen et al., 2018), e.g. during the deposition of Toarcian black marls in the Brusquet, compared to the Callovo-Oxfordian marls in the Laval. The Re/OC ratios in the Laval and Brusquet are consistent with ratios measured in other sedimentary rocks (Figure 4.3), which could suggest a common host and role of OC_{petro}. However, dispersed sedimentary pyrite is also common in the marl bedrock here (Graz et al., 2012), and may contain similar amount of Re as in

OC_{petro} (Miller et al., 2011). To estimate the quantity of Re hosted in sulfide minerals, we use the pyrite vein sample from the Laval which has Re/S ratio of 3.25×10^{-3} pmol μmol^{-1}. If we assume that all sulfur in the bed load is derived from sulfides, then the S concentration of 50,472 μmol kg^{-1} would result in a Re concentration of 164 pmol kg^{-1}. This is ~1.4% of the Re concentration in bed load, suggesting a negligible contribution of Re from sulfides. Further constraint could come from sequential extractions to isolate the sulfide fractions (Matamoros-Veloza et al., 2011; Newton et al., 1995). Here we will turn to the stream water to further explore the source of dissolved Re.

4.5.2 Source of dissolved Re from sulfides and OC_{petro}

Previous work has established that in catchments with moderate to high rates of denudation, the main source of Re to the dissolved load of rivers is rock weathering (Colodner et al., 1995; Miller et al., 2011) and that Re is enriched in OC-rich sedimentary rocks (Colodner et al., 1993; Dalai et al., 2002; Georgiev et al., 2012; Horan et al., 2019). However, the role of OC_{petro} versus sulfide minerals as the host of Re remain poorly constrained in most settings (Miller et al., 2011). Sulfides form under anoxic environments during organic matter preservation and when they are exposed to the near-surface, the reaction kinetics of sulfide minerals are often faster than oxidation of OC_{petro} (Chapter 3, Bolton et al., 2006; Jaffe et al., 2002). Previous work has used ratios of dissolved ions to identify Re contributions from OC_{petro} and sulfide minerals, in addition to their potential input from silicates (Dalai et al., 2002; Horan et al., 2019). The Laval and Brusquet catchments provide a case study where sulfide content (Graz et al., 2011) and

sulfide oxidation rates (Chapter 5) are both high, allowing us to explore the role of sulfides in the supply of Re to streams and rivers.

Here we adopt a mixing model approach which uses Re/Na and Re/SO_4 ratios (Horan et al. 2019) to explore and quantify the sources of Re to the dissolved load. Generally, silicate minerals are Re poor and have a low Re/Na ratio. Horan et al. (2019) defined the silicate end-member with Re/Na ratios between 2×10^{-3} and 4×10^{-2} based on a range of measurements of mafic rock samples and Icelandic rivers draining basalts. In this study, we use improved constraint on a felsic end-member, which is likely to be more representative in most clastic sediments, using a lower Re/Na range (2.4×10^{-4} – 2.2×10^{-3}; Table 4.5 and Figure 4.7) as a silicate end-member, based on a Re/Na ratio in Himalayan crystalline rocks (2.4×10^{-4}; Dalai et al., 2002) and new insights from plagioclase feldspar (anorthosite) and rivers draining granite catchments in the Andes (Dellinger et al., In prep.).

The sulfide end-member is defined locally, due to high rates of pyrite oxidation occurring in these catchments (Chapter 5). Samples collected at low flow have extremely high SO_4^{2-} concentrations, ranging between 6.1 mmol l^{-1} and 16.3 mmol l^{-1} in the Laval and between 3.6 mmol l^{-1} and 5.3 mmol l^{-1} in the Brusquet. These low flow samples are characterized by lower Re concentrations, between 1.0 pmol l^{-1} and 6.9 pmol l^{-1} in the Laval, and between 0.4 pmol l^{-1} and 2.0 pmol l^{-1} in the Brusquet. The resulting Re/SO_4 ratios during low flow are between 9.1×10^{-5} pmol μmol^{-1} and 7.1×10^{-4} pmol μmol^{-1} in the Laval, and between 9.3×10^{-5} pmol μmol^{-1} and 5.6×10^{-4} pmol μmol^{-1} in the Brusquet (Table 4.5; Figure 4.7A). These inferred end-members are supported by seep and porewater samples collected in the Laval, which have Re/SO_4 ratios as low as

3.1 ± 2.1×10^{-4} pmol µmol^{-1} (±1SD n=4), within the range of the low flow samples. The low flow and seep samples from Draix are in the same location of the mixing domain (low Re/SO_4 and low Re/Na – Figure 4.7) as the sulfide end-member suggested by Horan et al. (2019), but is now much better constrained. In terms of assigning an end-member, this can be based on the median Re/SO_4 value of low flow samples or the minimum Re/SO_4 across the sample set. The former is likely to provide a minimum estimate of the proportion of Re from OC_{petro}. The latter recognizes that OC_{petro} oxidation appears to be occurring across all seasons (Soulet et al., 2021).

Table 4.5. The end-members for determining the Re source. For the sulfide end-member, two approaches are tested: Method 1 using the median Re/SO_4 ratio of all low flow samples and Method 2 using the minimum Re/SO_4 ratio of all low flow samples. See text for details.

End-member	**Catchment**		**n**	**Re/Na Min**	**Re/Na Max**	**Re/Na Median**	**Re/Na SD**
Silicate	Both		4	2.4 × 10^{-4}	2.2 × 10^{-3}	9.7 × 10^{-4}	9.2 × 10^{-4}
End-member	**Catchment**	**Method**	**n**	**Re/SO_4 Min**	**Re/SO_4 Max**	**Re/SO_4 Median**	**Re/SO_4 SD**
Sulfide	Laval	1	29	9.1 × 10^{-5}	7.1 × 10^{-4}	2.3 × 10^{-4}	1.4 × 10^{-4}
	Laval	2	1	9.1 × 10^{-5}	-	-	-
	Brusquet	1	16	9.3 × 10^{-5}	5.6 × 10^{-4}	1.6 × 10^{-4}	1.1 × 10^{-4}
	Brusquet	2	1	9.3 × 10^{-5}	-	-	-

To quantify the relative contribution of mineralogical Re sources for each water sample, we use the following assumptions: i) Na^+ in stream water is derived from weathering of silicate minerals and atmospheric deposition, ii) SO_4^{2-} in stream water is derived from weathering of sulfide minerals and atmospheric deposition, and iii) measured dissolved Re concentration in stream water is derived from weathering of silicate, sulfide and OC_{petro} minerals. The standard

mixing equations were applied to partition the Re source for each individual sample:

$$Re_{sil} = \left(\frac{Re}{Na}\right)_{sil} \times Na^{*} \quad (4.2)$$

$$Re_{S} = \left(\frac{Re}{SO_4}\right)_{S} \times SO_4^{*} \quad (4.3)$$

$$Re_{OC} = Re_{tot} - Re_{sil} - Re_{S} \quad (4.4)$$

where "sil", "S", "OC" and "tot" refer to silicate, sulfide, OC_{petro} and total concentrations and ratios, and Na* and SO_4* were corrected for atmospheric inputs. Uncertainties were assessed by running 10,000 simulations, accounting for the spread of the silicate and sulfide end-member ratios. The values were varied across normal probability density function with the observed standard deviations and the median value (Table 4.5). The mean value of all 10,000 computed models ±1SD is reported as the final value of Re proportion from different sources on each sample. The two choices of sulfide end-member (median value vs. minimum value) return Re_{OC} mean values (Equation 4.4) within uncertainty of each other (Table S4.3, Supplementary materials). Results obtained from the first method are used to provide a conservative estimate for the rest of the discussion.

The mixing analysis returns the absolute concentration of Re_{OC} (Equation 4.4) and Re_S (Equation 4.3) to the dissolved Re load for each sample. In the Laval, the mean proportion of Re_{OC} in Re_{tot} (concentration) is 41±25 % (n=87, ±1SD), while it is 57±34 % (n=50, ±1SD) in the Brusquet. The large variability around the mean proportion of Re_{OC} in both catchments may be explained by seasonality (Figure 4.7B) in climate factors, such as temperature and runoff as discussed in the following.

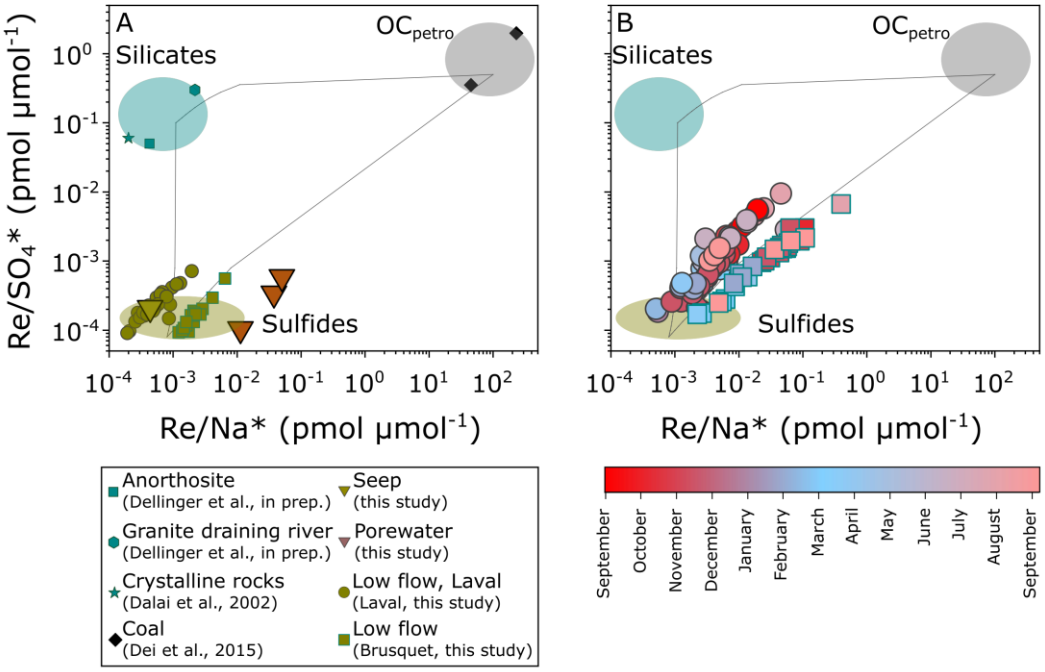

Figure 4.7: Mixing model for dissolved Re source partition. A: Locally defined sulfide end-member (low flow samples, porewaters, seep). **B:** Time series stream water samples collected in the Laval (circles) and the Brusquet (squares), color-coded by collection day in a calendar year. The model is adopted from Horan et al. (2019).

4.5.2.1 Decoupling of OC_{petro} and sulfide weathering

To investigate the variability in the Re source we first explore the discharge versus proportion of Re_{OC} (%) and Re_S (%) for the Laval and Brusquet (Figure 4.8). In both catchments the Re_{OC} dominates the Re export (up to 100% in Figure 4.8A and B) at high discharges. In contrast, at low discharges (<10^2 l s^{-1} in the Laval and <10^1 l s^{-1} in the Brusquet) the export of Re_S presents a more important contribution, up to ~40% in the Laval and up to ~60% in the Brusquet (Figure 4.8C and D). This observation may suggest a decoupling of the OC_{petro} and sulfide weathering fronts in the studied catchments. The dominance of Re_{OC} during the high flow regime implies that the OC_{petro} weathering front is located closer to the surface, while the sulfide oxidation extends deeper in the subsurface. Such a decoupling of weathering has been observed in several other studies (Chapter 3,

Jaffe et al., 2002) and is attributed to faster oxidation kinetics of sulfide minerals compared to OC_{petro} oxidation (Bolton et al., 2006; Williamson and Rimstidt, 1994).

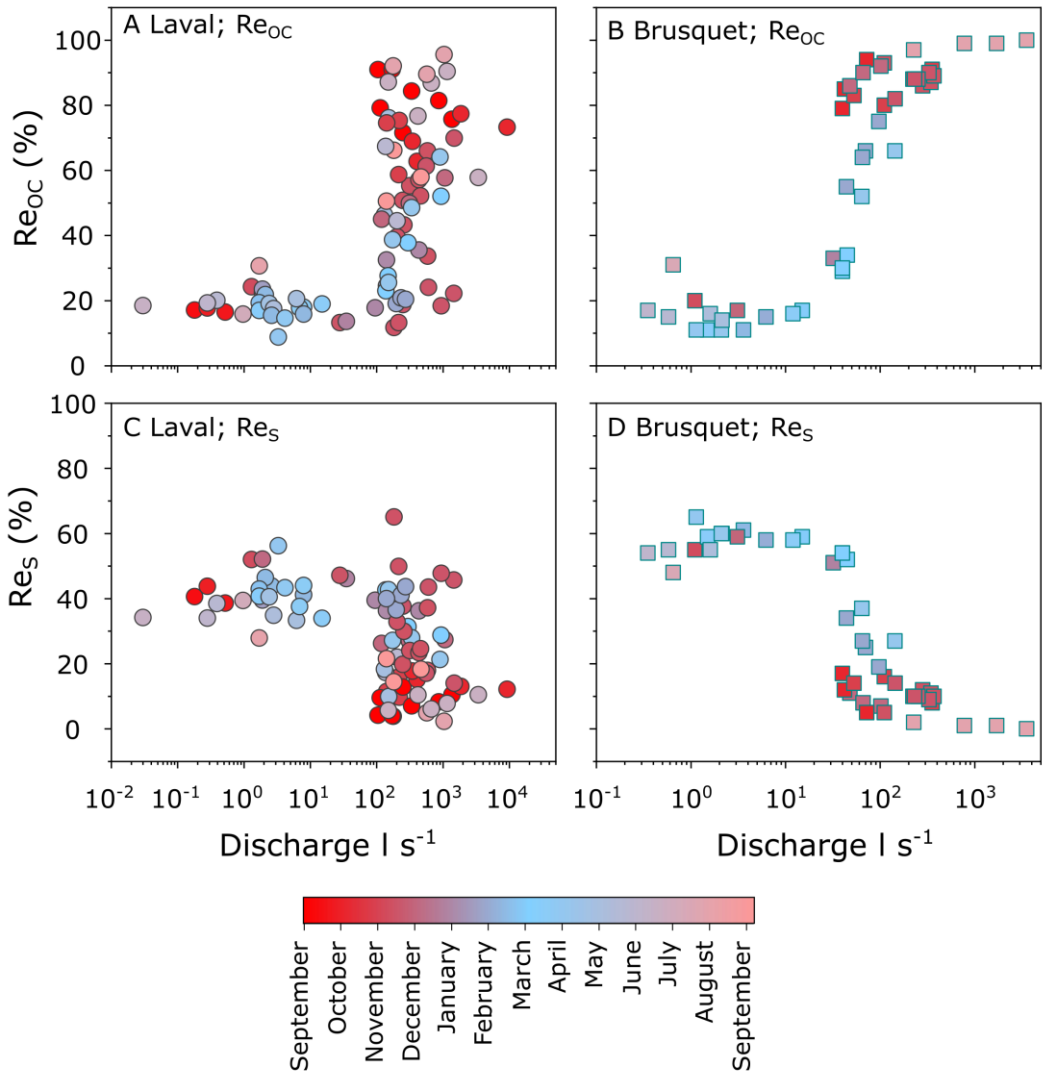

Figure 4.8: Discharge dependency on the relative proportions of Re associated to OC_{petro} (Re_{OC}, %) and S (Re_S, %). A and C: The Laval catchment. **B and D:** The Brusquet catchment. Samples are color-coded based on a sampling day of the year.

Furthermore, we observe seasonal patterns in the relative proportion of Re_{OC} and Re_S during the high flow regime (>10^2 l s^{-1} in the Laval, >10^1 l s^{-1} in the Brusquet) in both catchments (Figure 4.8). The relative proportion of Re_{OC} during the winter and spring months is between ~20% and ~50%, while in summer and

autumn months the Re_{OC} contribution can reach up to 100% in both catchments. To answer the question what is causing these higher relative proportions of Re_{OC} in a summer and autumn seasons, and lower relative proportions of Re_{OC} in a winter and spring seasons (both with similar ranges in discharge) we must consider: i) the production of oxidized Re in the weathering zone; and ii) the mobilization of the produced Re during flood events.

4.5.3 Climate and erosion control on Re production and mobilization

4.5.3.1 Temperature control on Re production in the Laval

In the Laval catchment, the dissolved Re concentrations during flood events show a striking seasonality (Figure 4.9). The absolute Re concentration varies profoundly in the 09/2016–09/2017 observation period, with the highest concentrations of 37.1±4.6 pmol l^{-1} (11/09/16; n=3; ±1SD) measured during a September flood event, and the lowest concentrations of 2.0±0.4 pmol l^{-1} (05/02/17; n=4; ±1SD) measured during a February flood event. This pattern is repeated in the 09/2017–09/2018 observation period, with the highest concentrations of 16.2±3.3 pmol l^{-1} (04/08/18; n=3; ±1SD) measured in a storm event in August, and the lowest concentrations of 3.2±0.3 pmol l^{-1} (11/03/18; n=4; ±1SD) measured in a March flood event (Figure S4.2, Supplementary materials). During high flow events, Re concentrations show minimal dilution and a chemostatic behavior with increasing discharge (Figure 4.9). For example, the steepest negative slopes (b coefficient in a power law: $y=a\times x^b$) are observed in September 2016 flood events ($slope_{11/09/2016}$ = -0.26, $slope_{12/09/2016}$ = -0.18), while all the following events (i.e. winter, spring, summer) exhibit positive slopes between +0.04 and +0.13 (Figure 4.9). This behavior contrasts with all major ions

that are increasingly diluted during high flow (Chapter 5, Figure 5.3, p177) and show no flood-event scale variability.

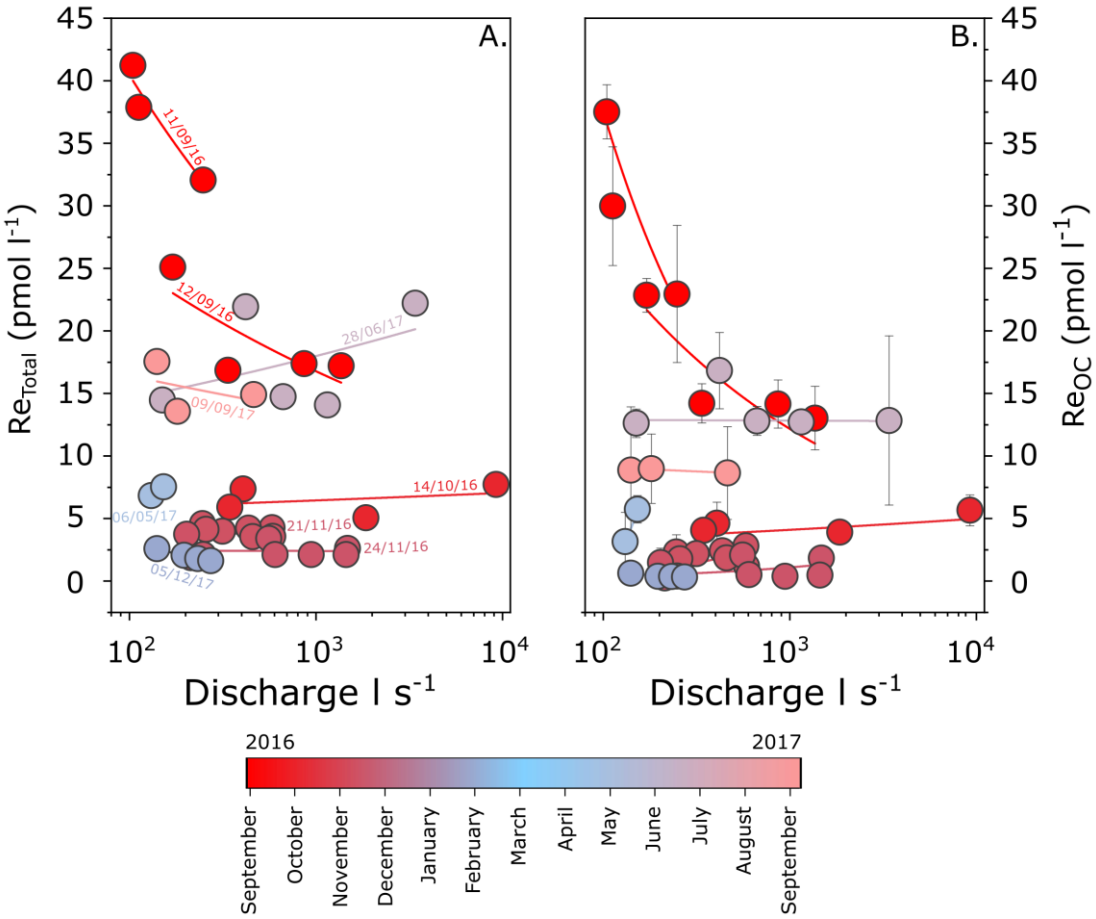

Figure 4.9: Inter-annual seasonal variability in Re concentrations within high flow event samples in the Laval. Samples for the first observation period: 09/2016 – 09/2017 are shown. Each storm event is color-coded by the sampling date. Lines represent a power law fit through a single storm event. **A:** Total Re concentration (Re_{Total}) and **B:** Re associated to OC_{petro} (Re_{OC}). Seasonal variability for the second year (09/2017–09/2018) shows a similar trend and is shown in the Supplementary material, Figure S4.2.

In summer, higher temperatures may govern the OC_{petro} oxidation through increased kinetics reactions and microbial activity (Hemingway et al., 2018; Kump et al., 2000; Petsch et al., 2000). Direct measurements of CO_2 emissions in the shallow weathering zone of the Laval catchment (Soulet et al., 2021) suggest that OC_{petro} oxidation rates are highest in the summer months. In the absence of continuous flushing of the weathering zone by water, this could lead to an

accumulation of oxidized Re in the shallow, near-surface weathering zone. During a subsequent intense rainfall event, rapid surface runoff would then mobilize these weathering products and export them from the catchment to the stream. In the winter months, colder temperatures seem to be related to a reduction of OC_{petro} oxidation rates (Soulet et al., 2021) and thus Re production. Any subsequent high flow event would therefore produce water with lower Re concentration.

To investigate the temperature correlation with the reaction kinetics of Re production we study Re_{OC} concentrations measured at low flow regime and air temperatures (T) averaged over 7-and 30-days before the sample collection (Figure 4.10). The Re_{OC} concentrations in the low flow samples provide a metric for Re production from OC_{petro} oxidation in the weathering zone, with hydrological conditions more similar between samples. We model the relationship by fitting an exponential growth model, $y=y_0 \times \exp(\alpha T)$ in Figure 4.10, with correlation coefficients (r^2) of 0.49 (7-days T average) and 0.52 (30-days T average) and a growth coefficient (α) of 0.08±0.02 (7-days T average) and 0.1±0.02 (30-days T average). The positive correlation is also observed when temperature is plotted against total Re concentrations, with r^2 of 0.59 (7-days T average) and 0.55 (30-days T average). The good correlation between the short (7-days) T interval and longer (30-days) T interval and Re_{OC} concentrations (Figure 4.10) suggests that reaction kinetics of OC_{petro} oxidation is sensitive to short-term as well as long-term (seasonal) temperature changes.

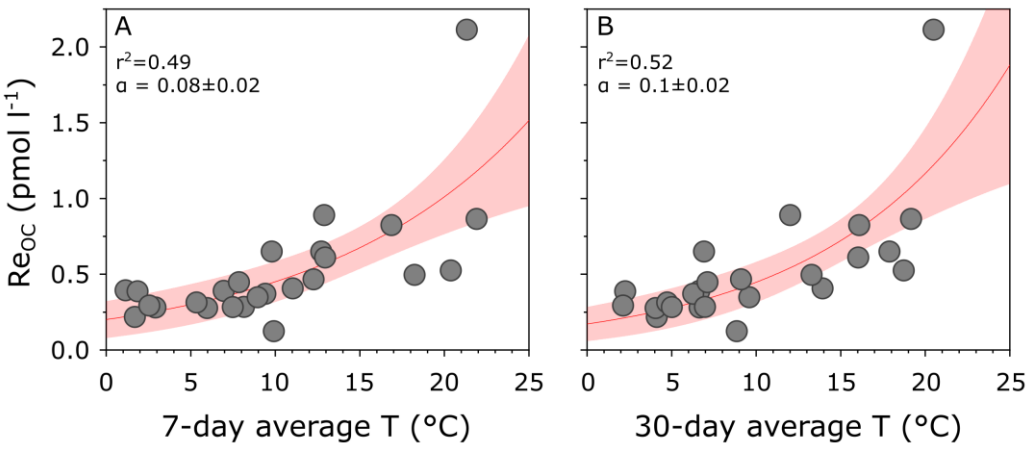

Figure 4.10: Temperature sensitivity on the Re_{OC} in the low flow Laval samples. The exponential growth model is described by the correlation coefficient (r^2) and the growth coefficient (α). **A:** Air temperature is averaged over 7-days before the sample collection. **B:** Air temperature is averaged over the 30-days before the sample collection.

These results can be directly compared to the measured CO_2 fluxes from a marl outcrop in the Laval (Soulet et al., 2021), where the positive correlation between the CO_2 release partitioned for OC_{petro} source with temperature is described with a similar exponential growth model (r^2=0.44) with a growth coefficient (α) of 0.06±0.02. The growth parameter based on the dissolved Re_{OC} data and the 7-day T average (α=0.08±0.02) is within uncertainty of the CO_2 gas flux measurements (Soulet et al., 2021). These two independent methods give strong evidence that higher oxidation rates of OC_{petro} occur during higher air temperatures in a kinetically-limited regime. In a global application, these results suggest that in a future warmer climate, the chemical weathering of OC_{petro} and related CO_2 release to the atmosphere may be enhanced, which is an important parameter for future climate studies.

4.5.3.2 Less pronounced seasonality in Re production in the Brusquet

The stark seasonal shifts in flood-event Re concentrations observed in the Laval (Figure 4.9) are far less pronounced in the Brusquet catchment (Figure S4.3, Supplementary materials). For example, in the 10/2016 – 10/2017 observation period, the highest Re concentrations of 2.5±0.5 pmol l^{-1} (14/10/16; n=3; ±1SD) were measured during an October flood event, and the lowest concentrations of 1.5±0.2 pmol l^{-1} (05/02/17; n=4; ±1SD) were measured during a February flood event. This could mean that kinetic controls on Re production are not the same in both catchments. The lower sediment yield in the Brusquet (Table 4.1) could suggest that Re production is limited by the supply of OC_{petro} to the near-surface, oxic-weathering zone. Across a set of global catchments, the Re yield has been shown to increase with erosion rate (Hilton et al., 2014; Hilton and West, 2020; Horan et al., 2017), suggesting a limitation of oxidation reactions by sediment supply at low to moderate denudation rates.

In a supply-limited environment, silicate weathering rates are thought to be less sensitive to temperature differences than in a kinetically-limited regime (Riebe et al., 2004; West et al., 2005; West, 2012). Here, we explore the temperature feedback on the OC_{petro} weathering rates in the supply-limited Brusquet by plotting air temperature averaged over 7- and 30-days before sample collection with Re_{OC} concentrations at low flow (Figure 4.11). In both cases, the correlation with temperature is less clear compared to the kinetically-limited regime in the Laval (Figure 4.10), however, the correlation coefficient (r^2) increases to 0.59 when the 30-days temperature average is plotted against the Re_{OC} concentrations. This improvement in correlation suggests that in a supply-limited environment, OC_{petro} oxidation rates are not govern by short-term

(weekly) changes in air temperatures, but are, to some degree, correlated to the longer-lasting seasonal variations in the air temperature.

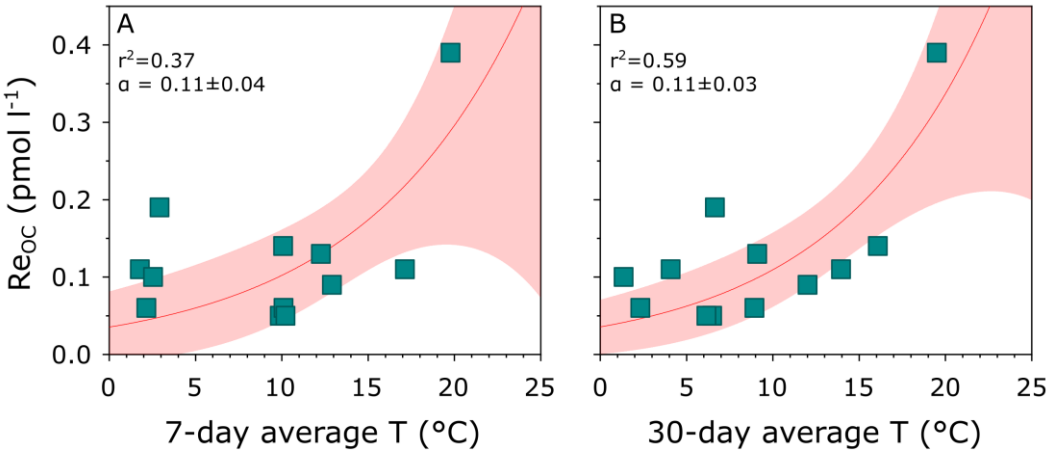

Figure 4.11: Less pronounced temperature sensitivity on the Re_{OC} in the low flow Brusquet samples. The exponential growth model is described by the correlation coefficient (r^2) and the slope parameter (α). **A:** Air temperature is averaged over 7-days before the sample collection. **B:** Air temperature is averaged over 30-days before the sample collection.

The weaker correlation between temperature and Re_{OC} concentrations in the Brusquet may also reflect the forested slopes and near-surface organic soils which became more widespread following afforestation in this catchment. While soil and vegetation may partly buffer temperature changes in the oxidative subsurface, it may also navigate hydrological pathways operating in the catchments. The vegetation and soil cover can slow down and divert flow paths that deliver solutes to the stream. Therefore, Re mobilization could be less efficient in the Brusquet compared to the Laval where bare rock outcrops are more common. In the first observation year, all sampled storm events in the Brusquet display low discharge (~25 to 375 l s^{-1}) and minor annual variability in Re concentration (Figure S3, Supplementary materials). Towards the end of the second observation year, in August 2018, the largest storm event in the last 30 years occurred at the study site. Water discharge in the Brusquet reached to a

maximum value of 3,568 l s^{-1} and Re concentrations reached above 20 pmol l^{-1} (Figure 4.12). This is the highest Re concentration measured in the Brusquet during the two years observation period. Monitoring this single storm event gives direct evidence that large quantities of water are needed to move the weathered products from the weathering zones to the main stream in this catchment, which may have an important impact on annual Re flux estimates.

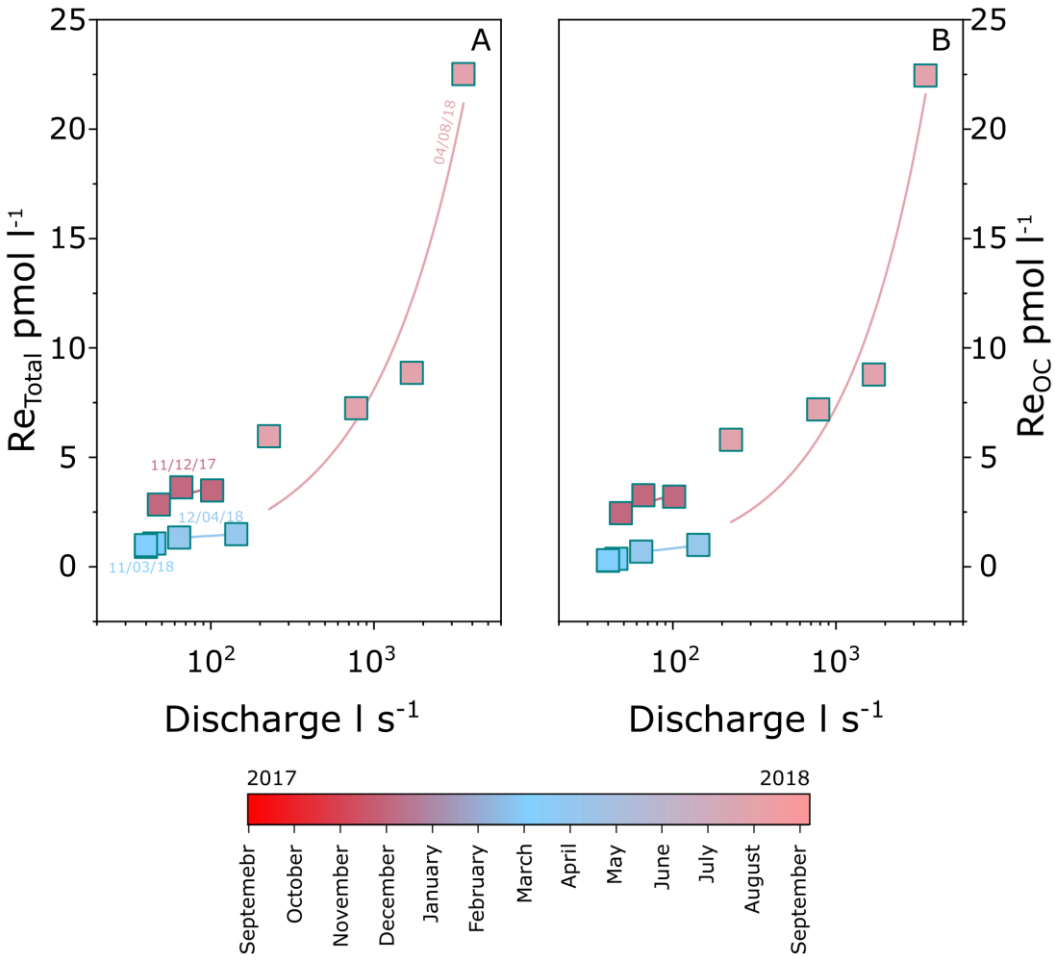

Figure 4.12: Inter-annual seasonal variability in Re concentrations within high flow event samples in the Brusquet. Samples for the second observation period: 10/2017 – 10/2018 are show. Each storm event is color-coded by the sampling date. Lines represent a power law fit through a single storm event. **A:** Total Re concentration (Re_{Total}) and **B:** Re associated to OC_{petro}

In summary, the high resolution Re concentration dataset studied here, revealed a striking seasonality in Re production and positive correlation with air temperature in a high erosive (kinetically-limited) regime of the Laval catchment. In contrast, in the Brusquet, where erosion rates are lower and weathering is supply-limited, the seasonality and temperature correlation is less pronounced. However, the hydrological regime may have an important impact on Re export from this catchment.

4.5.4 Application of the Re proxy for OC_{petro} oxidation

The CO_2 release from oxidation of OC_{petro} ($J_{OCpetro}$), can be estimated from the dissolved Re yield from OC_{petro}, J_{ReOC}, following the approach from Horan et al. (2019) in Equation 4.5.

$$J_{OC_{petro}} = J_{ReOC} \times \left(\frac{OC}{Re}\right) \times (1 - f_{graphite}) \quad (4.5)$$

The $f_{graphite}$ is the graphitic fraction of OC_{petro}, a term to account for OC_{petro} which may be physically and chemical resilient to weathering (Galy et al., 2008). However, graphite is likely to be negligible in both catchments based on the low thermal maturity of organic matter in marls from the catchment (Copard et al., 2006). The (OC/Re) ratio is the average value from the bed load samples ($4.1\pm0.3\times10^{-7}$ g g^{-1} in Laval; $1.6\pm0.2\times10^{-7}$ g g^{-1} in Brusquet). This ratio assumes that all Re in the solid samples is sourced from OC_{petro} (Section 4.5.1), which represents a significant uncertainty and needs to be better constrained in future studies. The $J_{Re\text{-}OC}$ yields are estimated from the total annual Re yields and the partitioning of Re source in the dissolved load (Table 4.4, Figure 4.7). The proportion of the dissolved Re flux sourced from OC_{petro} is 54±3 % for the Laval and 77±5 % for the Brusquet (averaged between the two sampling years).

The Re-derived estimates of OC_{petro} oxidation are remarkably similar for the Laval and Brusquet. This is because while $J_{OC\text{-}Re}$ is higher in the Laval, the Re/OC ratio in the Brusquet is notably lower. The OC_{petro} oxidation yields in the first observation period are 0.3±0.05 tC km^{-2} yr^{-1} in the Laval and 0.2±0.02 tC km^{-2} yr^{-1} in the Brusquet. Rates increase in the second observation period to 0.5±0.21 tC km^{-2} yr^{-1} and 0.4±0.22 tC km^{-2} yr^{-1}, for the Laval and Brusquet, respectively (Table 4.6).

Table 4.6. Estimates of CO_2 release from OC_{petro} weathering in the Laval and Brusquet.

Catchment	Area	Observation period	SSY	Re_{OC} flux	Re/OC	CO_2
	km^2		t km^{-2} yr^{-1}	x10^{-4} mol km^{-2} yr^{-1}	x10^{-7} g g^{-1}	tC km^{-2} yr^{-1}
Laval	0.86	11/09/2016-10/09/2017	8,693	6.2 ±1.0	4.1 ± 0.3	0.3 ± 0.05
		11/09/2017-10/09/2018	15,829	11.0 ± 4.7		0.5 ± 0.21
Brusquet	1.07	14/10/2016-13/10/2017	45	1.6 ± 0.2	1.6 ± 0.2	0.2 ±0.02
		14/10/2017-13/10/2018	492	3.6 ± 1.9		0.4 ± 0.22

In the Brusquet, the vegetation cover may omit physical rock degradation and availability of fresh oxygen, resulting in low OC_{petro} oxidation rates. However, the estimated low OC_{petro} oxidation yields are surprising for the Laval catchment. There, exposed surfaces of marl lithology in combination with Mediterranean-alpine climate (i.e. hot and dry summer and cold winters with freeze-thaw cycles) form an ideal environment for enhanced physical and chemical degradation of rocks. The oxidation rates presented for the Laval are also much lower than Re-proxy based measurements from other high erosive environments; e.g. Taiwan, (4–20 tC km^{-2} yr^{-1}; Hilton et al., 2014), or catchments draining New Zealand's Southern Alps (14–30 tC km^{-2} yr^{-1}; Horan et al., 2017). The Laval is the only catchment where we also have direct measurements of CO_2 flux from chambers, which capture processes in the near-surface weathering zone (Soulet et al., 2018). The CO_2 release from oxidative weathering of OC_{petro} was, on average, 76±54 mgC m^{-2} day^{-1} (n=10) for a chamber near the Laval stream on an exposed rock outcrop (Soulet et al., 2021). While these chamber-based measurements are inherently local, and do not capture the catchment-average, this value up-scaled to the catchment would be 28±20 tC km^{-2} yr^{-1}, which is ~100-times higher than the Re-proxy based estimates.

To examine these discrepancies, we note that the direct CO_2 measurements have also been used to partition the fluxes between OC_{petro} oxidation (OC) and carbonate dissolution by sulfuric acid (IC). The IC:OC source ratios were measured as 2.6 and 5.3 in two chambers (Soulet et al., 2021). Given the CO_2 release estimated from carbonate dissolution by sulfuric acid using dissolved ions 22.1 tC km^{-2} yr^{-1} (averaged over 2 sampling years; Chapter 5, Table 5.3, p187), an IC:OC ratio of 5.3 would suggest OC_{petro} oxidation rates of

~4.2 t km^{-2} yr^{-1}. This is ~10-times higher compared to estimates made with the dissolved Re proxy presented above (~0.4 t km^{-2} yr^{-1}; averaged over the two sampling years), and so indicates the discrepancy in the Re proxy is also present in the ratio of weathering pathways.

However, the mismatch between the CO_2 release rates measured in the local chambers and catchment-wide estimates presented here may reflect the scaling issues between the two methods. The Laval catchment exhibit a number of specific catchment characteristics, which could indeed result in low catchment-wide average CO_2 release rates from OC_{petro} oxidation. For example, the extremely thin weathering zone (~cm thick) and the absence of vegetation may limit the reactive surface area of minerals in the Laval. Another feasible explanation is that extremely high suspended sediment yields promote the export of the oxidized Re through the solid load, rather than in the dissolved load (Table 4.4). Additionally, the relatively low runoff in the catchment (367 mm yr^{-1}) and high rates of transpiration and evaporation (runoff:precipitation ratio of 0.38) may promote the precipitation of secondary phases (e.g. secondary gypsum) that could capture some ions produced during weathering. In the Laval, suspended and bed load samples are the product of physical erosion of the regolith and bedrock, and these show minimal evidence for weathering losses, as previously discussed by Copard et al. (2006) and Graz et al. (2011). Here, we can use the Re concentration measured in those materials to estimate Re export in the solid load. This assumes that the samples here are representative of the total flux, and so these estimates have considerable uncertainty. Suspended sediment Re transfer is 1602±639×10^4 mol km^{-2} yr^{-1} (average between the two years; Table 4.4Table 4.4), which is ~100-times higher than the Re export through dissolved load

($16\pm7.7\times10^{4}$ mol km^{-2} yr^{-1}). Thus, only a relatively small faction of this Re would need to have been oxidized but immobilized to explain the lower Re yield observed in the Laval.

In summary, several characteristics of the Laval catchment, such as low runoff, extremely thin weathering zone, limited surface area and high suspended sediment yield may indeed result in low OC_{petro} oxidation rates at this site. Therefore, further attention is required to fully understand the effect on weathering of the soft marl lithology on the atmospheric CO_2 and O_2 levels in these specific landscapes.

4.6 Conclusions

This study explored production and mobility of a trace element rhenium (Re) across a large gradient in physical erosion in a pair of marl-dominated catchments, the Laval and Brusquet, in the South French Alps. An unprecedented, high temporal resolution stream water sampling campaign was completed to measure dissolved Re and other weathering products across two years.

In the highly erosive Laval catchment, we found a pronounced seasonal variability in dissolved Re concentration in both a series of sequential high flow events, and during the low flow regime. Rhenium concentrations were up to ~10-times higher during the summer months compared to the winter months. This seasonality suggests a kinetic control on the production of Re in the weathering zone, and flushing of the produced Re from the near-surface during flood events. A close association was found between dissolved Re associated to OC_{petro} weathering (Re_{OC}) concentration at low flow and air temperature, which is consistent with a kinetic control on OC_{petro} oxidation in erosive catchments. The

strong temperature dependency on OC_{petro} and Re oxidation may have a profound application for the future warming climate, with expected higher CO_2 release rates from the oxidative weathering of sedimentary rocks. In contrast, in the supply-limited (less erosive) Brusquet the seasonal patterns are less pronounced in the high flow events. However, a less clear, but positive correlation was found between the Re_{OC} concentrations at the low flow regime and the 30-day air temperature average, which suggests that seasonal shifts in temperature may to some degree govern the OC_{petro} weathering also in a supply-limited environment.

The dissolved Re yields were surprisingly low in the highly erosive catchment of Laval (~16±7.1×10^{-4} mol km^{-2} yr^{-1}; averaged over the two years), when compared to global datasets. When we apply the Re-proxy for OC_{petro} oxidation, the carbon transfers are also low, and much lower than direct measurements of CO_2 release made in the shallow weathering zone of this catchment in other work. We estimate high Re export in suspended sediments is high (1,602±639×10^{-4} mol km^{-2} yr^{-1}) and suggest that some weathering products may be exported in the solid load, however, this requires further attention.

4.7 Supplementary materials

Table S4.1*. Cold seep and soil porewater chemistry sampled in the Laval catchment.*

Field ID	Sample Type	N	E	Date	Cl µmol	SO_4 µmol	Na µmol	K µmol	Mg µmol	Ca µmol	Re pmol
DRA16 19	*Seep*	44.14115	6.37208	04/08/2016	1873	12150	318	25.6	2353	2310	7.85
DRA17-37	*Seep*	44.14107	6.37482	30/03/2017	313	8631	4143	56.5	4429	4431	1.81
DRA18-110	*Seep*	44.14154	6.37283	25/09/2018	3033	10100	10107	72.9	3539	3054	-
DRA17-6	*Soil Pore water in colluvium*	44.14042	6.36307	26/03/2017	27	4761	56	48.9	3012	2370	2.79
DRAI17-51	*Soil Pore water in colluvium*	44.14042	6.36307	24/06/2017	26	6438	58	48.9	4073	3169	2.18
DRA18-03	*Soil Pore water in colluvium*	44.14047	6.36300	19/02/2018	22	11391	104	52.9	6036	5729	1.18

***Table S4.2**. Precipitation chemistry for the observation period 2016-2018 sampled at the Laval gauging station. Samples in grey were not used in the calculations of cycling input estimates.*

Field ID	Date	Daily precipitation Laval	Daily precipitation Brusquet	Cl	SO4	Na	Mg	Ca	Al	Zn	Mn	Re		Na/Cl
		mm day-1	mm day-1	µmol	µmol	µmol	µmol	µmol	µmol	pmol	pmol	pmol		
PL 12-9-16	11/09/2016	12.2	3.8	18	35	88	20	70	0.32	5841	72	1.12		4.97
PL 13-9-16	12/09/2016	18.0	15.3	13	25	75	16	49	0.08	5970	68	0.99		5.77
PL 16-10-16	14/10/2016	54	53.7	22	30	54	16	147	0.49	1062	17	0.31		2.45
PL 8-11-16	05/11/2016	37	59.9	20	19	45	15	133	0.13	3521	21	0.46		2.26
PL 22.11.16	21/11/2016	64	67.0	3	3	12	12	16	0.03	2444	10	<DL		4.32
PL 7.2.17	05/02/2017	26	23.4	6	10	16	15	80	0.12	1022	25	0.10		2.72
P 9.5.17	06/05/2017	19	14.9	15	63	28	30	87	0.21	3072	17	0.42		1.86
P 29.6.17	28/06/2017	34	27.0	17	21	16	13	45	0.22	4318	86	0.32		0.94
PL 11.9.17	09/09/2017	19	19.8	17	21	17	14	46	0.25	5250	39	0.25		0.96
PL_130318	10-11/03/2018	49	22.2	8	6	5	2	9	0.03	2812	19	0.10		0.72
PL_05062018	02/06/2018	44	10.2	4	7	6	7	23	0.05	2631	6	0.15		1.52
PL_06082018	04/08/2018	28.8	40.6	9	19	2	4	49	0.25	4261	35	0.97		0.24

***Table S4.3**. Statistics on the Re partition output when testing the mean Re/SO_4 (Method 1) and the minimum Re/SO_4 (Method 2) as a sulfate end-member.*

Catchment	pmol	Method	Min	Median	Max	Mean	SD
Laval	Re_{OC}	1	0.00	1.31	37.52	4.33	6.87
	Re_{OC}	2	0.01	1.84	38.58	4.87	7.16
	Re_S	1	0.00	1.01	4.11	1.20	0.67
	Re_S	2	0.01	0.46	1.71	0.54	0.30
Brusquet	Re_{OC}	1	0.05	1.08	22.44	1.99	3.49
	Re_{OC}	2	0.02	1.29	22.47	2.08	3.49
	Re_S	1	0.05	0.33	0.6	0.34	0.13
	Re_S	2	0.03	0.23	0.4	0.23	0.11

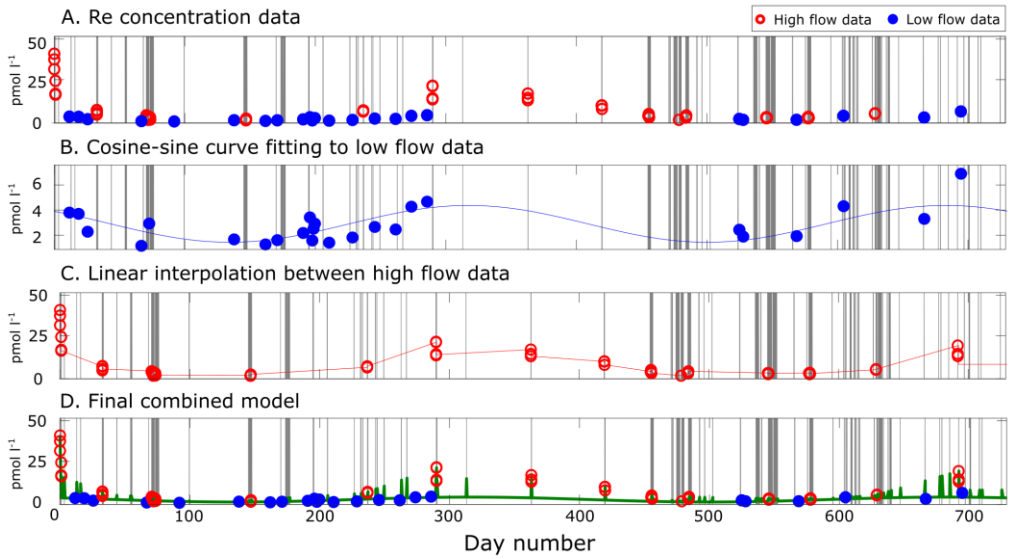

Figure S4.1: *Modelling steps for determining dissolved Rhenium (Re) concentrations for un-sampled periods. Example for the Laval dataset.* ***A:*** *Concentration separation into a low flow (blue) and high flow (red) regime.* ***B:*** *Seasonal variability in the low flow regime, modelled with a cosine-sine curve fit.* ***C:*** *Linear interpolation between the high flow samples.* ***D:*** *The final concentration model integrating low flow and high flow regime. The vertical grey bars represent time intervals, when discharge is above the low flow value, that is >28.5 l* s^{-1} *for the Laval dataset. For details see Chapter 2, Section 2.3.4, p44.*

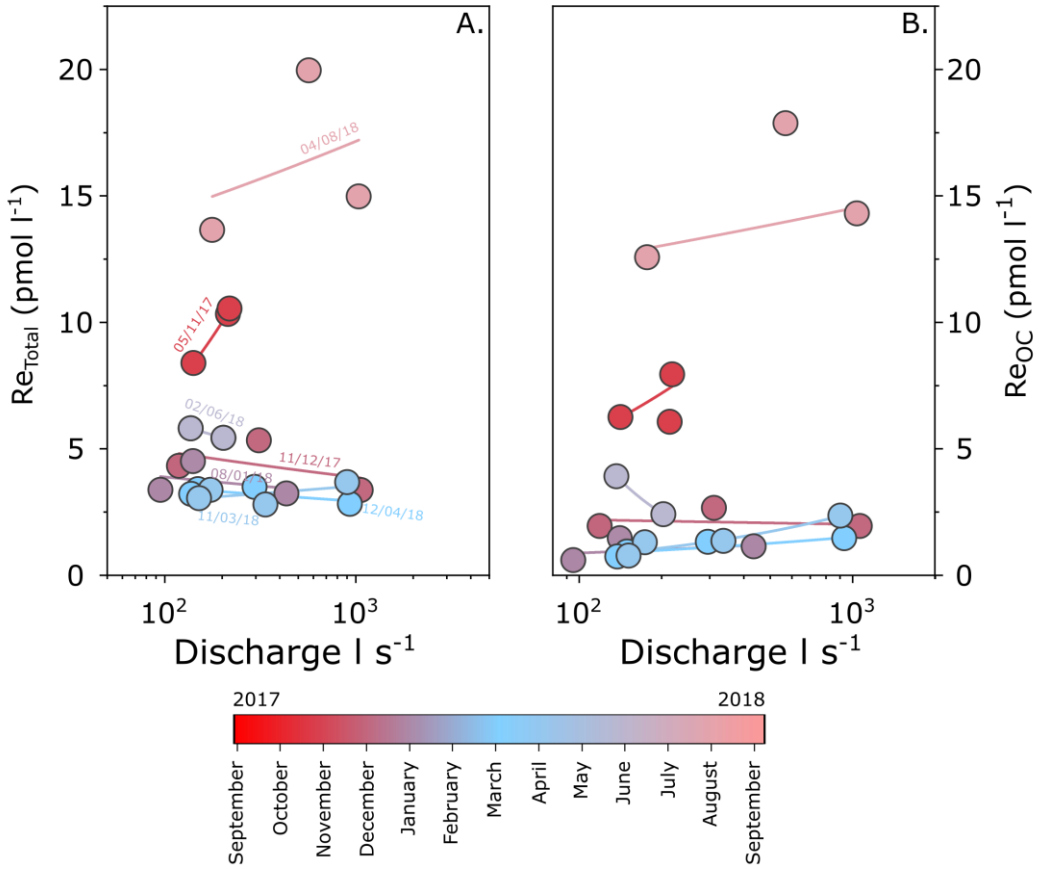

Figure S4.2: *Inter-annual seasonal variability in Re concentrations within high flow event samples in the Laval for the second sampling year (09/2017 – 09/2018). Each storm event is color-coded by the sampling date. Lines represent a power law fit through a single storm event.* ***A:*** *Total Re concentration (Re_{Total}) and* ***B:*** *Re associated to OC_{petro} (Re_{OC}).*

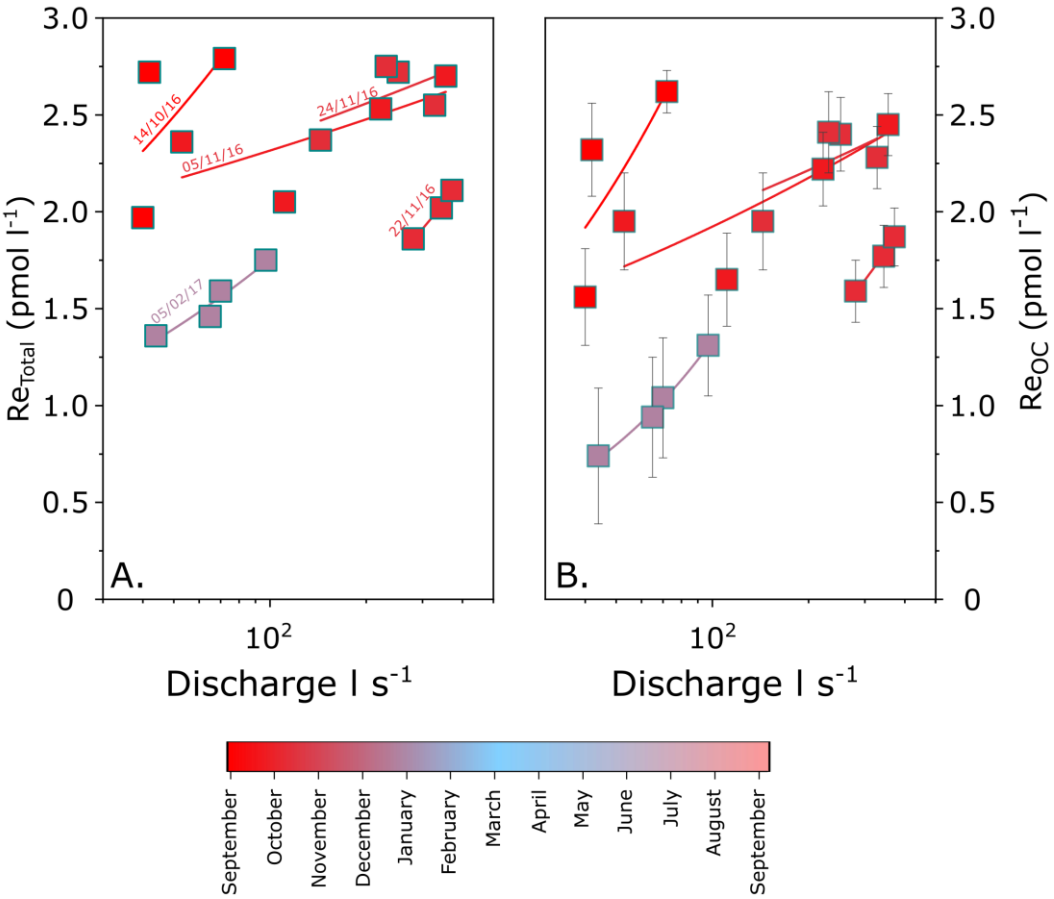

***Figure S4.3**: Inter-annual seasonal variability in Re concentrations within high flow event samples in the Brusquet for the first sampling year (10/2016 – 10/2017). Each storm event is color-coded by the sampling date. Lines represent a power law fit through a single storm event. **A:** Total Re concentration (Re_{Total}) and **B:** Re associated to OC_{petro} (Re_{OC}).*

CHAPTER 5
CO_2 release from carbonate weathering by sulfuric acid driven by seasonality in sulfuric acid production

The Laval catchment at the Draix-Bléone Critical Zone Observatory, South French Alps; Photo taken from the south ridge towards the catchment headwaters; October 2017; Photo: Robert G. Hilton

A version of this chapter will be submitted to a peer-reviewed journal.

The authors on this paper will be:
Mateja Ogrič[1], Mathieu Dellinger[1], Guillaume Soulet[2], Jordan Hemingway[3], Alexandra V. Turchyn[4], Sebastien Klotz[5], Caroline Le Bouteiller[5], Christian Schiffer[6] & Robert G. Hilton[1]

Affiliations:
[1]*Department of Geography, Science Laboratories, South Road, DH1 3LE Durham, UK.*
[2]*Institut Français de Recherche pour l'Exploitation de la Mer (IFREMER), Unité de Recherche 12 Géosciences Marines, F-29280 Plouzané, France.*
[3]*Department of Earth and Planetary Sciences, Harvard University, Cambridge, MA 02138*
[4]*Department of Earth Sciences, University of Cambridge, Cambridge, CB2 3EQ, UK*
[5]*Univ. Grenoble Alpes, INRAE, UR ETNA, 2 rue de la papeterie, BP 76, 38402 Saint-Martin-d'Hères, Cedex, 10 France.*
[6]*Department of Earth Sciences, Uppsala University, Villavägen 16, 75236 Uppsala, Sweden.*

Authors contributions:
The research design and project goals were devised by myself with guidance from Robert G. Hilton and Mathieu Dellinger. The samples were collected by myself, Robert G. Hilton, Mathieu Dellinger, Guillaume Soulet and Sebastien Klotz (time series sampling). The analytical work was carried out under supervision of Mathieu Dellinger. The extraction of $BaSO_4$ powders were prepared under supervision of Alexandra V. Turchyn, who measured $\delta^{34}S_{SO4}$, and Jordan Hemingway, who measured $\delta^{18}O_{SO4}$. The hydrological data were provided by Sébastien Klotz and Caroline Le Bouteiller. The chemical weathering fluxes were modelled with assistance of Christian Schiffer. Data processing and critical scientific evaluation was carried out with Robert G. Hilton and Mathieu Dellinger. The chapter was written and edited by myself, Robert G. Hilton and Mathieu Dellinger.

Abstract

Recent work has highlighted that the oxidation of sulfide minerals during weathering and the production of sulfuric acid can lead to a release of CO_2 from rocks to the atmosphere. However, catchment-scale estimates of the CO_2 release through sulfide oxidation coupled to carbonate weathering remain sparse. It is important to better constrain the mechanisms of sulfuric acid production and to determine how environmental variables (e.g. temperature, hydrology) may drive this CO_2 release. Here we study the stream water chemistry of two marl-dominated catchments with contrasting rates of physical erosion (the Laval and the Brusquet) in the Draix-Bléone Critical Zone Observatory, Provence, France. In the highly erosive Laval, cation partitioning suggests a dominance of carbonate (73±13 %) over silicate weathering, which is even more pronounced in the less erosive Brusquet (>92 %). The stable sulfur isotopic signature suggests sulfide oxidation is the dominant source of sulfate in these catchments. Examination of dissolved ion rations ($HCO_3/\sum Cat^+$, $SO_4//\sum Cat^+$) confirms that sulfuric acid governs mineral dissolution, rather than carbonic acid, accounting for 90±6 % and 63±9 % in the Laval and Brusquet, respectively. We find that carbonate dissolution by sulfuric acid is the dominant weathering pathway in both catchments, resulting in higher CO_2 release for the Laval (22.1±7.1 tC km^{-2} yr^{-1}) compared to the Brusquet (4.6±0.8 tC km^{-2} yr^{-1}). The CO_2 consumption rates by silicate weathering are lower than the CO_2 emissions from weathering in both catchments, at 1.3±0.3 tC km^{-2} yr^{-1} and 0.2±0.1 tC km^{-2} yr^{-1} in the Laval and Brusquet, respectively. Physical erosion is the primary control on the sulfuric acid weathering. However, in the more erosive catchment, we find that the rates are

moderated by seasonal changes in air temperature that control production of sulfuric acid, which is elevated in summer. From these seasonal patterns, it can be inferred that CO_2 release from sulfide oxidation may increase in a warmer climate.

5.1 Introduction

Sedimentary rocks, such as shales, carbonates, and sandstones underlay ~65 % of the total continental surface (Amiotte Suchet et al., 2003) and constitute one of the largest reservoirs of inorganic and organic carbon on Earth (Sundquist & Visser, 2005). Chemical weathering of these lithologies act to regulate atmospheric O_2 and CO_2 concentrations over geological time scales (Hilton & West, 2020); weathering of silicate minerals by carbonic acid is a long-term CO_2 sink (Chamberlin, 1899; Gaillardet et al., 1999; Maher and Chamberlain, 2014; Moon et al., 2014), whereas chemical weathering of carbonate minerals by sulfuric acid (Calmels et al., 2007; Torres et al., 2014) and the oxidation of rock organic carbon are long-term CO_2 sources (Hilton et al., 2014; Hilton and West, 2020; Petsch, 2014). The current estimate for the combined modern day CO_2 release during oxidative weathering of sulfides and rock organic carbon (40–140 Mt C yr^{-1}; Burke et al., 2018; Petsch, 2014; Torres et al., 2017) is of similar magnitude, although less well-constrained, as volcanic degassing (79±9 Mt C yr^{-1}; Plank & Manning, 2019). Obtaining quantitative knowledge of global and regional (e.g. catchment-scale) CO_2 weathering budgets (Hilton and West, 2020; Torres et al., 2017) and recognizing the controls on oxidative weathering (Hemingway et al., 2020; Turchyn et al., 2013) is of prime importance to understand the evolution of the long-term carbon cycle.

Chemical weathering is controlled by acid-base reactions, with carbonic (H_2CO_3) and sulfuric (H_2SO_4) acids being the main acidity sources involved in the dissolution of weathered minerals (Meybeck, 1987). Carbonic acid, produced either by dissolution of atmospheric CO_2 or CO_2 from soil respiration, in reaction with silicates produces alkalinity (Equation 5.1), resulting in a net CO_2 drawdown from the atmosphere (Equation 5.2).

$$2CO_2 + 3H_2O + CaAl_2Si_2O_8 \longrightarrow Ca^{2+} + 2HCO_3^- + Al_2Si_2O_5(OH)_4 \quad (5.1)$$

$$Ca^{2+} + 2HCO_3^- \longrightarrow CaCO_3 + CO_2 + H_2O \quad (5.2)$$

Carbonic acid weathering of carbonate minerals can influence atmospheric CO_2 concentrations on time-scale $<10^6$ years. On time-scale $>10^6$ years, Dissolved Inorganic Carbon (DIC) derived from carbonate weathering is removed from the ocean by carbonate precipitation and has no net effect on the atmospheric CO_2 (Gaillardet et al., 1999).

In contrast, oxidation of pyrite-rich lithologies can produce sulfuric acid (H_2SO_4) via reactions involving O_2 (Equation 5.3) iron redox cycling (Equation 5.4).

$$15O_2 + 14H_2O + 15FeS_2 \longleftrightarrow 8H_2SO_4 + 4Fe(OH)_3 \quad (5.3)$$

$$FeS_2 + 14Fe^{3+} + 8H_2O \longrightarrow 15Fe^{2+} + 2SO_4^{2-} + 16H^+ \quad (5.4)$$

Sulfuric acid can dissolve carbonates, and lead to an immediate release of CO_2 to the atmosphere (Equation 5.5). Alternatively, carbon from carbonate dissolution may enter the bicarbonate pool of river water, in which case the CO_2 release to

the atmosphere may be delayed by carbonate precipitation in the ocean (~10^6 yr; Equation 5.6; Berner & Berner, 2012; Torres et al., 2014).

$$CaCO_3 + H_2SO_4 \longrightarrow CO_{2\,(g)} + H_2O + Ca^{2+} + SO_4^{2-} \quad (5.5)$$

$$2CaCO_3 + H_2SO_4 \longrightarrow 2Ca^{2+} + 2HCO_3^- + SO_4^{2-} \quad (5.6)$$

Sulfuric acid can also dissolve silicate minerals, which does not directly impact atmospheric CO_2 budget, but has been shown to result in high concentrations of dissolved major elements in river water (Cras et al., 2007; Ross et al., 2018).

The relative importance of carbonic versus sulfuric acid weathering on the net carbon exchange between rocks and the atmosphere has been recognized by a growing number of studies (Blattmann et al., 2019; Bufe et al., 2021; Li et al., 2008; Spence and Telmer, 2005; Torres et al., 2016; Winnick et al., 2017). One of the main outcomes of this prior work is a positive correlation between physical erosion and pyrite oxidation rates, as first revealed in the Mackenzie river basin (Calmels et al., 2007) and supported more widely in Hilton & West (2020) by data from mountain catchments of Taiwan (Das et al., 2012; Torres et al., 2014), and the Andes (Torres et al., 2016). However, only a handful of studies have sought to constrain how pyrite oxidation proceeds over seasonal or inner-annual timescales (Crawford et al., 2019; Winnick et al., 2017). This is important in order to better quantify weathering fluxes, and to explore the environmental controls on pyrite oxidation at the catchment scale.

Here, we report new high-resolution time-series measurements of dissolved and solid major element concentrations and isotopic composition of sulfate in two pre-alpine catchments, at the Draix-Bléone Critical Zone

Observatory. At the study site, local fluxes of CO_2 released by chemical weathering have been independently determined by a chamber method (Soulet et al., 2018) allowing comparison with flux estimates derived from dissolved river chemistry presented here. The main objective of this study is to provide the inorganic carbon budget estimate, by exploring mineral and acid sources, the origin and oxidation environment of sulfate, and to investigate controls on the chemical weathering regime and the CO_2 budget. We find that carbonate dissolution by sulfuric acid is the dominant weathering reaction in both catchments, which is navigated by seasonality in air temperature.

5.2 Study area

The Draix-Bléone Critical Zone Observatory (CZO) is part of the French Network Observatories for the Critical Zone, OZCAR (Gaillardet et al., 2018). The catchments are located in the South French Alps near the village of Draix (Figure 5.1), and have been monitored since the 1980s (Mathys and Klotz, 2008). Here, we focus on two nearby catchments, the Laval (0.86 km^2) and the Brusquet (1.07 km^2). They have large differences in vegetation cover and sediment export, while having similar bedrock and climatic conditions (Figure 5.1). An Alpine-Mediterranean climate, with cold winters and hot and dry summers prevails at the study site. The main rainfall periods are in autumn and spring. The dry and hot summers can be interrupted by short and intensive storm events (Mathys and Klotz, 2008). The long-term mean annual precipitation (1985-2018) in the Laval is 918 mm, and 850 mm in the Brusquet.

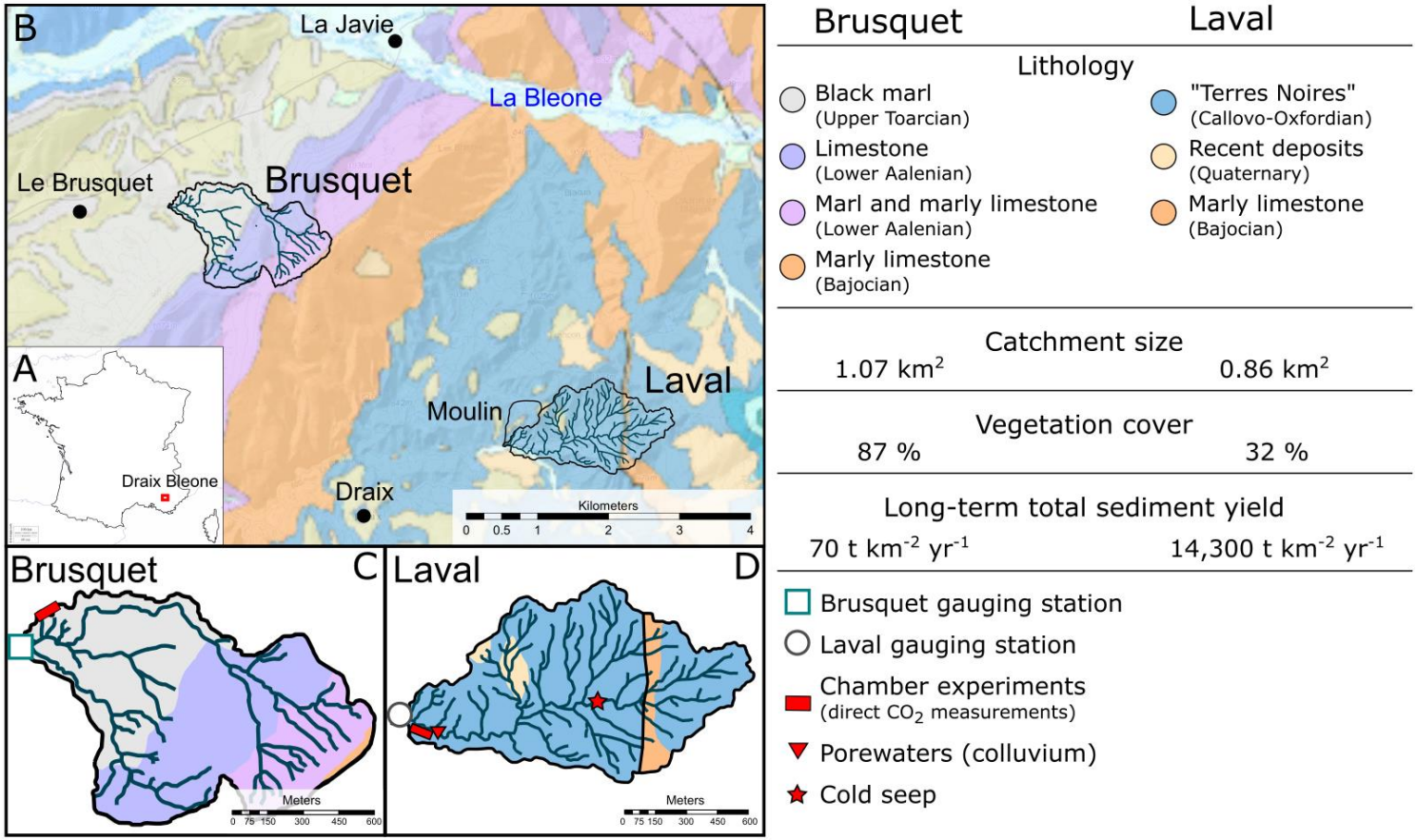

Figure 5.1: Geography of the Draix-Bléone CZO. A: Location of the Draix-Bléone observatory in the South French Alps. **B:** Geological map of the study sites. **C:** Geology and stream network of the Brusquet with location of the gauging station (square), and location of CO_2 chamber experiments (red rectangular; Roylands et al., in prep.). **D:** Geology and stream network of the Laval, with locations of the gauging station (white circle), porewaters (red triangle), seep (red star), and location of CO_2 chamber experiments (red rectangular; Soulet et al., 2018). Characteristics of the Brusquet and Laval are from Carrere et al., 2020.

The main bedrock lithologies are marl and shale, which are extremely prone to physical degradation, and the landscape has developed a "badlands-type" morphology with V-shaped gullies (Cras et al., 2007; Mathys et al., 2003). The Laval catchment drains mostly Callovo-Oxfordian marls (Figure 5.1D) that contain 0.5–0.7 % organic carbon (OC) and ~0.6 % sulfur (S). The rocks have a very high carbonate content ~45 % (Graz et al., 2011). In the Brusquet catchment, the geology is comprised of Toarcian black marls, lower Aalenian limestones, Upper Aalenian grey shales and Bajoncian marly limestone (Figure 5.1C). The Toarcian black marls cover one third of the catchment and were deposited at the end of the Toarcian Anoxic Oceanic event, which globally corresponds to enrichment in OC and pyrite deposition (Gill et al., 2011). The Toarcian black shales comprise higher OC (0.7 %), compared to grey shales (0.5 %), marls (0.26 %), and limestones (0.13 %) (Graz et al., 2011). Sulfide minerals are widespread in both catchments, mainly in form of dispersed pyrite or pyrite veins (Cras et al., 2007; Graz et al., 2011).

5.3 Materials and Methods

5.3.1 Sample collection procedure

5.3.1.1 Solid samples

We collected a range of solid samples that include surface rock samples, bed load material, and suspended load. Most surface rock samples were collected at the same locations as where CO_2 chambers measurements were conducted in the Brusquet (Figure 5.1C; Roylands et al., In prep.) and in the Laval (Figure 5.1D; Soulet et al., 2018). In the latter, two sets of surface rock samples were collected from a single outcrop; the loose detrital cover composed of millimeter- to

centimeter-sized fragments of marls, and rock powders from drilling approx. 40 cm deep cylindrical chamber into the outcrop. Fine-grained bed load material was collected in the outlets of both catchments. Suspended load samples were recovered from one storm event in each catchment, after settling samples, removing the clear stream water, and oven dried at 60 °C.

5.3.1.2 Water samples

Time-series water samples were collected from September/October 2016 to September/October 2018 at gauging stations located at the catchment outlets (Laval/Brusquet). The gauging stations are equipped with a calibrated Parshall flumes to measure flow and a flow-controlled automatic water sampler (Cras et al., 2007; Mathys and Klotz, 2008). In total, 91 water samples were collected from the Laval and 50 from the Brusquet outlets. These samples were collected by two different methods depending on the nature of the river flow. During the majority of storm events and periods of high flow, samples were collected by an ISCO auto-sampler with an aim of collecting at least three samples during increasing discharge, peak flow, and decreasing discharge. In total, 68 and 34 samples were collected during high flow regime from the Laval and Brusquet, respectively. Low flow samples were sampled by hand in a pre-rinsed 1L bottle, approximately monthly, resulting in 23 and 14 samples collected in the Laval and Brusquet, respectively (See Figure 4.2, p108 in Chapter 4).

Stream water samples were also obtained from the Moulin catchment, which is a small (0.09 km^2), surface flow dominated catchment, neighboring the Laval (Figure 5.1B). These samples are used to help quantify rainfall inputs to the studied streams (Section 5.4.3). Precipitation samples were collected at the rain

gauge in the Laval catchment during 12 precipitation events across the sampling period.

To investigate the signal of chemical weathering reactions, samples from seeps and porewaters were sampled across the Laval catchment. The porewaters were collected using Rhizon pore water samplers from recently deposited surface colluvium material (Figure 5.1D). The cold seep samples were collected at low flow in August 2016 and March 2017, from natural bedrock fractures near the channel bed (Figure 5.1D).

All water samples were filtered following collection through syringe-mounted 0.22 µm PES filters. Pre-acid cleaned LDPE bottles were rinsed with filtered water, before collection of two filtered aliquots: 30 ml un-acidified for major anions and sulfate isotopes; 60 ml acidified (with trace analysis grade HNO_3 after filtration to pH~2) for major cations. Samples were stored in a fridge (4 °C) and shipped to Durham for further analysis.

5.3.2 Analytical techniques

5.3.2.1 Geochemical analysis of solid samples

Solid samples collected in the Laval and Brusquet were freeze-dried and then hand- or ball-milled. Sample powders were analyzed for major and trace elements using flow injection and low pressure on-line liquid chromatography coupled to Inductively Coupled Plasma Mass Spectrometer (ICP-MS) at the French National Center for Scientific Research (CNRS), Service d'Analyse des Roches et des Minéraux (SARM) following a protocol described in Carignan et al. (2001).

A subset of samples (n=8) was analyzed for total sulfur concentration and stable sulfur isotope ($\delta^{34}S$) on a Costech Elemental Analyzer coupled to a Thermo Fisher Delta V Plus in the Stable Isotope Biogeochemistry Laboratory at Durham University, Department of Archeology. Precision and accuracy were monitored through repeated runs of standard material (sulphanilamide) and international standards (IAEA-SO-5, IAEA-SO-6, NBS-127), providing isotopic range of $\delta^{34}S$ from -31 ‰ to +20.3 ‰. The percentage of sulfur was calculated as part of the isotopic analysis using sulphanilamide (S = 18.62 %).

5.3.2.2 Geochemical analysis of water samples

Major dissolved ions in water samples were measured via a Thermo Scientific Dionex ICS 6000 ion chromatograph at Durham University, Department of Geography. Many samples were analyzed at 5- to 50-times dilution due to the high ion concentrations. Repeated measurements of a certified river water reference standard material (Sangamon-03) are used to validate the analytical results. Analytical precision is better than 5 % for SO_4^{2-}, Na^+, K^+, Ca^{2+}, and Mg^{2+} and better than 10 % for Cl^-. Sample replicates (during and between each batch), have precision better than 1 % for Ca^{2+} and Mg^{2+}, better than 2 % for SO_4^{2-}, Na^+ and K^+, and better than 3 % for Cl^- (Chapter 2, Section 2.2.4.1, p37).

Calculation of bicarbonate concentrations (HCO_3^-) on individual samples was done by charge balance, assuming that excess positive charge is equal to concentration of the HCO_3^- in milliequivalents. In the Laval, a number of low flow samples have high SO_4^{2-} concentrations (>10,000 µmol l^{-1}). Given an uncertainty of ~5 %, this high absolute value makes residual using the charge balance more uncertain. For some these samples (19 % of the dataset) we find negative

estimates of HCO_3^-, which are not reported, and assumed to be within uncertainty (±500 µmol l^{-1}) of zero.

5.3.2.3 Sulfur and oxygen isotopes of dissolved sulfate

A subset of 11 water samples from the Laval and 8 from the Brusquet were prepared and analyzed for stable sulfur ($\delta^{34}S_{SO4}$) and oxygen ($\delta^{18}O_{SO4}$) isotopes of dissolved sulfate. To capture a large range in water discharge, the samples were selected from flood events in August and November 2016, and cover four orders of magnitude for the Laval (10^{-1}–10^{3} l s^{-1}) and the Brusquet (10^{-2}–10^{2} l s^{-1}).

Barite ($BaSO_4$) was precipitated from river water samples following the method of Turchyn et al. (2013), see Chapter 2, Section 2.2.3, p36 for details. The $BaSO_4$ powders were analyzed for $\delta^{34}S$ by flash EA coupled by continuous flow to Delta V Mass Spectrometer at the Godwin Laboratory for Paleoclimate research at the University of Cambridge. The samples were run with NBS 127 bracketing sets of samples. The $\delta^{18}O$ on the barite was measured in triplicates on a High Temperature Conversion Elemental Analyzer (TC/EA) at Department of Earth & Planetary Sciences, Harvard University. All measurements were corrected to the Vienna Standard Mean Ocean Water (VSMOW) using a 2-point calibration curve. The accuracy was monitored through repeated analysis of international standards IAEA SO-6 =-11.3±0.3 ‰ VSMOW and NIST NBS-127=+8.6±0.3 ‰ VSMOW. Average precision, based on triplicates of samples, was 0.2 ‰ (n=20).

5.4 Results

5.4.1 Solid phase geochemistry

5.4.1.1 Geochemistry and weathering intensity of solid samples

The elemental composition of the rock clasts samples collected in the Laval (Table 5.1; geochemistry for each sample is available in Appendix 2) reflects silicate (smectite/illite, illite, kaolinite and chlorite) and carbonate (limestone) mineral fractions previously described in Marc et al. (2017). Surface rock samples from the Brusquet have similar elemental concentrations, except for a higher mean calcium and strontium concentrations compared to the Laval (Table 5.1). Overall, the lithological signature is dominated by carbonate minerals, as it is apparent from high $Ca/\Sigma Cat^{+}$ ratio (~0.8–1.0) and low $Na/\Sigma Cat^{+}$ ratio (~0.006–0.014) (Figure 5.2A). These ratios directly correspond to the limestone end-member used for lithological partitioning in the Andes-Amazon system (Torres et al., 2016) and to the calcite end-member defined in the Langtamg-Trisuli-Narayani River system in Nepal Himalaya (Kemeny et al., 2021).

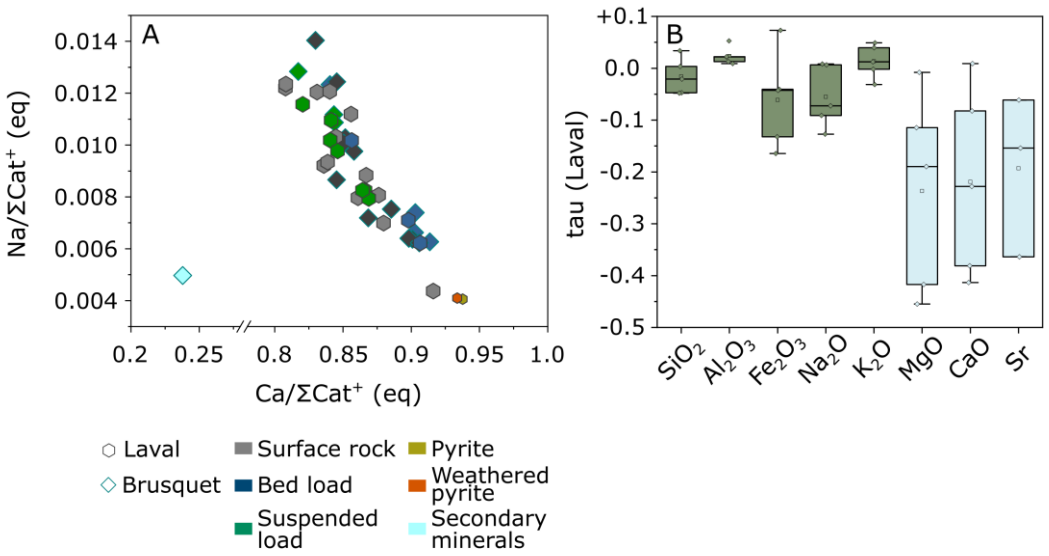

Figure 5.2: Geochemical characteristics of the solid samples. A: Solid phase Ca/∑Cat+ versus Na/∑Cat+, suggesting dominant carbonate signal in both catchments. **B:** Loss of elements associated to carbonate (Mg, Ca, Sr) and silicate (Si, Al, Fe, Na, K) weathering from "rock-drilled" to "rock-surface" samples. See text for details.

The elemental composition and variability observed in surface rock samples is similar to those of the bed load and suspended load sediments collected in both catchments (Table 5.1, Figure 5.2A). However, suspended sediment samples generally have lower relative Ca/∑Cat⁺ ratios compared to the bed loads (Figure 5.2A), suggesting a signal of carbonate weathering. The intensity of weathering in solid samples can be further examined by calculating a mass transfer coefficient, tau (τ) (Brantley et al., 2013; Chapter 3). We do this to compare the loose detrital, weathered sediments ("Rock-surface" in Table 5.1) and drilling powders, the least-weathered ("parent") material ("Rock-drilled" in Table 5.1). The tau (τ) is calculated as follows in Equation 5.7 (Chapter 3, Brantley et al., 2013).

$$\tau_{i,j} = \frac{C_{j,w} \times C_{i,p}}{C_{j,p} \times C_{i,w}} - 1 \quad (5.7)$$

Here C is elemental concentration of immobile (i) or mobile element (j) of the parent (p) or weathered material (w). A positive τ suggest elemental gain, and a negative τ suggest elemental loss, relative to the parent material. The composition of the parent material is determined by taking a mean value of the "Rock-drilled" samples (n=5) for each major element presented in Table 5.1. Titanium (Ti) is used as a non-soluble, immobile element during chemical weathering, due to similar concentrations measured in rock fractures (0.6±0.1 %), bed load (0.5±0.1 %), and suspended load (0.6±0.1 %).

The average $\tau_{i,Ti}$ values for the rock surface samples collected from a marl outcrop in the Laval are shown in Figure 5.2B. Most elements associated with silicate minerals (Si, Fe, Na, K) show negligible change in concentration, with mean $\tau_{Si,Ti}$ values between +0.02 and -0.05. In contrast, elements dominating carbonate minerals (Ca, Mg, Sr) all show significant depletions in the "Rock Surface" samples, with a mean $\tau_{Ca,Ti}$ of -0.22, mean $\tau_{Mg,Ti}$ of -0.24 and mean $\tau_{Sr,Ti}$ of -0.19.

5.4.1.2 Sulfide minerals and secondary minerals

In the Laval, S concentrations in two surface rock and a bed load sample are 0.21 %, 0.72 %, 0.48 %, respectively and their $\delta^{34}S$ values are -1.3 ‰, -2.6 ‰, and -6.7 ‰, respectively. Pyrite collected from a ~5 cm thick vein has S concentration of 49 % and $\delta^{34}S$ of +9.4 ‰. In the Brusquet, four surface rock samples from outcrop of Triassic black marls have S concentrations between 0.33 % and 0.47 %, and much higher $\delta^{34}S$ values, between +18.35 ‰ to +21.96 ‰.

Secondary precipitation of evaporite minerals has been observed within both catchments, particularly during the summer months. This surficial white powdery substance was sampled for analysis in the Brusquet. This sample has low concentrations of all major elements compared to other samples, but relatively high concentrations of MgO (13 %), which has not been observed in any other solid material.

Table 5.1. Solid phase geochemistry of the Draix-Bléone CZO. *Rock clasts represent the average values of rock-surface and rock-drilled samples together. See Appendix 2 for elemental concentrations on each sample.

Catchment	Sample Type	n	SiO_2		Al_2O_3		Fe_2O_3		MgO		CaO		Na_2O		K_2O		n	Sr	
			%		%		%		%		%		%		%			ug/g	
			Mean	SD	Mean	SD	Mean	SD	Mean	SD	Mean	SD	Mean	SD	Mean	SD		Mean	SD
Laval	*Rock clasts**	10	38.0	4.3	13.3	2.4	4.4	0.5	1.6	0.2	18.6	4.3	0.42	0.05	2.0	0.4	7	477	67
	Rock-surface	5	39.8	2.5	14.2	1.5	4.5	0.3	1.5	0.3	17.2	2.4	0.43	0.02	2.2	0.2	3	437	39
	Rock-drilled	5	36.2	5.3	12.4	2.9	4.3	0.7	1.7	0.2	20.1	5.5	0.41	0.07	1.9	0.4	4	507	72
	Bed load	3	34.1	3.7	10.8	1.3	5.4	0.8	1.5	0.2	22.4	3.0	0.43	0.06	1.7	0.2	3	558	102
	Suspended load	7	36.7	1.7	13.3	0.8	4.8	0.7	1.8	0.1	18.7	1.5	0.46	0.05	2.1	0.2	7	473	44
	Pyrite vein	1	11.1	-	4.5	-	26.4	-	0.5	-	14.2	-	0.14	-	0.7	-	1	734	-
	Pyrite weathered	1	3.9	-	2.7	-	42.1	-	0.3	-	6.7	-	0.06	-	0.2	-	1	356	-
Brusquet	*Surface rock*	8	37.9	4.1	12.9	1.0	4.2	0.4	1.7	0.2	19.5	3.3	0.48	0.06	2.0	0.2	7	660	104
	Bed load	7	33.9	4.1	10.3	1.2	3.9	0.4	1.6	0.3	23.9	3.2	0.44	0.05	1.6	0.2	3	750	107
	Suspended load	3	39.8	1.0	13.2	0.5	3.7	0.1	1.8	0.1	17.1	1.0	0.53	0.02	2.2	0.1	3	657	7.7
	Iron Oxide Precipitant	1	2.7	-	0.6	-	31.5	-	0.3	-	4.6	-	0.04	-	0.2	-	1	904	-
	Secondary Minerals	1	6.3	-	2.0	-	0.9	-	8.1	-	4.2	-	0.20	-	0.5	-	1	260	-

5.4.2 Hydrological measurements

Simultaneous measurements of stream discharge (l s^{-1}) for the observation period in the Laval (09/2016–09/2017, 09/2017–09/2018) and Brusquet (10/2016–10/2017, 10/2017–10/2018) are available by the Draix-Bléone Observatory (Cambon et al., 2015). The two sampling years had large differences in precipitation and water discharge (Table 4.1, p115 in Chapter 4). In the Laval, the annual discharge was 2.53×10^{8} l yr^{-1} in the 09/2016–09/2017, and 4.17×10^{8} l yr^{-1} in the 09/2017–09/2018 (294 mm yr^{-1} and 485 mm yr^{-1} annual runoff, normalized by catchment area, respectively). The annual discharge for the Brusquet was 1.32×10^{8} l yr^{-1} and 1.55×10^{8} l yr^{-1} for the 10/2016–10/2017 and the 10/2017–10/2018, respectively (123 mm yr^{-1} and 144 mm yr^{-1}; annual runoff). The runoff in the first observation period is close to the long term (1995–2015) annual mean, which is ~300 mm yr^{--1} and ~100 mm yr^{-1} in the Laval and Brusquet, respectively (Smetanová et al., 2018). The second observation period had annual runoff values above the long-term annual mean in both catchments.

Stream discharge measurements are used to set a threshold for a hydrograph separation into low flow and high flow regimes. This threshold was defined by the maximum of the lower quartile (Q1; <25%; Smakhtin, 2001) of all recorded discharge values in the observation period. Full details are provided in Chapter 2, Section 2.3.4.1, p45. For the Laval the low flow boundary is 28.5 l s^{-1}, and for the Brusquet 7.2 l s^{-1}.

5.4.3 Rain water chemistry and cyclic input

Local rainwater samples were collected between 08/2016 and 08/2018. As discussed in Chapter 4, some of the samples show evidence for the dissolution of atmospheric dust in elevated Zn concentrations (1,022–5,970 μmol l^{-1}) and Na/Cl ratios greater than those of seawater (up to 5.8). Therefore, we only use the chemistry of the rain samples with Na/Cl ratios <1 (n=3), broadly reflecting the Na/Cl ratio of sea salt composition (~0.87; West et al., 2005).

To estimate the atmospheric contribution of major elements to the stream dissolved load the "rain ratio" method (Equation 5.8) is adopted from Moquet et al. (2011) and Spence & Telmer (2005):

$$X^*_{Stream} = X_{Stream} - Cl_{Crit} \times \left(\frac{X}{Cl}\right)_{Rain} \quad (5.8)$$

here X^*_{Stream} is the precipitation corrected ion concentration in stream water, X_{Stream} is the measured ion concentration in stream water, Cl_{Crit} is the mean Cl^- concentration measured in a catchment without evaporite, and $(X/Cl)_{Rain}$ is the average element over Cl ratio measured in precipitation samples collected in the Laval.

The Moulin catchment provides a way to determine the Cl_{Crit} value. The Moulin is a first order catchment (0.09 km^2, Figure 5.1B) that drains the same lithology as the Laval near its outlet. Hydrological models show that fast surface runoff is the only water mass contributing to the catchment runoff in the Moulin (Cras et al., 2007; Marc et al., 2017). Since surface rock samples in these catchments do not contain primary evaporite minerals (Section 5.4.1), the Cl^-

concentration measured in the Moulin is assumed to be that derived from the atmosphere (Cl_{Crit}). The Cl^- concentration in this small catchment covers a range of values between 20 µmol l^{-1} and 299 µmol l^{-1}, and a mean value of 58±51 µmol l^{-1} (±1SD, n=41). Using this approach, the mean atmospheric contribution for all major ions is negligible (<1%) in both catchments, suggesting that chemical weathering is the main process supplying elements to the dissolved load (Cras et al., 2007).

5.4.4 Stream water chemistry and trends with discharge

The stream water chemistry corrected for atmospheric inputs for each sample is available in Appendix 3. The dissolved load (corrected for atmospheric inputs) in the Laval is dominated by SO_4^{2-} ions, with a mean value of 7.5±4.2 mmol l^{-1} (all Laval stream waters: ±1SD; n=91; unless otherwise stated), whose concentration displays a negative correlation with discharge (Figure 5.3). The Cl^- concentrations measured in the Laval are also high compared to the global rivers, displaying a large range of values, between 0 and 1.5 mmol l^{-1}, with a mean of 0.24±0.4 mmol l^{-1}. The mean cation concentrations for Na^+, Ca^{2+} and Mg^{2+} are 2.5±2.1 mmol l^{-1}, 3.3±1.6 mmol l^{-1} and 3.4±1.7 mmol l^{-1}, respectively. The mean HCO_3^- concentration is 1.7±1.3 mmol l^{-1} (±1SD, n=81). The mean SO_4^{2-}/HCO_3^- ratio is 6.6±8.3 mol mol^{-1} (±1SD, n=81) and generally declines with increased discharge (Figure 5.3). In contrast, the Ca^{2+}/SO_4^{2-} ratio (mean=0.5±0.1 mol mol^{-1}) and the Ca^{2+}/Na^+ ratio (mean=1.8±0.9 mol mol^{-1}) increase with discharge (Figure 5.3). The concentrations and trends with discharge presented here are similar to time series data measured in the Laval between years 2001 and 2002 (Cras et al., 2007), however, our study extends the dataset to the low flow regimes which

were not previously sampled ($Q=10^{-1}$ to 10^{-2} l s^{-1}), with higher concentrations in all solutes (Figure 5.3).

For comparison, concentrations of most ions are lower in the Brusquet, particularly SO_4^{2-} (2.9±1.5 mmol l^{-1}; all Brusquet stream waters: ±1SD; n=50; unless otherwise stated) and Na^+ (0.21±0.38 mmol l^{-1}). The mean Ca^{2+} and Mg^{2+} concentrations are 2.3±1.0 mmol l^{-1} and 2.1±1.0 mmol l^{-1}, respectively. The mean Ca^{2+}/SO_4^{2-} ratio is higher in the Brusquet than in the Laval, at 0.9±0.2 mol mol^{-1}. The mean HCO_3^- in the Brusquet is 3.7±1.3 mmol l^{-1} (±1SD, n=48), resulting in a mean SO_4^{2-}/HCO_3^- ratio of 0.76±0.31 mol mol^{-1} (±1SD, n=48). The Ca^{2+}/Na^+ displays a large variability, between 1.3 and 62.7 mol mol^{-1} and a mean value of 18.8±11.5 mol mol^{-1}.

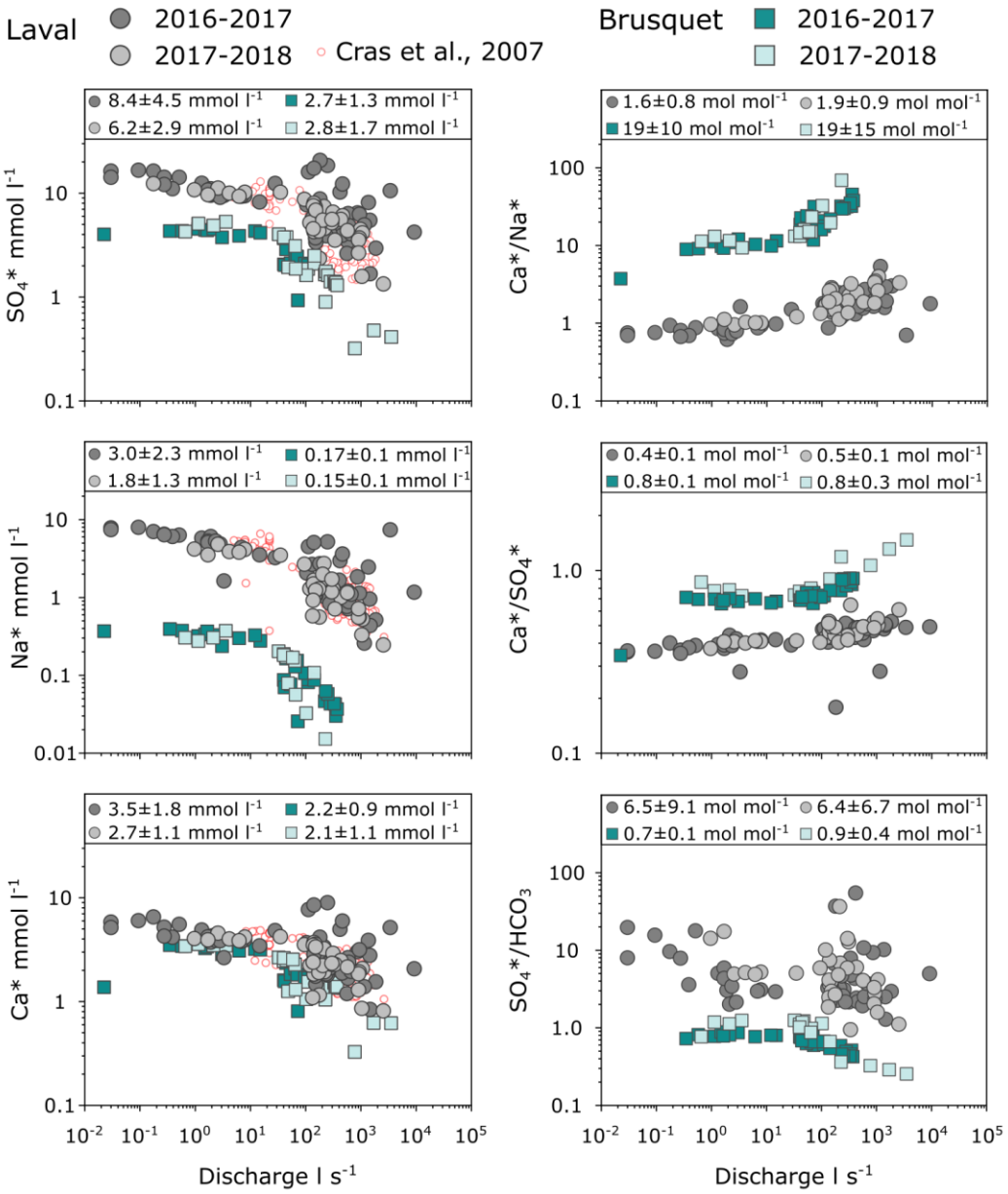

Figure 5.3: Time series concentration data with discharge. Using the log-log scale to compare the Laval samples (grey circles) and the Brusquet samples (green squares) for the two sampling years. Samples collected in the second (2017-2018) observation year are shaded in lighter colors. The annual mean value ±1SD is reported in each plot for both catchments and two sampling years. Small red circles are data from Laval collected in 2002, published in Cras et al (2007).

5.4.5 Seasonal variability in low flow and porewater/seep chemistry

All major dissolved ions within the low flow samples of the first observation year in the Laval have higher concentrations in the summer months (June, July, August) than in the winter months (December, January, February). The temporal patterns in concentration can be fit by a sine-cosine curve with 6-month periodicity (Figure 5.4). The closest data fit to the sine function is observed for SO_4^{2-} ($r^2 = 0.84$), followed by Ca^{2+} ($r^2 = 0.74$), Cl^- ($r^2 = 0.68$) and Mg^{2+} ($r^2 = 0.66$), while less pronounced seasonal variability is observed in Na^+ ($r^2 = 0.53$) and HCO_3^- ($r^2 = 0.44$). A strong seasonal trend is also observed in the SO_4^{2-}/HCO_3^- ratio in the Laval samples ($r^2 = 0.69$) (Figure 5.4B). A distinct seasonal variability in ion concentrations is not observed in the Brusquet low flow samples (Figure 5.4C and D), with exception of Na^+, for which a sine-curve was fitted with moderate r^2 of 0.61 (not shown here).

Seep samples are generally more concentrated in major ions compared to stream samples, with particularly high SO_4^{2-} (8.6 – 12.2 mmol l^{-1}), Cl^- (0.3 – 3.0 mmol l^{-1}), Na^+ (0.3 – 10.1 mmol l^{-1}) and HCO_3^- (0.1 – 4.4 mmol l^{-1}). In comparison, Mg^{2+} and Ca^{2+} in seep samples have similar concentrations as measured in stream water, varying between 2.4 – 4.4 mmol l^{-1}, and 3.1 – 4.4 mmol l^{-1}, respectively. The variability in the chemical composition of the seep samples generally follows the seasonal trend observed in the low flow dataset from the Laval, although there are much fewer samples (Figure 5.4A and B). Porewaters have lower Cl^- (0.02–0.03 mmol l^{-1}) and Na^+ (0.06 – 0.10 mmol l^{-1}) concentrations than the cold seep samples, while SO_4^{2-} (4.8 – 11.4 mmol l^{-1}), Mg^{2+} (3.0 – 6.0 mmol l^{-1}), and Ca^{2+} (2.4 – 5.7 mmol l^{-1})

concentrations are more similar between the two datasets. The seasonal trend in porewater samples is less clear (Figure 5.4A and B).

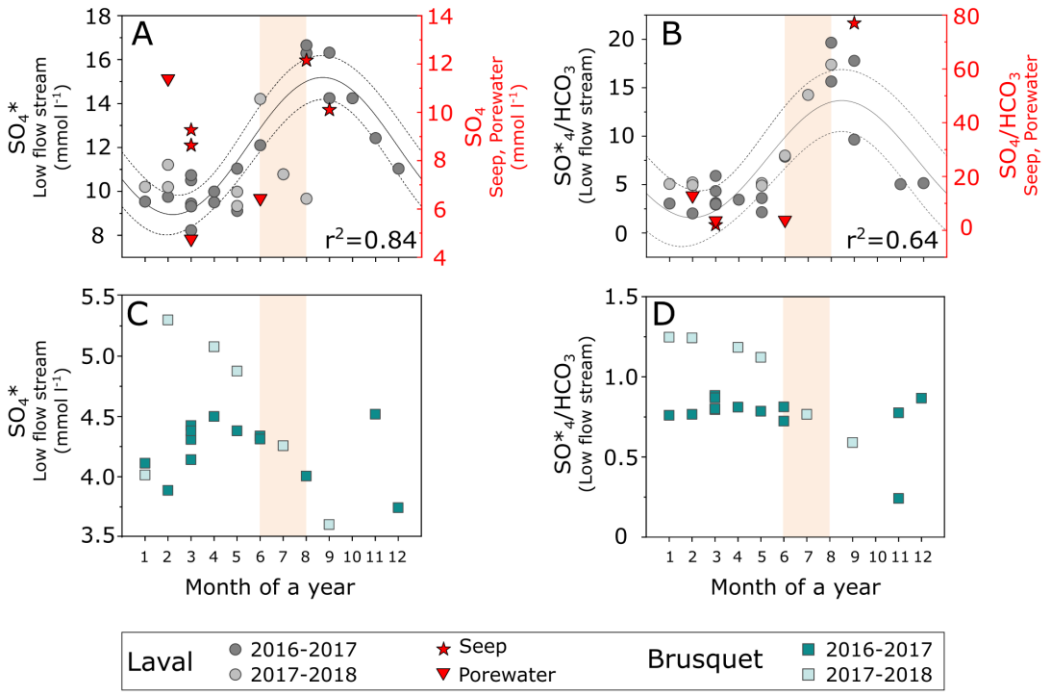

Figure 5.4: Seasonal variability in low flow stream water chemistry. The sine-cosine curve with 6-months periodicity is fitted to the samples collected during the first observation period (09/2016-09/2017) in the Laval (**A** and **B**). The stippled envelope around the mean line represents the 95% confidence interval. The curve fit is furthermore presented with r^2 value in plots A and B. Note the double Y axis in figures A and B, the left showing stream water concentration (grey) and the right showing seep (stars) and porewater (triangles) concentration (red). Negligible seasonal variability is observed in Brusquet samples (**C** and **D**).

5.4.6 Sulfur and oxygen isotopes of dissolved sulfate

The isotopic composition of dissolved sulfate ($\delta^{34}S_{SO4}$ and $\delta^{18}O_{SO4}$) helps inform on the source, redox environment, and flow pathways of sulfate in the researched catchments. The two catchments have very different $\delta^{34}S_{SO4}$ values (Table 5.2); samples from the Laval have more negative $\delta^{34}S_{SO4}$ values, with a mean of -2.3±1.25 ‰ (±SD, n=12), while samples from the Brusquet have more positive $\delta^{34}S_{SO4}$ values, with a mean of +7.9±1.3 ‰ (±SD, n=7). Together, these

measurements from small catchments span the range of reported measurements of $\delta^{34}S_{SO4}$ from rivers around the world (Burke et al., 2018). The contrast between the Laval and Brusquet is broadly consistent with the solid samples analyzed for $\delta^{34}S$ (Section 5.4.1.2).

Table 5.2. Stable sulfur and oxygen isotopes of dissolved sulfate.

Catchment	Sample collection date/time	Discharge	$\delta^{34}S_{SO4}$	SD	$\delta^{18}O_{SO4}$	SD	$\delta^{18}O_W$	Ca/SO_4
		l s^{-1}	‰		‰		‰	
Laval	04/08/2016 10:00	0.03	-1.92	0.24		-	-	0.3
Laval	11/09/2016 17:28	105	0.52	0.24	-5.9	0.1	-	0.5
Laval	11/09/2016 17:44	249	-1.82	0.24	-6.2	0.0	-	0.5
Laval	11/09/2016 18:03	113	-2.19	0.24	-6.1	0.0	-	0.5
Laval	12/09/2016 15:37	171	-0.47	0.24	-5.2	0.1	-4.88	0.5
Laval	12/09/2016 15:44	1364	-2.15	0.24	-5.2	0.1	-5.24	0.5
Laval	12/09/2016 15:58	337	-3.76	0.24	-4.8	0.4	-5.42	0.5
Laval	14/10/2016 08:24	407	-3.40	0.24	-4.5	0.4	-5.25	0.4
Laval	14/10/2016 08:34	9241	-2.80	0.24	-5.0	0.4	-5.69	0.5
Laval	14/10/2016 08:45	1855	-3.47	0.24	-4.3	0.2	-5.99	0.5
Laval	14/10/2016 10:16	345	-2.96	0.24	-5.9	0.1	-6.33	0.5
Laval	23/11/2016 11:29	28	-2.63	0.24	-6.9	0.1	-	0.4
Brusquet	03/08/2016 10:00	0.02	10.53	0.24	-	-	-	0.3
Brusquet	14/10/2016 21:57	40	6.41	0.24	-1.2	0.1	-	0.8
Brusquet	14/10/2016 22:57	42	7.19	0.24	-2.2	0.4	-	0.8
Brusquet	05/11/2016 09:53	53	-	-	-3.2	0.2	-	0.9
Brusquet	05/11/2016 14:36	111	8.28	0.24	-2.4	0.2	-	0.8
Brusquet	05/11/2016 16:07	222	8.05	0.24	-3.2	0.1	-	0.9
Brusquet	05/11/2016 17:07	355	7.42	0.24	-3.6	0.2	-	1.0
Brusquet	22/11/2016 11:00	-	7.89	0.24	-3.2	0.2	-	1.5

The oxygen isotope ratios of dissolved sulfate ($\delta^{18}O_{SO4}$) differ in the two catchments, with a mean value of -5.5±0.8 ‰ (±SD, n=11) for the Laval, and a mean of -2.7±0.9 ‰ (±SD, n=7) for the Brusquet. The Laval values are higher but within the broad range of values sampled for local rainwater (-7.4±3.8 ‰, ±1SD, n=203), stream water sampled between 2001-2002 (-7.2±2.4 ‰, ±1SD, n=84), soil porewaters from the Moulin (-7.2±1.5 ‰, ± 1SD, n=43), and colluvium porewaters from the Laval (-7.5±1.7‰, ± 1SD, n=24) published in Cras et al.

(2007). For 7 (out of 13) samples collected in the Laval paired measurements of $\delta^{18}O_{SO4}$ and $\delta^{18}O_w$ are available (Table 5.2). The oxygen isotope values measured in stream water vary between -6.33‰ and -4.88 ‰, with a mean value of -5.54±0.5 ‰ (± 1SD, n=7).

5.5 Discussion

To better understand how oxidative weathering of sulfide minerals contributes to chemical weathering fluxes and the net transfer of inorganic carbon between rocks and the atmosphere (Hilton and West, 2020), we interrogate new data from two marl-dominated catchments in the Draix-Bléone CZO. The catchment pair experiences similar climatic conditions, but contrast in terms of their modern-day runoff and sediment yields, which is linked to their vegetation cover (Carriere et al., 2020; Mathys et al., 2003). Here we determine relative roles of silicate and carbonate mineral weathering and assess the contribution of carbonic versus sulfuric acid. We further explore the oxidation environment using isotopic compositions of sulfate in stream water (Turchyn et al., 2013). Finally, we discuss how seasonal variations in runoff and temperature impact sulfide oxidation rates across differences in physical erosion between the two catchments.

5.5.1 Carbonate versus silicate weathering

5.5.1.1 Cation source partitioning

To determine weathering rates and the CO_2 budget on a catchment scale, the dissolved load concentrations are apportioned between carbonate and silicate lithological sources (Burke et al., 2018; Gaillardet et al., 1999; Jacobson and Blum, 2003; Torres et al., 2016). The high $Ca/\Sigma Cat^+$ ratio of ~0.8–1.0 of solid samples suggests that the lithology of both catchments is dominated by carbonate over

silicate minerals (Figure 5.2A). To assess their contributions to the dissolved load, we attempt to constrain the local composition of silicate versus carbonate end-members (Quade et al., 2003) using seep and porewaters samples (Figure 5.5A). The seep samples are thought to originate from deeper water reservoirs, therefore, their chemistry is inferred to reflect the signal of chemical weathering reactions requiring longer reaction times, such as silicate weathering (Maher, 2010; Tipper et al., 2006). In contrast, the chemistry of porewaters reflects reactions with rapid kinetics, such as carbonate weathering (Calmels et al., 2011). Plotted together, the seep and porewater samples collected in the Laval (Figure 5.5A) cover the range of Ca/Na and Mg/Na ratios that have been identified for silicate and carbonate end-members in a global assessment (Gaillardet et al., 1999).

The dissolved load of the Laval and Brusquet stream waters plots on a trend between the carbonate and silicate end-member (Figure 5.5B). We apply well established techniques to partition the cations between the carbonate and silicate sources (Galy & France-Lanord, 1999) assuming that: i) Cl^- is a conservative element and, as such, it is only derived from dissolution of evaporate minerals and atmospheric precipitation; and ii) Na^+ is mainly sourced from weathering of alumosilicate phases and evaporites. Then the Cl^- derived from evaporite (Cl_{evap}) dissolution is calculated with Equation 5.9.

$$Cl_{evap} = Cl_{stream} - Cl_{crit} \quad (5.9)$$

Where Cl_{stream} is the Cl^- concentration measured in stream water and Cl_{crit} is the critical Cl^- concentration as determined in section 5.4.3 above. Furthermore, Na^+ derived from silicate fraction (Na_{sil}) may be isolated as follows in Equation 5.10.

$$Na_{sil} = Na^{*}_{stream} - Cl_{evap} \quad (5.10)$$

Finally, the carbonate fraction of Ca^{2+} (Ca_{carb}; Equation 5.11) and Mg^{2+} (Mg_{carb}; Equation 5.12) are calculated:

$$Ca_{carb} = Ca^{*}_{stream} - [Na]_{sil} \times \left(\frac{Ca}{Na}\right)_{sil} \quad (5.11)$$

$$Mg_{carb} = Mg^{*}_{stream} - Na_{sil} \times \left(\frac{Mg}{Na}\right)_{sil} \quad (5.12)$$

here Ca^{*}_{stream} and Mg^{*}_{stream} are the concentrations measured in stream water, corrected for atmospheric inputs (Section 5.4.3) and $(Ca/Na)_{sil}$ and $(Mg/Na)_{sil}$ are ratios from the literature (Figure 5.5A, Gaillardet et al., 1999). The silicate fraction (Ca_{sil} and Mg_{sil}) is determined by subtracting the carbonate fraction from the total concentration corrected for atmospheric input. A Monte Carlo sampling approach is used to account for uncertainty in the composition of the carbonate and silicate end-member.

This method assumes congruent dissolution of silicate rocks and a conservative behavior of the solutes, which may be violated in a case of removal of Ca^{2+} by the precipitation of secondary carbonates, as previously observed in catchments experiencing high erosion rates, such as in the Himalaya, e.g. Bickle et al. (2015), English et al. (2000), Galy & France-Lanord (1999). Precipitation of secondary carbonates is expected in Draix catchments, due to extreme seasonal differences in air temperature and low runoff and this can result in overestimation of the silicate fraction. Precipitation of secondary fractions require further investigations in the studied catchments.

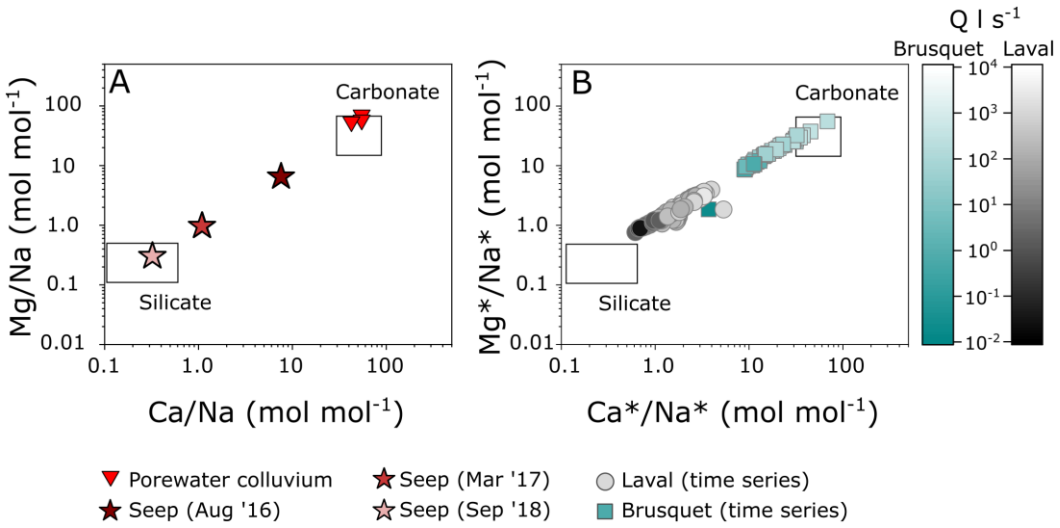

Figure 5.5: Cation partitioning of carbonate and silicate sources in stream water. A: Ca/Na and Mg/Na molar ratio in seeps and porewaters collected at the Laval catchment. The rectangles are marking the global assessment of silicate and carbonate end-member (Gaillardet et al., 1999). **B:** Ca*/Na* and Mg*/Na* molar ratio (corrected for atmospheric inputs) in time series water samples collected at the catchment outlet for the Laval (grey-shaded circles) and the Brusquet (green-shaded squares). The time series data is color-coded by discharge.

The cations exported by the Laval have a notable contribution from silicate weathering, which varies between 22 % and 44 %. In contrast, the contribution of cations from silicate minerals in the Brusquet is estimated to be minor (<8 %; Figure 5.5B). In both catchments, the proportion of cations derived from silicate versus carbonate weathering is related to discharge. The silicate fraction dominates during the low flow regimes and the carbonate fraction during the high flow regimes. This is consistent with previous work showing that a longer fluid residence time results in a higher silicate fraction in steep catchments around the world (Calmels et al., 2011; Tipper et al., 2006; Winnick et al., 2017).

5.5.1.2 Silicate and carbonate annual weathering rates

The cation partitioning allows us to determine silicate cation and carbonate annual weathering rates applying the same approach as presented in Chapter 2,

Section 2.3.4, p44. In short, the continuous measurements of stream discharge, high-temporal sampling frequency of storm events (over hours), and ~monthly sampling of low flow regime, are modelled by a combination of linear interpolation for estimating solute concentrations during high flow regime and a seasonal sine-cosine model to estimate solute concentrations during low flow regime. Total silicate cation ($J_{Sil}=Na_{Sil}^{+}+K^{+}+Ca_{Sil}^{2+}+Mg_{Sil}^{2+}$), Ca+Mg silicate ($J_{Ca+MgSil}=Ca_{Sil}^{2+}+Mg_{Sil}^{2+}$) and carbonate ($J_{Carb}=Ca_{Carb}^{2+}+Mg_{Carb}^{2+}$) annual weathering rates in t km^{-2} yr^{-1} are calculated and the uncertainty is estimated by using an error propagation of the analytical error, data variability, and error associated with carbonate and silicate proportion of cations.

As suggested from cation-source partitioning (Figure 5.5), carbonate weathering rates dominate over the silicate cation weathering rates in both catchments (Table 5.3). In the Laval, the mean carbonate weathering rate between the two sampling years is 63.5±20.4 t $km^{-2}yr^{-1}$, while the mean total silicate cation weathering rate is approx. half that, at 36.3±9.8 t km^{-2} yr^{-1}. In the Brusquet, the mean carbonate weathering rate is 19.0±3.4 t $km^{-2}yr^{-1}$ and the mean silicate cation weathering rate is much lower, at 1.4±0.2 t $km^{-2}yr^{-1}$. The dominance of carbonate weathering rates in mountain catchments has been shown in many other studies, even when carbonate fraction represent only a minor proportion of the weathered lithology (e.g. English et al., 2000; Galy & France-Lanord, 1999; Jacobson & Blum, 2003; Karim & Veizer, 2000). This has been attributed to much faster kinetics of carbonate mineral dissolution compared to silicate minerals (Morse and Arvidson, 2002). The fast kinetics of carbonate weathering in the Laval catchment is supported by the relatively high

Ca and Mg loss (~20 %) from the surface rocks samples ("rock-surface") compared to the drilled samples ("rock-drilled), while negligible change in tau values of elements associated to silicate weathering across the same sample-set is observed (Figure 5.2B).

A notable difference between the two catchments is in their respective silicate cation weathering rates, which are more than 25-times higher in the Laval compared to the Brusquet (Table 5.3), even though both catchments drain similar lithologies (Figure 5.2A). This may reflect the acidity source that drives the mineral dissolution. Sulfuric acid may enhance the dissolution of silicate minerals (Blattmann et al., 2019; Calmels et al., 2007) and result in elevated concentrations of silicate-derived solutes in stream water (Cras et al., 2007; Ross et al., 2018). The role of sulfuric acid weathering is also critical to establish in terms of assessing the impact on the net carbon transfers. As such, we now turn to assess the source of sulfate in the stream water, and the role of carbonic versus sulfuric acid weathering in these catchments.

Table 5.3. Chemical weathering rates in the Laval and Brusquet.

					Weathering rates			Carbon balance		
Observation period	Catchment	Annual precipitation mm yr^{-1}	Annual runoff mm yr^{-1}	Dataset	Total Silicate cations t km^{-2} yr^{-1}	Ca+Mg Silicate t km^{-2} yr^{-1}	Carbonate t km^{-2} yr^{-1}	CO_2 consumption Mg+Ca Silicate t km^{-2} yr^{-1}	CO_2 consumption Carbonate t km^{-2} yr^{-1}	CO_2 release Carbonate t km^{-2} yr^{-1}
11/09/2016-10/09/2017	Laval	865	294	Complete	29.3 ± 1.7	13.4 ± 0.8	49.1 ± 1.8	1.02 ± 0.6	1.9 ± 1.1	17.1 ± 1.4
				High flow	9.3 ± 1.3	4.2 ± 0.6	29.7 ± 1.6			
				Low Flow	20.0 ± 1.1	9.2 ± 0.5	19.4 ± 0.7			
11/09/2017-10/09/2018	Laval	1157	485	Complete	43.2 ± 4.5	19.7 ± 2.6	77.9 ± 12.4	1.5 ± 1.0	3.0 ± 1.9	27.1 ± 1.9
				High flow	16.7 ± 1.9	7.5 ± 0.9	48.3 ± 3.0			
				Low Flow	26.5 ± 2.1	12.2 ± 1.0	29.7 ± 1.8			
14/10/2016-13/10/2017	Brusquet	757	123	Complete	1.5 ± 0.4	1.04 ± 0.4	16.6 ± 1.4	0.26 ± 0.12	2.2 ± 0.5	4.0 ± 0.8
				High flow	0.5 ± 0.09	0.2 ± 0.06	10.4 ± 0.6			
				Low Flow	1.0 ± 0.4	0.8 ± 0.4	6.2 ± 0.4			
14/10/2017-13/10/2018	Brusquet	957	144	Complete	1.2 ± 0.2	0.59 ± 0.14	21.4 ± 2.4	0.15 ± 0.06	2.9 ± 0.7	5.1 ± 1.1
				High flow	0.6 ± 0.1	0.35 ± 0.08	10.5 ± 0.74			
				Low Flow	0.6 ± 0.1	0.24 ± 0.09	10.8 ± 0.23			

5.5.2 Contribution of sulfide oxidation to dissolved sulfate

The high dissolved SO_4^{2-} concentrations measured in both catchments suggest that pyrite oxidation may produce sulfuric acid that supplies protons involved in chemical weathering. To explore this hypothesis, we must identify the source of dissolved SO_4^{2-} (Calmels et al., 2007). The main sources of SO_4^{2-} in river waters alongside the oxidation of sulfide minerals are atmospheric deposition and dissolution of sulfate-bearing evaporite minerals (Karim and Veizer, 2000). In addition, secondary processes may act on the SO_4^{2-} pool in river catchments, for instance microbial sulfate reduction (Turchyn et al., 2013). In the studied catchments, the contribution of atmospherically derived SO_4^{2-} is negligible (Section 5.4.3) and chemical weathering dominates the dissolved load. In the following, the potential role of sulfide oxidation, evaporite dissolution, and evidence for sulfate reduction, is explored using S and O isotopes and major ion ratios.

5.5.2.1 Dominance of sulfide oxidation in the Laval catchment

The sulfate in water samples collected in the Laval catchment has a mean $\delta^{34}S_{SO4}$ value of -2.3±1.25 ‰ (±1SD, n=12), which is within the range of $\delta^{34}S$ values measured in the bulk S pool of bedrocks in the catchment, -6.7 ‰ and -1.3 ‰ (Figure 5.6A). Disseminated pyrite is common in the Laval rocks (Graz et al., 2011) and the bulk S pool is likely to be dominated by sulfides. The $\delta^{34}S$ values of sulfate derived from sulfide oxidation can track the parent material, due to negligible fractionation during oxidation (Taylor et al., 1984). The variability in $\delta^{34}S_{SO4}$ values in the Laval (from -3.7 ‰ to +0.5 ‰) could reflect variability in the pyrite S isotope composition within the catchment. For instance, a pyrite vein

sampled from Laval has an isotopically heavy $\delta^{34}S$ value (+9.2 ‰), suggesting that vein-derived sulfides may contrast in isotopic composition from disseminated pyrite within the marl bedrock. This is plausible since the $\delta^{34}S$ signature of the disseminated pyrite reflects the environment and mechanisms of sulfur incorporation during the sediment deposition in the ocean (Fisher and Hudson, 1987). Opposite, $\delta^{34}S$ signal in pyrite veins varies between the hydrothermal fluid sources and/or temperature of hydrothermal fluids responsible for the formation of the pyrite veins. The lower $\delta^{34}S_{SO4}$ values in the Laval stream could indicate that larger pyrite veins are not common, and/or less susceptible to physical and chemical weathering than the disseminated pyrite in the fractured marl lithology.

Previous studies form the Laval catchment have proposed that high concentrations of Cl^- and SO_4^{2-}, particularly at low discharge, could be due to dissolution of evaporite minerals (Cras et al., 2007; Marc et al., 2017). At the time of deposition in the middle to upper Jurassic (Bajocian to Oxfordian), $\delta^{34}S$ values associated to seawater were ~ +15 ‰ to +18 ‰ (Claypool et al., 1980; Gill et al., 2011), which contrasts to the low $\delta^{34}S$ values measured in the Laval (-2.3±1.25 ‰; ±1SD, n=12). This is further supported by the low Ca^{2+}/SO_4^{2-} ratio of ~0.5 (Figure 5.6B). If SO_4^{2-} was sourced from gypsum dissolution, Ca^{2+}/SO_4^{2-} ratios would be ~1, which is consistent with minor evaporate-derived SO_4 in this catchment.

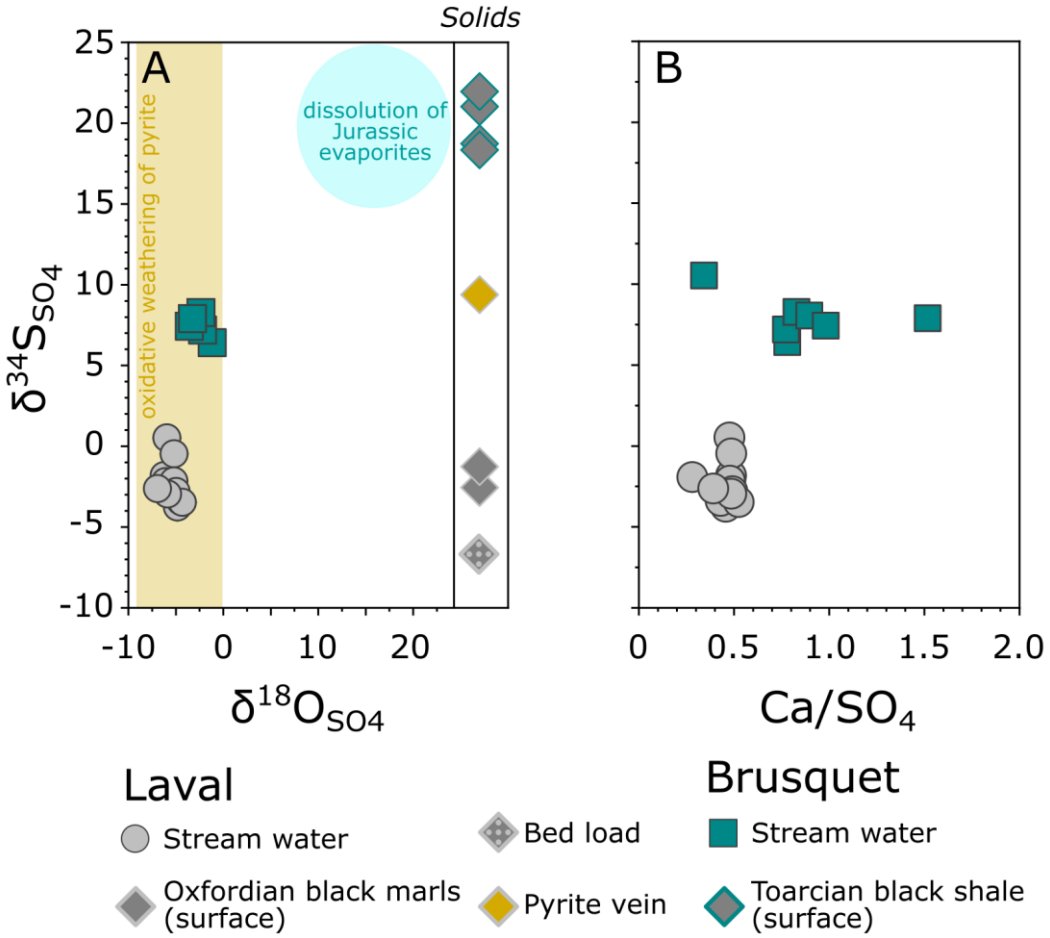

Figure 5.6: Sulfate source. A: Stable oxygen ($\delta^{18}O_{SO4}$) versus sulfur ($\delta^{34}S_{SO4}$) isotope on dissolved sulfate in the Laval (circles) and the Brusquet (squares), and $\delta^{34}S$ on solid phase samples collected in the Laval (diamonds, light grey edge) and Brusquet (diamonds, blue edge). Similar $\delta^{34}S$ in water and solid samples in the Laval suggest a common source. Yellow shading show expected isotopic composition of dissolved sulfate during oxidative weathering of pyrite. Blue shading shows expected isotopic composition of dissolved sulfate originating from evaporite dissolution. **B:** Ca/SO_4 molar ratio vs. $\delta^{34}S_{SO4}$ in the Laval stream water samples (circles), Brusquet stream water samples (squares).

5.5.2.2 Origin of high $\delta^{34}S_{SO4}$ values in the Brusquet catchment

In the Brusquet, the $\delta^{34}S_{SO4}$ values are higher, reaching +10.5 ‰ (Figure 5.6A). The contrast between the two catchments could reflect the depositional environment of the black shales across the Toarcian Oceanic Anoxic Event (T-OAE) that outcrop in the Brusquet but not in the Laval (Figure 5.1). This could result in different $\delta^{34}S_{SO4}$ values of sulfides (Pasquier et al., 2021), influence the

relative contribution of gypsum, and/or reflect sulfate reduction that can fractionate $\delta^{34}S_{SO4}$ values (Hemingway et al., 2020; Turchyn et al., 2013).

Potential sulfur-bearing evaporite minerals (e.g. gypsum) in the Brusquet catchment may have higher $\delta^{34}S$ values than those of the Laval. The positive S isotope excursion recorded during the T-OAE resulted in seawater sulfate $\delta^{34}S$ values reaching ~+24‰, (Gill et al., 2011; Newton et al., 2011). Thus, dissolution of Toarcian evaporites could result in the higher $\delta^{34}S_{SO4}$ values measured in the Brusquet. An evaporite source of SO_4 is also consistent with the high Ca^{2+}/SO_4^{2-} ratios of the stream water in the Brusquet (Figure 5.6B), with a mean of 0.9±0.3 (± 1SD, n=8), which is typical of evaporite dissolution (Turchyn et al., 2013).

However, there are other lines of evidence, which suggest a less important role of evaporite inputs in the SO_4 budget of the Brusquet. Lower Cl^- and Na^+ concentrations in the dissolved load (Figure 5.3) and the negative $\delta^{18}O_{SO4}$ signal (-2.7±0.9‰; ± 1SD, n=7) contrasts values expected for Jurassic seawater and any associated SO_4-bearing evaporates ($\delta^{18}O_{SO4}$~+10‰; Claypool et al., 1980). Indeed, the $\delta^{18}O_{SO4}$ values of the Brusquet stream waters are more similar to the $\delta^{18}O$ values of rainwater, with a mean value of -7.4±3.8‰ (±1SD, n=203, Cras et al., 2007). This would be consistent with an oxygen source of the dissolved SO_4 incorporated during pyrite oxidation (Equation 5.3; Taylor et al., 1984).

Shales deposited during the Toarcian Anoxic Event globally exhibit a positive S isotope excursion (Newton et al., 2011). Fractionation between seawater SO_4^{2-} and authigenic pyrite can vary between ~70 ‰ to <5 ‰ (the reduced phase having lower values) depending upon the sedimentation rate of the depositional environment (Pasquier et al., 2021). As such, a seawater value of

+24 ‰ during the anoxic event (Gill et al., 2011; Newton et al., 2011) could translate into a pyrite S isotope value that is higher than the rocks in the neighboring Laval catchment. A $\delta^{34}S$ value of pyrite of between +6 ‰ and +11 ‰ is thus reasonable, and could explain the Brusquet stream SO_4^{2-} isotopic composition (Figure 5.6). Indeed, the bulk rock samples from Toarcian outcrops of the catchment with no visible evidence for evaporites have positive $\delta^{34}S$ values between +18.4 ‰ and +22.0 ‰ (Figure 5.6A). Therefore, the higher $\delta^{34}S_{SO4}$ values in the Brusquet can also result from oxidation of pyrite with a higher $\delta^{34}S$ composition, which would be consistent with the negative $\delta^{18}O_{SO4}$ values (Figure 5.6A and Table 5.2).

A final possibility is that the more positive $\delta^{34}S_{SO4}$ values in the Brusquet result from isotopic fractionation during microbial sulfate reduction. This process is most pronounced in reducing environments, with sufficient availability of sulfate and organic matter (Tuttle et al., 2009). Bacterial sulfate reduction can modify $\delta^{34}S_{SO4}$ values in the range of ~+2 ‰ to +42 ‰ (Detmers et al., 2001), depending on temperature, pH, and the nature of the reducing bacteria. During this process, O isotopes are also thought to be fractionated, modifying the $\delta^{18}O_{SO4}$ by ~25% of the magnitude of the S isotope fractionation (Aharon and Fu, 2000). Bacterial sulfide reduction has been invoked to explain a shift towards more enriched $\delta^{34}S_{SO4}$ and $\delta^{18}O_{SO4}$ in catchments with developed thicker organic rich soils, denser vegetation cover, and warm climate, providing more favorable conditions for sulfate reducing bacterial communities (Hemingway et al., 2020; Turchyn et al., 2013). The Brusquet catchment has certain characteristics that may support the bacterial sulfide reduction. The source of organic matter in the

Brusquet catchment could be either the ancient OC in black shales (Graz et al., 2012), or more recent organic matter in surface soils derived from the denser vegetation cover, which is not so prevalent in the Laval catchment (Mathys and Klotz, 2008). However, the soil is still only weekly developed in many places of the catchment due to the recent change in land use (Burylo et al., 2011).

In summary, the measured $\delta^{34}S_{SO4}$ and $\delta^{18}O_{SO4}$ values in the Brusquet could, like in the Laval, be explained by pyrite oxidation. However, a role of sulfate reduction cannot be ruled out and requires further attention in future studies.

5.5.3 Temporal decoupling of sulfate production and its fluvial export

The oxygen isotope ratio of dissolved sulfate ($\delta^{18}O_{SO4}$) has been recognized as a proxy to track the oxidation pathway of sulfide minerals (Calmels et al., 2007; Taylor et al., 1984; Turchyn et al., 2013). Here, the oxidation environment of pyrite minerals is investigated and linked to different water reservoirs in the Laval catchment, which have been previously characterized in hydrological models by Cras et al. (2007) and Marc et al. (2017). Identifying the environment of pyrite oxidation and water pathways involved in SO_4^{2-} mobilization may reveal factors controlling the pyrite oxidation, production of sulfuric acid and consequently, weathering fluxes.

Oxidation of pyrite occurs under either aerobic or anaerobic conditions, with either atmospheric oxygen (Equation 5.3) or ferric iron Fe^{3+} (Equation 5.4) being the dominant oxidant agent, respectively (Taylor et al., 1984). The resultant value of $\delta^{18}O_{SO4}$ is set when the aqueous sulfate molecule is formed, and not thought to undergo subsequent oxygen isotope exchange with H_2O (Lloyd, 1968; Taylor et al., 1984). The large isotopic difference between $\delta^{18}O$ of the atmosphere

(~+23 ‰) and meteoric water (<0 ‰) suggests that SO_4 formed by the oxidation of atmospheric oxygen may result in a more positive $\delta^{18}O_{SO4}$ signal than $\delta^{18}O_{SO4}$ formed by the Fe^{3+} cycling (Balci et al., 2007; Taylor et al., 1984). Therefore, the light $\delta^{18}O_{SO4}$ values measured in the studied catchments (Table 5.2, Figure 5.6A) would indicate that pyrite oxidation is taking place in an environment with liquid water present (Calmels et al., 2007; Taylor et al., 1984).

However, the $\delta^{18}O_{SO4}$ is not only controlled by the oxygen sources (atmosphere vs. meteoric water), but also by isotopic fractionation during oxygen uptake (Balci et al., 2007; Taylor et al., 1984). This can lead to a contrast between $\delta^{18}O_{SO4}$ and $\delta^{18}O_W$ values, $\Delta^{18}O_{SO4\text{-}W}$. Laboratory studies generally reported $\Delta^{18}O_{SO4\text{-}W}$ values between +2.6 ‰ and +4.1 ‰ during oxygen uptake into the SO_4 (Balci et al., 2007; Taylor et al., 1984; van Everdingen and Krouse, 1985). Previous studies from large river catchments with dominant pyrite oxidation signature report higher $\Delta^{18}O_{SO4\text{-}W}$ values. For example, in the Mackenzie river system the mean $\Delta^{18}O_{SO4\text{-}W}$ is +13.6 ± 3.7 ‰ (± SD, n=20; Calmels et al., 2007), suggesting an exchange of wet and dry conditions within the oxidation environment (Calmels et al., 2007). The tributaries of the Marsyandi catchment in the Nepalese Himalaya show a large range of $\Delta^{18}O_{SO4\text{-}W}$, between +3.0 ‰ and +22.2 ‰ and the lower values were explained by deep anoxic pyrite oxidation, involving $\delta^{18}O_w$ depleted groundwater (Turchyn et al., 2013). The lowest $\Delta^{18}O_{SO4\text{-}W}$ found in Marsyandi relate to $\Delta^{18}O_{SO4\text{-}W}$ values reported in anaerobic laboratory experiments (Fe^{3+} oxidant; Equation 5.4) conducted under low pH (2-5).

In contrast to previous work, the samples from the Laval have very similar $\delta^{18}O_{SO4}$ and $\delta^{18}O_W$ values, with a mean $\Delta^{18}O_{SO4\text{-}W}$ of +0.6 ± 0.6 ‰ (± SD, n=7). To

explain the low $\Delta^{18}O_{SO4\text{-}W}$ values observed in the Laval we suggest a decoupling of the water source involved in pyrite oxidation (setting $\delta^{18}O_{SO4}$) and the water that mobilizes SO_4 from the weathering zone (setting $\delta^{18}O_W$). Cras et al. (2007) proposed that pyrite oxidation in the Laval occurs in temporary, oxygen-depleted shallow surface water reservoirs. Porewater samples collected below 40 cm depth from regosols (in the Moulin catchment) or in colluvium (the Laval catchment), have depleted $\delta^{18}O_W$ signal with a mean value of -8.4 ±1.0 ‰ (±1SD, n=25). These porewater samples share their isotopic composition with winter stream water, suggesting recharge of shallow water aquifers during this time of the year (Figure 5.7A). If these porewaters represent the type of water that is involved in the oxidative weathering reactions in the near sub-surface (yellow shading in Figure 5.7B), they would result in a fractionation factor, $\Delta^{18}O_{SO4\text{-}PW}$ between +1.5 ‰ and +4.1 ‰, which is comparable with laboratory experiments (Balci et al., 2007). An expanded set of stream water $\delta^{18}O_{SO4}$ and $\delta^{18}O_W$ analyses from this catchment would help to shed light on this hypothesis. However, we note that the decoupling between the products of chemical weathering and their export was also observed in the study on the Re oxidation (Chapter 4) and its further discussed in Section 5.5.6.

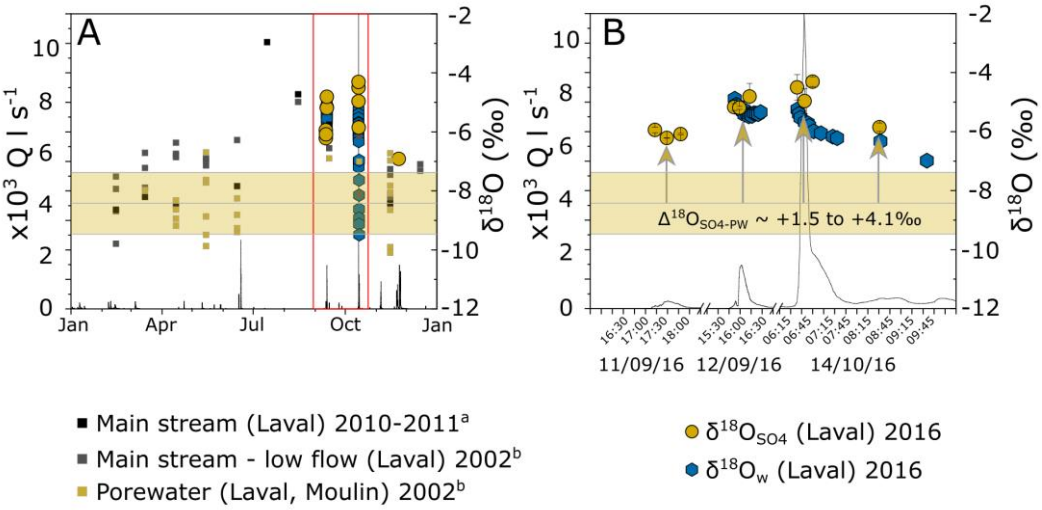

Figure 5.7: The oxidation environment of pyrite. A: Stable oxygen isotope of porewaters ($\delta^{18}O_{PW}$; yellow squares) collected in Laval and Moulin in 2002 show more depleted $\delta^{18}O$ signal compared to stream water samples ($\delta^{18}O_W$; grey squares). A mean $\delta^{18}O_{PW}$ is -8.4 ± 1‰ (yellow rectangle). **B:** If the porewaters are involved in pyrite oxidation then the $\Delta^{18}O_{SO4\text{-}PW}$ is 1.5 to 4.1 ‰, which is in range of isotopic fractionation during anoxic pyrite oxidation observed in laboratory studies. Data on $\delta^{18}O$ of stream water and porewaters are from [a]Marc et al. (2016) and [b]Cras et al. (2007).

5.5.4 The source of acidity for chemical weathering

The source of acid for chemical weathering reactions, i.e. carbonic acid versus sulfuric acid, plays a central role in the impact on the catchment-scale CO_2 budget. Carbonic acid weathering can drawdown atmospheric CO_2 into the river bicarbonate pool (Equation 5.1), while sulfuric acid weathering can result in the release of CO_2 from the carbonate mineral matrix to the atmosphere (Equation 5.5) – i.e. release of C stored in rocks for millions of years as CO_2. The main products of carbonic and sulfuric acid weathering are bicarbonate (HCO_3^-) and sulfate (SO_4^{2-}), respectively. To partition between the two acid sources, the HCO_3^- and SO_4^{2-} concentrations can be normalized for the weathered mineral unit, characterized as a sum of total cations ($\sum Cat^+ = Na^+ + K^+ + Mg^{2+} + Ca^{2+}$) in unit equivalent (Figure 5.8).

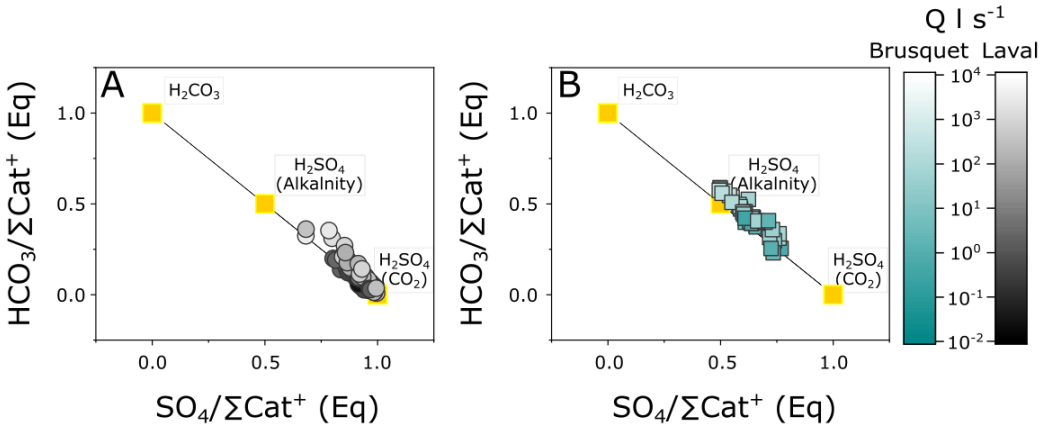

Figure 5.8: Partitioning carbonic acid and sulfuric acid weathering reactions. The end-members follow reactions stoichiometry (Table 5.4). **A:** Model for the Laval catchment (grey circles). **B:** Model for the Brusquet catchment (green squares). Symbols in both plots are color-coded by discharge.

In this framework, the ions in the stream are explained by some combination of: i) carbonic acid weathering; ii) sulfuric acid weathering producing HCO_3 (alkalinity); or iii) sulfuric acid weathering producing gas (CO_2) that does not enter stream water. These pathways result in distinct end-member values of $HCO_3/\sum Cat^+$ and $SO_4/\sum Cat^+$ (Table 5.4). We note that silicate weathering by sulfuric acid does not produce any net transfer of C, and so this pathway cannot be distinguished from sulfuric acid weathering that produces CO_2.

Table 5.4. Theoretical stoichiometry of the weathering reactions involved in the carbonate and silicate weathering. The sulfate and bicarbonate concentrations are normalized to a mineral unit, characterized by a sum of cations ($\sum Cat^+ = Na^+ + K^+ + Mg^{2+} + Ca^{2+}$) in unit equivalent.

Lithology	Acid source	HCO_3^-	SO_4^{2-}	$HCO_3/\sum Cat^+$	$SO_4/\sum Cat^+$
Silicate	Carbonic	2	0	1	0
	Sulfuric	0	1	0	1
Carbonate	Carbonic	2	0	1	0
	Sulfuric (alkalinity)	1	0.5	0.5	0.5
	Sulfuric (CO_2)	0	1	0	1

Previous studies have assumed that sulfuric acid-driven weathering of carbonate minerals results in the production of alkalinity, not CO_2 release at the reaction site (Blattmann et al., 2019; Winnick et al., 2017). However, we find that none of the Laval samples can be explained by this mechanism. The $SO_4^{2-}/\sum Cat^+$ values are too high, and $HCO_3^-/\sum Cat^+$ values in the Laval are too low. Instead, we have to invoke that a large part of the C liberated from carbonate weathering is released as a gas (CO_2), and does not enter the stream water. At the Laval site we benefit from the first attempts to measure gases during oxidative weathering of sedimentary rocks (Soulet et al., 2018). This study reports significant local release of CO_2 from the shallow weathering zone in the Laval catchment - directly supporting the observations from the stream.

In the Laval, sulfuric acid is clearly the dominant weathering agent, on average accounting for 90±6 % (±1SD) of mineral dissolution. We estimate that of this, 80±12 % results in direct CO_2 release and 20±12 % results in produced alkalinity (Figure 5.8A). In the Brusquet, the sulfuric acid is also the dominant weathering agent, with on average 63±9 %, of which 28±15 % results in direct CO_2 release and 72±15 % results in produced alkalinity (Figure 5.8B). Both catchments show a discharge dependency on the prevailing acidity source, as it has been previously observed in the East River (Colorado) by Winnick et al. (2017) and in catchments of the Nepalese Himalaya (Kemeny et al., 2021). In dry, low flow regimes, with limited water supply, higher contribution of sulfuric acid weathering resulting in direct CO_2 release is observed (Figure 5.8). In contrast, during wet, high flow regimes, some of the carbon from carbonate dissolution by sulfuric acid is exported in water, entering the stream discharge as bicarbonate.

This reaction still results in a CO_2 release, but on a time scale of carbonate precipitation in the ocean (10^6 years; Torres et al., 2014). A dynamic between direct release of CO_2 to the atmosphere during dry, low flow periods and CO_2 bounding to water producing alkalinity during increased water supply has been also observed in direct measurements of gaseous CO_2 from bedrock surface in the Laval (Soulet et al., 2021). In their study, a drop in gaseous CO_2 fluxes is observed in the hours following precipitation events, which has been interpreted as CO_2 bounding into the bicarbonate and release to the stream dissolved load. Dominance of sulfuric acid weathering in both catchments may have a profound impact on the inorganic carbon budget, as discussed in the following.

5.5.5 Catchment-scale inorganic carbon budget

We now apply the silicate and carbonate weathering rates from the Section 5.5.1.2, and proportion of the acid source from the Section 5.5.4. to assess the net inorganic carbon budgets for the studied catchments. First, the CO_2 release rates through carbonate dissolution by sulfuric acid (Equation 5.13) is estimated from the carbonate weathering rate ($J_{Carb} = Ca_{Carb}^{2+}+Mg_{Carb}^{2+}$) and the mean proportion of sulfuric acid ($\overline{X_{H2SO4}}$).

$$J_{Carb-rel.} = J_{Carb} \times \overline{X_{H2SO4}} \quad (5.13)$$

This calculation solely accounts for carbonate dissolution by sulfuric acid. The annual CO_2 release rates associated to carbonate dissolution by sulfuric acid are substantial in both catchments, with a mean value across the two years of 22.1±7.1 tC km^{-2} yr^{-1} for the Laval and 4.6±0.8 tC km^{-2} yr^{-1} for Brusquet (Table 5.3).

Next, the long term CO_2 consumption rates from silicate weathering ($J_{Sil\text{-}Cons.}$) in t km^{-2} yr^{-1} are calculated as follows in Equation 5.14 (Jacobson and Blum, 2003).

$$J_{Sil-Cons.} = 2 \times J_{Ca+MgSil} \times \overline{X_{H2CO3}} \quad (5.14)$$

Here, the $J_{Ca+MgSil}$ (g km^{-2} yr^{-1}) is the Ca+Mg silicate weathering rate, and $\overline{X_{H2CO3}}$ is the mean fraction of carbonic acid involved in chemical weathering (Figure 5.8). The factor 2 arises from stoichiometric reaction between carbonic acid and plagioclase (Jacobson and Blum, 2003). The second reaction involved in the CO_2 consumption at the catchment scale is carbonate weathering by carbonic acid (Equation 5.15).

$$J_{Carb-Cons.} = J_{Carb} \times \overline{X_{H2CO3}} \quad (5.15)$$

Here, the J_{Carb} is the carbonate weathering rate (g km^{-2} yr^{-1}) and $\overline{X_{H2CO3}}$ is the mean fraction of carbonic acid involved in chemical weathering. The factor 2 is not included in this calculation, since only half of the alkalinity produced from reaction of carbonic acid and carbonate is derived from atmospheric CO_2 (Gaillardet et al., 1999; Spence and Telmer, 2005). We note that over long time scales (>10^6 years) this reaction does not result in CO_2 consumption, since the carbon supplied to the oceans through carbonate weathering is removed by calcite precipitation and returned to the atmosphere as CO_2 (Gaillardet et al., 1999). As expected from previous discussion, the CO_2 consumption rates associated to silicate weathering are low, at 1.3±0.3 tC km^{-2} yr^{-1} in the Laval and 0.21±0.1 tC km^{-2} yr^{-1} in the Brusquet. The CO_2 consumption rates associated to carbonate weathering are somewhat higher, at

2.5±0.8 tC km^{-2} yr^{-1} in the Laval and 2.6±0.5 tC km^{-2} yr^{-1} in the Brusquet (Table 5.3)

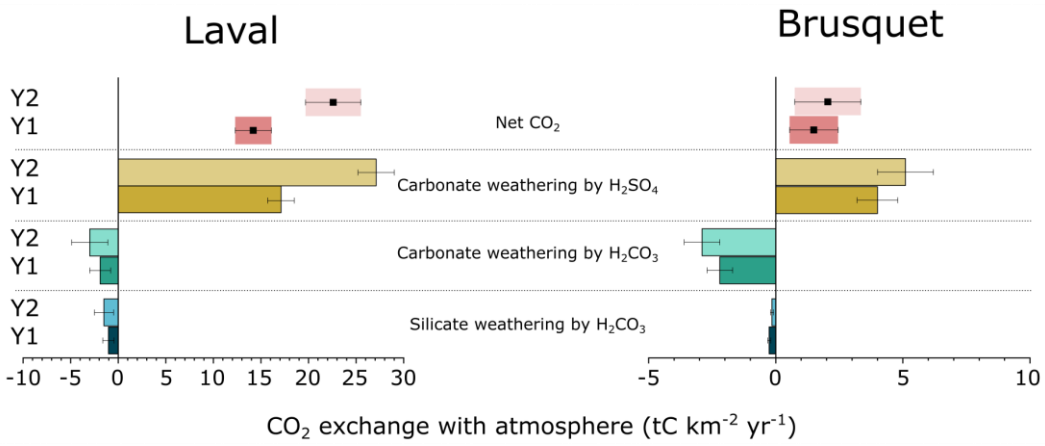

Figure 5.9: Catchment scale inorganic carbon budget for the timescale <10^6 years. The potential CO_2 sinks through silicate weathering by carbonic acid (blue) and carbonate weathering by carbonic acid (green) for the two measurement years (Y1, Y2). The potential CO_2 release by carbonate weathering by sulfuric acid (yellow). All estimates are in tC km^{-2} yr^{-1}.

Both catchments result in a net source of CO_2 from rock to the atmosphere, with large fluxes of carbonate weathering by sulfuric acid being the driving processes of the positive CO_2 balance (Figure 5.9). A striking observation here is that the potential CO_2 drawdown by silicate weathering is more than 15-times lower than the CO_2 release by sulfuric acid weathering of carbonate across both catchments. The low CO_2 consumption rates presented for the highly erosive Laval could be explained by the kinetic-limited silicate weathering (Calmels et al., 2011; Jacobson and Blum, 2003), opposite to supply-limited sulfide mineral oxidation (Hilton and West, 2020; Kemeny et al., 2021; Nevers et al., 2020). Recently, Bufe et al. (2021) showed that in sedimentary catchments, where silicate, carbonate, and sulfide weathering regimes co-operate, the products of carbonate weathering could buffer the weathering fluids, which would prevent

the increase in silicate weathering rates. This is most probably explanation for the carbon balance presented for the Laval and Brusquet.

Overall, we observe a distinct contrast between the two studied catchments in the rates of carbonate dissolution by sulfuric acid, which are more than 5-times higher in the Laval compared the Brusquet (Table 5.3). In the following, we provide constrains on factors that may drive this these processes and may help explaining the difference between the two study sites.

5.5.6 Controls on sulfuric acid production

5.5.6.1 Supply-limited sulfide weathering

The differences in the chemical weathering rates between the Laval and Brusquet catchments may be explored through their contrasting erosion rates and consequently the rate of exposure fresh mineral surfaces available for oxidation. One measure of erosion is the suspended sediment yield, which is positively correlated with CO_2 release from carbonate weathering by sulfuric acid (Calmels et al., 2007; Hilton and West, 2020; Torres et al., 2014), as presented in Figure 5.10. The suspended sediment yield export is more than two-orders of magnitude lower in the Brusquet (45 t $km^{-2}yr^{-1}$ and 492 t $km^{-2}yr^{-1}$; 10/2016 – 10/2017 and 10/2017 – 10/2018, respectively) compared to the Laval (8,693 t $km^{-2}yr^{-1}$ and 15,829 t $km^{-2}yr^{-1}$; 09/2016 – 09/2017 and 09/2017 – 09/2018, respectively). The Laval catchment follows the global trend, showing similar CO_2 release rates as high erosive catchments in Taiwan (Das et al., 2012; Torres et al., 2014), suggesting that sulfide weathering could be partly limited by the supply of the fresh mineral surfaces to the near surface weathering zone (Calmels et al., 2007). The dominant role of mechanical erosion on sulfide weathering has been

previously shown in several landslides studies in New Zealand (Emberson et al., 2016a), Taiwan (Emberson et al., 2016b), the French Alps (Nevers et al. 2020) and in catchments across a large erosion gradient in south Taiwan (Bufe et al., 2021).

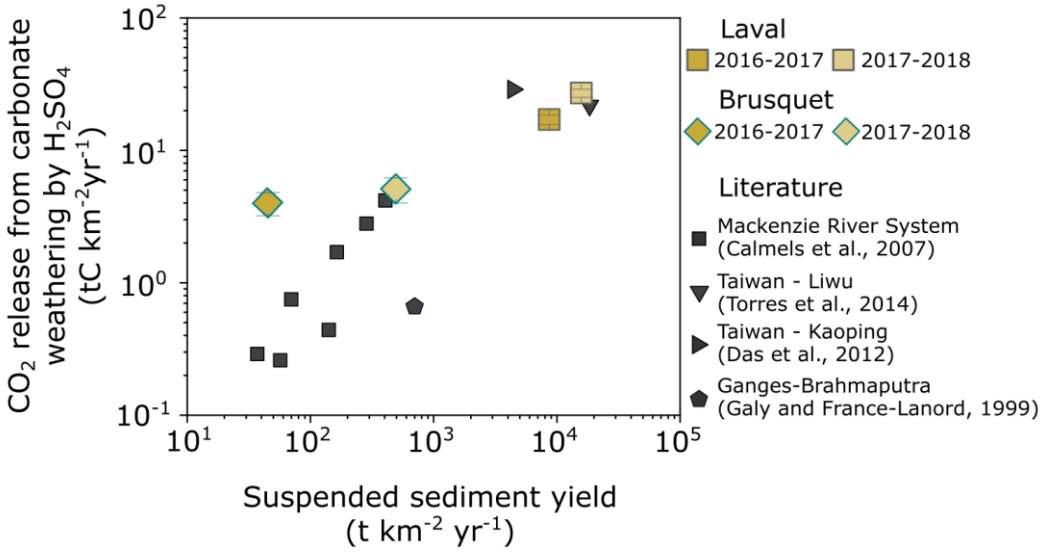

Figure 5.10. Physical erosion as a control on the CO_2 release from carbonate dissolution by sulfuric acid. Literature data (dark grey) with new data from Laval (yellow squares) and Brusquet (yellow diamonds).

The Brusquet displays a deviation from the global trend in the 10/2016 – 10/2017 observation period (Figure 5.10), which may result from decoupling of actual physical degradation of the bedrock and suspended sediment yield export. Previous studies have suggested that a dense vegetation cover may act as a cascade for sediment transport within catchments (e.g. Fryirs, 2013; Kirchner et al., 2001), meaning that the suspended sediment yield measure may underestimate the actual erosion rate (Milliman and Syvitski, 1992). That may be the case for the Brusquet, where in average 85 % of the surface area has been afforested in the 19th century (Mathys and Klotz, 2008). Field observations revealed that the vegetation is particular dense in the lower part of the

catchment, while steep, non-vegetated black shales and marl outcrops remained exposed in the catchment headwaters. These outcrops may still experience high physical and chemical rock degradation, which is reflected in high concentration of dissolved components (Figure 5.3). After a significant change in land use, a sufficient time is required for the chemical weathering regime to reach a steady-state of mineral supply (West et al., 2005). The soil cover in the Brusquet is generally thin (~10 cm), containing larger fragments of the weathered lithology (Cosandey et al., 2005; Graz et al., 2011), suggesting that the soil is in the early stages of development and that chemical weathering rates are not at steady-state. The impact on the chemical weathering rates with the change in land use is an interesting feature of the Brusquet catchment, which requires further investigation.

5.5.6.2 Temperature control on sulfuric acid production

The Mediterranean-Alpine climate at the research sites has a strong seasonal cycle in temperature, and this could drive differences in the rates of sulfide oxidation and associated CO_2 release. This is of particular relevance in catchments with high erosion rates and rapid supply of fresh mineral surfaces such as the Laval. Indeed, in 5 chambers installed in the Laval catchment to monitor gaseous CO_2 release, a seasonal variability is observed (Soulet et al., 2021), which would imply a seasonal variability in the reaction products. To our best knowledge, this is the first time that independent datasets on dissolved stream load and direct gas measurements can be directly compared, by simultaneously tracking evidence for seasonal variability in sulfide oxidation in the dissolved load.

The seasonality in the low flow and the SO_4 flux is shifted (Figure S5.1, Supplementary figures), with highest fluxes occurring in autumn and winter months. Due to the flashy hydrograph nature of the studied catchments with extreme fluxes during storm events and low, ambient fluxes in the intermediate periods, the chemical weathering products are flushed episodically during the distinct intensive storm events (Mathys and Klotz, 2008). Therefore, instead of fluxes, the SO_4^{2-}/HCO_3^- ratio in the low flow regime is used as a proxy to track production of sulfuric acid. The first indications of seasonal variability in SO_4^{2-}/HCO_3^- ratio come from cold seep samples, which have higher SO_4^{2-}/HCO_3^- ratio in the summer ~77 than in winter ~2 (Figure 5.4B). Similarly, elemental ratios (SO_4^{2-}/HCO_3^-) measured at low flow regimes show a notable seasonality as well (Figure 5.4B). A positive correlation between mean monthly temperature and low flow SO_4^{2-}/HCO_3^- ratio, is found through an exponential growth model: $y = y_0 \times \exp(\alpha T)$ in Figure 5.11. The growth rate parameter (α) in Figure 5.11 applied to the low flow data from this study is 0.08±0.03 $°C^{-1}$. This is remarkably similar to the α value range 0.057–0.079 $°C^{-1}$ of the exponential model that describes how measured CO_2 flux attributed to carbonate dissolution increases with temperature at the Laval site (Soulet et al., 2021). The seasonality in direct measurements of CO_2 fluxes (Soulet et al., 2021) and low flow SO_4^{2-}/HCO_3^- ratio, suggests a strong temperature dependency of these processes.

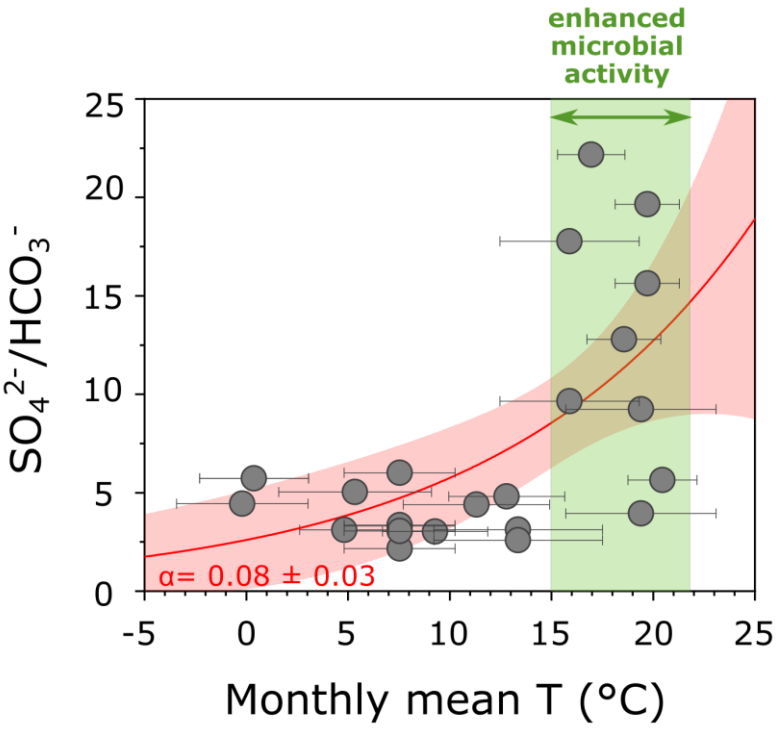

Figure 5.11: Temperature and microbial control on the production of sulfuric acid. SO_4^{2-} over HCO_3^- ratio measured in the low flow samples is used as a proxy for sulfuric acid production. The red line represents exponential grow fit through the data; the pink shading represents the 95% confidence interval. The grow rate parameter (α) is given. The green shading shows steep growth of the SO_4^{2-}/HCO_3^- ratio in a narrow temperature range between 15 °C and 20 °C. The activity of microbes involved in pyrite oxidation is enhanced in this temperature range.

The increase in pyrite oxidation and sulfuric acid production with increased temperature is also supported in laboratory studies (e.g. Janzen et al., 2000; Steger, 1982). Temperature can enhance microbial activity that can oxidize sulfide minerals (Calmels et al., 2007; Percak-Dennett et al., 2017). For example, *Thiobacilli*, one of most common bacteria involved in oxidation of inorganic sulfur compounds to sulfuric acid are most active in temperature range between 20 °C and 55 °C (Belzile et al., 2004). This is within the range of summer temperatures in the researched catchment (+15 °C to +35 °C). The sharp increase in the SO_4^{-2}/HCO_3^- ratio in the monthly average temperatures above 15°C as seen in

Figure 5.11 would suggest that the activity of microbes involved in pyrite oxidation is enhanced in this temperature range.

In contrast to the Laval, there is negligible seasonality in low flow SO_4^{2-}/HCO_3^- ratio (Figure 5.4D) and total SO_4 flux observed in the Brusquet (Figure S 5.2, Supplementary figures). Different factors may govern this steady SO_4 export in the Brusquet throughout the year. First, higher vegetation cover and a more developed organic soil layer in Brusquet means that the overall physical erosion rates are lower (Carriere et al., 2020; Mathys et al., 2003), resulting in lower oxidation rates (Brantley et al., 2013) and potentially developing deeper chemical weathering fronts. Hercod et al. (1998) came to a similar conclusion when studying seasonal production of H_2SO_4 in a small, slowly eroding and densely vegetated watershed, White Rock Creek in Dallas, USA. Second, the differences in the production of sulfuric acid between the two investigated catchments could also result from a difference in water table level and variable saturated/non-saturated conditions within the catchments (Mathys et al., 2005). The prolonged and delayed storm events in the Brusquet (Cosandey et al., 2005; Mathys and Klotz, 2008) suggest higher soil saturation rates. Due to slower oxygen diffusion rates through saturated environments (Brantley et al., 2013; Manning et al., 2013), lower H_2SO_4 production rates may be expected in regions with more developed soil cover.

In summary, our results suggest that low flow stream water chemistry ascertain a pronounced seasonality in sulfuric acid production in a catchment characterized by high erosion rates, large areas of bare surfaces, and a temperate climate (the Laval). In the same climatic environment, vegetation and soil cover

may buffer the temperature control, and create more saturated environment, resulting in more even sulfuric acid production and export throughout the year (the Brusquet).

5.6 Conclusions

In this study, we investigate the inorganic carbon budget associated with chemical weathering of carbonate and silicate minerals in two marl-dominated catchments (the Laval and Brusquet) in the South French Alps. Both catchments drain carbonate and sulfide mineral-bearing rocks and have similar climate, but large differences are observed in the present-day suspended sediment yield and the extent of the vegetation cover. High temporal resolution time-series sampling of stream water in small catchments was applied for a precise determination of chemical weathering rates and in-depth understanding of processes governing weathering reactions.

In the Laval, cation partitioning suggests an important contribution of silicate weathering (22 – 44 %), while the Brusquet is dominated by carbonate weathering (92 %). When we compare the stable sulfur isotope signature from dissolved sulfate to solid samples, this suggest that oxidation of pyrite minerals is the primary source of SO_4^{2-} and sulfuric acid is the dominant weathering agent in both catchments (90±6 % and 63±9 % in the Laval and Brusquet, respectively). As such, both catchments represent a net positive CO_2 release to the atmosphere; +18.4±5.9 tC km^{-2} yr^{-1} in the Laval and +2.0±0.4 tC km^{-2} yr^{-1} in the Brusquet.

Seasonality in temperature appears to impact the production of sulfuric acid in the catchment with higher erosion rate and larger areal exposure of bare surfaces (the Laval). In contrast, in the catchment with denser vegetation cover

(the Brusquet), the production of sulfuric acid is steadier throughout the year, which is most probably due to lower erosion rates, lower temperature variation in the ground (due to vegetation and soil buffer), and higher saturation state of the soils. We conclude that Earth surface areas with exposed weak marl lithologies may be hot spots for the CO_2 release to the atmosphere though carbonate dissolution by sulfuric acid, and that the CO_2 release associated to this process may increase in the future warm climate.

5.7 Supplementary figures

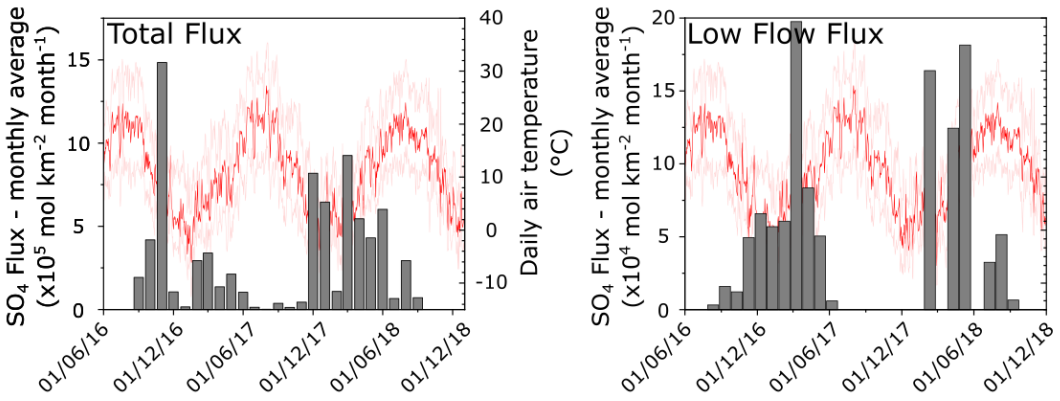

Figure S5.1 Seasonality in the sulfate flux in the Laval catchment. **A** Total sulfate flux. **B** Low flow sulfate flux. The highest fluxes (mol km^{-2} yr^{-1}) were measured in autumn 2016 and winter/spring 2017-2018. Grey bars represent fluxes averaged by month. Red line represents seasonal variability in air temperature monitored at the Laval gauging station for the observation period.

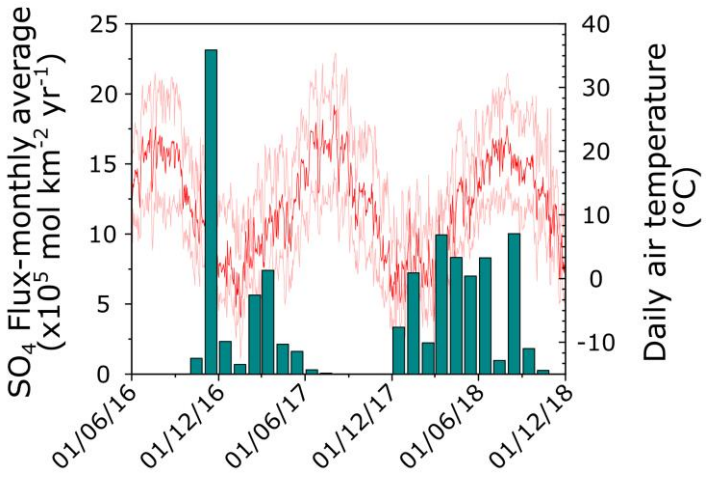

Figure S 5.2. Absence of seasonality in the sulfate flux in the Brusquet catchment. Monthly averaged SO_4 fluxes (mol km^{-2} yr^{-1}) show less distinct seasonality, in particular in the 2017-2018 observation period. Green bars represent fluxes averaged by month. Red line represents seasonal variability in air temperature monitored at the Laval gauging station for the observation period.

CHAPTER 6
Main conclusions and future aspects

Drone image of the Laval catchment; Draix-Bléone Critical Zone Observatory. February 2018; Photo: Thomas Croissant

Chemical weathering of sedimentary rocks significantly influences the chemical composition of rivers, the ocean, and the atmosphere through geological time. This work determined fluxes and controls on two key weathering processes, which are central to the operation of the geological carbon cycle: i) rock organic carbon (OC_{petro}) oxidation; and ii) carbonate weathering by sulfuric acid. The trace element rhenium (Re) was explored to track OC_{petro} oxidation within the critical zone of the Earth's surface. The catchment-scale inorganic carbon cycle was studied by investigating major elements in stream water and stable oxygen and sulfur isotopes of dissolved sulfate.

The research took place in two critical zone observatories (CZO): The Susquehanna Shale Hills CZO (Pennsylvania, US) and the Draix-Bléone CZO (France). The study sites are representative of the large proportion of the Earth's surface, due their exposure to temperate climate and catchment lithology, which is characterized by sedimentary rocks with low OC_{petro} concentrations (<1 %). Additionally, the sites are characterized by large differences in erosion rates and variable extent of the vegetation cover.

6.1 Main conclusions

The new research presented in this PhD thesis improves our current understanding of the catchment-scale CO_2 release rates from weathering of sedimentary rocks, the application of the Re proxy to track OC_{petro} oxidation and controls on the CO_2 release. These aspects are summarized in the following five main conclusions of this thesis.

6.1.1 Rhenium association with OC_{petro} in OC-poor shales

Deep (~15 m and ~30 m) weathering profiles from the Shale Hills study site offer a unique opportunity to explore the association of Re and OC_{petro} in a lithology with very low OC concentrations (<0.05 %; Jin et al., 2014). The borehole samples revealed a complete loss of S, and high loses of Re (~90 %) and OC_{petro} (~40 %) at roughly the same depths (Chapter 3, Figure 3.4, p74). The differences in Re and OC_{petro} depletion may be related to an overestimation of the OC_{petro} in these profiles, potential resistance of OC_{petro} to oxidation, or Re persistence in the silicate phase. Nonetheless, the similar, steady loss of Re and OC_{petro} across the weathering front suggest a close association of these two elements. This was the first time that the Re mobility was studied alongside OC_{petro} mobility in a weathering profile exhibiting extremely low OC_{petro} concentrations and it validates the applicability of the Re proxy for the large range of sedimentary rocks (Chapter 3; Jaffe et al., 2002; Peucker-Ehrenbrink and Hannigan, 2000).

6.1.2 Seasonal patterns in Re production and mobilization

Another novel aspect of this thesis was the use of high temporal resolution stream water sampling to investigate dissolved Re concentration and flux over a period of two years (Chapter 4, Figure 4.2, p108). Previously, the dissolved Re-proxy for OC_{petro} oxidation and modern-day CO_2 release has been applied only to a hand-full of studies: Dalai et al. (2002), Hilton et al. (2014), Horan et al. (2017, 2019), which all used only a limited number of samples and did not take into account potential seasonal variability in Re concentrations. Here, the high temporal resolution time-series dataset from the Draix-Bléone CZO revealed a striking seasonality in dissolved Re export, suggesting ~ten-times higher Re

concentrations in the summer months compared to the winter months (Chapter 4, Figure 4.9, p137). The seasonality is most pronounced in the Laval catchment characterized by high erosion rates and large exposed bare surfaces, while the seasonal variability is less clear in the catchment with lower erosion rates and denser vegetation cover, exemplified by the Brusquet (Chapter 4, Figure 4.12, p142). This observation carries important implications for future studies determining OC_{petro} oxidation rates.

6.1.3 Catchment-scale inorganic carbon budget

The high temporal resolution stream water chemistry dataset was further explored to estimate the CO_2 balance between sources and sinks involved in the inorganic carbon cycle for the Laval and Brusquet catchments of the Draix-Bléone CZO (Chapter 5). Here, we applied well-adopted models in river geochemistry in order to partition between the lithological sources (carbonate and silicate) and the prevailing weathering agent (carbonic versus sulfuric acid). In both catchments, the net inorganic carbon balance was dominated by carbonate weathering by sulfuric acid (Chapter 5, Figure 5.9, p201). Estimates for the highly erosive catchment (Laval) return extremely high CO_2 release rates, which is consistent with previous estimates from settings exposed to high physical rock degradation (Das et al., 2012; Emberson et al., 2016; Nevers et al., 2020; Torres et al., 2014). In the catchment with lower erosion rates and denser vegetation cover (Brusquet), the CO_2 release by sulfuric acid-carbonate weathering is ~five-times lower. We suggest that lower erosion rates, denser vegetation cover and more developed soil organic layer may decrease sulfide and carbonate weathering, due to lower physical degradation, supply of fresh bedrock and

buffering the temperature impact on the production of sulfuric acid. In contrast to carbonate weathering, the CO_2 consumption through silicate weathering remains low in both catchments, which may result from altered carbonic acid equilibrium in streams by the excess of carbonate weathering.

6.1.4 Erosion control on chemical weathering

This work includes three catchments with contrasting erosion rates (from ~25 t km^{-2} yr^{-1} to >10,000 t km^{-2} yr^{-1}), while are all exposed to similar climatic conditions within temperate climate, and draining shale dominated sedimentary lithologies with variable, but generally low OC_{petro} concentration (from <0.05 % to ~1 %). Here we provided new constrains for the OC_{petro} oxidation rates in the low erosion settings at the Shale Hills catchment by using radiocarbon isotope and the trace element Re. Both proxies resulted in expected low OC_{petro} oxidation rates (<2.0×10^{-2} tC km^{-2} yr^{-1}), suggesting that OC_{petro} oxidation is limited by the supply of fresh mineral surfaces available for oxidation (i.e. a supply-limited process) (Figure 6.1A. The application of the Re proxy in the Laval and Brusquet catchments of Draix-Bléone CZO returns relatively low Re yields and consequently a low estimate of OC_{petro} oxidation rate. This may be explained by the shallow weathering zone, Re mobility though the catchment and extremely high Re export through the solid load.

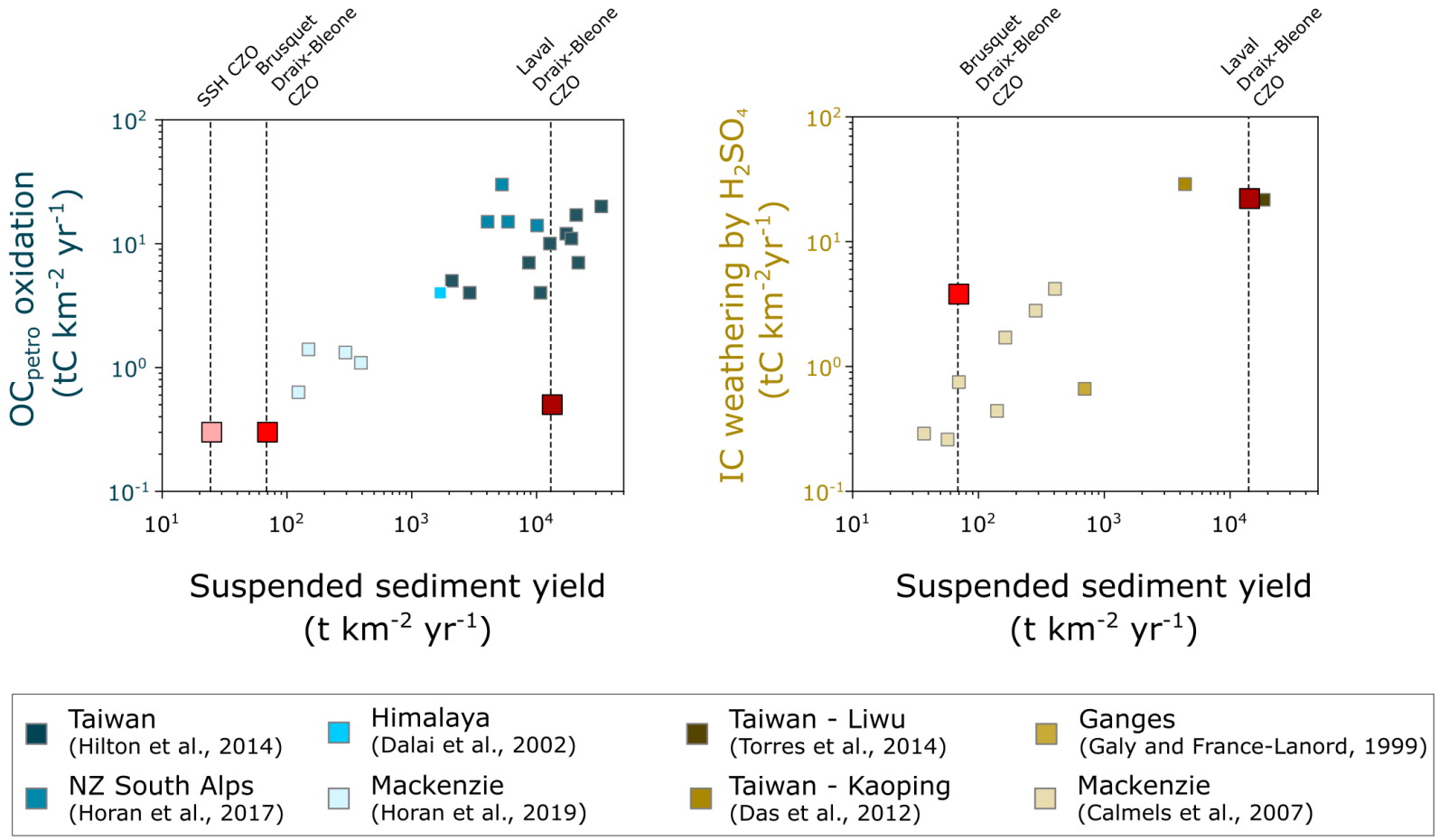

Figure 6.1: Erosion control on the oxidation of OC_{petro} and sulfide minerals. A: Erosion control on the OC_{petro} oxidation with new data from this thesis (red) filling the research gap in the low erosive setting. **B:** Erosion control on the sulfide mineral oxidation with the two catchment studied here (red) following the global trend.

Further, this study confirms that oxidation of sulfide minerals and production of sulfuric acid is also a supply-limited process (Figure 6.1B), as previously suggested by Calmels et al. (2007) and Hilton and West (2020). As such, highly erosive, vegetation free, gully catchments consisting of soft, pyrite-rich, marly lithologies (e.g. the Laval) represent hot spots for the CO_2 release to the atmosphere.

6.1.5 Temperature control on chemical weathering

Only recently, climatic factors such as temperature became of interest in terms of their role in setting oxidative weathering rates and associated CO_2 release (Crawford et al., 2019; Zhi et al., 2020). Here we explored the high temporal resolution stream water chemistry to investigate the potential temperature control on the production of solutes from chemical weathering (Chapter 4 and Chapter 5). In the two catchments of the Draix-Bléone CZO, we observe seasonality in dissolved Re concentrations (Chapter 4, Figure 4.9, p137) and in the SO_4/HCO_3 ratio (Chapter 5, Figure 5.4, p179) in stream water. We interpret the Re concentrations and SO_4/HCO_3 ratio as proxies for OC_{petro} oxidation and production of sulfuric acid, respectively. A complimentary study by (Soulet et al., 2021), measures the CO_2 release from a chamber at an outcrop in the Laval and also sees the same seasonality. This is the first opportunity to observe the seasonality in chemical weathering of sedimentary rocks with two complimentary methods in the same catchment. Together our studies provide strong evidence that in a warmer environment, chemical weathering of sedimentary rocks may result in positive feedback. This means that in the future climate, chemical weathering of sedimentary rocks may enhance, releasing more

CO_2, which will further increase air temperature. This is in particular enhanced in catchments exhibiting kinetically-limited weathering regimes (high erosion rates). Catchments exhibiting supply-limited weathering regime (lower erosion rates) may have a lower impact on the CO_2 release from chemical weathering (Figure 6.2). This observation is of profound importance for modelling the geological carbon cycle and past climate, while also relevant to understanding how natural carbon cycle processes will respond to ongoing and future climate warming.

The controls on chemical weathering rates are here studied in small, mountainous catchments, which dominate the global erosion and chemical weathering rates (Bluth and Kump, 1994; Kirchner et al., 2001), are important in terms of freshwater supply (Viviroli et al., 2011, 2007; Zhi et al., 2020) and may experience the greatest impact in the warming climate (IPCC, 2019). The positive climatic feedback proposed here, may result in higher concentration of solutes in the dissolved load, having important implicates for global biogeochemical cycles and freshwater quality (Crawford et al., 2019). However, open questions remain how these findings apply over larger scales to provide constrains on the global rates.

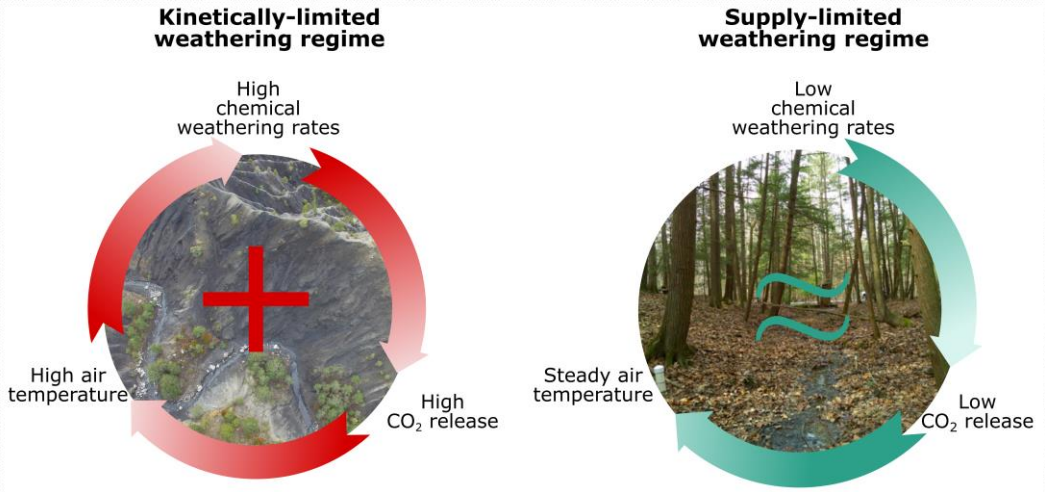

Figure 6.2. Climatic feedback on chemical weathering rates of sedimentary rocks. In a high erosive setting, high sulfide and carbonate weathering rates release high CO_2 rates which may increase air temperature and further enahnce chemical weathering rates. Opposite, in a low erosive setting, the chemical weathering rates are lower, releasing lower CO_2 rates, leading to smaller changes in air temperature.

6.2 Future research aspects

This work investigated many aspects on the chemical weathering of sedimentary rocks, but also raised new questions and revealed knowledge gaps that require attention in future research. Some of which are presented in the following.

6.2.1 Anthropogenic Re cycling in surface soils

In the third chapter of this thesis, an attempt is made to present the Re mass balance in terms of Re inputs on catchment scale. This topic requires more work by investigating the mass, speciation and nature of Re sequestration in surface soils, but also whether Re can cycle through vegetation. Previous studies suggested that Re may be involved in bio-cycling with certain grass communities (Novo et al., 2015). In small catchments, impacted by past or present anthropogenic contamination, bio-cycling of Re may be important, since it could

result in longer persistence of Re in the top soil, as it is seen on a case of Mn (Herndon et al., 2015b) and Mo (King et al., 2018).

6.2.2 Mineral-scale assessment of the sources of Re

The mixing model presented by Horan et al. (2019) and applied in this study tends to efficiently separate the mineral fractions contribution to the total Re concentration measured in the dissolved load and solid samples. However, the partitioning of Re in sulfide versus the organic matter in sedimentary rocks may be further studied using additional techniques. One such method could be using a sequential extraction, for instance with a chromos-chloride reduction technique to isolate sulfide vs organic phases, as it has been done for Selenium (Se) in shales (Matamoros-Veloza et al., 2011). Another, feasible approach could be to apply density separation, using sodium polytungstate (Gregory and Johnston, 1987) and hand selection of mineral grains for analysis, since the pyrite fraction has very different density compared to organic matter and silicate minerals in rock powders.

6.2.3 Export of weathering products through the solid load

In the Laval, the Re export through the solid load is ~100-times larger compared to the Re export through the dissolved load (Chapter 4). The extremely high physical degradation of the soft rocks within the catchment and high intensity storm events, result in short residence time of the sediments within the catchments (Mathys et al., 2005). A large proportion of this Re in the solid load is likely to "un-weathered", alongside sulfide and OC_{petro} phases (Graz et al., 2012). The fate of these reduced phases in downstream river systems is important to understand the integrated impact of erosion on oxidative weathering fluxes, as it

has been shown for the Amazon (Clark et al., 2017). However, our results suggest that a part of the solid load may contain weathering products which were mobilized, but subsequently re-sequestered into secondary solids. This is potentially relevant for Re, but could also be the case for S and Ca produced from sulfide oxidation and carbonate weathering. To better understand whether this mechanism is operating, and its impact on dissolved load fluxes (and the weathering fluxes we calculate from them), sequential extractions could be explored – for instance in the easily exchangeable fractions of river sediments. The Re isotope system may also shed new light on this, with recent method developments making it possible to measure the Re isotope ratios in stream and river waters, alongside river sediments (Dellinger et al., In review).

6.2.4 Exploring environmental controls on oxidative weathering

This study provides strong evidence for a role of temperature on the rates of OC_{petro} oxidation (Figure 4.10, p139). This raises the important question whether or not these patterns prevail in other climatic settings, and for other sedimentary rock lithologies. The dynamics of OC_{petro} and carbonate weathering in Arctic climates, which are particularly impacted by the global rise in air temperatures, should be a future research focus. Here, we showed that increased temperatures are an important control on chemical weathering of sedimentary rocks and production of solutes into the stream (Chapter 4 and Chapter 5). However, an open question remains what will the impact of climate change be in different scenarios, i.e. decreasing, steady or accelerating warming.

References

Aharon, P., Fu, B., 2000. Microbial sulfate reduction rates and sulfur and oxygen isotope fractionations at oil and gas seeps in deepwater Gulf of Mexico. Geochimica et Cosmochimica Acta 64, 233–246. https://doi.org/10.1016/S0016-7037(99)00292-6

Amiotte Suchet, P., Probst, J.-L., Ludwig, W., 2003. Worldwide distribution of continental rock lithology: Implications for the atmospheric/soil CO2 uptake by continental weathering and alkalinity river transport to the oceans. Global Biogeochemical Cycles 17, n/a-n/a. https://doi.org/10.1029/2002GB001891

Antoine, P., Giraud, A., Meunier, M., Van Asch, T., 1995. Geological and geotechnical properties of the "Terres Noires" in southeastern France: Weathering, erosion, solid transport and instability. Engineering Geology 40, 223–234. https://doi.org/10.1016/0013-7952(95)00053-4

Appling, A.P., Leon, M.C., McDowell, W.H., 2015. Reducing bias and quantifying uncertainty in watershed flux estimates: the R package loadflex. Ecosphere 6, art269. https://doi.org/10.1890/ES14-00517.1

Aulenbach, B.T., 2013. Improving regression-model-based streamwater constituent load estimates derived from serially correlated data. Journal of Hydrology 503, 55–66. https://doi.org/10.1016/j.jhydrol.2013.09.001

Aulenbach, B.T., Hooper, R.P., 2006. The composite method: an improved method for stream-water solute load estimation. Hydrological Processes 20, 3029–3047. https://doi.org/10.1002/hyp.6147

Balci, N., Shanks, W.C., Mayer, B., Mandernack, K.W., 2007. Oxygen and sulfur isotope systematics of sulfate produced by bacterial and abiotic oxidation of pyrite. Geochimica et Cosmochimica Acta 71, 3796–3811. https://doi.org/10.1016/j.gca.2007.04.017

Belzile, N., Chen, Y.-W., Cai, M.-F., Li, Y., 2004. A review on pyrrhotite oxidation. Journal of Geochemical Exploration 84, 65–76. https://doi.org/10.1016/j.gexplo.2004.03.003

Berner, E.K., Berner, R.A., 2012. Global environment: water, air, and geochemical cycles, 2nd ed. ed. Princeton University Press, Princeton, N.J.

Berner, R.A., 2003. The long-term carbon cycle, fossil fuels and atmospheric composition. Nature 426, 323–326. https://doi.org/10.1038/nature02131

Berner, R.A., 1982. Burial of organic carbon and pyrite sulfur in the modern ocean; its geochemical and environmental significance. American Journal of Science 282, 451–473. https://doi.org/10.2475/ajs.282.4.451

Berner, R.A., Canfield, D.E., 1989. A new model for atmospheric oxygen over Phanerozoic time. American Journal of Science 289, 333–361.

Berner, R.A., Raiswell, R., 1984. C/S method for distinguishing freshwater from marine sedimentary rocks. Geology 12, 365–368.

Bertine, K.K., Goldberg, E.D., 1971. Fossil Fuel Combustion and the Major Sedimentary Cycle. Science 173, 233–235. https://doi.org/10.1126/science.173.3993.233

Bickle, M.J., Tipper, E., Galy, A., Chapman, H., Harris, N., 2015. On discrimination between carbonate and silicate inputs to Himalayan rivers. American Journal of Science 315, 120–166. https://doi.org/10.2475/02.2015.02

Blair, N.E., Leithold, E.L., Ford, S.T., Peeler, K.A., Holmes, J.C., Perkey, D.W., 2003. The persistence of memory: the fate of ancient sedimentary organic carbon in a modern sedimentary system. Geochimica et Cosmochimica Acta 67, 63–73. https://doi.org/10.1016/S0016-7037(02)01043-8

Blattmann, T.M., Wang, S.-L., Lupker, M., Märki, L., Haghipour, N., Wacker, L., Chung, L.-H., Bernasconi, S.M., Plötze, M., Eglinton, T.I., 2019. Sulphuric acid-mediated weathering on Taiwan buffers geological atmospheric carbon sinks. Scientific Reports 9. https://doi.org/10.1038/s41598-019-39272-5

Bluth, G.J.S., Kump, L.R., 1994. Lithologic and climatologic controls of river chemistry. Geochimica et Cosmochimica Acta 58, 2341–2359. https://doi.org/10.1016/0016-7037(94)90015-9

Bolton, E.W., Berner, R.A., Petsch, S.T., 2006. The Weathering of Sedimentary Organic Matter as a Control on Atmospheric O2: II. Theoretical Modeling. American Journal of Science 306, 575–615. https://doi.org/10.2475/08.2006.01

Bouchez, J., Beyssac, O., Galy, V., Gaillardet, J., France-Lanord, C., Maurice, L., Moreira-Turcq, P., 2010. Oxidation of petrogenic organic carbon in the Amazon floodplain as a source of atmospheric CO2. Geology 38, 255–258. https://doi.org/10.1130/G30608.1

Brand, W.A., Coplen, T.B., Aerts-Bijma, A.T., Böhlke, J.K., Gehre, M., Geilmann, H., Gröning, M., Jansen, H.G., Meijer, H.A.J., Mroczkowski, S.J., Qi, H., Soergel, K., Stuart-Williams, H., Weise, S.M., Werner, R.A., 2009. Comprehensive inter-laboratory calibration of reference materials for δ18O versus VSMOW using various on-line high-temperature conversion techniques. Rapid Communications in Mass Spectrometry 23, 999–1019. https://doi.org/10.1002/rcm.3958

Brantley, S.L., Goldhaber, M.B., Ragnarsdottir, K.V., 2007. Crossing Disciplines and Scales to Understand the Critical Zone. Elements 3, 307–314. https://doi.org/10.2113/gselements.3.5.307

Brantley, S.L., Holleran, M.E., Jin, L., Bazilevskaya, E., 2013. Probing deep weathering in the Shale Hills Critical Zone Observatory, Pennsylvania (USA): the hypothesis of nested chemical reaction fronts in the subsurface. Earth Surface Processes and Landforms 38, 1280–1298. https://doi.org/10.1002/esp.3415

Brantley, S.L., McDowell, W.H., Dietrich, W.E., White, T.S., Kumar, P., Anderson, S.P., Chorover, J., Lohse, K.A., Bales, R.C., Richter, D.D., Grant, G., Gaillardet, J., 2017. Designing a network of critical zone observatories to explore the living skin of the terrestrial Earth. Earth Surface Dynamics 5, 841–860. https://doi.org/10.5194/esurf-5-841-2017

Brimhall, G.H., Dietrich, W.E., 1987. Constitutive mass balance relations between chemical composition, volume, density, porosity, and strain in metasomatic hydrochemical systems: Results on weathering and pedogenesis. Geochimica et Cosmochimica Acta 51, 567–587. https://doi.org/10.1016/0016-7037(87)90070-6

Brookins, D.G., 1986. Rhenium as analog for fissiogenic technetium: Eh-pH diagram (25°C, 1 bar) constraints. Applied Geochemistry 1, 513–517. https://doi.org/10.1016/0883-2927(86)90056-9

Bufe, A., Hovius, N., Emberson, R., Rugenstein, J.K.C., Galy, A., Hassenruck-Gudipati, H.J., Chang, J.-M., 2021. Co-variation of silicate, carbonate and sulfide weathering drives CO2 release with erosion. Nat. Geosci. 14, 211–216. https://doi.org/10.1038/s41561-021-00714-3

Burke, A., Present, T.M., Paris, G., Rae, E.C.M., Sandilands, B.H., Gaillardet, J., Peucker-Ehrenbrink, B., Fischer, W.W., McClelland, J.W., Spencer, R.G.M., Voss, B.M., Adkins, J.F., 2018. Sulfur isotopes in rivers: Insights into global weathering budgets, pyrite oxidation, and the modern sulfur cycle. Earth and Planetary Science Letters 496, 168–177. https://doi.org/10.1016/j.epsl.2018.05.022

Burylo, M., Hudek, C., Rey, F., 2011. Soil reinforcement by the roots of six dominant species on eroded mountainous marly slopes (Southern Alps, France). CATENA 84, 70–78. https://doi.org/10.1016/j.catena.2010.09.007

Calmels, D., Gaillardet, J., Brenot, A., France-Lanord, C., 2007. Sustained sulfide oxidation by physical erosion processes in the Mackenzie River basin: Climatic perspectives. Geology 35, 1003–1006. https://doi.org/10.1130/G24132A.1

Calmels, D., Galy, A., Hovius, N., Bickle, M., West, A.J., Chen, M.-C., Chapman, H., 2011. Contribution of deep groundwater to the weathering budget in a rapidly eroding mountain belt, Taiwan. Earth and Planetary Science Letters 303, 48–58. https://doi.org/10.1016/j.epsl.2010.12.032

Cambon, J.P., Esteves, K., Klotz, S., Le Bouteiller, K., Legout, C., Liebault, F., Mathys, N., Meunier, M., Olivier, J.E., Richard, D., 2015. Observatoire hydrosedimentaire de montagne Draix-Bleone [WWW Document]. URL http://oredraixbleone.irstea.fr

Carignan, J., Hild, P., Mevelle, G., Morel, J., Yeghicheyan, D., 2001. Routine Analyses of Trace Elements in Geological Samples using Flow Injection and Low Pressure On-Line Liquid Chromatography Coupled to ICP-MS: A Study of Geochemical Reference Materials BR, DR-N, UB-N, AN-G and GH. Geostandards and Geoanalytical Research 25, 187–198. https://doi.org/10.1111/j.1751-908X.2001.tb00595.x

Carriere, A., Le Bouteiller, C., Tucker, G.E., Klotz, S., Naaim, M., 2020. Impact of vegetation on erosion: Insights from the calibration and test of a landscape evolution model in alpine badland catchments. Earth Surface Processes and Landforms 45, 1085–1099. https://doi.org/10.1002/esp.4741

Chamberlin, T.C., 1899. An Attempt to Frame a Working Hypothesis of the Cause of Glacial Periods on an Atmospheric Basis. The Journal of Geology 7, 545–584. https://doi.org/10.1086/608449

Chang, S., Berner, R.A., 1999. Coal weathering and the geochemical carbon cycle. Geochimica et Cosmochimica Acta 63, 3301–3310. https://doi.org/10.1016/S0016-7037(99)00252-5

Chappaz, A., Gobeil, C., Tessier, A., 2008. Sequestration mechanisms and anthropogenic inputs of rhenium in sediments from Eastern Canada lakes. Geochimica et Cosmochimica Acta 72, 6027–6036. https://doi.org/10.1016/j.gca.2008.10.003

Clark, K.E., Hilton, R.G., West, A.J., Robles Caceres, A., Gröcke, D.R., Marthews, T.R., Ferguson, R.I., Asner, G.P., New, M., Malhi, Y., 2017. Erosion of organic carbon from the Andes and its effects on ecosystem carbon dioxide balance: Andean River Organic Carbon Yields. J. Geophys. Res. Biogeosci. 122, 449–469. https://doi.org/10.1002/2016JG003615

Claypool, G.E., Holser, W.T., Kaplan, I.R., Sakai, H., Zak, I., 1980. The age curves of sulfur and oxygen isotopes in marine sulfate and their mutual interpretation. Chemical Geology 28, 199–260. https://doi.org/10.1016/0009-2541(80)90047-9

Cohen, A.S., Coe, A.L., Bartlett, J.M., Hawkesworth, C.J., 1999. Precise Re–Os ages of organic-rich mudrocks and the Os isotope composition of Jurassic seawater. Earth and Planetary Science Letters 167, 159–173. https://doi.org/10.1016/S0012-821X(99)00026-6

Colodner, D., Edmond, J., Boyle, E., 1995. Rhenium in the Black Sea: comparison with molybdenum and uranium. Earth and Planetary Science Letters 131, 1–15. https://doi.org/10.1016/0012-821X(95)00010-A

Colodner, D., Sachs, J., Ravizza, G., Turekian, K., Edmond, J., Boyle, E., 1993. The geochemical cycle of rhenium: a reconnaissance. Earth and Planetary Science Letters 117, 205–221. https://doi.org/10.1016/0012-821X(93)90127-U

Cooper, D.M., Watts, C.D., 2002. A comparison of river load estimation techniques: application to dissolved organic carbon. Environmetrics 13, 733–750. https://doi.org/10.1002/env.525

Copard, Y., Amiotte-Suchet, P., Di-Giovanni, C., 2007. Storage and release of fossil organic carbon related to weathering of sedimentary rocks. Earth and Planetary Science Letters 258, 345–357. https://doi.org/10.1016/j.epsl.2007.03.048

Copard, Y., Di-Giovanni, C., Martaud, T., Albéric, P., Olivier, J.-E., 2006. Using Rock-Eval 6 pyrolysis for tracking fossil organic carbon in modern environments: implications for the roles of erosion and weathering. Earth Surface Processes and Landforms 31, 135–153. https://doi.org/10.1002/esp.1319

Cosandey, C., Andréassian, V., Martin, C., Didon-Lescot, J.F., Lavabre, J., Folton, N., Mathys, N., Richard, D., 2005. The hydrological impact of the mediterranean forest: a review of French research. Journal of Hydrology 301, 235–249. https://doi.org/10.1016/j.jhydrol.2004.06.040

Cras, A., Marc, V., Travi, Y., 2007. Hydrological behaviour of sub-Mediterranean alpine headwater streams in a badlands environment. Journal of Hydrology 339, 130–144. https://doi.org/10.1016/j.jhydrol.2007.03.004

Crawford, J.T., Hinckley, E.-L.S., Litaor, M.I., Brahney, J., Neff, J.C., 2019. Evidence for accelerated weathering and sulfate export in high alpine environments. Environmental Research Letters 14, 124092. https://doi.org/10.1088/1748-9326/ab5d9c

Dai, S., Seredin, V.V., Ward, C.R., Hower, J.C., Xing, Y., Zhang, W., Song, W., Wang, P., 2015. Enrichment of U–Se–Mo–Re–V in coals preserved within marine carbonate successions: geochemical and mineralogical data from the Late Permian Guiding Coalfield, Guizhou, China. Mineralium Deposita 50, 159–186. https://doi.org/10.1007/s00126-014-0528-1

Dalai, T.K., Singh, S.K., Trivedi, J.R., Krishnaswami, S., 2002. Dissolved rhenium in the Yamuna river system and the Ganga in the Himalaya: role of black shale weathering on the budgets of Re, Os, and U in rivers and CO2 in the atmosphere. Geochimica et Cosmochimica Acta 66, 29–43. https://doi.org/10.1016/S0016-7037(01)00747-5

Das, A., Chung, C.-H., You, C.-F., 2012. Disproportionately high rates of sulfide oxidation from mountainous river basins of Taiwan orogeny: Sulfur isotope evidence. Geophysical Research Letters 39. https://doi.org/10.1029/2012GL051549

Dellinger, M., Hilton, R.G., Nowell, G.M., 2020. Measurements of rhenium isotopic composition in low-abundance samples. Journal of Analytical Atomic Spectrometry 35, 377–387. https://doi.org/10.1039/C9JA00288J

Dellinger, M., Hilton, R.G., Nowell, G.M., In review. Fractionation of rhenium isotopes in the Mackenzie River basin and insights on oxidative weathering. Earth and Planetary Science Letters.

Dellinger, M., Hilton, R.G., Torres, M.A., Burt, E., Clark, K.E., Baronas, J., Ccahuana Quispe, A.J., West, A.J., In prep. Tracing oxidative weathering from the Andes to the lowland Amazon Basin using dissolved rhenium.

Derry, L.A., France-Lanord, C., 1996. Neogene growth of the sedimentary organic carbon reservoir. Paleoceanography 11, 267–275. https://doi.org/10.1029/95PA03839

Detmers, J., Bruchert, V., Habicht, K.S., Kuever, J., 2001. Diversity of Sulfur Isotope Fractionations by Sulfate-Reducing Prokaryotes. Applied and Environmental Microbiology 67, 888–894. https://doi.org/10.1128/AEM.67.2.888-894.2001

Dewey, J.F., Horsfield, B., 1970. Plate Tectonics, Orogeny and Continental Growth. Nature 225, 521–525. https://doi.org/10.1038/225521a0

Dubin, A., Peucker-Ehrenbrink, B., 2015. The importance of organic-rich shales to the geochemical cycles of rhenium and osmium. Chemical Geology 403, 111–120. https://doi.org/10.1016/j.chemgeo.2015.03.010

EBAS, 2017. EBAS [WWW Document]. URL http://ebas.nilu.no/ (accessed 12.18.20).

Edmond, J.M., 1970. High precision determination of titration alkalinity and total carbon dioxide content of sea water by potentiometric titration. Deep Sea Research and Oceanographic Abstracts 17, 737–750. https://doi.org/10.1016/0011-7471(70)90038-0

Emberson, R., Hovius, N., Galy, A., Marc, O., 2016a. Chemical weathering in active mountain belts controlled by stochastic bedrock landsliding. Nature Geoscience 9, 42–45. https://doi.org/10.1038/ngeo2600

Emberson, R., Hovius, N., Galy, A., Marc, O., 2016b. Oxidation of sulfides and rapid weathering in recent landslides. Earth Surface Dynamics 4, 727–742. https://doi.org/10.5194/esurf-4-727-2016

English, N.B., Quade, J., DeCelles, P.G., Garzione, C.N., 2000. Geologic control of Sr and major element chemistry in Himalayan Rivers, Nepal. Geochimica et Cosmochimica Acta 64, 2549–2566. https://doi.org/10.1016/S0016-7037(00)00379-3

Fisher, I.St.J., Hudson, J.D., 1987. Pyrite formation in Jurassic shales of contrasting biofacies. Geological Society, London, Special Publications 26, 69–78. https://doi.org/10.1144/GSL.SP.1987.026.01.04

France-Lanord, C., Derry, L.A., 1997. Organic carbon burial forcing of the carbon cycle from Himalayan erosion. Nature 390, 65–67. https://doi.org/10.1038/36324

Fryirs, K., 2013. (Dis)Connectivity in catchment sediment cascades: a fresh look at the sediment delivery problem. Earth Surf. Process. Landforms 38, 30–46. https://doi.org/10.1002/esp.3242

Fu, Y., Desboeufs, K., Vincent, J., Bon Nguyen, E., Laurent, B., Losno, R., Dulac, F., 2017. Estimating chemical composition of atmospheric deposition fluxes from mineral insoluble particles deposition collected in the western Mediterranean region. Atmospheric Measurement Techniques 10, 4389–4401. https://doi.org/10.5194/amt-10-4389-2017

Gabet, E.J., Mudd, S.M., 2009. A theoretical model coupling chemical weathering rates with denudation rates. Geology 37, 151–154. https://doi.org/10.1130/G25270A.1

Gaillardet, J., Braud, I., Hankard, F., Anquetin, S., Bour, O., Dorfliger, N., de Dreuzy, J.R., Galle, S., Galy, C., Gogo, S., Gourcy, L., Habets, F., Laggoun, F., Longuevergne, L., Le Borgne, T., Naaim-Bouvet, F., Nord, G., Simonneaux, V., Six, D., Tallec, T., Valentin, C., Abril, G., Allemand, P. et al., 2018. OZCAR: The French Network of Critical Zone Observatories. Vadose Zone Journal 17, 180067. https://doi.org/10.2136/vzj2018.04.0067

Gaillardet, J., Dupré, B., Louvat, P., Allègre, C.J., 1999. Global silicate weathering and CO2 consumption rates deduced from the chemistry of large rivers. Chemical Geology 159, 3–30. https://doi.org/10.1016/S0009-2541(99)00031-5

Gaillardet, J., Galy, A., 2008. Himalaya-Carbon Sink or Source? Science 320, 1727–1728. https://doi.org/10.1126/science.1159279

Galy, A., France-Lanord, C., 1999. Weathering processes in the Ganges–Brahmaputra basin and the riverine alkalinity budget. Chemical Geology 159, 31–60. https://doi.org/10.1016/S0009-2541(99)00033-9

Galy, V., Beyssac, O., France-Lanord, C., Eglinton, T., 2008. Recycling of Graphite During Himalayan Erosion: A Geological Stabilization of Carbon in the Crust. Science 322, 943–945. https://doi.org/10.1126/science.1161408

Georgiev, S., Stein, H.J., Hannah, J.L., Weiss, H.M., Bingen, B., Xu, G., Rein, E., Hatlø, V., Løseth, H., Nali, M., Piasecki, S., 2012. Chemical signals for oxidative weathering predict Re–Os isochroneity in black shales, East Greenland. Chemical Geology 324–325, 108–121. https://doi.org/10.1016/j.chemgeo.2012.01.003

Gill, B.C., Lyons, T.W., Jenkyns, H.C., 2011. A global perturbation to the sulfur cycle during the Toarcian Oceanic Anoxic Event. Earth and Planetary Science Letters 312, 484–496. https://doi.org/10.1016/j.epsl.2011.10.030

Godsey, S.E., Kirchner, J.W., Clow, D.W., 2009. Concentration-discharge relationships reflect chemostatic characteristics of US catchments. Hydrological Processes 23, 1844–1864. https://doi.org/10.1002/hyp.7315

Grant, K.E., Galy, V.V., Chadwick, O.A., Derry, L.A., 2019. Thermal oxidation of carbon in organic matter rich volcanic soils: insights into SOC age differentiation and mineral stabilization. Biogeochemistry 144, 291–304. https://doi.org/10.1007/s10533-019-00586-1

Graz, Y., Di-Giovanni, C., Copard, Y., Elie, M., Faure, P., Laggoun Defarge, F., Lévèque, J., Michels, R., Olivier, J.E., 2011. Occurrence of fossil organic matter in modern environments: Optical, geochemical and isotopic evidence. Applied Geochemistry 26, 1302–1314. https://doi.org/10.1016/j.apgeochem.2011.05.004

Graz, Y., Di-Giovanni, C., Copard, Y., Mathys, N., Cras, A., Marc, V., 2012. Annual fossil organic carbon delivery due to mechanical and chemical weathering of marly badlands areas. Earth Surface Processes and Landforms 37, 1263–1271. https://doi.org/10.1002/esp.3232

Gregory, M.R., Johnston, K.A., 1987. A nontoxic substitute for hazardous heavy liquids—aqueous sodium polytungstate solution (Note). New Zealand Journal of Geology and Geophysics 30, 317–320. https://doi.org/10.1080/00288306.1987.10552626

Gu, X., Rempe, D.M., Dietrich, W.E., West, A.J., Lin, T.-C., Jin, L., Brantley, S.L., 2020. Chemical reactions, porosity, and microfracturing in shale during weathering: The effect of erosion rate. Geochimica et Cosmochimica Acta 269, 63–100. https://doi.org/10.1016/j.gca.2019.09.044

Guédron, S., Amouroux, D., Sabatier, P., Desplanque, C., Develle, A.-L., Barre, J., Feng, C., Guiter, F., Arnaud, F., Reyss, J.L., Charlet, L., 2016. A hundred year record of industrial and urban development in French Alps combining Hg accumulation rates and isotope composition in sediment archives from Lake Luitel. Chemical Geology 431, 10–19. https://doi.org/10.1016/j.chemgeo.2016.03.016

Guo, Y., Markus, M., Demissie, M., 2002. Uncertainty of nitrate-N load computations for agricultural watersheds. Water Resour. Res. 38, 3-1-3–12. https://doi.org/10.1029/2001WR001149

He, H., Dong, Z., Pang, J., Wu, G.-L., Zheng, J., Zhang, X., 2018. Phytoextraction of rhenium by lucerne (Medicago sativa) and erect milkvetch (Astragalus adsurgens) from alkaline soils amended with coal fly ash. Science of The Total Environment 630, 570–577. https://doi.org/10.1016/j.scitotenv.2018.02.252

Hemingway, J.D., Galy, V.V., Gagnon, A.R., Grant, K.E., Rosengard, S.Z., Soulet, G., Zigah, P.K., McNichol, A.P., 2017. Assessing the Blank Carbon Contribution, Isotope Mass Balance, and Kinetic Isotope Fractionation of the Ramped Pyrolysis/Oxidation Instrument at NOSAMS. Radiocarbon 59, 179–193. https://doi.org/10.1017/RDC.2017.3

Hemingway, J.D., Hilton, R.G., Hovius, N., Eglinton, T.I., Haghipour, N., Wacker, L., Chen, M.-C., Galy, V.V., 2018. Microbial oxidation of lithospheric organic carbon in rapidly eroding tropical mountain soils. Science 360, 209–212. https://doi.org/10.1126/science.aao6463

Hemingway, J.D., Olson, H., Turchyn, A.V., Tipper, E.T., Bickle, M.J., Johnston, D.T., 2020. Triple oxygen isotope insight into terrestrial pyrite oxidation. Proceedings of the National Academy of Sciences 117, 7650–7657. https://doi.org/10.1073/pnas.1917518117

Hemingway, J.D., Rothman, D.H., Grant, K.E., Rosengard, S.Z., Eglinton, T.I., Derry, L.A., Galy, V.V., 2019. Mineral protection regulates long-term global preservation of natural organic carbon. Nature 570, 228–231. https://doi.org/10.1038/s41586-019-1280-6

Hercod, D.J., Brady, P.V., Gregory, R.T., 1998. Catchment-scale coupling between pyrite oxidation and calcite weathering. Chemical Geology 151, 259–276. https://doi.org/10.1016/S0009-2541(98)00084-9

Herndon, E.M., Brantley, S.L., 2011. Movement of manganese contamination through the Critical Zone. Applied Geochemistry 26, S40–S43. https://doi.org/10.1016/j.apgeochem.2011.03.024

Herndon, E.M., Dere, A.L., Sullivan, P.L., Norris, D., Reynolds, B., Brantley, S.L., 2015a. Landscape heterogeneity drives contrasting concentration–discharge relationships in shale headwater catchments. Hydrology and Earth System Sciences 19, 3333–3347. https://doi.org/10.5194/hess-19-3333-2015

Herndon, E.M., Jin, L., Andrews, D.M., Eissenstat, D.M., Brantley, S.L., 2015b. Importance of vegetation for manganese cycling in temperate forested watersheds: Biogeochemistry of Mn contaminants. Global Biogeochemical Cycles 29, 160–174. https://doi.org/10.1002/2014GB004858

Herndon, E.M., Jin, L., Brantley, S.L., 2011. Soils Reveal Widespread Manganese Enrichment from Industrial Inputs. Environmental Science & Technology 45, 241–247. https://doi.org/10.1021/es102001w

Hilley, G.E., Chamberlain, C.P., Moon, S., Porder, S., Willett, S.D., 2010. Competition between erosion and reaction kinetics in controlling silicate- weathering rates. Earth Planet. Sci. Lett. 293, 191–199. https://doi.org/10.1016/j.epsl.2010.01.008

Hilton, R. G., Gaillardet, J., Calmels, D., Birck, J.-L., 2014. Geological respiration of a mountain belt revealed by the trace element rhenium. Earth and Planetary Science Letters 403, 27–36. https://doi.org/10.1016/j.epsl.2014.06.021

Hilton, R.G., Galy, A., Hovius, N., Horng, M.-J., Chen, H., 2011. Efficient transport of fossil organic carbon to the ocean by steep mountain rivers: An orogenic carbon sequestration mechanism. Geology 39, 71–74. https://doi.org/10.1130/G31352.1

Hilton, R.G., West, A.J., 2020. Mountains, erosion and the carbon cycle. Nature Reviews Earth & Environment 1, 284–299. https://doi.org/10.1038/s43017-020-0058-6

Hindshaw, R.S., Tipper, E.T., Reynolds, B.C., Lemarchand, E., Wiederhold, J.G., Magnusson, J., Bernasconi, S.M., Kretzschmar, R., Bourdon, B., 2011. Hydrological control of stream water chemistry in a glacial catchment (Damma Glacier, Switzerland). Chemical Geology 285, 215–230. https://doi.org/10.1016/j.chemgeo.2011.04.012

Horan, K., 2018. The oxidative weathering of organic matter and its carbon dioxide emissions: Insight from the trace elements rhenium and molybdenum (Durham Thesis). Durham Univeristy, Durham.

Horan, K., Hilton, R.G., Dellinger, M., Tipper, E., Galy, V., Calmels, D., Selby, D., Gaillardet, J., Ottley, C.J., Parsons, D.R., Burton, K.W., 2019. Carbon dioxide emissions by rock organic carbon oxidation and the net geochemical carbon budget of the Mackenzie River Basin. Am J Sci 319, 473–499. https://doi.org/10.2475/06.2019.02

Horan, K., Hilton, R.G., Selby, D., Ottley, C.J., Gröcke, D.R., Hicks, M., Burton, K.W., 2017. Mountain glaciation drives rapid oxidation of rock-bound organic carbon. Science Advances 3, e1701107. https://doi.org/10.1126/sciadv.1701107

IPCC, 2019. IPCC Special Report on the Ocean and Cryosphere in a Changing Climate.

Jacobson, A.D., Blum, J.D., 2003. Relationship between mechanical erosion and atmospheric CO2 consumption in the New Zealand Southern Alps. Geology 31, 865. https://doi.org/10.1130/G19662.1

Jaffe, L. A, Peucker-Ehrenbrink, B., Petsch, S.T., 2002. Mobility of rhenium, platinum group elements and organic carbon during black shale weathering. Earth and Planetary Science Letters 198, 339–353. https://doi.org/10.1016/S0012-821X(02)00526-5

Janzen, M.P., Nicholson, R.V., Scharer, J.M., 2000. Pyrrhotite reaction kinetics: reaction rates for oxidation by oxygen, ferric iron, and for nonoxidative dissolution. Geochimica et Cosmochimica Acta 64, 1511–1522. https://doi.org/10.1016/S0016-7037(99)00421-4

Jiang, H., Liu, W., Xu, Z., Zhou, X., Zheng, Z., Zhao, T., Zhou, L., Zhang, X., Xu, Y., Liu, T., 2018. Chemical weathering of small catchments on the Southeastern Tibetan Plateau I: Water sources, solute sources and weathering rates. Chemical Geology 500, 159–174. https://doi.org/10.1016/j.chemgeo.2018.09.030

Jin, L., Andrews, D.M., Holmes, G.H., Lin, H., Brantley, S.L., 2011. Opening the "Black Box": Water Chemistry Reveals Hydrological Controls on Weathering in the Susquehanna Shale Hills Critical Zone Observatory. Vadose Zone Journal 10, 928–942. https://doi.org/10.2136/vzj2010.0133

Jin, L., Ogrinc, N., Yesavage, T., Hasenmueller, E.A., Ma, L., Sullivan, P.L., Kaye, J., Duffy, C., Brantley, S.L., 2014a. The CO2 consumption potential during gray shale weathering: Insights from the evolution of carbon isotopes in the Susquehanna Shale Hills critical zone observatory. Geochimica et Cosmochimica Acta 142, 260–280. https://doi.org/10.1016/j.gca.2014.07.006

Jin, L., Ravella, R., Ketchum, B., Bierman, P.R., Heaney, P., White, T., Brantley, S.L., 2010. Mineral weathering and elemental transport during hillslope evolution at the Susquehanna/Shale Hills Critical Zone Observatory. Geochimica et Cosmochimica Acta 74, 3669–3691. https://doi.org/10.1016/j.gca.2010.03.036

Jochum, K.P., Weis, U., Schwager, B., Stoll, B., Wilson, S.A., Haug, G.H., Andreae, M.O., Enzweiler, J., 2016. Reference Values Following ISO Guidelines for Frequently Requested Rock Reference Materials. Geostandards and Geoanalytical Research 40, 333–350. https://doi.org/10.1111/j.1751-908X.2015.00392.x

Karim, A., Veizer, J., 2000. Weathering processes in the Indus River Basin: implications from riverine carbon, sulfur, oxygen, and strontium isotopes. Chemical Geology 170, 153–177. https://doi.org/10.1016/S0009-2541(99)00246-6

Kemeny, P.C., Lopez, G.I., Dalleska, N.F., Torres, M., Burke, A., Bhatt, M.P., West, A.J., Hartmann, J., Adkins, J.F., 2021. Sulfate sulfur isotopes and major ion chemistry reveal that pyrite oxidation counteracts CO2 drawdown from silicate weathering in the Langtang-Trisuli-Narayani River system, Nepal Himalaya. Geochimica et Cosmochimica Acta 294, 43–69. https://doi.org/10.1016/j.gca.2020.11.009

Kim, E., Benedetti, M.F., Boulègue, J., 2004. Removal of dissolved rhenium by sorption onto organic polymers: study of rhenium as an analogue of radioactive technetium. Water Research 38, 448–454. https://doi.org/10.1016/j.watres.2003.09.033

King, E.K., Perakis, S.S., Pett-Ridge, J.C., 2018. Molybdenum isotope fractionation during adsorption to organic matter. Geochimica et Cosmochimica Acta 222, 584–598. https://doi.org/10.1016/j.gca.2017.11.014

Kirchner, J.W., Finkel, R.C., Riebe, C.S., Granger, D.E., Clayton, J.L., King, J.G., Megahan, W.F., 2001. Mountain erosion over 10 yr, 10 ky, and 10 my time scales. Geology 29, 591–594.

Kraepiel, A.M.L., Dere, A.L., Herndon, E.M., Brantley, S.L., 2015. Natural and anthropogenic processes contributing to metal enrichment in surface soils of central Pennsylvania. Biogeochemistry 123, 265–283. https://doi.org/10.1007/s10533-015-0068-5

Kump, L.R., Brantley, S.L., Arthur, M.A., 2000. Chemical Weathering, Atmospheric CO2, and Climate. Annual Review of Earth and Planetary Sciences 28, 611–667. https://doi.org/10.1146/annurev.earth.28.1.611

Kuntz, B.W., Rubin, S., Berkowitz, B., Singha, K., 2011. Quantifying Solute Transport at the Shale Hills Critical Zone Observatory. Vadose Zone Journal 10, 843–857. https://doi.org/10.2136/vzj2010.0130

Larsen, I.J., Montgomery, D.R., Greenberg, H.M., 2014. The contribution of mountains to global denudation. Geology 42, 527–530. https://doi.org/10.1130/G35136.1

Larson, S.J., Capel, P.D., Goolsby, D.A., Zaugg, S.D., Sandstrom, M.W., 1995. Relations between pesticide use and riverine flux in the Mississippi River basin. Chemosphere 31, 3305–3321. https://doi.org/10.1016/0045-6535(95)00176-9

Li, S.-L., Calmels, D., Han, G., Gaillardet, J., Liu, C.-Q., 2008. Sulfuric acid as an agent of carbonate weathering constrained by δ13CDIC: Examples from Southwest China. Earth and Planetary Science Letters 270, 189–199. https://doi.org/10.1016/j.epsl.2008.02.039

Li, X., Gan, Y., Zhou, A., Liu, Y., 2015. Relationship between water discharge and sulfate sources of the Yangtze River inferred from seasonal variations of sulfur and oxygen isotopic compositions. Journal of Geochemical Exploration 153, 30–39. https://doi.org/10.1016/j.gexplo.2015.02.009

Lima, A.L., Bergquist, B.A., Boyle, E.A., Reuer, M.K., Dudas, F.O., Reddy, C.M., Eglinton, T.I., 2005. High-resolution historical records from Pettaquamscutt River basin sediments: 2. Pb isotopes reveal a potential new stratigraphic marker. Geochimica et Cosmochimica Acta 69, 1813–1824. https://doi.org/10.1016/j.gca.2004.10.008

Lin, H.S., Kogelmann, W., Walker, C., Bruns, M.A., 2006. Soil moisture patterns in a forested catchment: A hydropedological perspective. Geoderma 131, 345–368. https://doi.org/10.1016/j.geoderma.2005.03.013

Lloyd, R.M., 1968. Oxygen isotope behavior in the Sulfate-Water System. Journal of Geophysical Research 73, 6099–6110. https://doi.org/10.1029/JB073i018p06099

Ma, L., Chabaux, F., Pelt, E., Blaes, E., Jin, L., Brantley, S., 2010. Regolith production rates calculated with uranium-series isotopes at Susquehanna/Shale Hills Critical Zone Observatory. Earth and Planetary Science Letters 297, 211–225. https://doi.org/10.1016/j.epsl.2010.06.022

Ma, L., Chabaux, F., West, N., Kirby, E., Jin, L., Brantley, S., 2013. Regolith production and transport in the Susquehanna Shale Hills Critical Zone Observatory, Part 1: Insights from U-series isotopes. Journal of Geophysical Research: Earth Surface 118, 722–740. https://doi.org/10.1002/jgrf.20037

Ma, L., Konter, J., Herndon, E., Jin, L., Steinhoefel, G., Sanchez, D., Brantley, S., 2014. Quantifying an early signature of the industrial revolution from lead concentrations and isotopes in soils of Pennsylvania, USA. Anthropocene 7, 16–29. https://doi.org/10.1016/j.ancene.2014.12.003

Maher, K., 2011. The role of fluid residence time and topographic scales in determining chemical fluxes from landscapes. Earth and Planetary Science Letters 312, 48–58. https://doi.org/10.1016/j.epsl.2011.09.040

Maher, K., 2010. The dependence of chemical weathering rates on fluid residence time. Earth and Planetary Science Letters 294, 101–110. https://doi.org/10.1016/j.epsl.2010.03.010

Maher, K., Chamberlain, C.P., 2014. Hydrologic Regulation of Chemical Weathering and the Geologic Carbon Cycle. Science 343, 1502–1504. https://doi.org/10.1126/science.1250770

Manning, A.H., Verplanck, P.L., Caine, J.S., Todd, A.S., 2013. Links between climate change, water-table depth, and water chemistry in a mineralized mountain watershed. Applied Geochemistry 37, 64–78. https://doi.org/10.1016/j.apgeochem.2013.07.002

Maquaire, O., Malet, J.-P., Remaître, A., Locat, J., Klotz, S., Guillon, J., 2003. Instability conditions of marly hillslopes: towards landsliding or gullying? The case of the Barcelonnette Basin, South East France. Engineering Geology 70, 109–130. https://doi.org/10.1016/S0013-7952(03)00086-3

Marc, V., Bertrand, C., Malet, J.-P., Carry, N., Simler, R., Cervi, F., 2017. Groundwater-Surface waters interactions at slope and catchment scales: implications for landsliding in clay-rich slopes: Hydrochemistry and geochemical modelling to infer groundwater flows. Hydrological Processes 31, 364–381. https://doi.org/10.1002/hyp.11030

Marin-Spiotta, E., Chadwick, O.A., Kramer, M., Carbone, M.S., 2011. Carbon delivery to deep mineral horizons in Hawaiian rain forest soils. Journal of Geophysical Research 116. https://doi.org/10.1029/2010JG001587

Marx, A., Dusek, J., Jankovec, J., Sanda, M., Vogel, T., van Geldern, R., Hartmann, J., Barth, J.A.C., 2017. A review of CO2 and associated carbon dynamics in headwater streams: A global perspective: Carbon Dioxide in Headwater Streams. Reviews of Geophysics 55, 560–585. https://doi.org/10.1002/2016RG000547

Matamoros-Veloza, A., Newton, R.J., Benning, L.G., 2011. What controls selenium release during shale weathering? Applied Geochemistry 26, S222–S226. https://doi.org/10.1016/j.apgeochem.2011.03.109

Mathys, N., Brochot, S., Meunier, M., Richard, D., 2003. Erosion quantification in the small marly experimental catchments of Draix (Alpes de Haute Provence, France). Calibration of the ETC rainfall–runoff–erosion model. CATENA 50, 527–548. https://doi.org/10.1016/S0341-8162(02)00122-4

Mathys, N., Klotz, S., 2008. Draix: A field laboratory for research on hydrology and erosion in mountain areas, in: Proceedings of the 4th Canadian Conference on Geohazards : From Causes to Management. Presented at the Comptes rendus de la 4e Conférence canadienne sur les géorisques: des causes à la gestion., Presse de l'Université Laval, Québec, p. 594.

Mathys, N., Klotz, S., Esteves, M., Descroix, L., Lapetite, J.M., 2005. Runoff and erosion in the Black Marls of the French Alps: Observations and measurements at the plot scale. CATENA 63, 261–281. https://doi.org/10.1016/j.catena.2005.06.010

McLennan, S.M., 2001. Relationships between the trace element composition of sedimentary rocks and upper continental crust. Geochemistry, Geophysics, Geosystems 2, n/a-n/a. https://doi.org/10.1029/2000GC000109

McNichol, A.P., Osborne, E.A., Gagnon, A.R., Fry, B., Jones, G.A., 1994. TIC, TOC, DIC, DOC, PIC, POC — unique aspects in the preparation of oceanographic samples for 14C-AMS. Nuclear Instruments and Methods in Physics Research Section B: Beam Interactions with Materials and Atoms 92, 162–165. https://doi.org/10.1016/0168-583X(94)95998-6

Meisel, T., Moser, J., 2004. Reference materials for geochemical PGE analysis: new analytical data for Ru, Rh, Pd, Os, Ir, Pt and Re by isotope dilution ICP-MS in 11 geological reference materials. Chemical Geology 208, 319–338. https://doi.org/10.1016/j.chemgeo.2004.04.019

Meybeck, M., 1987. Global chemical weathering of surficial rocks estimated from river dissolved loads. American Journal of Science 287, 401–428. https://doi.org/10.2475/ajs.287.5.401

Meybeck, M., 1982. Carbon, nitrogen, and phosphorus transport by world rivers. American Journal of Science 282, 401–450.

Miller, C.A., Peucker-Ehrenbrink, B., Walker, B.D., Marcantonio, F., 2011. Re-assessing the surface cycling of molybdenum and rhenium. Geochimica et Cosmochimica Acta 75, 7146–7179. https://doi.org/10.1016/j.gca.2011.09.005

Milliman, J.D., Syvitski, J.P.M., 1992. Geomorphic/Tectonic Control of Sediment Discharge to the Ocean: The Importance of Small Mountainous Rivers. The Journal of Geology 100, 525–544. https://doi.org/10.1086/629606

Millot, R., Gaillardet, J., Dupré, B., Allègre, C.J., 2003. Northern latitude chemical weathering rates: clues from the Mackenzie River Basin, Canada. Geochimica et Cosmochimica Acta 67, 1305–1329. https://doi.org/10.1016/S0016-7037(02)01207-3

Moon, S., Chamberlain, C.P., Hilley, G.E., 2014. New estimates of silicate weathering rates and their uncertainties in global rivers. Geochimica et Cosmochimica Acta 134, 257–274. https://doi.org/10.1016/j.gca.2014.02.033

Moquet, J.-S., Crave, A., Viers, J., Seyler, P., Armijos, E., Bourrel, L., Chavarri, E., Lagane, C., Laraque, A., Casimiro, W.S.L., Pombosa, R., Noriega, L., Vera, A., Guyot, J.-L., 2011. Chemical weathering and atmospheric/soil CO2 uptake

in the Andean and Foreland Amazon basins. Chemical Geology 287, 1–26. https://doi.org/10.1016/j.chemgeo.2011.01.005

Morford, J.L., Martin, W.R., Carney, C.M., 2012. Rhenium geochemical cycling: Insights from continental margins. Chemical Geology 324–325, 73–86. https://doi.org/10.1016/j.chemgeo.2011.12.014

Morse, J.W., Arvidson, R.S., 2002. The dissolution kinetics of major sedimentary carbonate minerals. Earth-Science Reviews 58, 51–84. https://doi.org/10.1016/S0012-8252(01)00083-6

NADP Program Office, 2020. National Atmospheric Deposition Program (NRSP-3) [WWW Document]. URL http://nadp.slh.wisc.edu/

Neal, C., House, W., Down, K., 1998. An assessment of excess carbon dioxide partial pressures in natural waters based on pH and alkalinity measurements. Science of The Total Environment 210–211, 173–185. https://doi.org/10.1016/S0048-9697(98)00011-4

Nevers, P., Bouchez, J., Gaillardet, J., Thomazo, C., Faure, L., Bertrand, C., 2020. Landslides as geological hotspots of CO2 to the atmosphere: clues from the instrumented Séchilienne landslide, Western European Alps (preprint). Chemical: Isotopic tracing of Earth's surface processes. https://doi.org/10.5194/esurf-2020-42

Newton, R.J., Bottrell, S.H., Dean, S.P., Hatfield, D., Raiswell, R., 1995. An evaluation of the use of the chromous chloride reduction method for isotopic analyses of pyrite in rocks and sediment. Chemical Geology 125, 317–320. https://doi.org/10.1016/0009-2541(95)00098-7

Newton, R.J., Reeves, E.P., Kafousia, N., Wignall, P.B., Bottrell, S.H., Sha, J.-G., 2011. Low marine sulfate concentrations and the isolation of the European epicontinental sea during the Early Jurassic. Geology 39, 7–10. https://doi.org/10.1130/G31326.1

Novo, L.A.B., Mahler, C.F., González, L., 2015. Plants to harvest rhenium: scientific and economic viability. Environmental Chemistry Letters 13, 439–445. https://doi.org/10.1007/s10311-015-0517-3

Pasquier, V., Bryant, R.N., Fike, D.A., Halevy, I., 2021. Strong local, not global, controls on marine pyrite sulfur isotopes. Sci. Adv. 7, eabb7403. https://doi.org/10.1126/sciadv.abb7403

Percak-Dennett, E., He, S., Converse, B., Konishi, H., Xu, H., Corcoran, A., Noguera, D., Chan, C., Bhattacharyya, A., Borch, T., Boyd, E., Roden, E.E., 2017. Microbial acceleration of aerobic pyrite oxidation at circumneutral pH. Geobiology 15, 690–703. https://doi.org/10.1111/gbi.12241

Petsch, S.T., 2014. Weathering of Organic Carbon, in: Holland, H.D., Turekian, K.K. (Eds.), Treatise on Geochemistry (Second Edition). Elsevier, Oxford, pp. 217–238. https://doi.org/10.1016/B978-0-08-095975-7.01013-5

Petsch, S.T., Berner, R.A., Eglinton, T.I., 2000. A field study of the chemical weathering of ancient sedimentary organic matter. Organic Geochemistry 31, 475–487. https://doi.org/10.1016/S0146-6380(00)00014-0

Peucker-Ehrenbrink, B., Hannigan, R.E., 2000. Effects of black shale weathering on the mobility of rhenium and platinum group elements. Geology 28, 475–478. https://doi.org/10.1130/0091-7613(2000)28<475:EOBSWO>2.0.CO;2

Pierson-Wickmann, A.-C., Reisberg, L., France-Lanord, C., 2002. Behavior of Re and Os during low-temperature alteration: Results from Himalayan soils

and altered black shales. Geochimica et Cosmochimica Acta 66, 1539–1548. https://doi.org/10.1016/S0016-7037(01)00865-1

Plank, T., Manning, C.E., 2019. Subducting carbon. Nature 574, 343–352. https://doi.org/10.1038/s41586-019-1643-z

Prouty, N.G., Roark, E.B., Koenig, A.E., Demopoulos, A.W.J., Batista, F.C., Kocar, B.D., Selby, D., McCarthy, M.D., Mienis, F., Ross, S.W., 2014. Deep-sea coral record of human impact on watershed quality in the Mississippi River Basin. Global Biogeochemical Cycles 28, 29–43. https://doi.org/10.1002/2013GB004754

Quade, J., English, N., DeCelles, P.G., 2003. Silicate versus carbonate weathering in the Himalaya: a comparison of the Arun and Seti River watersheds. Chemical Geology 202, 275–296. https://doi.org/10.1016/j.chemgeo.2002.05.002

Rahaman, W., Singh, S.K., Shukla, A.D., 2012. Rhenium in Indian rivers: Sources, fluxes, and contribution to oceanic budget. Geochemistry, Geophysics, Geosystems 13. https://doi.org/10.1029/2012GC004083

Richey, J.E., Melack, J.M., Aufdenkampe, A.K., Ballester, V.M., Hess, L.L., 2002. Outgassing from Amazonian rivers and wetlands as a large tropical source of atmospheric CO2. Nature 416, 617–620. https://doi.org/10.1038/416617a

Riebe, C.S., Kirchner, J.W., Finkel, R.C., 2004. Erosional and climatic effects on long-term chemical weathering rates in granitic landscapes spanning diverse climate regimes. Earth and Planetary Science Letters 224, 547–562. https://doi.org/10.1016/j.epsl.2004.05.019

Rode, M., Wade, A.J., Cohen, M.J., Hensley, R.T., Bowes, M.J., Kirchner, J.W., Arhonditsis, G.B., Jordan, P., Kronvang, B., Halliday, S.J., Skeffington, R.A., Rozemeijer, J.C., Aubert, A.H., Rinke, K., Jomaa, S., 2016. Sensors in the Stream: The High-Frequency Wave of the Present. Environmental Science & Technology 50, 10297–10307. https://doi.org/10.1021/acs.est.6b02155

Rodríguez-Tovar, F.J., 2021. Ichnology of the Toarcian Oceanic Anoxic Event: An understimated tool to assess palaeoenvironmental interpretations. Earth-Science Reviews 103579. https://doi.org/10.1016/j.earscirev.2021.103579

Ross, D.J.K., Bustin, M.R., 2009. The importance of shale composition and pore structure upon gas storage potential of shale gas reservoirs. Marine and Petroleum Geology 26, 916–927. https://doi.org/10.1016/j.marpetgeo.2008.06.004

Ross, M.R.V., Nippgen, F., Hassett, B.A., McGlynn, B.L., Bernhardt, E.S., 2018. Pyrite oxidation drives exceptionally high weathering rates and geologic CO2 release in mountaintop-mined landscapes. Global Biogeochemical Cycles. https://doi.org/10.1029/2017GB005798

Roylands, T., Hilton, R.G., McClymont, E., Garnett, M., Soulet, G., Klotz, S., Degler, M., Napoleoni, F., Le Bouteiller, C., In prep. Probing the exchange of CO2 and O2 in the shallow critical zone during weathering of marl and black shale.

Schleppi, P., Waldner, P.A., Stähli, M., 2006. Errors of flux integration methods for solutes in grab samples of runoff water, as compared to flow-proportional

sampling. Journal of Hydrology 319, 266–281. https://doi.org/10.1016/j.jhydrol.2005.06.034

Schwab, V.F., Nowak, M.E., Elder, C.D., Trumbore, S.E., Xu, X., Gleixner, G., Lehmann, R., Pohnert, G., Muhr, J., Küsel, K., Totsche, K.U., 2019. 14C-Free Carbon Is a Major Contributor to Cellular Biomass in Geochemically Distinct Groundwater of Shallow Sedimentary Bedrock Aquifers. Water Resour. Res. 55, 2104–2121. https://doi.org/10.1029/2017WR022067

Selby, D., Creaser, R.A., 2003. Re–Os geochronology of organic rich sediments: an evaluation of organic matter analysis methods. Chemical Geology 200, 225–240. https://doi.org/10.1016/S0009-2541(03)00199-2

Selby, D., Creaser, R.A., Fowler, M.G., 2007. Re–Os elemental and isotopic systematics in crude oils. Geochimica et Cosmochimica Acta 71, 378–386. https://doi.org/10.1016/j.gca.2006.09.005

Sen, I.S., Peucker-Ehrenbrink, B., 2012. Anthropogenic Disturbance of Element Cycles at the Earth's Surface. Environmental Science & Technology 46, 8601–8609. https://doi.org/10.1021/es301261x

Sheen, A.I., Kendall, B., Reinhard, C.T., Creaser, R.A., Lyons, T.W., Bekker, A., Poulton, S.W., Anbar, A.D., 2018. A model for the oceanic mass balance of rhenium and implications for the extent of Proterozoic ocean anoxia. Geochimica et Cosmochimica Acta 227, 75–95. https://doi.org/10.1016/j.gca.2018.01.036

Skarbøvik, E., Stålnacke, P., Bogen, J., Bønsnes, T.E., 2012. Impact of sampling frequency on mean concentrations and estimated loads of suspended sediment in a Norwegian river: Implications for water management. Science of The Total Environment 433, 462–471. https://doi.org/10.1016/j.scitotenv.2012.06.072

Smakhtin, V.U., 2001. Low flow hydrology: a review. Journal of Hydrology 240, 147–186. https://doi.org/10.1016/S0022-1694(00)00340-1

Smetanová, A., Le Bissonnais, Y., Raclot, D., Pedro Nunes, J., Licciardello, F., Le Bouteiller, C., Latron, J., Rodríguez Caballero, E., Mathys, N., Klotz, S., Mekki, I., Gallart, F., Solé Benet, A., Pérez Gallego, N., Andrieux, P., Moussa, R., Planchon, O., Santos, J.M., Alshihabi, O., Chikhaoui, M., Follain, S., 2018. Temporal variability and time compression of sediment yield in small Mediterranean catchments: impacts for land and water management. Soil Use and Management 34, 388–403. https://doi.org/10.1111/sum.12437

Soulet, G., Hilton, R.G., Garnett, M.H., Dellinger, M., Croissant, T., Ogrič, M., Klotz, S., 2018. Technical note: in situ measurement of flux and isotopic composition of CO2 released during oxidative weathering of sedimentary rocks. Biogeosciences 15, 4087–4102.

Soulet, G., Hilton, R.G., Garnett, M.H., Roylands, T., Klotz, S., Croissant, T., Dellinger, M., Le Bouteiller, C., 2021. Temperature control on CO2 emissions from the weathering of sedimentary rocks. Nat. Geosci. 14, 665–671. https://doi.org/10.1038/s41561-021-00805-1

Spence, J., Telmer, K., 2005. The role of sulfur in chemical weathering and atmospheric CO2 fluxes: Evidence from major ions, δ13CDIC, and δ34SSO4 in rivers of the Canadian Cordillera. Geochimica et Cosmochimica Acta 69, 5441–5458. https://doi.org/10.1016/j.gca.2005.07.011

Stallard, R.F., Edmond, J.M., 1983. Geochemistry of the Amazon: 2. The influence of geology and weathering environment on the dissolved load. Journal of Geophysical Research: Oceans 88, 9671–9688. https://doi.org/10.1029/JC088iC14p09671

Steger, H.F., 1982. Oxidation of sulfide minerals. Chemical Geology 35, 281–295. https://doi.org/10.1016/0009-2541(82)90006-7

Stenback, G.A., Crumpton, W.G., Schilling, K.E., Helmers, M.J., 2011. Rating curve estimation of nutrient loads in Iowa rivers. Journal of Hydrology 396, 158–169. https://doi.org/10.1016/j.jhydrol.2010.11.006

Stuiver, M., Polach, H.A., 1977. Discussion Reporting of 14C Data. Radiocarbon 19, 355–363. https://doi.org/10.1017/S0033822200003672

Sullivan, P.L., Hynek, S.A., Gu, X., Singha, K., White, T., West, N., Kim, H., Clarke, B., Kirby, E., Duffy, C., Brantley, S.L., 2016. Oxidative dissolution under the channel leads geomorphological evolution at the Shale Hills catchment. American Journal of Science 316, 981–1026. https://doi.org/10.2475/10.2016.02

Sundquist, E.T., Visser, K., 2005. Geologic hystory of the carbon cycle, in: Biogeochemistry, 8. Elsevier, pp. 425–472.

Taylor, B.E., Wheeler, M.C., Nordstrom, D.K., 1984. Isotope composition of sulphate in acid mine drainage as measure of bacterial oxidation. Nature 308, 538–541. https://doi.org/10.1038/308538a0

Tipper, E.T., Bickle, M.J., Galy, A., West, A.J., Pomiès, C., Chapman, H.J., 2006. The short term climatic sensitivity of carbonate and silicate weathering fluxes: Insight from seasonal variations in river chemistry. Geochimica et Cosmochimica Acta 70, 2737–2754. https://doi.org/10.1016/j.gca.2006.03.005

Torres, M.A., Moosdorf, N., Hartmann, J., Adkins, J.F., West, A.J., 2017. Glacial weathering, sulfide oxidation, and global carbon cycle feedbacks. Proceedings of the National Academy of Sciences 114, 8716–8721. https://doi.org/10.1073/pnas.1702953114

Torres, M.A., West, A.J., Clark, K.E., 2015. Geomorphic regime modulates hydrologic control of chemical weathering in the Andes–Amazon. Geochimica et Cosmochimica Acta 166, 105–128. https://doi.org/10.1016/j.gca.2015.06.007

Torres, M.A., West, A.J., Clark, K.E., Paris, G., Bouchez, J., Ponton, C., Feakins, S.J., Galy, V., Adkins, J.F., 2016. The acid and alkalinity budgets of weathering in the Andes–Amazon system: Insights into the erosional control of global biogeochemical cycles. Earth and Planetary Science Letters 450, 381–391. https://doi.org/10.1016/j.epsl.2016.06.012

Torres, M.A., West, A.J., Li, G., 2014. Sulphide oxidation and carbonate dissolution as a source of CO 2 over geological timescales. Nature 507, 346–349. https://doi.org/10.1038/nature13030

Trumbore, S., 2009. Radiocarbon and Soil Carbon Dynamics. Annu. Rev. Earth Planet. Sci. 37, 47–66. https://doi.org/10.1146/annurev.earth.36.031207.124300

Turchyn, A.V., Tipper, E.T., Galy, A., Lo, J.-K., Bickle, M.J., 2013. Isotope evidence for secondary sulfide precipitation along the Marsyandi River, Nepal, Himalayas. Earth and Planetary Science Letters 374, 36–46. https://doi.org/10.1016/j.epsl.2013.04.033

Tuttle, M.L.W., Breit, G.N., Cozzarelli, I.M., 2009. Processes affecting δ34S and δ18O values of dissolved sulfate in alluvium along the Canadian River, central Oklahoma, USA. Chemical Geology 265, 455–467. https://doi.org/10.1016/j.chemgeo.2009.05.009

van Everdingen, R.O., Krouse, H.R., 1985. Isotope composition of sulphates generated by bacterial and abiological oxidation. Nature 315, 395–396. https://doi.org/10.1038/315395a0

Vanni, M.J., Renwick, W.H., Headworth, J.L., Auch, J.D., Schaus, M.H., 2001. Dissolved and particulate nutrient flux from three adjacent agricultural watersheds: A five-year study. Biogeochemistry 54, 85–114. https://doi.org/10.1023/A:1010681229460

Verma, S., Markus, M., Cooke, R.A., 2012. Development of error correction techniques for nitrate-N load estimation methods. Journal of Hydrology 432–433, 12–25. https://doi.org/10.1016/j.jhydrol.2012.02.011

Viviroli, D., Archer, D.R., Buytaert, W., Fowler, H.J., Greenwood, G.B., Hamlet, A.F., Huang, Y., Koboltschnig, G., Litaor, M.I., López-Moreno, J.I., Lorentz, S., Schädler, B., Schreier, H., Schwaiger, K., Vuille, M., Woods, R., 2011. Climate change and mountain water resources: overview and recommendations for research, management and policy. Hydrol. Earth Syst. Sci. 15, 471–504. https://doi.org/10.5194/hess-15-471-2011

Viviroli, D., Dürr, H.H., Messerli, B., Meybeck, M., Weingartner, R., 2007. Mountains of the world, water towers for humanity: Typology, mapping, and global significance. Water Resour. Res. 43. https://doi.org/10.1029/2006WR005653

West, A., Galy, A., Bickle, M., 2005. Tectonic and climatic controls on silicate weathering. Earth and Planetary Science Letters 235, 211–228. https://doi.org/10.1016/j.epsl.2005.03.020

West, A.J., 2012. Thickness of the chemical weathering zone and implications for erosional and climatic drivers of weathering and for carbon-cycle feedbacks. Geology 40, 811–814. https://doi.org/10.1130/G33041.1

West, A.J., Bickle, M.J., Collins, R., Brasington, J., 2002. Small-catchment perspective on Himalayan weathering fluxes. Geology 30, 355. https://doi.org/10.1130/00917613(2002)030<0355:SCPOHW>2.0.CO;2

West, N., Kirby, E., Bierman, P., Slingerland, R., Ma, L., Rood, D., Brantley, S., 2013. Regolith production and transport at the Susquehanna Shale Hills Critical Zone Observatory, Part 2: Insights from meteoric 10Be. Journal of Geophysical Research: Earth Surface 118, 1877–1896. https://doi.org/10.1002/jgrf.20121

White, A.F., 2003. Natural Weathering Rates of Silicate Minerals, in: Treatise on Geochemistry. Elsevier, pp. 133–168. https://doi.org/10.1016/B0-08-043751-6/05076-3

White, A.F., Blum, A.E., 1995. Effects of climate on chemical weathering in watersheds. Geochimica et Cosmochimica Acta 59, 1729–1747. https://doi.org/10.1016/0016-7037(95)00078-E

White, A.F., Brantley, S.L., 2003. The effect of time on the weathering of silicate minerals: why do weathering rates differ in the laboratory and field? Chemical Geology 202, 479–506. https://doi.org/10.1016/j.chemgeo.2003.03.001

Wilding, M.W., Rhodes, D.W., 1970. Solubility isotherms for calcium fluoride in nitric acid solution. J. Chem. Eng. Data 15, 297–298. https://doi.org/10.1021/je60045a032

Wildman, R.A., 2004. The weathering of sedimentary organic matter as a control on atmospheric O2: I. Analysis of a black shale. American Journal of Science 304, 234–249. https://doi.org/10.2475/ajs.304.3.234

Willett, S.D., 1999. Orogeny and orography: The effects of erosion on the structure of mountain belts. J. Geophys. Res. 104, 28957–28981. https://doi.org/10.1029/1999JB900248

Williamson, M.A., Rimstidt, J.D., 1994. The kinetics and electrochemical rate-determining step of aqueous pyrite oxidation. Geochimica et Cosmochimica Acta 58, 5443–5454. https://doi.org/10.1016/0016-7037(94)90241-0

Winnick, M.J., Carroll, R.W.H., Williams, K.H., Maxwell, R.M., Dong, W., Maher, K., 2017. Snowmelt controls on concentration-discharge relationships and the balance of oxidative and acid-base weathering fluxes in an alpine catchment, East River, Colorado. Water Resources Research 53, 2507–2523. https://doi.org/10.1002/2016WR019724

Worrall, F., Howden, N.J.K., Burt, T.P., 2013. Assessment of sample frequency bias and precision in fluvial flux calculations – An improved low bias estimation method. Journal of Hydrology 503, 101–110. https://doi.org/10.1016/j.jhydrol.2013.08.048

Xu, G., Hannah, J.L., Bingen, B., Georgiev, S., Stein, H.J., 2012. Digestion methods for trace element measurements in shales: Paleoredox proxies examined. Chemical Geology 324–325, 132–147. https://doi.org/10.1016/j.chemgeo.2012.01.029

Yan, J., Manelski, R., Vasilas, B., Jin, Y., 2018. Mobile Colloidal Organic Carbon: An Underestimated Carbon Pool in Global Carbon Cycles? Frontiers in Environmental Science 6. https://doi.org/10.3389/fenvs.2018.00148

Yeghicheyan, D., Bossy, C., Bouhnik Le Coz, M., Douchet, C., Granier, G., Heimburger, A., Lacan, F., Lanzanova, A., Rousseau, T.C.C., Seidel, J.-L., Tharaud, M., Candaudap, F., Chmeleff, J., Cloquet, C., Delpoux, S., Labatut, M., Losno, R., Pradoux, C., Sivry, Y., Sonke, J.E., 2013. A Compilation of Silicon, Rare Earth Element and Twenty-One other Trace Element Concentrations in the Natural River Water Reference Material SLRS-5 (NRC-CNRC). Geostandards and Geoanalytical Research 37, 449–467. https://doi.org/10.1111/j.1751-908X.2013.00232.x

Yu, Z., Wu, G., Keys, L., Li, F., Yan, N., Qu, D., Liu, X., 2019. Seasonal variation of chemical weathering and its controlling factors in two alpine catchments, Nam Co basin, central Tibetan Plateau. Journal of Hydrology 576, 381–395. https://doi.org/10.1016/j.jhydrol.2019.06.042

Zhi, W., Williams, K.H., Carroll, R.W.H., Brown, W., Dong, W., Kerins, D., Li, L., 2020. Significant stream chemistry response to temperature variations in a high-elevation mountain watershed. Commun Earth Environ 1, 43. https://doi.org/10.1038/s43247-020-00039-w